

Atomic-scale Investigation of Deformation

Mechanisms in Polycrystalline

Magnesium

by

Huicong Chen

Department of Mining and Materials Engineering



McGill University

Montréal, Quebec, Canada

October 2023

A thesis submitted to McGill University in partial fulfillment of the requirements of the degree
of Doctor of Philosophy

© Huicong Chen, 2023

Abstract

Magnesium (Mg) has attracted significant interest in the manufacturing and transportation sectors due to its low density, abundance in the earth's crust, high specific strength, and good castability. However, Mg and its alloys typically exhibit poor room temperature ductility and formability, which limits their use as wrought materials. These limitations are directly linked to the underlying hexagonal-close-packed (hcp) crystal structure, which lacks sufficient independent deformation modes for homogeneous deformation at low temperatures. To address these drawbacks, twinning has been proposed as a potential means to provide additional deformation modes for homogeneous deformation at low temperatures. This thesis focuses on twinning in polycrystalline Mg and aims to characterize twinning structures and reveal twinning growth mechanism assisted by formation and migration of disconnections at twinning boundary (TB) interface. Additionally, the effect of solutes on TB strengthening and on the activity of main dislocations were investigated to uncover the underlying mechanism of solute-enhanced activity of these defects in Mg alloys.

To investigate the twinning response of a Mg polycrystal during deformation, large-scale classical molecular dynamics (MD) simulations were conducted. A novel algorithm based on crystallographic misorientation was developed to identify twin variants in deformed polycrystal. Schmid factors were then calculated to predict twinning activation. The findings suggest that twin variants with high Schmid factors are more likely to be activated.

In the following, the three-dimensional twinning structures were characterized and examined to provide information about microstructural evolution and the characteristic of three twinning modes i.e., $\{10\bar{1}2\}$ $\{10\bar{1}1\}$ and $\{11\bar{2}1\}$ twins. Specifically, for $\{10\bar{1}1\}$ twin, four types of disconnections were identified with step height of h_0 , $2h_0$, $3h_0$ and $4h_0$. Steps with heights of h_0 and $3h_0$ are immobile along twinning direction as they result from the interaction between stacking faults and

TB interface, while the other two disconnections, formed away from the interaction sites, can move freely along twinning direction. In case of $\{11\bar{2}1\}$ twin, only one type of disconnection with a step height of $(\mathbf{b}_{1/2}, h_{1/2})$ was characterized.

Then, similar MD simulations were carried out on Mg-Al and Mg-Y polycrystals to investigate the effect of rare earth elements on the activity of deformation modes. Results show that in the Mg-Y alloy system, twinning occurs only in compressed samples, while pyramidal slips are activated in tensile samples to accommodate plastic strain along the c-axis. This observation is attributed to the addition of Y.

Furthermore, DFT-based ab initio calculations were used to study solute segregation at TBs and its effect on grain boundary strengthening. A two-factor model, considering both lattice strain and electronegativity, was proposed to predict the solute segregation energy, and the model prediction was found to agree well with DFT calculations. The effect of solutes on either strengthening or weakening the TB was evaluated, and potential elements for TB strengthening were proposed.

Finally, Extensive MD simulations were also carried out to investigate the critical shear stress of the three main edge dislocations in Mg-Y alloy over a range of temperatures. Basal slip was found to be more sensitive to the Y solute compared to prismatic and pyramidal slip, leading to the easier activation of non-basal slip systems. Pyramidal slip was observed to be more sensitive to temperature, and in combination with Y addition, more pyramidal slips were potentially activated at finite temperature.

This research provides fundamental understanding of the deformation twinning mechanism in polycrystalline Mg, as well as the solute effect on the modification of deformation modes. These findings could serve as a basis for selecting promising solutes in the development of new high-performance Mg alloys.

Résumé

Le magnésium (Mg) a attiré un intérêt considérable dans les secteurs de la fabrication et du transport en raison de sa faible densité, de son abondance dans la croûte terrestre, de sa résistance spécifique élevée et de sa bonne coulabilité. Cependant, le Mg et ses alliages présentent généralement une faible ductilité et formabilité à température ambiante, ce qui limite leur utilisation en tant que matériaux travaillés. Ces limitations sont directement liées à la structure cristalline compacte hexagonale (hcp) sous-jacente, qui manque de modes de déformation indépendants suffisants pour une déformation homogène à basses températures. Pour remédier à ces inconvénients, le maclage a été proposé comme moyen potentiel de fournir des modes de déformation supplémentaires pour une déformation homogène à basses températures. Cette thèse se concentre sur le maclage dans le Mg polycristallin et vise à caractériser les structures de maclage et à révéler le mécanisme de croissance du maclage assisté par la formation et la migration de dislocations à l'interface du maclage. De plus, l'effet des solutés sur le renforcement de l'interface de maclage et sur l'activité des principales dislocations a été étudié pour découvrir le mécanisme sous-jacent de l'activité améliorée des défauts dans les alliages de Mg.

Pour étudier la réponse au maclage d'un polycristal de Mg lors de la déformation, des simulations de dynamique moléculaire (MD) classique à grande échelle ont été menées. Un nouvel algorithme basé sur la désorientation cristallographique a été développé pour identifier les variantes de maclage dans un polycristal déformé. Les facteurs de Schmid ont ensuite été calculés pour prédire l'activation du maclage. Les résultats suggèrent que les variantes de maclage ayant des facteurs de Schmid élevés sont plus susceptibles d'être activées.

Dans ce qui suit, des structures de macles tridimensionnelles ont été caractérisées et examinées pour fournir des informations sur l'évolution microstructurale et les caractéristiques de trois modes

de macles, c'est-à-dire, $\{10\bar{1}2\}$ $\{10\bar{1}1\}$ et $\{11\bar{2}1\}$. Spécifiquement, pour $\{10\bar{1}1\}$, nous avons déterminé quatre types de déconnexions avec une hauteur de pas de h_0 , $2h_0$, $3h_0$ et $4h_0$. $2h_0$ et $4h_0$ sont immobiles dans la direction de maclage car leur formation est due à l'interaction entre les failles de jalonnement et l'interface TB, tandis que les deux autres déconnexions se formant à partir des sites d'interaction peuvent se déplacer librement dans la direction de maclage. En cas de $\{11\bar{2}1\}$, un seul type de déconnexion est caractérisé.

Ensuite, des simulations de dynamique moléculaire (MD) similaires ont été effectuées sur des polycristaux Mg-Al et Mg-Y pour étudier l'effet des éléments des terres rares sur l'activité des modes de déformation. Les résultats montrent que la formation de maclage est limitée tandis que les glissements pyramidaux sont renforcés dans le polycristal de Mg-Y déformé.

De plus, des calculs ab initio basés sur la théorie de la fonctionnelle de la densité ont été utilisés pour étudier la ségrégation de solutés aux interfaces de maclage et son effet sur le renforcement des joints de grains. Un modèle à deux facteurs, considérant à la fois la contrainte de réseau et l'électronegativité, a été proposé pour prédire l'énergie de ségrégation des solutés, et la prédiction du modèle s'est avérée être en accord avec les calculs ab initio. L'effet des solutés sur le renforcement ou l'affaiblissement de l'interface de maclage a été évalué, et des éléments potentiels pour le renforcement des interfaces de maclage ont été proposés.

Enfin, des simulations de dynamique moléculaire étendues ont également été menées pour étudier la contrainte critique de cisaillement des trois principales dislocations d'arête dans l'alliage Mg-Y sur une plage de températures. Le glissement basal s'est avéré être plus sensible au soluté Y par rapport au glissement prismatique et pyramidale, conduisant à l'activation plus facile des systèmes de glissement non-basaux. Le glissement pyramidale a été observé pour être plus sensible à la

température, et en combinaison avec l'ajout de Y, davantage de glissements pyramidaux ont été potentiellement activés à une température finie.

Cette recherche fournit une compréhension fondamentale du mécanisme de maillage de déformation dans le Mg polycristallin, ainsi que l'effet des solutés sur la modification des modes de déformation. Ces résultats pourraient servir de base pour la sélection de solutés prometteurs dans le développement de nouveaux alliages de Mg à haute performance.

Acknowledgements

I would like to take this opportunity to convey my appreciation and gratitude to the people who have helped and encouraged me in completing this dissertation.

First of all, I would like to express my sincere gratitude to my advisor, Professor Jun Song, for his advice, encouragement, and support throughout my degree. Without his expertise and dedication, this research would not have been possible. He has been an exceptional mentor who provided me with insightful feedback, constructive criticism, and thought-provoking discussions. His guidance has challenged me to think critically and has helped me to develop as a researcher. I am also grateful for his patience and understanding during difficult times, and for his continued support even beyond the academic realm. I will always be grateful for his guidance and mentorship.

I would like to extend my heartfelt thanks to my co-supervisor, Professor Stephen Yue, for his invaluable contributions to this research. Working with him has been an absolute pleasure. His dedication, knowledge, and guidance have made a difference. I am so grateful to have had the opportunity to collaborate with him.

I would like to thank my important coauthors Professor Xin Yi and Dr. Jingli Li at Peking University and Dr. Yang Liu and Dr. Baoqi Guo at McGill University, for their important discussions, suggestions, and critical comments to my research work.

I would like to express my gratitude to all group members for their providing me with invaluable support, guidance, and friendship. Special thanks go to Dr. Cheng Chen for his willingness to help, share his expertise, and provide constructive feedback and help me to develop new ideas. I am also grateful for his support and encouragement during difficult times. Special thanks also go to Dr. Fanchao Meng, Dr. Xiao Zhou, Dr. Jie Hou and Dr. Juan Liu for their help and support. I feel incredibly fortunate to have had these former members as a mentor and friend. Special thanks also

go to my current group members and friends, Qiwen Qiu, Baihua Ren, Xiaohan Bie, Yiqing Chen, Ziyi Ding, Yuxuan Wang, Ziqi Cui, Haijun Zhang. I am grateful for all the laughs, conversations, and adventures we have shared. Every moment, whether we were exploring new places, trying new foods, or just hanging out and having a good time, has made my PhD journey a truly memorable experience. I will always cherish the memories of our time together.

I appreciate the financial support provided by the Natural Sciences and Engineering Research Council (NSERC) Strategic Project Grant, the China Scholarship Council (CSC), the McGill Engineering Doctoral Award (MEDA). I also thank Eastern Quebec and Compute Canada for providing computing power for all the simulation work in this thesis.

I would like to express my heartfelt gratitude to my sisters, who have gone above and beyond to support and help me like parents. They have provided me with the unfailing support and guidance in the road to pursue my dreams. I am forever grateful for their sacrifices, their love, and support, and for everything that they have done for me.

Last but not least, I would like to express my deepest gratitude to my wife, Yang for her unwavering support, companionship, and consideration throughout my degree. Her encouragement, patience, and understanding have been instrumental in helping me to navigate the challenges and joys of this experience. I am also grateful for her willingness to make sacrifices and adjustments to accommodate my hectic schedule, to listen and offer her advice when needed. Her kindness, empathy, and understanding have been a constant source of strength and motivation. Thank you, Yang, for being an amazing partner and friend, and for making this journey so much more meaningful and rewarding.

I would like to dedicate this work to my beloved parents for their unconditional love, support, and guidance have been an inspiration and motivation to me throughout my life. They encouraged me

to pursue my dreams, and their love gave me the strength and courage to overcome every obstacle that came my way. Although they are no longer with me, their words of wisdom, their unwavering faith in me, and their love will always be my constant guiding light. I know that they would be proud of me and of the accomplishments that I have achieved, and I will always honor their memory by continuing to pursue my goals with dedication and commitment.

Preface and Contributions of Authors

This thesis is manuscript-based format and four research articles shown in Chapter 4-7. The authorship and contributions of authors are summarized below (* indicates the corresponding author):

1. **Deformation Twinning Behavior in Polycrystalline Magnesium: An Atomistic Study**, Huicong Chen, Jun Song*, Cheng Chen, to be submitted.
2. **Atomic-scale Investigation of Deformation Behavior in Nanocrystalline Mg, Mg-Al and Mg-Y Alloys**, Huicong Chen, Jingli Li, Jun Song*, Xin Yi, to be submitted.
3. **Computational Assessment of Solute Segregation at Twin Boundaries in Magnesium: A Two-Factor Model and Solute Effect on Strengthening**, Huicong Chen, Jun Song*, under review.
4. **Temperature and Composition Dependent of the Critical Resolved Shear Stresses of Mg-Y alloys: an Atomistic Study**, Huicong Chen, Jun Song*, to be submitted.

Author contributions: For all papers 1, 3 and 4, HC and JS developed the idea. CC contributed to discussion and analysis in Paper1. For paper 2, HC and JS conceived the simulation idea based on the experimental work by JL and XY. JL and XY helped discussed the results in paper 2. HC performed all the atomic simulations under the supervision of JS.

Table of Contents

| | |
|--|-----------|
| Abstract | I |
| Résumé..... | III |
| Acknowledgements..... | VI |
| Preface and Contributions of Authors..... | IX |
| Table of Contents..... | X |
| List of Figures | XIV |
| List of Tables | XXII |
| Chapter 1: Introduction | 1 |
| 1.1 Motivation | 1 |
| 1.2 Research objective..... | 6 |
| 1.3 References | 7 |
| Chapter 2: Literature Review..... | 14 |
| 2.1 Plastic Deformation in Mg alloys..... | 14 |
| 2.1.1 Slip systems and deformation modes | 14 |
| 2.1.2 Characteristics of dislocations and generalized stacking faults | 17 |
| 2.1.3 Deformation Twinning | 21 |
| 2.2 Solute Effect on Properties of Mg Alloys..... | 23 |
| 2.2.1 Grain Boundary Segregation | 23 |
| 2.2.1.1 Evidence of Grain Boundary Segregation in Magnesium Alloys..... | 24 |
| 2.2.1.2 Effect of Grain Boundary Segregation on Material Behavior of Mg alloys | 28 |
| 2.2.1.3 Prediction of Grain Boundary Segregation..... | 34 |
| 2.2.2 Solute Effect on Dislocation Slips | 41 |
| 2.3 Twin-slip and Twin-twin Interaction..... | 45 |
| 2.4 References | 45 |
| Chapter 3: Methodology..... | 59 |

| | |
|---|-----------|
| 3.1 First Principles DFT Calculations | 60 |
| 3.2 Molecular Dynamics Simulation | 63 |
| 3.3 Voronoi Tessellation Technique..... | 67 |
| 3.4 Dislocation Mechanics | 69 |
| 3.5 References | 70 |
| Chapter 4: Deformation Twinning Behavior in Polycrystalline Magnesium: An Atomistic Study..... | 72 |
| 4.1 Preface | 72 |
| 4.2 Abstract..... | 73 |
| 4.3 Introduction | 73 |
| 4.4 Computational Methodology | 77 |
| 4.5 Results and Discussion | 80 |
| 4.5.1 Loading Dependence of Twinning Modes..... | 80 |
| 4.5.2 Selection of Twin Variants | 86 |
| 4.5.3 Evolution of Twin Structures | 91 |
| 4.5.3.1 $\{10\bar{1}2\}$ Extension Twin and $\{10\bar{1}1\}$ Contraction Twin..... | 91 |
| 4.5.3.2 $\{11\bar{2}1\}$ Extension Twin | 93 |
| 4.5.4 Disconnections at Twin-Matrix Interface | 96 |
| 4.5.4.1 $\{11\bar{2}1\}$ Extension Twin | 96 |
| 4.5.4.2 $\{10\bar{1}1\}$ Contraction Twin | 98 |
| 4.6 Conclusions | 102 |
| 4.7 Acknowledgement | 103 |
| 4.8 Supplementary Information | 103 |
| 4.8.1 Identification of Twin Variant | 103 |
| 4.8.2 Calculation of Schmid Factor | 106 |
| 4.9 References | 107 |

Chapter 5: Atomic-scale Investigation of Deformation Behavior in Polycrystalline Mg, Mg-Al and Mg–Y alloys..... 112

5.1 Preface 112

5.2 Abstract..... 113

5.3 Introduction 113

5.4 Simulation Method 115

5.5 Results and Discussions..... 116

 5.5.1 Microstructures in Compression and Tensile Simulation 116

 5.5.2 Effect of RE on Deformation Behavior of Magnesium 119

5.6 Conclusion 121

5.7 Acknowledgements 121

5.8 References 122

Chapter 6: Computational Assessment of Solute Segregation at Twin Boundaries in Magnesium: A Two-Factor Model and Solute Effect on Strengthening 126

6.1 Preface 126

6.2 Abstract..... 127

6.3 Introduction 127

6.4 Computational Methodology 130

 6.4.1 TB Structural Models 130

 6.4.2 First-principles Density Functional Theory Calculations 131

 6.4.3 Key Parameters for Segregation Analysis 131

6.5 Results and Discussion 132

 6.5.1 Site Preference and Energetics of Solutes at TBs 132

 6.5.2 Factors Affecting Segregation and Predictive Model 136

 6.5.3 Segregation Coverage of Solutes at TBs 143

 6.5.4 Mapping of Solute Strengthening and Embrittlement 146

6.6 Conclusion..... 147

| | |
|---|------------|
| 6.7 Acknowledgements | 148 |
| 6.8 Supplementary Information | 149 |
| 6.9 References | 150 |
| Chapter 7: Temperature and Composition Dependent of the Critical Resolved Shear Stresses of Mg-Y Alloys: An Atomistic Study..... | 155 |
| 7.1 Preface | 155 |
| 7.2 Abstract..... | 156 |
| 7.3 Introduction | 156 |
| 7.4 Methodology..... | 158 |
| 7.5 Results and Discussion | 162 |
| 7.5.1 Solute Effect on CRSS at 0K..... | 162 |
| 7.5.1.1 Stress-Strain Curves | 162 |
| 7.5.1.2 Evolution of CRSS with Y Content..... | 164 |
| 7.5.2 Solute Effect on CRSS at Finite Temperature | 165 |
| 7.5.2.1 Stress-strain Curves | 165 |
| 7.5.2.2 Evolution of CRSS Versus Y Content and Temperature..... | 168 |
| 7.5.3 Descriptor Map of CRSS Versus Y Content and Temperature | 171 |
| 7.6 Conclusions | 172 |
| 7.7 Acknowledgements | 173 |
| 7.8 References | 173 |
| Chapter 8: Conclusions | 178 |
| 8.1 Final Conclusions | 178 |
| 8.2 Contributions to Original Knowledge..... | 180 |
| 8.3 Future Work..... | 181 |

List of Figures

| | |
|---|----|
| Figure 1.1. General Ashby plot of strength against density for a variety of materials [1] [Figure adapted with permissions]..... | 1 |
| Figure 1.2. Ashby plot of strength against density for ceramics and metals [1] [Figure adapted with permissions]..... | 2 |
| Figure 1.3. Schematically description of the development of Mg alloys reported in literatures. .. | 4 |
| Figure 2.1. Schematic of the HCP unit cell showing all possible: (a) slip and (b) twinning systems [9]. [Figure adapted with permissions]..... | 15 |
| Figure 2.2. Generalized stacking fault (GSF) energy on (a) basal, (b) prismatic, (c) pyramidal I and (d) pyramidal II planes. In each panel, the white, dotted line marks the minimum energy path in the γ surface [41]. [Figure adapted with permissions]..... | 18 |
| Figure 2.3. Dislocation core structures as visualized by the component of the Nye tensor and differential displacement plots: Basal $\langle a \rangle$ (a) edge and (b) screw dislocation; Prismatic $\langle a \rangle$ (c) edge and (d) screw dislocations; Pyramidal I $\langle c + a \rangle$ (e) edge and (f) screw dislocations; Pyramidal I $\langle c + a \rangle$ (g) edge and (h) screw dislocation [41]. [Figure adapted with permissions]..... | 20 |
| Figure 2.4. Illustration of twinning elements: K_1 —twinning plane, η_1 —twinning direction, K_2 —conjugate twinning plane, η_2 —conjugate twinning direction. | 22 |
| Figure 2.5. HAADF-STEM images showing periodic segregation of solutes (a-c) Gd to extension sites of the $\{10\bar{1}1\}$, $\{10\bar{1}2\}$ and $\{10\bar{1}3\}$ CTBs in a Mg–0.2 at. % Gd solid solution alloy and (d) Zn to compression sites of the $\{10\bar{1}2\}$ TB in a Mg–1.9 at. % Zn solid solution alloy [67]. (e) HAADF-STEM images showing periodic segregation of solutes Gd to extension sites of various tilt GBs in a Mg–0.2 at. % Gd solid solution alloy [69]. Calculated segregation energies when various solute atoms segregate to compression site (A) or extension site (B) of (f) $\{10\bar{1}1\}$ and (g) $\{10\bar{1}2\}$, respectively. The numbers 1, 2 and 3 in (f) and (g) correspond to supercells of $1 \times 1 \times 1$, $1 \times 1 \times 2$ and $1 \times 2 \times 2$ of the 90-atom unit cell for $\{10\bar{1}1\}$ and 60-atom unit cell for $\{10\bar{1}2\}$, respectively [109]. [Figure adapted with permissions]..... | 26 |
| Figure 2.6. HAADF-STEM images of a Mg–0.4 at. % Bi alloy aged at 80 °C for 48 h showing (a) a $\{10\bar{1}1\}$ CTB, where an enlarged part shown in the upper-right inset indicates Bi-rich columns at compression sites and (b) a $\{10\bar{1}2\}$ CTB, where no segregation of Bi atoms is observed. (c) | |

{11 $\bar{2}$ 0} plane contour maps of calculated results of DECD for Bi segregated into the compression site or extension site of {10 $\bar{1}$ 1} CTB. (d) PDOS for the cases where solute atoms Bi segregated into the compression site or extension site of {10 $\bar{1}$ 1} CTB: Bi segregation with 20% occupancy, and Bi segregation with 100% occupancy [89]. [Figure adapted with permissions]..... 27

Figure 2.7. (a) Engineering stress–strain curves of three samples of a Mg–0.2 at. % Gd alloy from compression tests. Curve 1 is for sample compressed, unloaded and immediately recompressed. Samples for curves 2 and 3 were annealed at 300 °C for 20 min and at 150 °C for 3 h, respectively, before the second loading. (b-e) Optical micrographs showing twins in samples (b) at a strain of 0.025 of the first loading in curve 1, and (c) at an accumulated strain of 0.045 of the second loading in curve 1, and (d) at a strain of 0.025 of the first loading in curve 2, and (e) at an accumulated strain of 0.045 of the second loading in curve 2 [67]. (f) Energy distribution of symmetric tilt $\langle c \rangle$ -axis boundaries. Pure Mg boundaries are compared to boundaries with random segregation of Y and idealized segregation of Y [98]. (g) Logarithm of the migration rate R vs. the inverse of the stress $1/\tau$, for pure Mg (squares), Mg–1 at. % Al (triangles), Mg–3 at. % Al (circles), Mg–5 at. % Al (diamonds), at 300 K and (h) Applied shear stress for unpinning of the twin boundary with solutes segregated under application of a constant applied strain rate as measured in the simulation (scattered points) vs. the stress predicted by the model (dashed line), for segregated concentrations at 10 at. %, 25 at. %, 50 at. % and 100 at. % [28]. [Figure adapted with permissions]..... 31

Figure 2.8. (a) Variations of recrystallized grain size as a function of annealing time at 350° C in cold-rolled (23% thickness reduction) Mg-0.3Zn-0.1Ca, Mg-0.1Ca, and Mg-0.4Zn alloys. (b) Histogram showing grain size distribution in each alloy in the fully recrystallized state (900 s annealing at 350 ° C). (c) HAADF-STEM image, and (d–f) EDX maps showing solute segregation to grain boundaries in Mg-0.3Zn-0.1Ca alloy subjected to 23% thickness reduction and annealing at 350 ° C for 900 s [97]. [Figure adapted with permissions]..... 32

Figure 2.9. (a-c) Pole figures of basal (0001) planes showing the texture of TRC-AZMX3110, IC-AZMX3110, and IC-AZX310, respectively. The numbers in red color indicate the maximum texture intensity. (d) Yield strength and stretch formability represented by the Index Erichsen (IE) value at room temperature of various Mg alloys sheets. Higher IE values mean that the alloys exhibit better formability [99]. [Figure adapted with permissions]..... 33

Figure 2.10. (a) Occupation versus binding energy, $-E_b$ (eV/S), at a segregation site calculated from McLean's equation (Eq. (2.7)) with respect to the aging temperature (K) and bulk S

concentration (atomic ppm, 10^{-4} atomic % S) in a (b) $\Sigma 5(012)$ symmetrical tilt GB, where gray balls indicate Ni atoms; yellow balls indicate S atoms. [131]. (c) Y concentration at the $\Sigma 7$, general tilt and 3-D GBs in Mg-Y system as a function of temperature using Eq. (2.9) and nominal bulk concentration $Cb=0.75\%$ [96]. [Figure adapted with permissions] 36

Figure 2.11. Predicted (on the basis of McLean model) and DFT-computed segregation energies of solutes in (a) compression TB and (b) tensile TB in Mg [109]. Plot of the lowest tilt segregation energy E_{seg}^X against (c) the relative metallic radius difference $\frac{R_X - R_{Mg}}{R_{Mg}}$ for each dopant X, and (d) the square of the relative Pauling electronegativity $(\chi_X - \chi_{Mg})^2$ [114]. [Figure adapted with permissions] 38

Figure 2.12. Predicted segregation energies using (a) a linear fit and (b) gradient-boosted decision trees plotted against calculated values for all six solutes. Results are taken from all 38 boundaries and data distribution plots are shown joint to their corresponding axes. Darkness of color indicates data frequency, and results are smoothed [113]. [Figure adapted with permissions] 40

Figure 2.13. (a) Tensile curves of nominal stress vs. strain, and (b) True stress-strain and strain hardening curves from tensile tests of pure Mg and Mg- wt.% 3Y [140]. (c) TEM bright-field images of slightly room-temperature-deformed pure Mg showing mainly basal $\langle a \rangle$ dislocations [137], and (d) TEM bright-field and dark-field images under different two-beam diffractions (see inlets for the diffraction vector), showing the activity of different perfect and partial dislocations with a $\langle c+a \rangle$ Burgers vector on pyramidal plane in 3% (engineering strain) cold-rolled Mg-3 wt.% Y; an intrinsic stacking fault I_2 (SF_2) is also visible [136]. (e) The ab initio determined I_1 SFEs of Mg-Y alloys with different Y concentrations (elemental Mg and Y, $Mg_{107}Y_1$, $Mg_{31}Y_1$, and $Mg_{15}Y_1$) [136]. (f) CRSS of Mg-Y alloys on the basal, prismatic, and pyramidal II planes obtained via MD simulation at 0 K [4]. [Figure adapted with permissions] 42

Figure 2.14. (a) Competing pyramidal-to-basal transition and pyramidal II-I cross-slip processes during the expansion of an $L \times L$ $\langle c+a \rangle$ dislocation loop on the pyramidal II plane. Activation energy for cross-slip and ductility index χ for binary and higher-order Mg alloys: (b) Average solute contribution to energy difference ΔE^{I-II} between the pyramidal I and II $\langle c+a \rangle$ screw dislocations for various solute elements; (c) Predicted pyramidal II-I cross-slip activation energy barrier including solute fluctuations and ductility index χ for binary Mg alloys as a function of solute concentration c for the same solutes. $\chi > 1$ indicates favorable conditions for ductility; (d) $Mg -$

| | |
|---|----|
| <i>Al - X - '</i> with varying Al concentrations and (e) <i>Mg - Zn - X - X'</i> with varying Zn concentrations [14]. [Figure adapted with permissions]..... | 44 |
| Figure 3.1. A flow chart illustrating the iteration scheme of electronic structure calculations based on DFT..... | 62 |
| Figure 3.2. A schematic of the molecular dynamics simulation algorithm..... | 67 |
| Figure 3.3. a) Voronoi tessellation in two dimensions. (b) Three-dimensional Voronoi tessellation for a set of particles shown as yellow spheres. The blue lines show the entire Voronoi tessellation, while the red lines highlight a single Voronoi cell as a convex polyhedron [14]. [Figure adapted with permissions]..... | 68 |
| Figure 3.4. Illustration of using a Voronoi tessellation to construct polycrystals [16]. [Figure adapted with permissions]..... | 69 |
| Figure 4.1. (a) the polycrystal Mg microstructure; (b) Example of forming a grain (G4) with specific orientation after three rotation operations; (c) the geometrical orientation distribution of each grain illustrated in pole figure. Atoms are colored by their local orientation in figure (a) and the same coloring method is adopted to reveal the microstructure in this work..... | 78 |
| Figure 4.2. Snapshots of microstructures viewed along X-direction for each sample deformed to a strain of 8% under uniaxial tensile stress loading (a-b) and (d-f) uniaxial compression stress loading, respectively; (g) geometrical orientation of each grain in the sample coordinate. | 81 |
| Figure 4.3. Representative overview of twinning evolution during uniaxial tensile stress loading along X-direction at a strain of (a) 4.6%, (b) 5.2%, (c) 6.2%, (d) 6.8%, (e) 7.6%, (f) 12%; (g) geometrical orientation of each grain in the sample coordinate, where Gi (i=1~15) represent each grain in the current polycrystal. | 82 |
| Figure 4.4. Representative overview of twinning evolution during uniaxial compression stress loading along X-direction at a strain of (a) 4.6%, (b) 5.2%, (c) 6.2%, (d) 6.8%, (e) 7.6%, (f) 12%; (g) geometrical orientation of each grain in the sample coordinate..... | 83 |
| Figure 4.5. 3D view of microstructural evolution of grain 9 (G9) under (a) tensile stress loading along X-direction and (b) compression stress loading along X-direction. | 84 |
| Figure 4.6. Variation of twinning volume in G9 as a function of strain during uniaxial tensile and compression stress loading along X-direction. | 85 |
| Figure 4.7. Schmid factors of possible twin variants, and the selected variants when the sample is deformed under tensile stress loading along X-direction. Note, Schmid factors in compression | |

stress loading simulation have the same absolute value but in opposite sign with case of tensile stress loading simulation. The embedded symbol “+” means the activated twin variants in simulation of tensile stress loading and “-” stands by the active twin variants in simulation of compression stress loading. Similar marking scheme is used in **Figure 4.9** and **Figure 4.10**. 87

Figure 4.8. Schmid factors of possible twin variants and the selected variants when the sample is deformed under tensile (“+”) and compression (“-”) stress loading along Y-direction. 87

Figure 4.9. Schmid factors of possible twin variants and the selected variants when the sample is deformed under tensile (“+”) and compression (“-”) stress loading along Z-direction. 88

Figure 4.10. The total number of active twins in the sample deformed under different lading directions plotted versus their ranking of Schmid factor. 90

Figure 4.11. Microstructural evolution of the $\{10\bar{1}2\}$ extension twin in G9 during uniaxial compression stress loading along X-direction at different strain levels. 91

Figure 4.12. Microstructural evolution of the $\{10\bar{1}1\}$ contraction twin in G9 during uniaxial tensile stress loading along X-direction at different strain levels. 92

Figure 4.13. Microstructural evolution of the $\{11\bar{2}1\}$ extension twin in G3 during uniaxial compression stress loading along X-direction at different strain levels. 94

Figure 4.14. Illustration of twinning boundary interface structures for (a) the $\{10\bar{1}2\}$ twin, (b) the $\{10\bar{1}1\}$ twin and (c) the $\{11\bar{2}1\}$ twin, respectively. 95

Figure 4.15. The $[10\bar{1}0]$ projection of (a) the undislocated $\{11\bar{2}1\}$ TB interface showing the twinning elements and the displacement by which matrix atoms move to the lattice sites in the twin; (b) the distorted $\{11\bar{2}1\}$ TB showing the interfacial step associated with a twinning dislocation at a time of 94 ps. In the matrix crystal of Figure (a), filled symbols represent lattice sites of the matrix and open symbols (red) are lattice sites of the twin. 97

Figure 4.16. Illustration of the growth of the $\{10\bar{1}1\}$ twin by movement of steps along the twin boundary interface in G9 during uniaxial tensile stress loading along X-direction at different timesteps. 99

Figure 4.17. The $[11\bar{2}0]$ projection of (a) the undislocated $\{1\bar{1}01\}$ TB interface showing the twinning elements and the displacement by which matrix atoms move to the lattice sites in the twin; (b) the disconnected $\{1\bar{1}01\}$ TBs showing the interfacial steps with different height in G9 deformed at a time of 122 ps under a uniaxial tensile stress loading along X-direction. In figure (a), filled symbols represent lattice sites (type A in black and type B in yellow) of the matrix and

open symbols (red) are lattice sites of the twin. In figure (b) Stacking faults consist of atoms in green color..... 101

Figure S4.1. (a) Definition of crystal (c) and sample (s) coordinate systems for cubic box, which are highlighted by red and black color, respectively. α , β and γ are defined as the direction angles between a crystal axis and X, Y and Z, respectively. (b) Schematics of HCP configurations, showing a central atom (red) and its nearest neighbors (purple)..... 105

Figure 5.1. (a) Initial polycrystal structures (atoms are colored according to its local lattice orientation) and (b) orientation distribution in pole (0001) figure. 116

Figure 5.2. Microstructural snapshots perpendicular to X-direction of (a) the initial sample and samples deformed at a strain of 7.4% under uniaxial compression stress loading along X-direction: (b) Pure Mg, (c) Mg-1at%Al and (d) Mg-1at%Y, where atoms Al and Y are colored in black in Figure (c) and (d). 117

Figure 5.3. Microstructural snapshots perpendicular to X-direction of (a) the initial sample and samples deformed at a strain of 7.4% under uniaxial tensile stress loading along X-direction: (b) Pure Mg, (c) Mg-1at%Al and (d) Mg-1at%Y, where atoms Al and Y are colored in black in Figure (c) and (d)..... 118

Figure 5.4. Twin volume fraction evolution with straining for three alloy systems of Mg, Mg-Al and Mg-Y under tensile and compression loading..... 118

Figure 5.5. Illustration of active deformation modes for grain 9 deformed to a total strain of 7.4% under compression stress (a) pure Mg, (c) Mg-Al and (e) Mg-Y, and under tensile stress (b) pure Mg, (d) Mg-Al and (f) Mg-Y. Atoms of the matrix are deleted and only twinned atoms are revealed in all Figures. 120

Figure 5.6. Illustration of active deformation modes for grain 7 deformed to a total strain of 7.4% under compression stress (a) pure Mg, (c) Mg-Al and (e) Mg-Y, and under tensile stress (b) pure Mg, (d) Mg-Al and (f) Mg-Y. Atoms of the matrix are deleted and only twinned atoms are revealed in all Figures. 121

Figure 6.1. Schematic illustration of the TB model used in the current study. (a) $\{10\bar{1}2\}$ TB, (b) $\{10\bar{1}1\}$ TB. The yellow (compression site) and green (extension site) color represent the two different sites at TB, which have different volumetric size for their corresponding sites in bulk, marked purple and grey respectively. 130

| | |
|---|-----|
| Figure 6.2. The segregation energies of different solute atoms at site A ($E_{seg}^{TB,A}$) versus those ($E_{seg}^{TB,B}$) at site B in (a) $\{10\bar{1}1\}$ and (b) $\{10\bar{1}2\}$ TBs..... | 135 |
| Figure 6.3. The comparison of segregation energy at preferential sites in $\{10\bar{1}1\}$ and $\{10\bar{1}2\}$ TBs. | 136 |
| Figure 6.4. The local mismatch around doping site (highlight with green circle) in bulk for three atoms with representative atomic size: (a) Ca; (b) Al; (c) Zr; and the atomic structure used for bulk Mg is shown in (d). The star shape stands by the Voronoi volume in dopant-free bulk and the green circle represents the solute atoms. The negative values in (a-c) indicate the Voronoi volume is reduced due to solute doping. | 137 |
| Figure 6.5. Distribution of Voronoi volume in a fully relaxed $\{10\bar{1}2\}$ TB..... | 138 |
| Figure 6.6. The local mismatch around doping site of $\{10\bar{1}2\}$ TB for three atoms with representative atomic size: (a, b) Ca; (c, d) Al; (e, f) Zr. | 140 |
| Figure 6.7. Plot of predicted and DFT-computed segregation energies of solutes in the (a) extension site of $\{10\bar{1}1\}$ TB, (b) compression site of $\{10\bar{1}1\}$ TB, (c) extension site of $\{10\bar{1}2\}$ TB and (d) compression site of $\{10\bar{1}2\}$ TB. | 142 |
| Figure 6.8. Solute concentrations at preferential segregation sites for (a) the compression TB and (b) the tensile TB as a function of temperature using Eq. (6.6) with a nominal bulk concentration of $C_b = 0.8$ at.%. | 145 |
| Figure 6.9. Plots of the strengthening energy E_{se} versus segregation energy E_{seg} for all solutes in the (a) $\{10\bar{1}1\}$ TB and (b) $\{10\bar{1}2\}$ TB. Positive and negative E_{seg} values indicate solutes would stay in bulk or segregate at TB, respectively, while positive and negative E_{se} indicate solute would lead to TB embrittlement or strengthening, respectively. | 147 |
| Figure 7.1. Core structures of edge dislocations on (a) basal, (b) prismatic and (c) pyramidal II planes using a MEAM interatomic potential for pure Mg [39]. (d) Schematic view of the simulation cell showing the shearing procedure to move a dislocation. | 159 |
| Figure 7.2. Simulated stress–strain curves for pure Mg on the basal, prismatic, and pyramidal II planes, at 0 K..... | 162 |
| Figure 7.3. The stress-strain responses of (a) basal dislocation, (b) prismatic dislocation and (c) pyramidal II dislocation moving at 0K and (d) the CRSS distribution with different Y content and the fitted results, where solid squares are simulation results, and dashed lines are the linear fitting. Error bars represent standard deviation. | 164 |

Figure 7.4. The stress-strain responses of the basal dislocation decorated with different Y content moving at temperatures of (a) 100K, (b) 200K, (c) 300K, (d) 400K and (e) 500K..... 167

Figure 7.5. The stress-strain responses of the prismatic dislocation decorated with different Y content moving at temperatures of (a) 100K, (b) 200K, (c) 300K, (d) 400K and (e) 500K..... 167

Figure 7.6. The stress-strain responses of the pyramidal dislocation decorated with different Y content moving at temperatures of (a) 100K, (b) 200K, (c) 300K, (d) 400K and (e) 500K..... 168

Figure 7.7. Plot of CRSS evolution as a function of Y content for (a) basal, (b) prismatic and (c) pyramidal dislocations moving at various temperatures. Error bars represent standard deviation. 169

Figure 7.8. Plot of CRSS as a function of temperature for (a) basal, (b) prismatic and (c) pyramidal dislocations decorated with different Y content. Error bars represent standard deviation. 171

Figure 7.9. The descriptor map for CRSS evolution as a function of temperature and Y concentration..... 172

List of Tables

| | |
|---|------------|
| Table 2.1. Critical resolved shear stresses (CRSS) of common deformation modes reported for Mg. | 16 |
| Table 4.2. Illustration of three twin modes and six twin variants of each twin mode represented by boundary misorientation axis and angles in Mg. The extension twin 1012 and 1121, and the contraction twin 1011 are defined as ET1012, ET1121 and CT1011, respectively. V_i ($i=1\sim6$) represent the six twin variants for each twin type..... | 80 |
| Table 6.1. Fitting parameters for the two-factor linear model and their Pearson's r coefficients. | 141 |
| Table S6.1. DFT-computed segregation energies (unit in eV) at site A and B, and strengthening energy (unit in eV) and solubility at 473K provided that solutes segregate at preferential sites. | 149 |

Chapter 1: Introduction

1.1 Motivation

One goal that engineers continuously strive to achieve in materials design is to decrease the weight of materials while maintain or increase their strength and ability to work in extreme environment, i.e., developing novel ultra-lightweight metallic materials with excellent mechanical and functional properties. Accordingly, highlighted by Ashby's mechanical design map shown in **Figure 1.1**, the design will be to push the envelope towards the top left, i.e., higher strength and lower density.

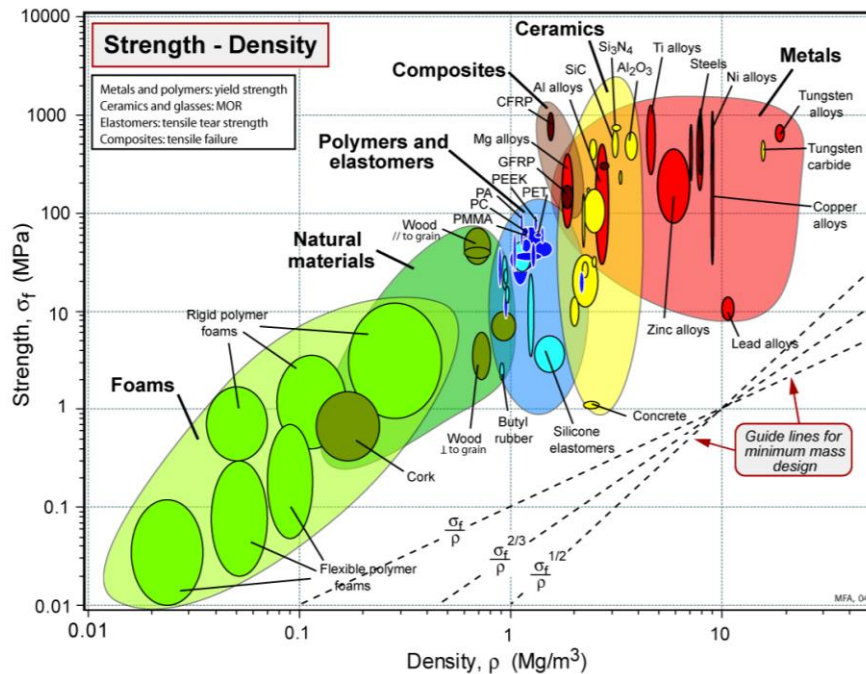


Figure 1.1. General Ashby plot of strength against density for a variety of materials [1]. [Figure adapted with permissions]

Among the category of structural metals, magnesium attracts great attention due to its low density. As shown in **Figure 1.2**, magnesium (Mg) is the lightest of all commonly used structural metals, with a density of 1.738 g/cm³, approximately two thirds that of aluminum and one quarter that of

steels, making it high specific strength [2, 3]. Mg also shows excellent castability and machinability. Moreover, Mg is of high supply, being very abundant in both the Earth's crust and the ocean [4]. The above makes Mg and its alloys, thereafter, together referred to as Mg alloys, an attractive option in materials design, and potential replacement for the traditional structural materials used in automotive, aerospace, and other structural applications. In addition, the potential weight reduction and associated energy saving resulted from the application of Mg alloys have great implication in the context of global challenges regarding energy saving and CO₂ emission reduction [4]. Despite these great benefits, Mg alloys have several major limitations, including limited ductility and poor low temperature formability, relatively low strength and fracture toughness, poor corrosion resistance and dissimilar joining issues [4, 5]. These limitations thus prevent widespread use of Mg alloys.

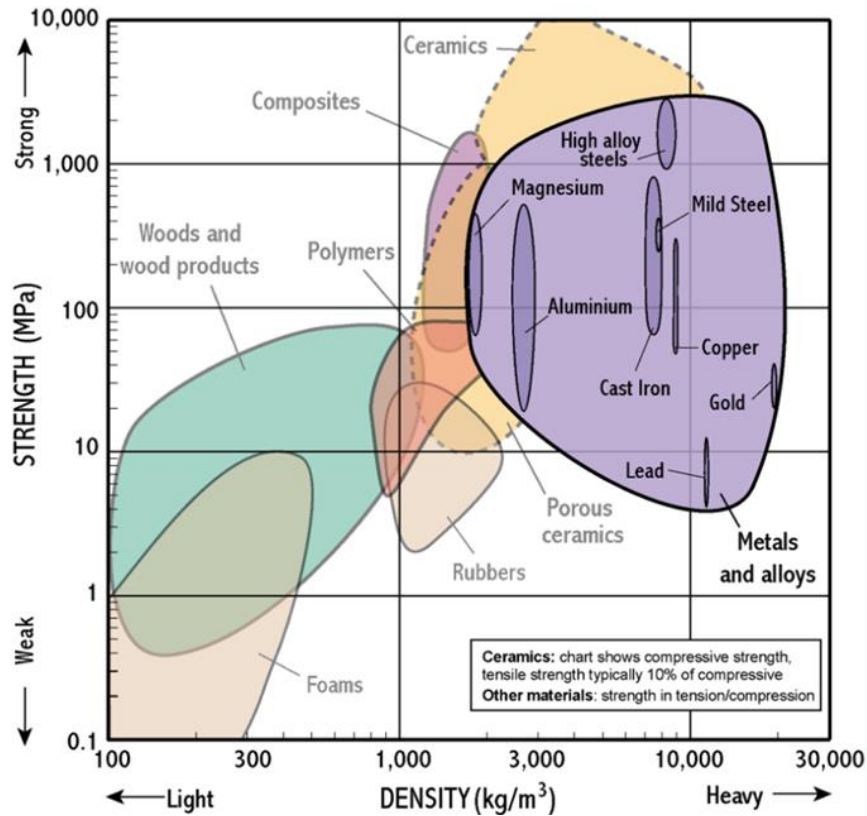


Figure 1.2. Ashby plot of strength against density for ceramics and metals [1]. [Figure adapted with permissions]

Among these limitations, the poor ductility, low-temperature formability as well as the low fracture toughness of Mg alloys are mainly due to their hexagonal closed packed (hcp) structure. At room temperature, the basal slip exhibits much lower critical resolved shear stress (CRSS) than other slip systems on prismatic and pyramidal planes [6]. This results in easy activation of basal slips and their dominance in plastic deformation. However, due to the lattice symmetry, the easy activation of basal slip provides only two independent deformation modes operating during plastic deformation at room temperature [7] and this deformation mode is incapable of accommodating plastic along c-axis of hcp Mg. According to the von-Mises criterion [7], a minimum of five independent slip systems is required for homogeneous plastic deformation. Even with extra two prismatic slip systems activated, the number of slip systems are still insufficient to satisfy the criteria and thus poor ductility of Mg alloys is expected at room temperature. At higher temperatures four independent pyramidal slip systems can be activated, which allows a deformation along c-axis. Therefore, elevated temperatures often become mandatory in order to obtain an increase in formability. Besides dislocation slips, twinning provides an alternative deformation mechanism that plays an important role in strain accommodation for Mg alloys. A reorientation of crystal lattice resulting from twinning can tailor basal texture [8, 9] to introduce slip planes favorably oriented for dislocation slips [9], which would otherwise be unavailable. Therefore, twinning deformation mode necessitates consideration in the design of new Mg alloys. To tackle those limitations of Mg alloys, various engineering strategies have been proposed to enhance the properties of Mg alloys, one strategy of which is microstructural design and modification (grain refinement) [10-15]. For instance, the refined microstructure, with reduced grain size and modified texture, can be obtained by using high-speed rolling process [10, 11] or

adding specific alloying elements [12-15]. In particular, addition of the rare-earth (RE) elements, such as Y, Nd, Gd, Ce and La, have been demonstrated to be capable of reducing the critical stress differential between basal and non-basal deformation modes to promote non-basal deformation modes, thus helping enhance the ductility of Mg alloys at moderate temperatures [16-18]. In addition, with alloying naturally solute segregation at internal interfaces, such as grain boundaries (GBs) and twinning boundaries (TBs), is expected. Several studies have shown that segregation or co-segregation of solutes, e.g., Zn and Gd, at TBs can stabilize the TB structure by reducing TB energy and exerting a strong pinning effect on TB migration, and hence strengthen TBs [16, 19]. Moreover, GB mobility would be reduced due to the solute segregation during recrystallization and grain growth, thereby inhibiting grain growth into preferable orientation [20-22]. As a result, basal texture can be weakened, and more uniform deformation is obtained after annealing, meaning the enhanced ductility and formability.

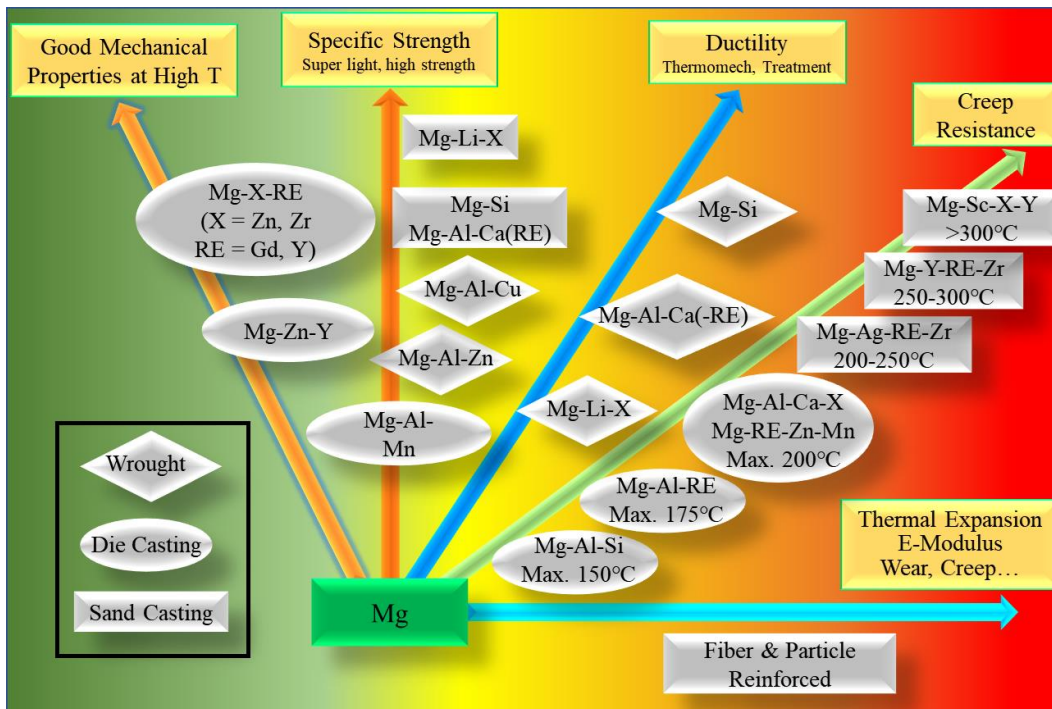


Figure 1.3. Schematically description of the development of Mg alloys reported in literature.

Although certain successes have been achieved in designing new Mg alloys [16, 19, 20, 23-25] with enhanced properties for various purposes, shown in **Figure 1.3**, there remain numerous questions with significant deficit in understanding of the physical principles underlying plasticity in Mg alloys. Consequently, the experimental work to explore Mg alloys is largely trial-and-error in nature. Therefore, to fast track the design and exploration of Mg alloys with more efficiency, it is imperative to develop better understanding of the fundamental deformation mechanisms. In recent years, with the great advances in simulation techniques and remarkable increase in computational power, computer simulations have shown great potential in providing information beyond the experimental resolution [26]. Computer simulations allow the researchers to quickly navigate through different composition spectrums, microstructural variations, and thermal/loading conditions, providing great flexibility and versatility in examining behaviors of Mg alloys under different situations. Different simulation techniques exist, such as ab initio calculation based on density functional theory (DFT) [16, 27-32], molecular dynamics (MD) simulations [33-43], dislocation dynamics [44-55], finite element method (FEM) [56-65] and phase fields simulations [53, 66-70]. Among those, atomistic simulations, where the material system is represented by a group of atoms, enable examination of the behaviors of materials at the atomic level. Atomistic simulations can reveal the most fundamental structure-property relationships, and in the case of Mg alloys, have played an increasingly important role in identifying the critical deformation and failure mechanisms. Both DFT and MD are within the category of atomistic simulations. In particular, DFT based first principles calculations is presently the most successful and promising approach to compute the electronic structure of matter on the basis of solving quantum mechanics while MD is capable of dealing with large systems and provides detailed structural, dynamic, and thermodynamic information. These two methods are the main tools used in this thesis work.

Specifically, the research objectives we aim to achieve through the DFT and MD efforts are listed in Section 1.2.

1.2 Research Objective

In this thesis, we investigate micromechanism of deformation modes in polycrystal Mg and Mg-Y at atomistic scale as well as the Y effect on activation of twinning and dislocation using state-of-the-art computational tools. The main objectives of this thesis are as follows:

In this thesis, we constructed a series of polycrystalline structures for Mg and its alloys and performed tension or compression simulation on these structures using MD simulations. Then, Detailed microstructure analysis were carried out to determine twinning structures and identify twin variants in deformed polycrystals. The main characteristics of three TB interfaces were studied. Furthermore, DFT calculation was performed to examine the effects of solute segregation on the strengthening and embrittling of TBs in Mg and MD simulations were carried out to calculate the critical shear stress of three main dislocations at various temperature and yttrium content. The main objectives of this thesis are as follows:

- A. Develop an algorithm to identify twinning structure and determine twin variant in deformed Mg polycrystalline.
- B. Evaluate twin variant selection by calculating Schmid factors of all twin variants in deformed polycrystalline and reveal evolution and characteristic of three TBs during deformation.
- C. Compare difference of the activation of deformation modes in Mg and Mg-Y polycrystalline.
- D. Investigate solute segregation at TBs and its effect on TB strengthening/embrittling.

- E Examine the effects of Y on motion of three main dislocations in Mg by calculating their critical shear stress.

The results obtained from the above objectives are presented in Chapters 4-7 of the thesis.

Specifically:

- Chapter 4 proposed a novel method based on misorientation character of twin variants in Mg and studied the activation of twin variants via Schmid factor analysis. Then, Microstructural evolution and characteristics of three twin boundaries were investigated.
- Chapter 5 investigated the effect of RE elements on deformation mechanism in a Mg polycrystalline. Here, solute Y was selected as a representative. Therefore, the difference of deformation structures in Mg, Mg-Al and Mg-Y alloy systems were characterized and compared to present Y effect.
- Chapter 6 examined the effects of solute segregation at TBs using DFT method. A two-factor model was proposed to predict the segregation energy by considering chemical and mechanical effect due to solute addition. Furthermore, TB strengthening/embrittling map due to solute segregation was built to provide potential elements for new alloy design.
- Chapter 7 studied the dependence of critical shear stress on temperature and Y content. In this study, how Y improves ductility of Mg alloy via tailoring the dislocation activity was presented. The underlying mechanism of modification in deformation modes observed in polycrystal simulations was revealed.

1.3 References

- [1] M.F. Ashby, *Materials Selection in Mechanical Design*, 2010.
- [2] J.-F. Nie, *Precipitation and Hardening in Magnesium Alloys*, *Metallurgical and Materials Transactions A* 43(11) (2012) 3891-3939.
- [3] T.M. Pollock, *Weight loss with magnesium alloys*, *Science* 328 (2010) 986-987.

- [4] Mihriban O. Pekguleryuz , K.U. Kainer, A.A. Kaya, Fundamentals of magnesium alloy metallurgy, Woodhead Publishing, Cambridge, UK, 2013.
- [5] W.A. Monteiro, Special Issues on Magnesium Alloys, 2011.
- [6] A. Staroselsky, L. Anand, A constitutive model for hcp materials deforming by slip and twinning, International Journal of Plasticity 19(10) (2003) 1843-1864.
- [7] M.Y. Hoo, Slip, twinning, and fracture in hexagonal close-packed metals, Materials Transactions A 12A (1981) 409-418.
- [8] S.H. Park, J.H. Lee, Y.-H. Huh, S.-G. Hong, Enhancing the effect of texture control using {10–12} twins by retarding detwinning activity in rolled Mg–3Al–1Zn alloy, Scripta Materialia 69(11-12) (2013) 797-800.
- [9] Y. Xin, M. Wang, Z. Zeng, G. Huang, Q. Liu, Tailoring the texture of magnesium alloy by twinning deformation to improve the rolling capability, Scripta Materialia 64 (2011) 986-989.
- [10] J.H. Lee, S.W. Lee, S.H. Park, Microstructural characteristics of magnesium alloy sheets subjected to high-speed rolling and their rolling temperature dependence, Journal of Materials Research and Technology 8(3) (2019) 3167-3174.
- [11] H. Utsunomiya, K.-i. Izumi, T. Sakai, T. Mukai, Grain refinement of magnesium alloy sheets by ARB using high-speed rolling mill, Journal of Physics: Conference Series 165 (2009) 012011.
- [12] S.Q. Zhu, S.P. Ringer, On the role of twinning and stacking faults on the crystal plasticity and grain refinement in magnesium alloys, Acta Materialia 144 (2018) 365-375.
- [13] M.G. Jiang, H. Yan, R.S. Chen, Enhanced mechanical properties due to grain refinement and texture modification in an AZ61 Mg alloy processed by small strain impact forging, Materials Science and Engineering: A 621 (2015) 204-211.
- [14] Y. Ali, D. Qiu, B. Jiang, F. Pan, M.-X. Zhang, Current research progress in grain refinement of cast magnesium alloys: A review article, Journal of Alloys and Compounds 619 (2015) 639-651.
- [15] B. Kim, C.H. Park, H.S. Kim, B.S. You, S.S. Park, Grain refinement and improved tensile properties of Mg–3Al–1Zn alloy processed by low-temperature indirect extrusion, Scripta Materialia 76 (2014) 21-24.
- [16] J.F. Nie, Y.M. Zhu, J.Z. Liu, X.Y. Fang, Periodic segregation of solute atoms in fully coherent twin boundaries, Science 340(6135) (2013) 957-60.

- [17] M. Ghazisaeidi, L.G. Hector, W.A. Curtin, Solute strengthening of twinning dislocations in Mg alloys, *Acta Materialia* 80 (2014) 278-287.
- [18] D. Zhang, L. Jiang, J.M. Schoenung, S. Mahajan, E.J. Lavernia, TEM study on relationship between stacking faults and non-basal dislocations in Mg, *Philosophical Magazine* 95(34) (2015) 3823-3844.
- [19] Z.R. Zeng, Y.M. Zhu, R.L. Liu, S.W. Xu, C.H.J. Davies, J.F. Nie, N. Birbilis, Achieving exceptionally high strength in Mg₃Al₁Zn-0.3Mn extrusions via suppressing intergranular deformation, *Acta Materialia* 160 (2018) 97-108.
- [20] T.T.T. Trang, J.H. Zhang, J.H. Kim, A. Zargaran, J.H. Hwang, B.C. Suh, N.J. Kim, Designing a magnesium alloy with high strength and high formability, *Nature communications* 9(1) (2018).
- [21] Z. Zhang, J. Zhang, J. Xie, S. Liu, Y. He, R. Wang, D. Fang, W. Fu, Y. Jiao, R. Wu, Significantly enhanced grain boundary Zn and Ca co-segregation of dilute Mg alloy via trace Sm addition, *Materials Science and Engineering: A* 831 (2022).
- [22] Z. Zhang, J. Zhang, J. Xie, S. Liu, Y. He, K. Guan, R. Wu, Developing a low-alloyed fine-grained Mg alloy with high strength-ductility based on dislocation evolution and grain boundary segregation, *Scripta Materialia* 209 (2022) 114414.
- [23] Z. Zeng, N. Stanford, C.H.J. Davies, J.-F. Nie, N. Birbilis, Magnesium extrusion alloys: a review of developments and prospects, *International Materials Reviews* 64(1) (2019) 27-62.
- [24] S. Sandlobes, M. Friak, S. Korte-Kerzel, Z. Pei, J. Neugebauer, D. Raabe, A rare-earth free magnesium alloy with improved intrinsic ductility, *Sci Rep* 7(1) (2017) 10458.
- [25] Z.R. Zeng, M.Z. Bian, S.W. Xu, C.H.J. Davies, N. Birbilis, J.F. Nie, Effects of dilute additions of Zn and Ca on ductility of magnesium alloy sheet, *Materials Science and Engineering: A* 674 (2016) 459-471.
- [26] D. Holec, L. Zhou, H. Riedl, C.M. Koller, P.H. Mayrhofer, M. Friák, M. Šob, F. Körmann, J. Neugebauer, D. Music, M.A. Hartmann, F.D. Fischer, Atomistic Modeling-Based Design of Novel Materials *Advanced Engineering Materials* 19(4) (2017) 1600688.
- [27] C. He, Z. Li, H. Chen, N. Wilson, J.F. Nie, Unusual solute segregation phenomenon in coherent twin boundaries, *Nature communications* 12(1) (2021) 722.

- [28] Z. Pei, R. Li, J.-F. Nie, J.R. Morris, First-principles study of the solute segregation in twin boundaries in Mg and possible descriptors for mechanical properties, *Materials & Design* 165 (2019) 107574.
- [29] H.-S. Jang, B.-J. Lee, Effects of Zn on $\langle c+a \rangle$ slip and grain boundary segregation of Mg alloys, *Scripta Materialia* 160 (2019) 39-43.
- [30] J. Wang, R. Janisch, G.K.H. Madsen, R. Drautz, First-principles study of carbon segregation in bcc iron symmetrical tilt grain boundaries, *Acta Materialia* 115 (2016) 259-268.
- [31] R. Tran, Z. Xu, N. Zhou, B. Radhakrishnan, J. Luo, S.P. Ong, Computational study of metallic dopant segregation and embrittlement at molybdenum grain boundaries, *Acta Materialia* 117 (2016) 91-99.
- [32] M.A. Gibson, C.A. Schuh, A survey of ab-initio calculations shows that segregation-induced grain boundary embrittlement is predicted by bond-breaking arguments, *Scripta Materialia* 113 (2016) 55-58.
- [33] M. Upmanyu, D.J. Srolovitz, L.S. Shvindlerman, G. Gottstein, Molecular dynamics simulation of triple junction migration, *Acta Materialia* 50(6) (2002) 1405-1420.
- [34] Z.C. Ma, X.Z. Tang, Y. Mao, Y.F. Guo, The Plastic Deformation Mechanisms of hcp Single Crystals with Different Orientations: Molecular Dynamics Simulations, *Materials (Basel)* 14(4) (2021).
- [35] Z. Li, X. Tian, J. Tang, Q. Wang, W. Jiang, H. Fan, Molecular dynamics simulations on the dislocation interactions in magnesium, *Computational Materials Science* 197 (2021).
- [36] K. Chu, M.E. Foster, R.B. Sills, X. Zhou, T. Zhu, D.L. McDowell, Temperature and composition dependent screw dislocation mobility in austenitic stainless steels from large-scale molecular dynamics, *npj Computational Materials* 6(1) (2020).
- [37] F. Granberg, D. Terentyev, K. Nordlund, Molecular dynamics investigation of the interaction of dislocations with carbides in BCC Fe, *Nuclear Instruments and Methods in Physics Research Section B: Beam Interactions with Materials and Atoms* 352 (2015) 77-80.
- [38] A.S. Côté, R. Darkins, D.M. Duffy, Deformation twinning and the role of amino acids and magnesium in calcite hardness from molecular simulation, *Physical Chemistry Chemical Physics* 17(31) (2015) 20178-20184.
- [39] R. Aghababaei, S.P. Joshi, Micromechanics of tensile twinning in magnesium gleaned from molecular dynamics simulations, *Acta Materialia* 69 (2014) 326-342.

- [40] T. Tang, S. Kim, M.F. Horstemeyer, Molecular dynamics simulations of void growth and coalescence in single crystal magnesium, *Acta Materialia* 58(14) (2010) 4742-4759.
- [41] H.N. Jarmakani, E.M. Bringa, P. Erhart, B.A. Remington, Y.M. Wang, N.Q. Vo, M.A. Meyers, Molecular dynamics simulations of shock compression of nickel: From monocrystals to nanocrystals, *Acta Materialia* 56(19) (2008) 5584-5604.
- [42] Z. Wu, R. Ahmad, B. Yin, S. Sandlöbes, W.A. Curtin, Mechanistic origin and prediction of enhanced ductility in magnesium alloys, *Science* 359 (2018) 447-452.
- [43] Z. Wu, W.A. Curtin, The origins of high hardening and low ductility in magnesium, *Nature* 526 (2015) 62-7.
- [44] S. Queyreau, Dislocation Based Mechanics-the various contributions of Dislocation Dynamics simulations, in: S. Forest, M. Bernacki (Eds.), *Continuum Numerical Methods at the Mesoscopic Scale* 2020.
- [45] M. Huang, S. Huang, S. Liang, Y. Zhu, Z. Li, An efficient 2D discrete dislocation Dynamics-XFEM coupling framework and its application to polycrystal plasticity, *International Journal of Plasticity* 127 (2020).
- [46] S. Lu, B. Zhang, X. Li, J. Zhao, M. Zaiser, H. Fan, X. Zhang, Grain boundary effect on nanoindentation: A multiscale discrete dislocation dynamics model, *Journal of the Mechanics and Physics of Solids* 126 (2019) 117-135.
- [47] M. Jiang, B. Devincre, G. Monnet, Effects of the grain size and shape on the flow stress: A dislocation dynamics study, *International Journal of Plasticity* 113 (2019) 111-124.
- [48] S. Amir H. Motaman, U. Prahl, Microstructural constitutive model for polycrystal viscoplasticity in cold and warm regimes based on continuum dislocation dynamics, *Journal of the Mechanics and Physics of Solids* 122 (2019) 205-243.
- [49] M. Monavari, M. Zaiser, Annihilation and sources in continuum dislocation dynamics, *Materials Theory* 2(1) (2018) 3.
- [50] C. Sobie, L. Capolungo, D.L. McDowell, E. Martinez, Scale transition using dislocation dynamics and the nudged elastic band method, *Journal of the Mechanics and Physics of Solids* 105 (2017) 161-178.
- [51] X. Niu, T. Luo, J. Lu, Y. Xiang, Dislocation climb models from atomistic scheme to dislocation dynamics, *Journal of the Mechanics and Physics of Solids* 99 (2017) 242-258.

- [52] F. Ram, Z. Li, S. Zaefferer, S.M. Hafez Haghghat, Z. Zhu, D. Raabe, R.C. Reed, On the origin of creep dislocations in a Ni-base, single-crystal superalloy: an ECCI, EBSD, and dislocation dynamics-based study, *Acta Materialia* 109 (2016) 151-161.
- [53] I.J. Beyerlein, A. Hunter, Understanding dislocation mechanics at the mesoscale using phase field dislocation dynamics, *Philos Trans A Math Phys Eng Sci* 374(2066) (2016).
- [54] S. Aubry, M. Rhee, G. Hommes, V.V. Bulatov, A. Arsenlis, Dislocation dynamics in hexagonal close-packed crystals, *Journal of the Mechanics and Physics of Solids* 94 (2016) 105-126.
- [55] H. Fan, S. Aubry, A. Arsenlis, J.A. El-Awady, The role of twinning deformation on the hardening response of polycrystalline magnesium from discrete dislocation dynamics simulations, *Acta Materialia* 92 (2015) 126-139.
- [56] M. Kasemer, P. Dawson, A finite element methodology to incorporate kinematic activation of discrete deformation twins in a crystal plasticity framework, *Computer Methods in Applied Mechanics and Engineering* 358 (2020) 112653.
- [57] R. Carson, P. Dawson, Formulation and characterization of a continuous crystal lattice orientation finite element method (LOFEM) and its application to dislocation fields, *Journal of the Mechanics and Physics of Solids* 126 (2019) 1-19.
- [58] N. Grilli, K.G.F. Janssens, J. Nellessen, S. Sandlöbes, D. Raabe, Multiple slip dislocation patterning in a dislocation-based crystal plasticity finite element method, *International Journal of Plasticity* 100 (2018) 104-121.
- [59] J. Cheng, J. Shen, R.K. Mishra, S. Ghosh, Discrete twin evolution in Mg alloys using a novel crystal plasticity finite element model, *Acta Materialia* 149 (2018) 142-153.
- [60] M. Ardeljan, I.J. Beyerlein, M. Knezevic, Effect of dislocation density-twin interactions on twin growth in AZ31 as revealed by explicit crystal plasticity finite element modeling, *International Journal of Plasticity* 99 (2017) 81-101.
- [61] H. Qiao, M.R. Barnett, P.D. Wu, Modeling of twin formation, propagation and growth in a Mg single crystal based on crystal plasticity finite element method, *International Journal of Plasticity* 86 (2016) 70-92.
- [62] H. Abdolvand, A.J. Wilkinson, On the effects of reorientation and shear transfer during twin formation: Comparison between high resolution electron backscatter diffraction experiments

- and a crystal plasticity finite element model, *International Journal of Plasticity* 84 (2016) 160-182.
- [63] M.H. Ulz, Coupling the finite element method and molecular dynamics in the framework of the heterogeneous multiscale method for quasi-static isothermal problems, *Journal of the Mechanics and Physics of Solids* 74 (2015) 1-18.
- [64] Y. Shao, T. Tang, D. Li, W. Tang, Y. Peng, Crystal plasticity finite element modelling of the extrusion texture of a magnesium alloy, *Modelling and Simulation in Materials Science and Engineering* 23(5) (2015).
- [65] H. Abdolvand, M. Majkut, J. Oddershede, J.P. Wright, M.R. Daymond, Study of 3-D stress development in parent and twin pairs of a hexagonal close-packed polycrystal: Part II – crystal plasticity finite element modeling, *Acta Materialia* 93 (2015) 235-245.
- [66] H. Liu, F.X. Lin, P. Zhao, N. Moelans, Y. Wang, J.F. Nie, Formation and autocatalytic nucleation of co-zone $\{101\bar{2}\}$ deformation twins in polycrystalline Mg: A phase field simulation study, *Acta Materialia* 153 (2018) 86-107.
- [67] C. Liu, P. Shanthraj, M. Diehl, F. Roters, S. Dong, J. Dong, W. Ding, D. Raabe, An integrated crystal plasticity–phase field model for spatially resolved twin nucleation, propagation, and growth in hexagonal materials, *International Journal of Plasticity* 106 (2018) 203-227.
- [68] H. Liu, J.F. Nie, Phase field simulation of microstructures of Mg and Al alloys, *Materials Science and Technology* 33(18) (2017) 2159-2172.
- [69] Z.P. Pi, Q.H. Fang, B. Liu, H. Feng, Y. Liu, Y.W. Liu, P.H. Wen, A phase field study focuses on the transverse propagation of deformation twinning for hexagonal-closed packed crystals, *International Journal of Plasticity* 76 (2016) 130-146.
- [70] J.D. Clayton, J. Knap, A phase field model of deformation twinning: Nonlinear theory and numerical simulations, *Physica D: Nonlinear Phenomena* 240(9-10) (2011) 841-858.

Chapter 2: Literature Review

This chapter provides some basic background, and a brief overview of research progress and scientific challenges with respect to plastic deformation in Mg and its alloys. The contents in this chapter are arranged as the follows. First, the two most common plastic deformation modes in Mg, i.e., dislocation and twinning as well as their contribution to strain accommodation of Mg will be reviewed. Then, solute effect on activity of these two defects will be surveyed, including the GB segregation and activation of non-basal slip systems. The corresponding toughening and strengthening strategies on the basis of defect-engineering in the literature will be summarized. Finally, studies on the interactions between dislocations and twinning will be reviewed.

2.1 Plastic Deformation in Mg alloys

2.1.1 Slip Systems and Deformation Modes

Mg and its alloys exhibit the HCP crystal structure. For HCP metals, the slip systems for dislocation activities occur on the basal, prismatic, and pyramidal planes respectively, as depicted in **Figure 2.1(a)**. Specifically for Mg, the common slip systems are $(0001)[11\bar{2}0]$, $(10\bar{1}0)[1\bar{2}10]$, $(\bar{1}011)[11\bar{2}3]$ and $(\bar{1}\bar{1}22)[11\bar{2}3]$. According to the Schmid law, the dislocation slip will be activated when the critical resolved shear stress (CRSS) acting on the dislocation reaches a threshold value. **Table 2.1** shows the CRSS values for different slip systems in Mg, where we can note that the basal slip exhibits a CRSS in the range of 0.45~0.81MPa, as reported by single-crystal experiments and computer simulations [1-4]. The CRSS value of the basal slip is significantly lower than other slip systems, indicative of its much less resistance to shear. Therefore, the basal slip is the easiest to be activated and often constitutes a dominant fraction of the total plastic deformation occurring at room temperature, particularly for randomly textured polycrystals [5].

The easily activated basal slip, however, is incapable of accommodating arbitrary strains, especially strain along the c -axis. As illustrated in **Figure 2.1**, the basal slip mode only contributes two independent co-planar slip systems. Consequently when the basal slip dominates the plastic deformation, homogenous deformation cannot be accommodated, leading to the finite elongation to failure in Mg and its alloys at ambient temperature [6], which is further reflected in the low ductility, insufficient formability and poor performance of structural components made of Mg alloys [1, 7, 8].

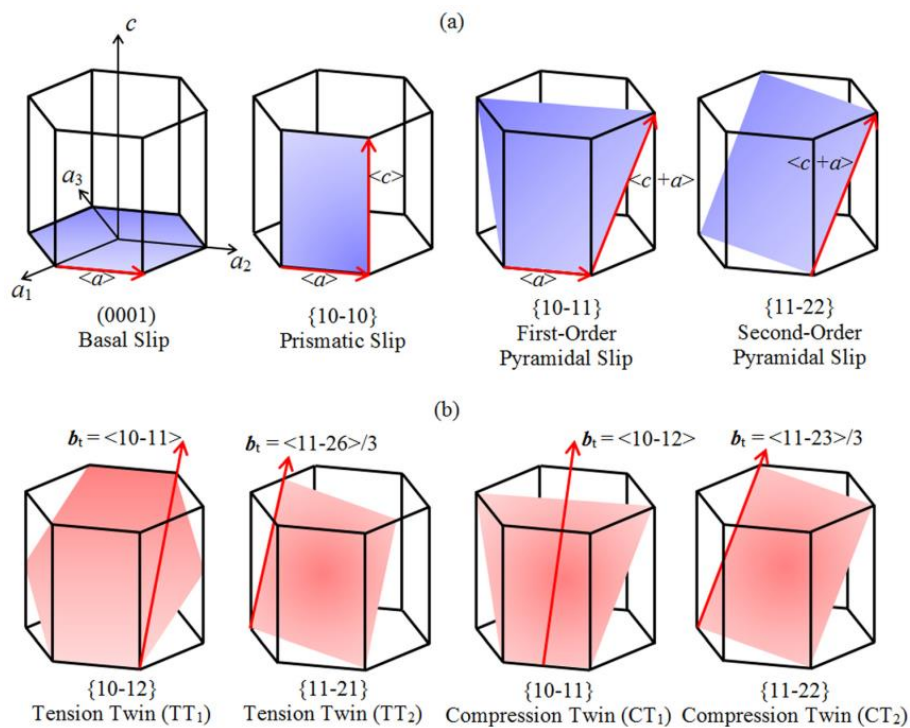


Figure 2.1. Schematic of the HCP unit cell showing all possible: (a) slip and (b) twinning systems [9]. [Figure adapted with permissions]

In addition to the basal slip, there exist non-basal slip systems of $\langle a \rangle$ and $\langle c \rangle$ on the prismatic $\{10\bar{1}0\}$ planes, $\langle a \rangle$ and $\langle c+a \rangle$ on pyramidal $\{10\bar{1}1\}$ planes and $\langle c+a \rangle$ on pyramidal $\{11\bar{2}2\}$ planes, which are reported in Mg and its alloys [7, 10-14] (see **Figure 2.1(a)**). The prismatic $\langle c \rangle$ and pyramidal $\langle a \rangle$ slips are usually produced as a result of the dissociation of the $\langle c+a \rangle$

dislocations on pyramidal planes [7, 14] and individual activation of $\langle c \rangle$ dislocations is only occasionally reported in some Mg-RE alloys [15]. Moreover, the prismatic $\langle c \rangle$ dislocation can not contribute to plastic straining due to its low mobility and would strongly inhibit the motion of all other dislocations [7]. The prismatic $\langle a \rangle$ slip can also be activated in favorable stress conditions due to its moderate CRSS as shown in **Table 2.1** [16, 17]. However, combination of basal and prismatic $\langle a \rangle$ slips only increases the number of independent slip systems from two to four [17] which is still insufficient to meet the von Mises criterion of five independent slip systems required. On the other hand, the $\langle c+a \rangle$ dislocations provide the desired route to accommodate deformation along c -axis to fulfil the von Mises criterion. There are two types of $\langle c+a \rangle$ dislocations as shown in **Figure 2.1**, namely pyramidal type I $\{10\bar{1}1\}\langle 11\bar{2}3 \rangle$ and type II $\{10\bar{2}2\}\langle 11\bar{2}3 \rangle$ [18-20]. However, these two slip modes have quite high CRSS values and thus are hardly to be activated in a pure Mg. In addition, the two $\langle c+a \rangle$ dislocation types have different characteristics and have been shown to behave differently when contributing to the plastic deformation, which are to be further detailed in the section 2.1.2.

Table 2.1. Critical resolved shear stresses (CRSS) of common deformation modes reported for Mg.

| Deformation modes | Basal $\langle a \rangle$ | Prismatic $\langle a \rangle$ | Pyramidal I $\langle c + a \rangle$ | Pyramidal II $\langle c + a \rangle$ | $\{10\bar{1}2\}$ Twin | $\{10\bar{1}1\}$ Twin | |
|-------------------|---------------------------|-------------------------------|-------------------------------------|--------------------------------------|-----------------------|-----------------------|--|
| CRSS (MPa) | | 9.3 [1] | | 24 [23, 26] | | 10-65 | |
| | | | 11 [4] | | | [30] | |
| | | 0.45~0.81 [1-4] | 13 [21, 22] | 54 [11] | 90-92 [21, 24] | 2.5~4.4 [3] | |
| | | | 15 [22, 23] | 44 [25] | 105 [24] | 25 [28] | |
| | | | 22 [23, 24] | | 188(197) [4] | 29 [29] | |
| | | | 23.7 [21, 24] | | 140(220) [27] | | |

2.1.2 Characteristics of Dislocations and Generalized Stacking Faults

As previously described, the dislocation slips exhibit substantial difference in their CRSS. To better understand and possibly manipulate such difference, there have been many studies to investigate the characteristics of dislocations, in particular with respect to the pyramidal $\langle c+a \rangle$ dislocations, whose activation is critical to accommodate the homogenous deformation in Mg alloys.

The generalized stacking fault (GSF) energy which is calculated from the energy difference between two adjacent planes during shear deformation for a specific slip system, represents the nature of slip and involves the stable and unstable stacking and twin fault energies [31-33]. The GSF curves and the resultant energies have been linked to many phenomena such as dislocation stability [34-36], phase transition [37, 38] and twinnability [32, 39, 40]. For Mg, the GSF energies are particularly important to accurately reproduce the strongly anisotropic slip behavior. As shown in **Figure 2.2** [41], the GSF energy (γ) surface on four planes indicates that the basal plane has the lowest GSF energy along the dislocation slip direction, followed by the prismatic plane. In addition, the GSF energies are similar on the pyramidal I and II planes, however, much higher than those on basal and prismatic planes [41]. These results are in consistence with those of CRSS analysis and support that the basal $\langle a \rangle$ slip system is dominated in deformation of pure Mg, followed by the prismatic $\langle a \rangle$ slip system.

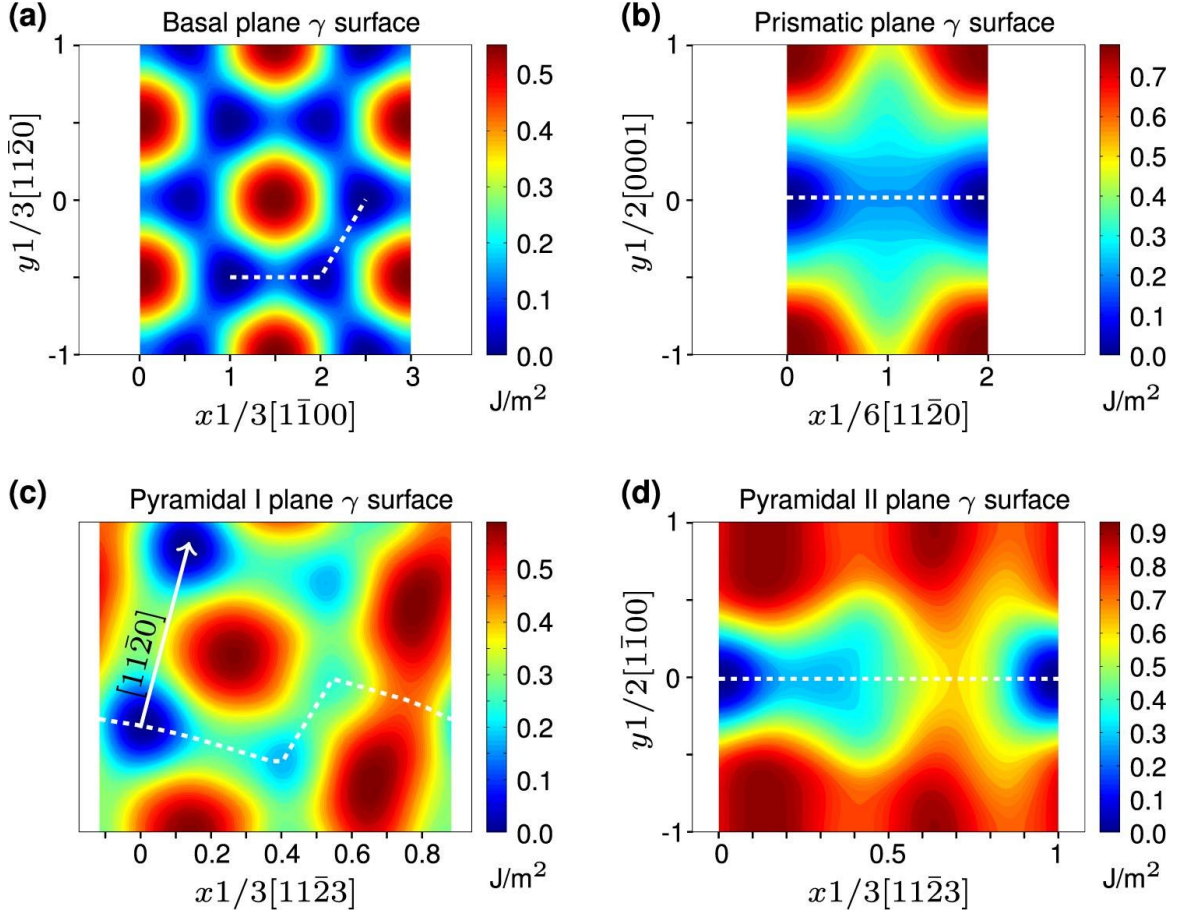
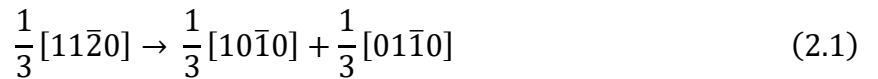


Figure 2.2. Generalized stacking fault (GSF) energy on (a) basal, (b) prismatic, (c) pyramidal I and (d) pyramidal II planes. In each panel, the white, dotted line marks the minimum energy path in the γ surface [41]. [Figure adapted with permissions]

As shown in **Figure 2.3(a)**, the core of basal edge dislocation tends to dissociate into two Shockley partials separated by a stable SF according to the reaction,



with a corresponding dissociation length of $12.5a$ ($a=3.187 \text{ \AA}$) and an intrinsic GSF energy γ_{I2} of 22.5 mJ/m^{-2} [41]. The similar dissociation is also observed for basal screw dislocation (see **Figure 2.3(b)**). In contrast, there is no stable SF for the prismatic plane and thus undissociated dislocation cores are obtained in the prismatic planes as shown in **Figure 2.3(c)** and (d). For both pyramidal I and II planes, the GSF energies have been calculated as 767 mJ/m^{-2} and 647 mJ/m^{-2} ,

respectively [41]. Despite their high stable SF energies, dislocation dissociation is likely due to the large $\langle c+a \rangle$ Burger's vector as shown in **Figure 2.3**(e-h), since the resultant partial productions can significantly reduce the elastic energy of the dislocation. The reaction follows,

$$\frac{1}{3}[11\bar{2}3] \rightarrow \frac{1}{6}[11\bar{2}3] + \frac{1}{6}[11\bar{2}3] \quad (2.2)$$

In addition, it is found that $\langle c+a \rangle$ is metastable on easy-glide pyramidal II planes and thus it tends to transform to lower-energy, basal-dissociated immobile dislocation structures, i.e., the pyramidal-to-basal (PB) transformation [7], contributing no plastic deformation. In case of low stress, it is found that a Shockley type partial dislocation $\langle p \rangle$ (i.e., $\frac{1}{6}[\bar{1}103]$) is nucleated from one of the $\frac{1}{6}[11\bar{2}3]$ as following [7],

$$\frac{1}{6}[11\bar{2}3] + \frac{1}{6}[11\bar{2}3] \rightarrow \frac{1}{6}[11\bar{2}3] + \frac{1}{6}[\bar{1}103] + \frac{1}{3}[10\bar{1}0] \quad (2.3)$$

A second Shockley partial is nucleated from the other $\frac{1}{6}[11\bar{2}3]$ as [7],

$$\frac{1}{6}[11\bar{2}3] + \frac{1}{6}[\bar{1}103] + \frac{1}{3}[10\bar{1}0] \rightarrow \frac{1}{6}[1\bar{1}03] + \frac{1}{3}[01\bar{1}0] + \frac{1}{6}[\bar{1}103] + \frac{1}{3}[10\bar{1}0] \quad (2.4)$$

Finally, the resulting partials in the above equation combine as [7],

$$\frac{1}{6}[1\bar{1}03] + \frac{1}{3}[01\bar{1}0] + \frac{1}{6}[\bar{1}103] + \frac{1}{3}[10\bar{1}0] \rightarrow \frac{1}{6}[02\bar{2}3] + \frac{1}{6}[20\bar{2}3] \quad (2.5)$$

These transition products during the reactions would server as obstacles to the motion of all other dislocations, leading to the high hardening and low ductility [7]. On the other hand, the $\langle c+a \rangle$ cross-slip from pyramidal II plane to pyramidal I plane enables continuous motion of dislocation, which is beneficial to the ductility of Mg [14]. However, because the energy barrier for the PB transition is lower than that for the cross-slip, the PB transition will dominate in the competition with the cross-slip in pure Mg [14]. Thanks to the alloying technique, the situation can be reversed with appropriate alloying elements such as Zr, Y and Gd to achieve the enhanced ductility by

activating more cross-slips. The underlying mechanism of solute effect on the improvement of ductility and formability will be discussed in section 2.2.

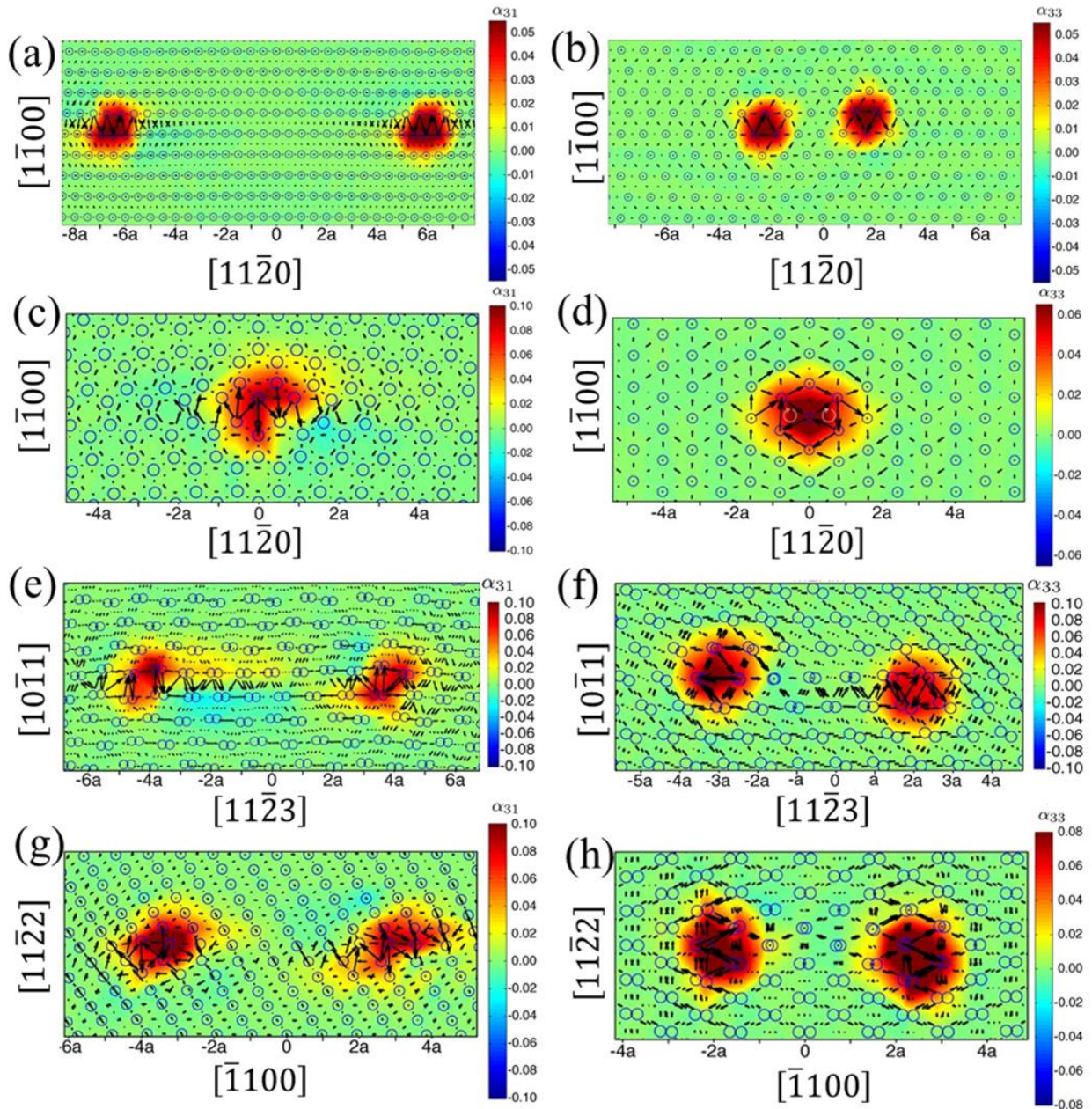


Figure 2.3. Dislocation core structures as visualized by the component of the Nye tensor and differential displacement plots: Basal $\langle a \rangle$ (a) edge and (b) screw dislocation; Prismatic $\langle a \rangle$ (c) edge and (d) screw dislocations; Pyramidal I $\langle c + a \rangle$ (e) edge and (f) screw dislocations; Pyramidal I $\langle c + a \rangle$ (g) edge and (h) screw dislocation [41]. [Figure adapted with permissions]

2.1.3 Deformation Twinning

Besides dislocation slips, deformation twinning provides another important mechanism of plastic strain accommodation in HCP metals. As described in the previous sections, only four independent slip systems are provided by the combination of the basal and prismatic $\langle a \rangle$ slips at room temperature while the pyramidal slips are difficult to be activated at room temperature. Meanwhile, twinning can occur at stresses lower or comparable to those required for the dislocation slips. Thus, twinning is often considered as a viable deformation mechanism in HCP metals to supplement the dislocation slips in accommodating plastic strain.

Generally, a deformation twin is defined as that part of a crystal undergoes a homogeneous shape deformation and the resulting product structure is identical with the parent but oriented differently [42]. As a result, a mirror symmetric relationship forms between the twinned region and the parental [17]. There are two constraints for applied deformation to produce a twin: (1) it must be an invariant strain to keep the twin and matrix in contact and (2) it must be a simple shear to keep a constant volume [42, 43]. Accordingly, twins are characterized by four crystallographic parameters as shown in **Figure 2.4**. The twinning plane K_1 is the first invariant plane and η_1 is the corresponding shear direction. The second invariant plane is denoted as K_2 and shear along η_2 direction. The plane S, called plane of shear, is perpendicular to K_1 and K_2 . A twinning mode is usually represented by the elements K_1 and η_1 . The corresponding conjugate (or reciprocal) twinning mode is defined by K'_1 and η'_1 , where $K'_1 = K_2$ and $\eta'_1 = \eta_2$.

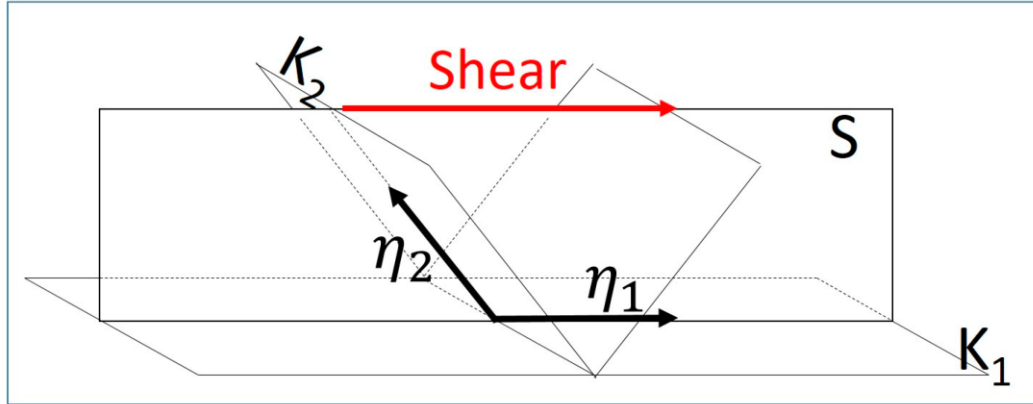


Figure 2.4. Illustration of twinning elements: K_1 —twinning plane, η_1 —twinning direction, K_2 —conjugate twinning plane, η_2 —conjugate twinning direction.

There are at least seven twinning modes in hcp metals and alloys i.e., $\{10\bar{1}1\}$, $\{10\bar{1}2\}$, $\{10\bar{1}3\}$, $\{11\bar{2}1\}$, $\{11\bar{2}2\}$, $\{11\bar{2}3\}$ and $\{11\bar{2}4\}$ twins [17, 44, 45], where four twinning modes are most commonly observed and reported and their systems are as shown in **Figure 2.1(b)**. Activation of the twinning modes strongly depends on the c/a ratios, lattice packing densities, interplanar spacings and stacking fault energies of a particular metal [44]. In Mg and its alloys, $\{10\bar{1}2\}\langle 10\bar{1}1 \rangle$ twin and $\{10\bar{1}1\}\langle 10\bar{1}2 \rangle$ twin are the most popular twinning modes. These two twinning modes are termed as tension twin and compression twin correspondingly due to their activation stress condition [46, 47]. $\{10\bar{1}2\}$ tension twin usually grows readily under favorable strain path and texture orientation. They tend to overtake the initial microstructure and contribute to strain accommodation. The activation of $\{10\bar{1}1\}$ compression twin requires a high CRSS, and they grow at a low rate, so their contribution to plasticity is usually very limited. Moreover, $\{10\bar{1}2\}$ compression twins can nucleate in $\{10\bar{1}1\}$ tension twins and the resulting $\{10\bar{1}1\} - \{10\bar{1}2\}$ double twins are reported to be related to the flow localization, void formation and fracture in Mg alloys [48, 49]. Twinning is also a dominant contributor to the development of texture due to reorientation of crystal after twinning. Accordingly, twinning is often introduced to modify the

orientation of microstructure and thus improve mechanical response of HCP metals. For example, primary $\{10\bar{1}2\}$ twins introduced by pre-deformation of sheet material changed the orientation of matrix crystals and followed by subsequent annealing, the product would present reduced mechanical anisotropy and desirable formability [50-55]. Besides, shear banding correlated to compression and double twins was found in rare earth Mg alloys and introduced modified recrystallization textures [56, 57]. In addition to the traditional twinning modes in Mg, the $\{11\bar{2}1\}$ tension twin is also reported in recent experimental work on Mg-RE alloys due to the addition of RE elements such as Y [46, 58].

2.2 Solute Effect on Properties of Mg Alloys

Mechanical properties of Mg are strongly dependent on the activation of available deformation modes as mentioned above. This can be modified by adding proper solute elements which potentially tailor the GB structures and modify activity of different slip systems. This section gives an overview of the solute effect on deformation modes and provides an insight into how certain materials properties can be modified in magnesium via alloying.

2.2.1 Grain Boundary Segregation

GBs are quite common defects in polycrystal metallic materials closely related to a range of mechanical properties, such as strength, fracture toughness, strain hardening and fatigue resistance [59-65]. The metallic alloys can either be weakened by undesirable segregation and coarsening [61, 62] or strengthened by periodical segregation and fine precipitates [66-71]. Thus, materials with excellent integrated mechanical properties can be obtained by modifying the GB microstructure. This procedure of modifying the geometry of GBs by specific processing is known as ‘grain boundary engineering’ (GBE) which aims at designing polycrystals with specific GB distributions [59, 64].

Thanks to the advanced characterization techniques including transmission electron microscopy (TEM), high-angle annular dark-field scanning transmission electron microscopy (HAADF-STEM) and atom probe tomography (APT), elemental segregation to GBs have been observed in many alloys such as iron-based alloys [65, 72-80], aluminum-based alloys [81-84], nickel-based alloys [85-88] and magnesium-based alloys [56, 67, 69, 71, 89-106]. Interface segregation of solute atoms has a profound effect on properties of engineering alloys. Accordingly, ‘grain boundary segregation engineering’ (GBSE) or ‘segregation engineering’ is proposed by Raabe et al [65] based on several scenarios at GBs relevant to segregation: 1) GB strengthening due to segregation enhanced coherence and preferential bonding; 2) GB weakening because of the loss of coherence or weakened bonding at interface; 3) GB phase transformation, precipitation and phase formation at GBs caused by segregation; 4) discontinuous precipitation; 5) a reduction in the GB energy due to solute segregation. These scenarios provide the basis for optimizing a material’s mechanical properties by manipulating GB structures via solute decoration [59, 65].

2.2.1.1 Evidence of Grain Boundary Segregation in Magnesium Alloys

Solute segregation is generally not expected in fully coherent twin boundaries which have much lower interfacial energies than partially coherent interfaces such as high-angle GBs and symmetrical tilt GBs [107]. However, the recent HAADF-STEM results [67] have demonstrated that solute atoms Gd and Zn, can segregate periodically on coherent twin boundaries (CTBs) e.g., $\{10\bar{1}1\}$, $\{10\bar{1}2\}$ and $\{10\bar{1}3\}$ twins in deformed Mg-Zn and Mg-Gd alloys after annealing. As shown in **Figure 2.5(a-c)**, the HAADF-STEM images indicated that atoms Gd were profusely distributed along the TBs in Mg-Gd alloys and they are located in the extension sites of the TBs whatever the twin is $\{10\bar{1}1\}$, $\{10\bar{1}2\}$ or $\{10\bar{1}3\}$ twins while **Figure 2.5(d)** shows periodical segregation of atoms Zn to the compression sites of the $\{10\bar{1}2\}$ TB in a Mg-Zn alloy. This

segregating preference was also observed in more general tilt GBs in a Mg-Gd alloy as shown in **Figure 2.5(e)** [69]. Segregation energies obtained by first-principles calculation in **Figure 2.5(f)** and (g), where a negative value means preferential segregation, also indicate that large atoms such as La, Lu, Nd and Y would occupy the extension site of the TBs whatever the twin is $\{10\bar{1}1\}$ or $\{10\bar{1}2\}$ twins while small atoms like Al, Zn, Be and Os would substitute the compression site. Therefore, the selection of segregation site for different solute atoms is ascribed to their atomic size difference from the host atom Mg. For example, the atomic radii of Mg, Zn and Gd are 0.160, 0.133, and 0.180 nm, respectively and hence the substitution of individual Gd or Zn at extension or compression sites of TBs and tilt GBs can minimize the elastic strains and lower interface energy, finally stabilizing these boundaries [67, 69, 108, 109]. That is, in terms of the elastic strain minimization, solute atoms with larger atomic radii tend to occupy the extension sites while smaller solute atoms prefer segregating to compression sites. Accordingly, solute co-segregation [97, 104, 106] can occur when multiple substitutional elements at different level of atomic size are involved and replace individual preferential sites, i.e., compression sites or extension sites.

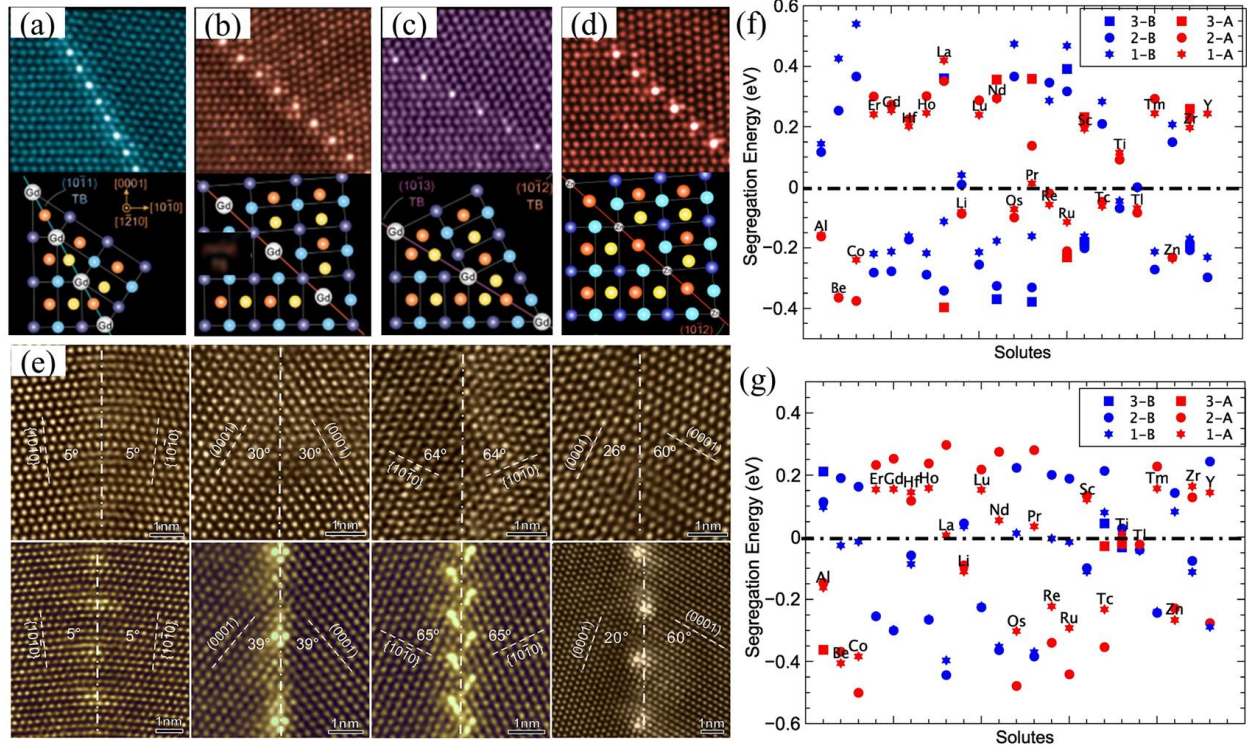


Figure 2.5. HAADF-STEM images showing periodic segregation of solutes (a-c) Gd to extension sites of the $\{10\bar{1}1\}$, $\{10\bar{1}2\}$ and $\{10\bar{1}3\}$ CTBs in a Mg-0.2 at. % Gd solid solution alloy and (d) Zn to compression sites of the $\{10\bar{1}2\}$ TB in a Mg-1.9 at. % Zn solid solution alloy [67]. (e) HAADF-STEM images showing periodic segregation of solutes Gd to extension sites of various tilt GBs in a Mg-0.2 at. % Gd solid solution alloy [69]. Calculated segregation energies when various solute atoms segregate to compression site (A) or extension site (B) of (f) $\{10\bar{1}1\}$ and (g) $\{10\bar{1}2\}$, respectively. The numbers 1, 2 and 3 in (f) and (g) correspond to supercells of $1\times 1\times 1$, $1\times 1\times 2$ and $1\times 2\times 2$ of the 90-atom unit cell for $\{10\bar{1}1\}$ and 60-atom unit cell for $\{10\bar{1}2\}$, respectively [109]. [Figure adapted with permissions]

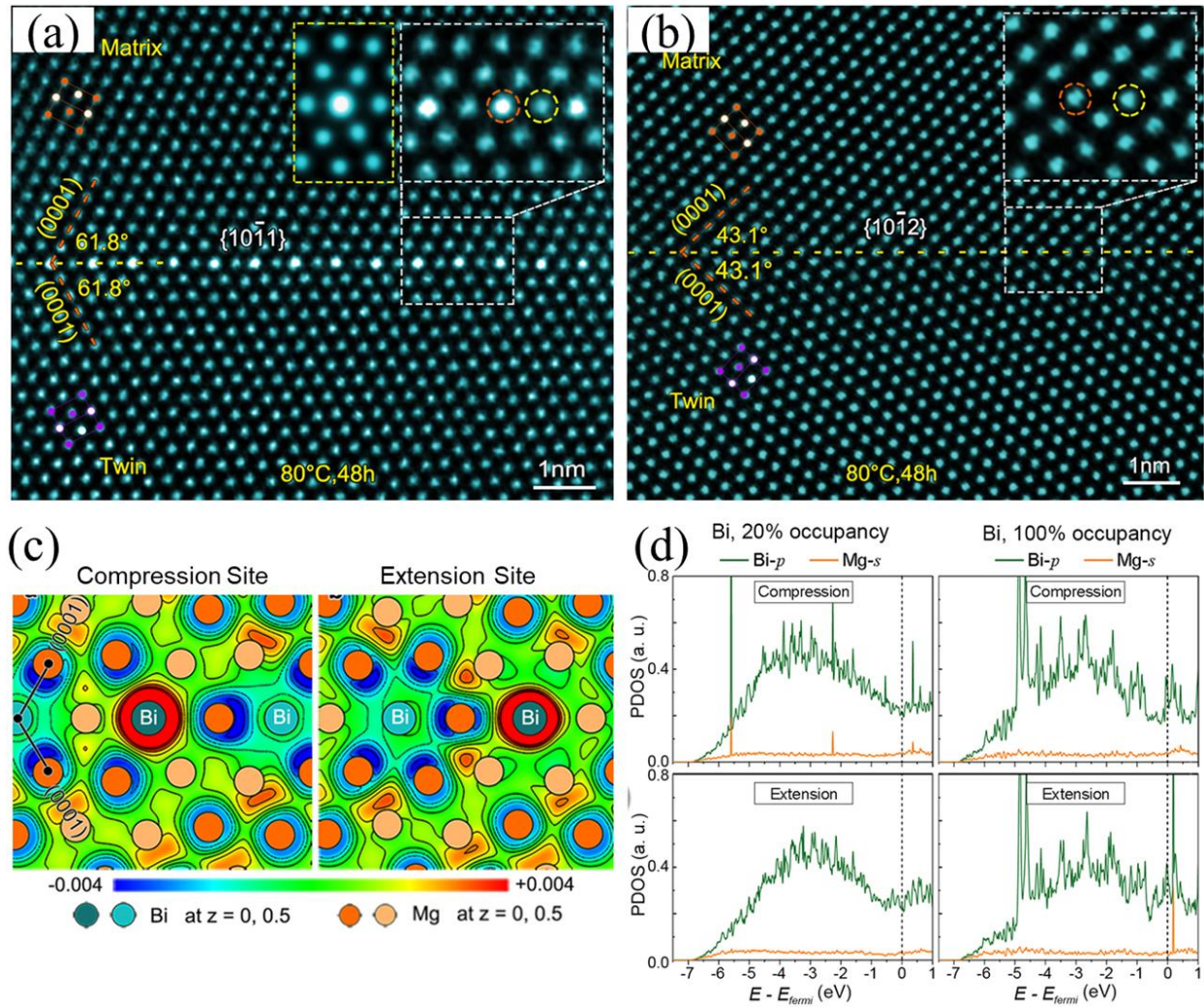


Figure 2.6. HAADF-STEM images of a Mg–0.4 at. % Bi alloy aged at 80 °C for 48 h showing (a) a $\{10\bar{1}1\}$ CTB, where an enlarged part shown in the upper-right inset indicates Bi-rich columns at compression sites and (b) a $\{10\bar{1}2\}$ CTB, where no segregation of Bi atoms is observed. (c) $(11\bar{2}0)$ plane contour maps of calculated results of DECD for Bi segregated into the compression site or extension site of $\{10\bar{1}1\}$ CTB. (d) PDOS for the cases where solute atoms Bi segregated into the compression site or extension site of $\{10\bar{1}1\}$ CTB: Bi segregation with 20% occupancy, and Bi segregation with 100% occupancy [89]. [Figure adapted with permissions]

However, the mechanical effect due to solute atoms, is not the only factor determining segregation preference for each element. Another factor, chemical bonding which has been reported to affect solute segregation in ceramic and semiconductor materials [110-112] is neglected in predicting interfacial segregation propensity in Mg alloys. Recently, an unusual solute segregation

phenomenon was reported in a Mg–0.4Bi alloy [89] where atoms Bi segregated to the compression sites of the $\{10\bar{1}1\}$ TB (see **Figure 2.6(a)**) although atoms Bi have larger atomic size (0.170 nm) than Mg and are expected to segregate to the extension sites to minimize elastic strain. More interestingly, no apparent Bi segregation to either compression or extension sites is found at the $\{10\bar{1}2\}$ TB as shown in **Figure 2.6(b)** [89]. Calculation for differential electron charge densities (DECD) of Bi (see **Figure 2.6(c)**) indicates that more valence electrons will be trapped for the case of the Bi substituting the compression site, showing the stronger chemical bonding between Bi and its surrounding host atoms Mg. The partial density of states (PDOS) of the atom Bi and its closest Mg atoms (see **Figure 2.6(d)**) shows that strong bonding interaction is observed when atom Bi segregates to the compression site, which is not found for the extension site. Therefore, chemical effect should be considered and combined with elastic strain minimization (mechanical effect), a more comprehensive view to the understanding of solute atom segregation to GBs can be well presented in metallic materials, such as Al [113], Mo [114], Fe [115] and Cu [116].

2.2.1.2 Effect of Grain Boundary Segregation on Material Behavior of Mg alloys

Solute segregation at GBs is a very important phenomenon because it affects the behavior of polycrystalline materials in practical applications. The alloy design concept based on GBSE has been proved to be an effective way to improve complex properties of Mg alloys.

Solute segregation may enhance the cohesion of GBs and significantly strengthen Mg alloys. As shown in **Figure 2.7(a)**, a larger strengthening effect is observed in curve 2, where the sample was annealed after unloading. The in-situ optical micrographs illustrate that further growth of twins generated during the first compression was detected in the sample without annealing (see **Figure 2.7(b, c)**) while most pre-existing twins in annealed specimen remained almost unchanged (see **Figure 2.7(d, e)**) [67]. Barrett et al. [98] suggested that GB mobilities were reduced proportionally

to the energy stabilization. For example, the segregated atoms, such as Y atoms, could stabilize GBs by lowering the GB energy as shown in **Figure 2.7(f)** and consequently, mobility of these boundaries is dramatically reduced [98], leading to the GB strengthening. In addition, Curtin et al. [28] proposed a new model for thermally activated, stress-driven growth of TBs in Mg alloys. In their prediction for Mg-Al alloys, mobility of TB was dramatically reduced due to the segregation of Al atoms (see **Figure 2.7(g)**) and a higher critical shear stress was required to overcome the solute pinning effect (see **Figure 2.7(h)**) [28]. That is segregation of solutes to the TBs strongly increased the energy barrier and suppresses twin growth. Accordingly, solute segregation during annealing of a deformed sample leads to very strong pinning so that the motion of pre-existing TBs was inhibited, and further twinning can only be completed by nucleation of new twins as observed in **Figure 2.7(e)**.

Relatively low ductility and formability of Mg alloys after thermomechanical processing are widely regarded as another bottleneck in the production process for various applications. Recently, GBSE has been successfully used in the improvement of ductility and formability by controlling microstructures, such as refining grain size [56, 95, 99, 100, 104, 105] and weakening texture [56, 97-100, 104, 105, 117] during recrystallization and grain growth. In the Mg-0.3Zn-0.1Ca alloy, the recrystallization occurred after 20 s annealing, later than the starting in the Mg-0.1Ca and Mg-0.4Zn alloys as shown in **Figure 2.8(a)** [97]. Also, size of recrystallized grains in the Mg-0.3Zn-0.1Ca alloy is smaller than that in the Mg-0.1Ca and Mg-0.4Zn alloys and the grain growth in the ternary alloy is much more uniform than those in the binary alloys during the static recrystallization (see **Figure 2.8(b)**) [97]. Formation of the finer microstructure in the Mg-0.3Zn-0.1Ca alloy is ascribed to co-segregation of Zn and Ca in GBs as shown in **Figure 2.8(c-f)**. Solute segregation would significantly reduce GB energy thermodynamically and exerts a drag effect on GB motion

kinetically [67, 97-99, 104]. The co-segregation of multiple elements would lead to more significant reduction in GB energy and stronger pinning effect than a single solute segregation, therefore retarding the growth of recrystallized grains more obviously [97, 99, 106]. In addition, solute segregation would suppress the preferential grain growth of grains with a basal texture during recrystallization and thus this texture is effectively weakened as shown in **Figure 2.9(a-c)**. In light of these findings, Trang et al. [99] recently developed a new Mg alloy, TRC-AZMX3110, which shows a combination of high strength and good formability at room temperature. As shown in **Figure 2.9(d)**, the TRC-AZMX3110 alloy has a higher Index Erichsen (IE) value of 8.0 mm as well as a higher yield strength of 219 MPa, showing much better comprehensive properties than AZMX3110 and IC-AZX310 alloys.

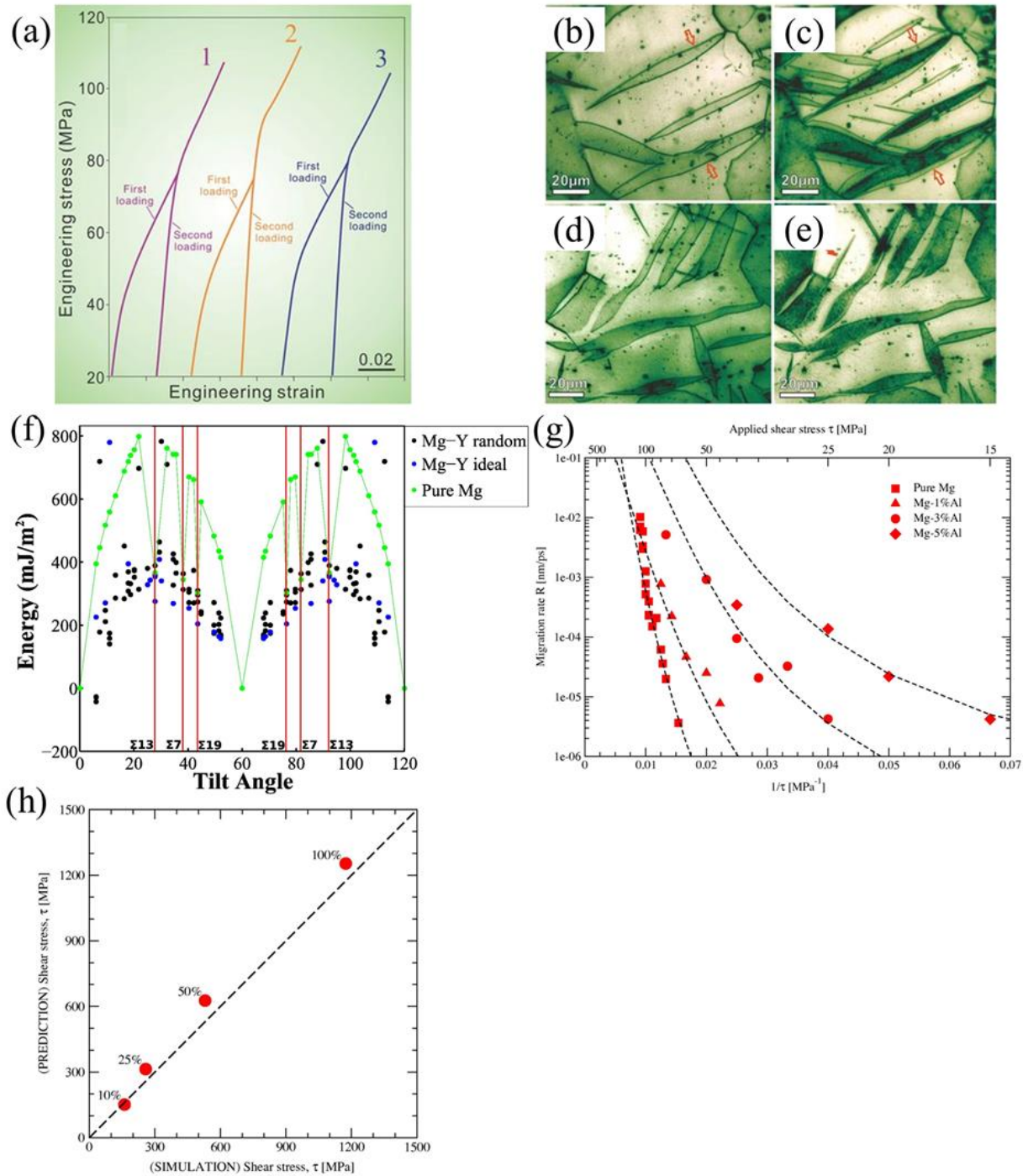


Figure 2.7. (a) Engineering stress–strain curves of three samples of a Mg–0.2 at. % Gd alloy from compression tests. Curve 1 is for sample compressed, unloaded and immediately recompressed. Samples for curves 2 and 3 were annealed at 300 °C for 20 min and at 150 °C for 3 h, respectively, before the second loading. (b–e) Optical micrographs showing twins in samples (b) at a strain of 0.025 of the first loading in curve 1, and (c) at an accumulated strain of 0.045 of the second loading in curve 1, and (d) at a strain of 0.025 of the first loading in curve 2, and (e) at an accumulated strain of 0.045 of the second loading in curve 2 [67]. (f) Energy distribution of symmetric tilt $\langle c \rangle$ -axis boundaries. Pure Mg boundaries are compared to

boundaries with random segregation of Y and idealized segregation of Y [98]. (g) Logarithm of the migration rate R vs. the inverse of the stress $1/\tau$, for pure Mg (squares), Mg–1 at. % Al (triangles), Mg–3 at. % Al (circles), Mg–5 at. % Al (diamonds), at 300 K and (h) Applied shear stress for unpinning of the twin boundary with solutes segregated under application of a constant applied strain rate as measured in the simulation (scattered points) vs. the stress predicted by the model (dashed line), for segregated concentrations at 10 at. %, 25 at. %, 50 at. % and 100 at. % [28]. [Figure adapted with permissions]

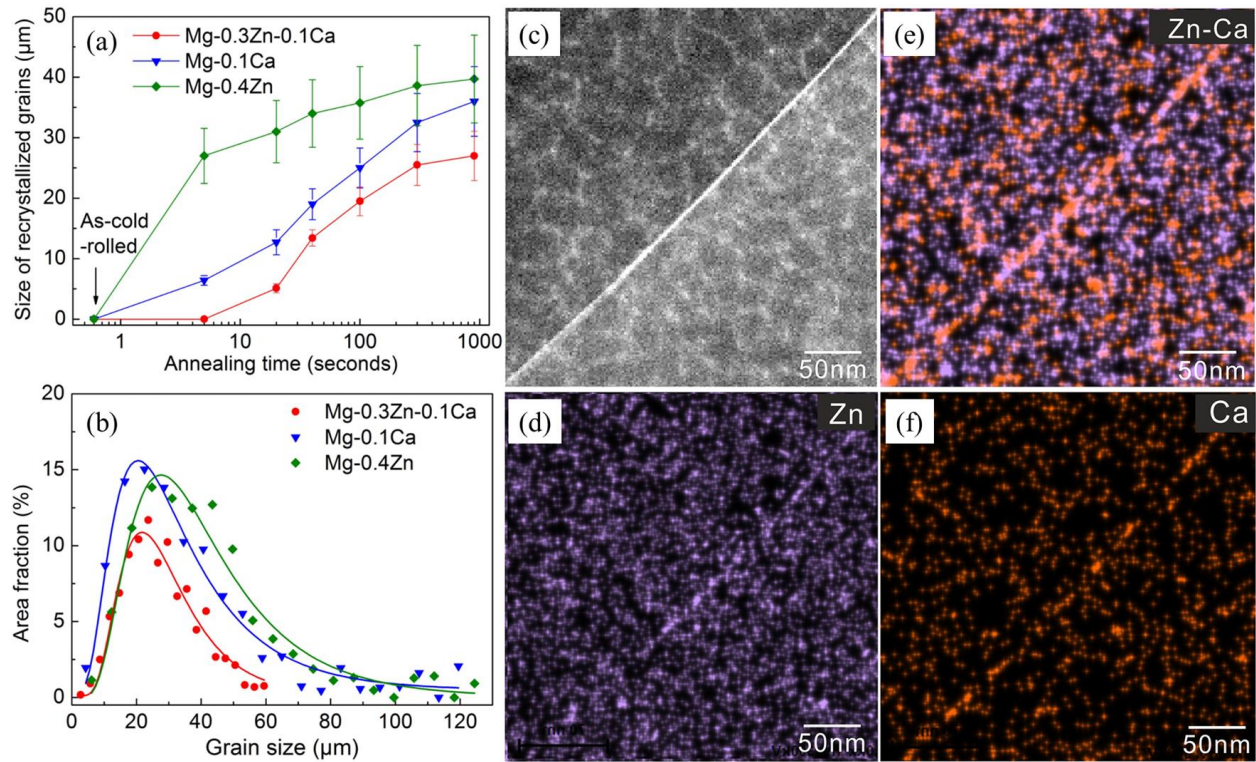


Figure 2.8. (a) Variations of recrystallized grain size as a function of annealing time at 350° C in cold-rolled (23% thickness reduction) Mg-0.3Zn-0.1Ca, Mg-0.1Ca, and Mg-0.4Zn alloys. (b) Histogram showing grain size distribution in each alloy in the fully recrystallized state (900 s annealing at 350 ° C). (c) HAADF-STEM image, and (d-f) EDX maps showing solute segregation to grain boundaries in Mg-0.3Zn-0.1Ca alloy subjected to 23% thickness reduction and annealing at 350 ° C for 900 s [97]. [Figure adapted with permissions]

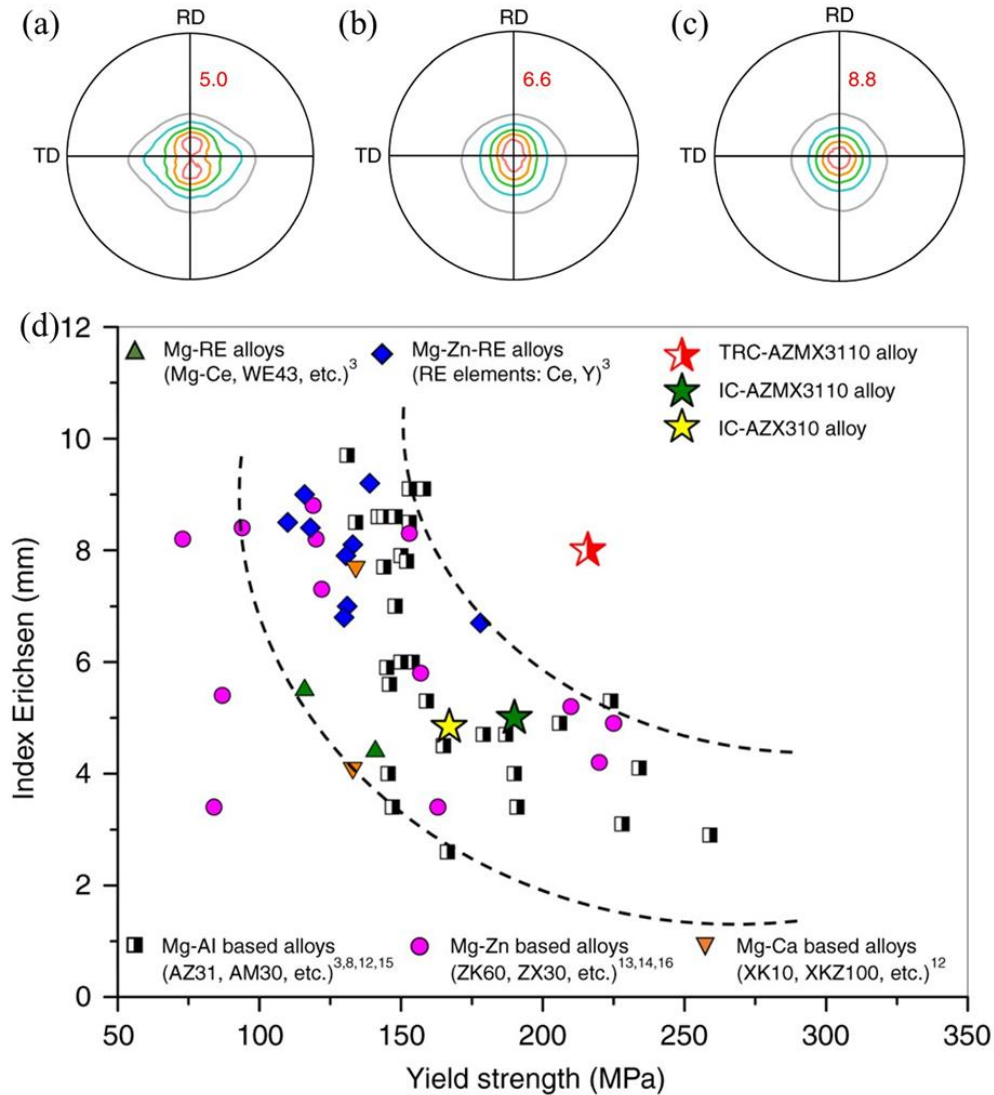


Figure 2.9. (a-c) Pole figures of basal (0001) planes showing the texture of TRC-AZMX3110, IC-AZMX3110, and IC-AZX310, respectively. The numbers in red color indicate the maximum texture intensity. (d) Yield strength and stretch formability represented by the Index Erichsen (IE) value at room temperature of various Mg alloys sheets. Higher IE values mean that the alloys exhibit better formability [99]. [Figure adapted with permissions]

In addition, solute segregation can assist the formation of nanocrystalline grains via pinning boundary migration during annealing, leading to a good combination of ductility and strength [118, 119]. Formation of precipitates is also favored near GBs due to the clustering of solute elements

and these precipitates can efficiently resist creep deformation when products of Mg alloys serve at high temperature [120-122].

Therefore, GBSE leads to new insights into the structure and chemistry of GBs in Mg alloys, as well as strategies for developing new alloys with desired formability and mechanical properties via engineering the design of alloy compositions and thermomechanical processes. As shown in **Figure 2.5(f, g)**, profuse elements can be selected as candidates in alloy design based on GBSE due to their high segregation probability with negative segregation energies. However, systematic work is still required to detect the factors influencing solute segregation and provide reliable prediction models for solute segregation design.

2.2.1.3 Prediction of Grain Boundary Segregation

Experimental characterization of chemical interface at atomic scale is complex to operate on all possible solutes and GBs, and thus cannot provide a full map of solute segregation via experimental. Therefore, theoretical analysis of GB segregation phenomena has been widely conducted on the basis of the Gibb's adsorption isotherm [123] combined with the McLean statistics [124] and also in terms of atomic calculation [108, 109, 114, 125, 126] as well as via machine learning method [103, 113, 127-129].

Difference of the interface energies between the pure host and the alloy is given by,

$$\Delta\gamma = k_B T \ln \left[1 + C_b \exp\left(\frac{\Delta G}{k_B T}\right) \right] \quad (2.6)$$

where ΔG is the interfacial free energy decrement due to solute addition, i.e., segregation energy and C_b is the solute concentration in bulk. According to the Langmuir–McLean theory [124], the concentration at the GB, C_{GB} , is given by,

$$\frac{C_{GB}}{C_{GB}^0 - C_{GB}} = \frac{C_b}{1 - C_b} \exp(E/k_B T) \quad (2.7)$$

where C_{GB}^0 is the saturation of the GB at 0 K, C_{GB} is actual solute concentration, depending on the solute concentration in the bulk lattice C_b and temperature T. k_B is Boltzmann constant and E is decrement in potential energy for a solute atom as it segregates to the GB region i.e. the segregation energy. White and Coghlan [130] extended this concept to segregation at a boundary with a distribution of binding energies, i.e., considering different segregation sites and thus they proposed a modified description separately as,

$$C_{GB}^i = \left(1 + \left(\frac{1 - C_b}{C_b} \right) \exp \left(- \frac{E_i}{k_B T} \right) \right)^{-1} \quad (2.8)$$

then the GB concentration is obtained by performing a weighted average of concentrations,

$$C_{GB} = \sum_i F_i C_{GB}^i \quad (2.9)$$

where F_i is the fraction of GB sites which have binding energy of E_i .

Figure 2.10(a) shows the occupation curves calculated from the Eq. (2.7) at different aging temperatures and bulk S concentrations for the segregation of S at a $\Sigma 5(012)$ symmetrical tilt GB (see **Figure 2.10(b)**). The curves indicate that the occupations of both the GB0 and GB2 sites are very close to 1.0 where those of the other sites (GB1 and GB3 to GB6) are under 0.1, showing a preferential segregation of S for a $\Sigma 5(012)$ symmetrical tilt GB [131]. Considering all possible segregation sites, Huber et al. [96] calculated concentration of Y versus temperature for three GBs in Mg-Y system using Eq. (2.8) with a nominal bulk concentration $C_b=0.75\%$. The same decreasing trend of Y concentration with increasing temperature was observed for general tilt and 3-D general GBs, whereas the $\Sigma 7$ GB plateaus at a concentration of 24% at a temperature of 500 K as shown in **Figure 2.10(c)**. This difference indicates that three possible sites at $\Sigma 7$ GB saturate very quickly, and very limited further segregation takes place until the temperature drops enough for segregation at sites only slightly larger than the bulk sites to occur [96].

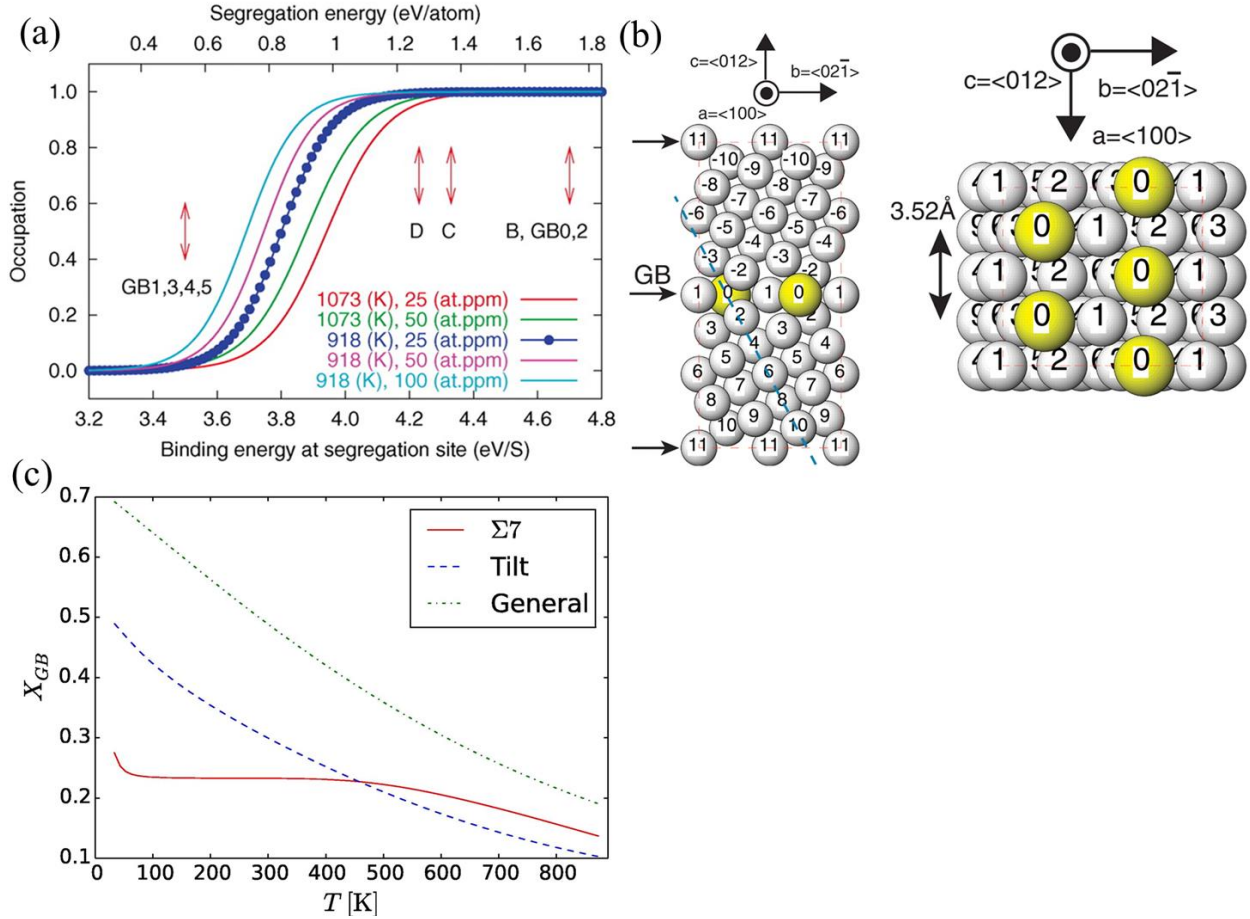


Figure 2.10. (a) Occupation versus binding energy, $-E_b$ (eV/S), at a segregation site calculated from McLean's equation (Eq. (2.7)) with respect to the aging temperature (K) and bulk S concentration (atomic ppm, 10^{-4} atomic % S) in a (b) $\Sigma 5(012)$ symmetrical tilt GB, where gray balls indicate Ni atoms; yellow balls indicate S atoms. [131]. (c) Y concentration at the $\Sigma 7$, general tilt and 3-D GBs in Mg-Y system as a function of temperature using Eq. (2.9) and nominal bulk concentration $C_b=0.75\%$ [96]. [Figure adapted with permissions]

The segregation energy is particularly important to predict the propensity of dopants to segregate into the GB/FS (free surface) and to calculate the dopant concentration at GB/FS as mentioned in Eq. (2.7) and Eq. (2.8). In terms of strain energy of the solute, McLean [124] developed a theoretical model to calculate the segregation enthalpy (ΔH_{el}^{seg}), which is given by,

$$\Delta H_{el}^{seg} = \frac{24\pi K_h G_d r_h r_d (r_h - r_d)^2}{3K_h r_h + 4G_d r_d} \quad (2.10)$$

where K and G are the bulk modulus and shear modulus, respectively, and r is the atomic radius, the subscript h and d denoting the host and dopant atoms, respectively. Recently, Pei et al. [109] introduced misfit volume to describe the mechanical contributions to segregation energies for TBs in Mg alloys. In their case, the segregation energy for a solute X segregating at site i of TB is given by,

$$E_{TB,i}^X = -B(V_{TB,i} - V_{Mg}) \frac{\Delta V_{msft}}{V_{Mg}} \quad (2.11)$$

where B is the bulk modulus, $V_{TB,i}$ and V_{Mg} represent the Voronoi volumes for TB sites and bulk-like sites, respectively, and ΔV_{msft} is the misfit volume which can be obtained by fitting to the quadratic energy-volume curve. As shown in **Figure 2.11**(a) and (b), compared with DFT-calculated results, their prediction model can well describe the signs of energy changes, i.e., telling segregation or non-segregation for a given solute. However, the model is not sufficiently to correctly determine segregation trend of all solute atoms and to quantitatively judge which solute have the larger segregation ability.

Miedema [132] proposed that the bonding energy differences between host and dopant atoms also contribute to GB segregation enthalpy and gave the following equation,

$$\Delta H^{seg} = -0.71 \times \frac{1}{3} \times \nu \times (-\Delta H_{sol}^h - c_0 \gamma_h^s V_h^{2/3} + c_0 \gamma_d^s V_h^{2/3}) + \Delta E_{el} \quad (2.12)$$

where ν is the ratio of lost bonds at GB core, $c_0 \gamma^s V^{2/3}$ is the molar surface enthalpy of the host or dopant atom, $-\Delta H_{sol}^h$ represents the enthalpy of solution of the dopant and ΔE_{el} is the solute strain energy. Obviously, Miedema model includes two contributions to solute segregation energy, i.e., mechanical part and chemical part, corresponding to the elastic energy and the atomic bonding energy, respectively. In the recent study of solute segregation in Mo, Tran et al. [114] correlated the mechanical and chemical contributions to the metallic radii difference and the Pauling

electronegativity difference, respectively. As shown in **Figure 2.11(c)**, a parabolic-like relationship between segregation energy and relative metallic radii is observed, indicating a significant contributing factor to segregation. In addition, a strong monotonic relationship between segregation energy and the square of the Pauling electronegativity difference is found in **Figure 2.11(d)**, indicating an unignorable rule of chemical effect in predicting the segregation propensity.

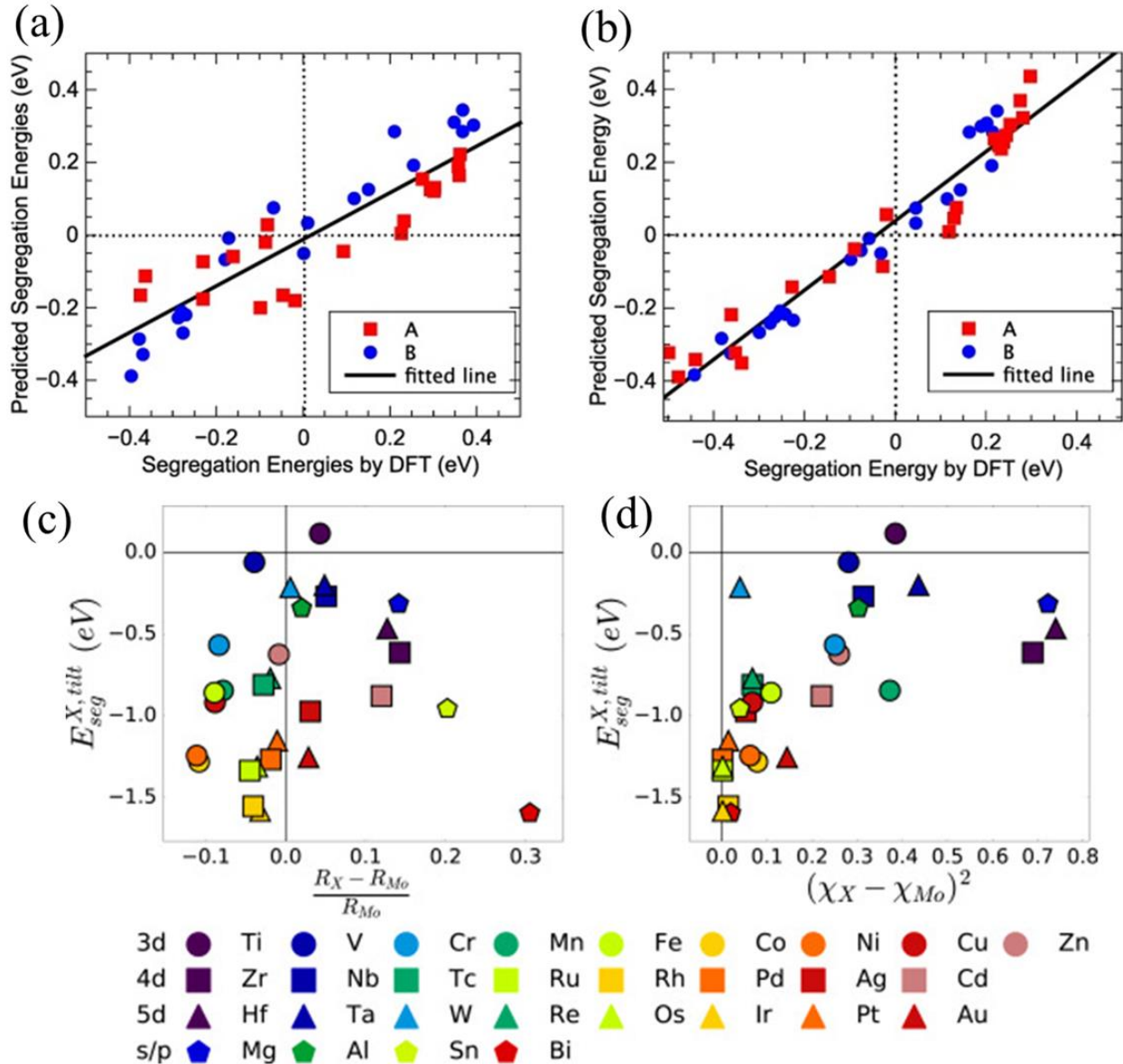


Figure 2.11. Predicted (on the basis of McLean model) and DFT-computed segregation energies of solutes in (a) compression TB and (b) tensile TB in Mg [109]. Plot of the lowest tilt segregation energy $E_{seg}^{X, tilt}$ against

(c) the relative metallic radius difference $\frac{R_X - R_{Mo}}{R_{Mo}}$ for each dopant X, and (d) the square of the relative Pauling electronegativity $(\chi_X - \chi_{Mo})^2$ [114]. [Figure adapted with permissions]

In addition to the theoretical methods above, recently, machine learning (ML) has become a popular tool in materials science for extracting meaningful relationships and new physical insight via processing big data with advanced algorithms. For example, GB structure-property relationships for energy and temperature-dependent mobility can be well understood by introducing a new descriptor, the Scattering Transform (ST) in a learning program [133]. By performing evolutionary search and machine learning on GBs within the entire misorientation range, Zhu et al. [129] found a general and common phenomenon: GB structures can be categorized into three families: Kites, Split-Kites and Extended-Kites and this is not limited to few special high-angle boundaries. Recently, Huber et al. [113] analyzed 1 million data points for solute segregation at thirty eight GBs using machine learning with gradient boosted decision trees. As shown in **Figure 2.12**, by introducing extra parameters with powers of the excess volume, such as ΔV^3 , prediction of segregation (see **Figure 2.12(b)**) is well improved and behaves better than that a simple linear model does (see **Figure 2.12(a)**) [113]. This implies that some pieces of physics such as site's structural anisotropy, were completely neglected in the simple linear model. Therefore, ML technique is extremely useful to encode information of the underlying physics beyond. However, this method requires enough large source data and well-performed algorithms and thus much work must be done to promote its application.

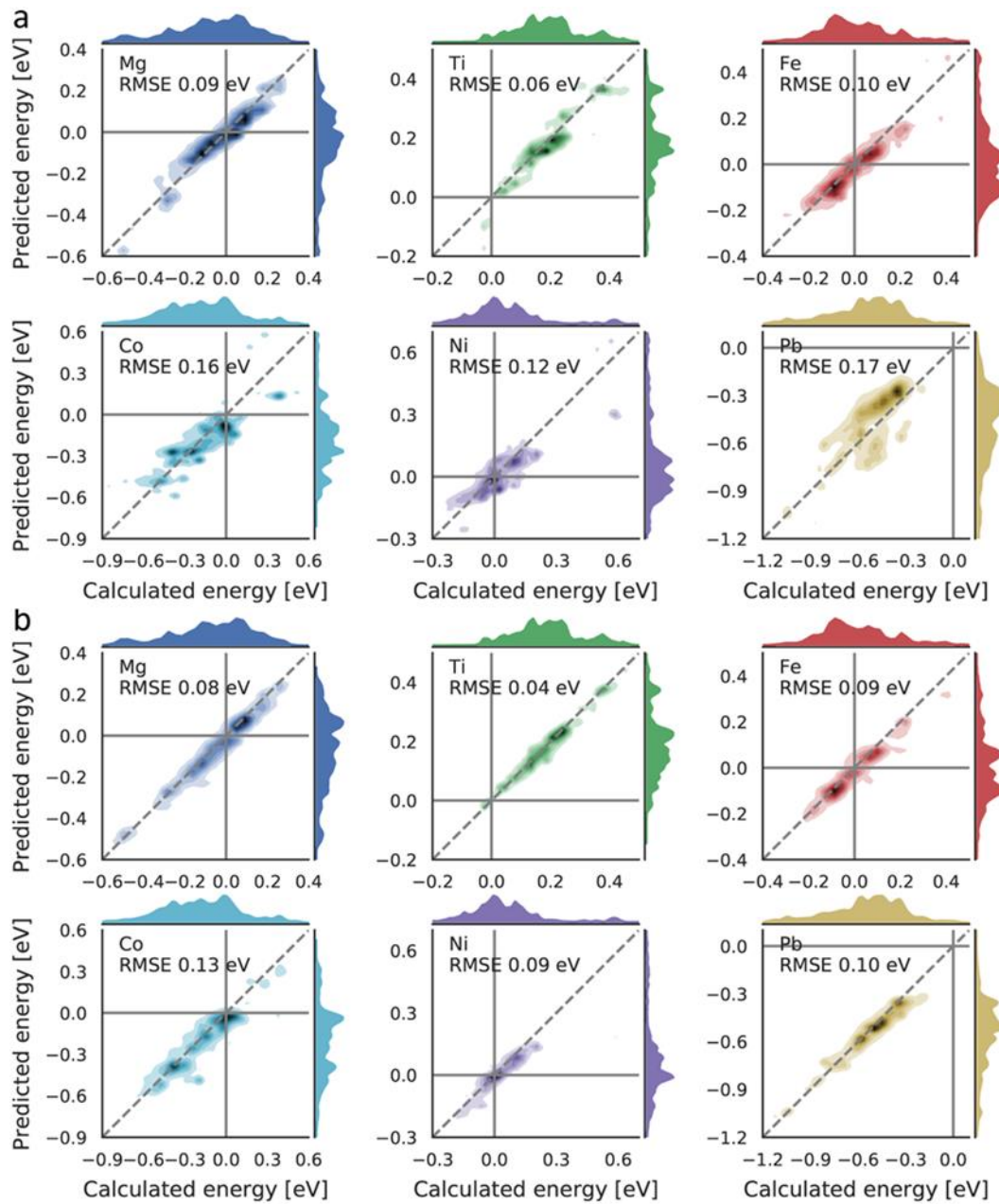


Figure 2.12. Predicted segregation energies using (a) a linear fit and (b) gradient-boosted decision trees plotted against calculated values for all six solutes. Results are taken from all 38 boundaries and data distribution plots are shown joint to their corresponding axes. Darkness of color indicates data frequency, and results are smoothed [113]. [Figure adapted with permissions]

2.2.2 Solute Effect on Dislocation Slips

Table 2.1 indicates that basal slip is dominant deformation mode due to its much lower CRSS than those of non-basal slip systems, being the key issue in using Mg for its low ductility and poor formability. In an effort to improve strength and formability at room temperature, many have focused on adding various solute elements such as Y, Gd, Zr, Sn, Nd, Ce and Ag into Mg to modify activation of more dislocation slips [14, 26, 90, 134-139].

As shown in **Figure 2.13(a)**, the annealed pure Mg and Mg-3Y alloy have comparable yield stress (YS, 0.2% proof stress) and ultimate tensile strength (UTS), which are ~ 50 MPa and ~ 130 MPa, respectively. However, the Mg-3Y alloy exhibits a much higher uniform elongation ($\sim 21 \pm 1.2\%$) than that of pure Mg ($\sim 5 \pm 0.5\%$) (see **Figure 2.13(a)**). In addition, the strain-hardening rate of the pure Mg significantly drops after 5% of tensile strain, which is not observed in Mg-3Y alloy (see **Figure 2.13(b)**) [140]. As shown in **Figure 2.13(c)**, basal $\langle a \rangle$ dislocations are dominated in deformed pure Mg, with very limited $\langle c \rangle$ or $\langle c+a \rangle$ dislocations. While in deformed Mg-3Y alloy, pyramidal $\langle c+a \rangle$ dislocations are profusely activated and stacking faults are also characterized (see **Figure 2.13(d)**). Therefore, the improved ductility is observed in Mg-3Y due to the enhanced activity of $\langle c+a \rangle$ dislocations [136, 137, 141]. Sandlöbes et al. [136] calculated SFEs using ab initio method and they found that the I_1 SFEs of Mg-Y decrease with Y concentrations as shown in **Figure 2.13(e)**. Accordingly, they proposed that the sessile I_1 stacking faults were stabilized through the addition of Y and hence enhanced the nucleation of dislocation structures on pyramidal planes. In addition, Kim et al. [4] determined that with the addition of Y, the increase in the CRSS of basal slip was more than those of non-basal slips (see **Figure 2.13(f)**), which increase the probability of non-basal slips at the same stress level, consequently improving the ductility of Mg-Y alloy.

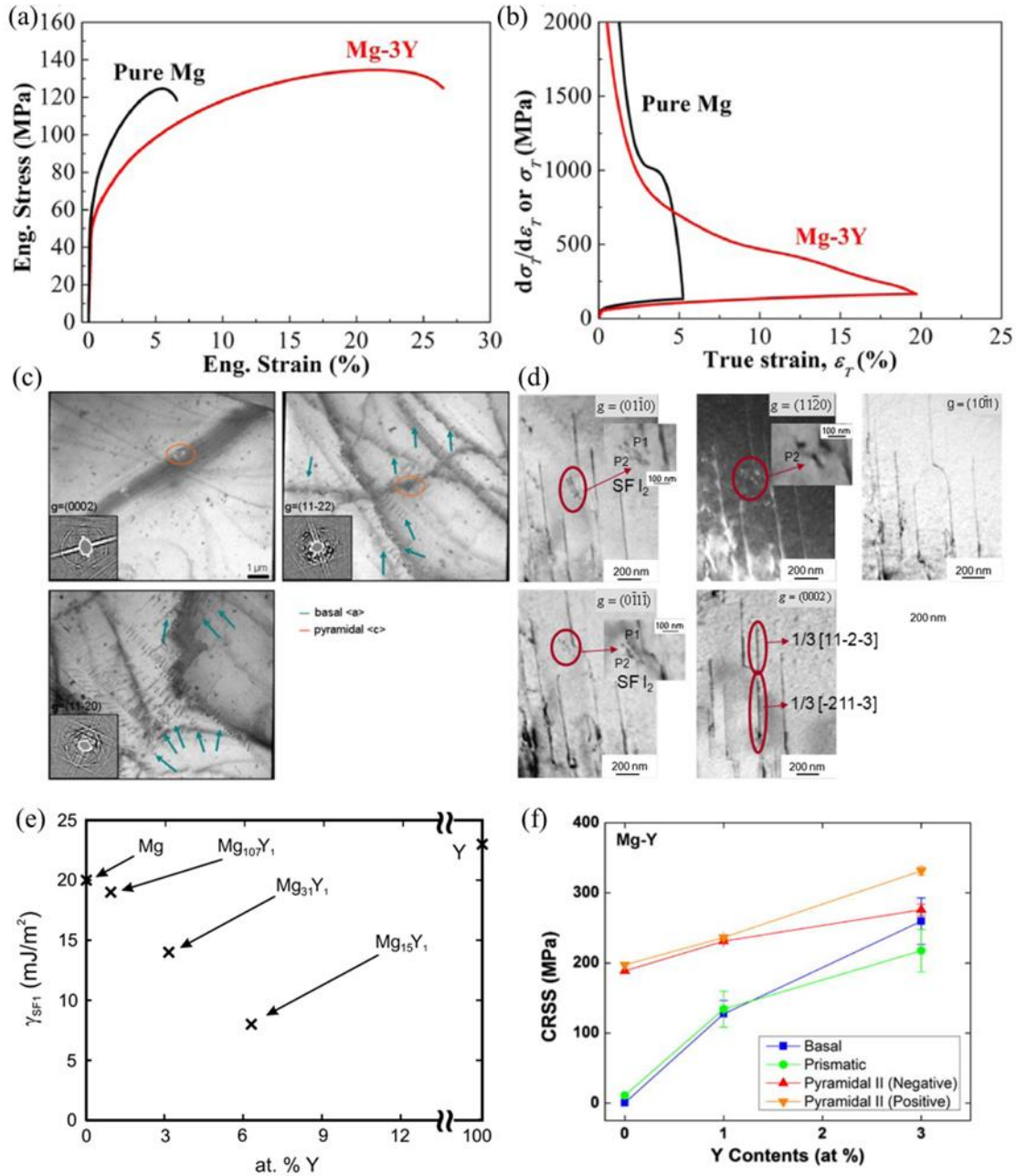


Figure 2.13. (a) Tensile curves of nominal stress vs. strain, and (b) True stress–strain and strain hardening curves from tensile tests of pure Mg and Mg- wt.% 3Y [140]. (c) TEM bright-field images of slightly room-temperature-deformed pure Mg showing mainly basal $\langle a \rangle$ dislocations [137], and (d) TEM bright-field and dark-field images under different two-beam diffractions (see inlets for the diffraction vector), showing the activity of different perfect and partial dislocations with a $\langle c+a \rangle$ Burgers vector on pyramidal plane in 3% (engineering strain) cold-rolled Mg–3 wt.% Y; an intrinsic stacking fault I_2 (SFI_2) is also visible [136]. (e) The ab initio determined I_1 SFEs of Mg–Y alloys with different Y concentrations (elemental Mg and Y, $Mg_{107}Y_1$, $Mg_{31}Y_1$, and $Mg_{15}Y_1$) [136]. (f) CRSS of Mg–Y alloys on the basal, prismatic, and pyramidal II planes obtained via MD simulation at 0 K [4]. [Figure adapted with permissions]

Recently, Wu et al. [7] proposed that the high hardening and low ductility in Mg is ascribed to the transition of easy-glide pyramidal II $\langle c+a \rangle$ dislocations to the basal-dissociated immobile dislocation structures. Due to this deleterious dissociation, the $\langle c+a \rangle$ dislocations cannot accommodate further deformation after they are activated in pure Mg. On the other hand, pyramidal $\langle c+a \rangle$ dislocation could cross slip from pyramidal II plane to pyramidal I plane as shown in **Figure 2.14(a)**, favoring the continuous slip of pyramidal dislocation and the plastic straining during deformation [14]. However, because activation energy for the pyramidal-to-basal (PB) transition is lower than that for the cross-slip, the PB transition will be dominant in pure Mg. Wu et al. [14] found that adding specific solute elements can modify the activation barrier so that the cross-slip is activated and the PB transition is restricted. For example, as shown in **Figure 2.14(b-e)** ductility generally decreases or saturates with increasing Zn while alloying with dilute RE solutes or even Ca, Mn can overcome this detrimental effect on ductility. Dilute solute addition of Y could increase the $\langle c+a \rangle$ cross-slip and multiplication rates to levels much faster than the deleterious $\langle c+a \rangle$ transformation which would hinder the further deformation, making alloys with better ductility.

The similar ductility improvement was also found in many other Mg alloys with enhanced activity of non-basal slips by solid solution [140, 142, 143]. Besides, in situ experiment by Stanford et al. [139] have shown that Y could strengthen the basal, non-basal $\langle c + a \rangle$ slips and extension twinning systems, resulting in enhanced hardening. Therefore, on the basis solute effect on slip activity, ductility and strength of Mg can be well modified by adding favorable solute elements combined with proper heat treatment.

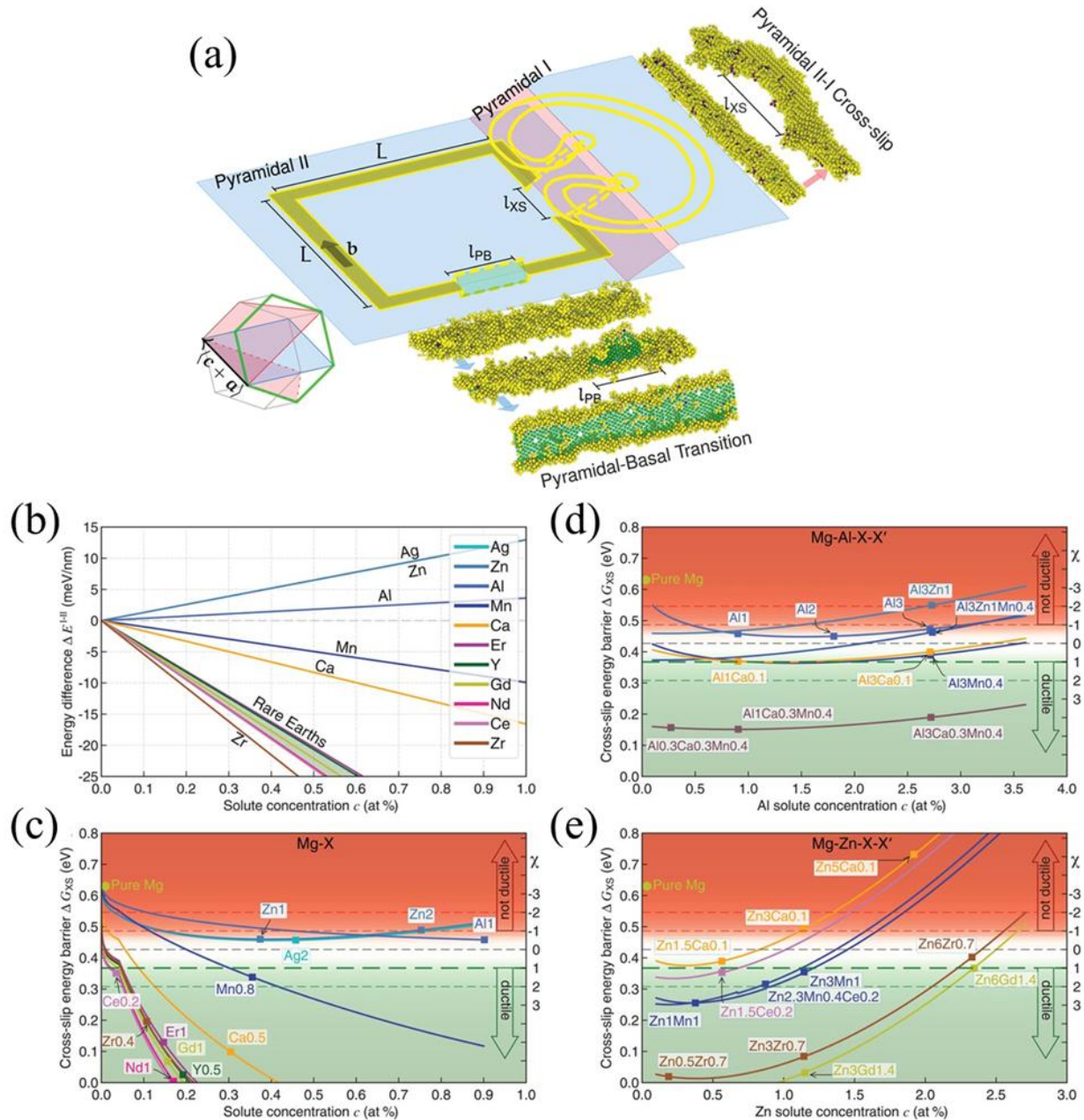


Figure 2.14. (a) Competing pyramidal-to-basal transition and pyramidal II-I cross-slip processes during the expansion of an $L \times L$ $\langle c+a \rangle$ dislocation loop on the pyramidal II plane. Activation energy for cross-slip and ductility index χ for binary and higher-order Mg alloys: (b) Average solute contribution to energy difference ΔE^{I-II} between the pyramidal I and II $\langle c+a \rangle$ screw dislocations for various solute elements; (c) Predicted pyramidal II-I cross-slip activation energy barrier including solute fluctuations and ductility index χ for binary Mg alloys as a function of solute concentration c for the same solutes. $\chi > 1$ indicates favorable conditions for ductility; (d) $Mg - Al - X - X'$ with varying Al concentrations and (e) $Mg - Zn - X - X'$ with varying Zn concentrations [14]. [Figure adapted with permissions]

2.3 Twin-slip and Twin-twin Interaction

Moreover, several computational studies [144-148] were performed on the interaction of dislocation and TBs, segregated by limited solute atoms such as Y, Sc, Nd, Al. Preliminary MD simulations in pure Mg [147] suggested that the interaction between dislocation and $\{10\bar{1}1\}$ twin was attractive, and the partials were absorbed readily into the TB while the partials would pass through $\{10\bar{1}2\}$ TB due to a repulsive interaction. In terms of solutes segregation to TBs, Yoshida et al. [146] found that no residual dislocation was observed after the interaction of a segregated $\{10\bar{1}2\}$ TB with screw partial dislocations corresponded to the behavior of the pure Mg. However, five scenarios such as transformation between glissile and sessile twinning dislocation, dislocation splitting and emission, were involved in the interaction of a $\{10\bar{1}1\}$ TB with partial dislocations. Besides, in case of $\{10\bar{1}1\} - \{10\bar{1}2\}$ double twin (DT), the monte Carlo simulations were conducted by Miyazawa et al. [144] and they proposed that Y atoms tend to segregate at the extension sites in the $\{10\bar{1}1\}$ and $\{10\bar{1}2\}$ twin boundaries while their segregating at the triple junction of the double twin was less observed. Furthermore, their MD simulation on M-Y and Mg-Al revealed that Y segregation resulted in emission of twinning dislocations from the DT boundary, while Al segregation suppressed the motion of the twinning dislocation. Therefore, the effect of different solute atoms on the dislocation behaviors in and around TBs are various, which is an interesting and meaningful research to determine the strengthening and toughening mechanism in Mg due to solute effect. furthermore, the co-effect of solute atoms on the TB structure and the interaction between dislocation and TBs needs further systematic studies.

2.4 References

- [1] M. Stricker, W.A. Curtin, Prismatic Slip in Magnesium, *The Journal of Physical Chemistry C* 124(49) (2020) 27230-27240.

- [2] W.B. Hutchinson, M.R. Barnett, Effective values of critical resolved shear stress for slip in polycrystalline magnesium and other hcp metals, *Scripta Materialia* 63(7) (2010) 737-740.
- [3] X.Y. Lou, M. Li, R.K. Boger, S.R. Agnew, R.H. Wagoner, Hardening evolution of AZ31B Mg sheet, *International Journal of Plasticity* 23 (2007) 44-86.
- [4] K.-H. Kim, J.B. Jeon, N.J. Kim, B.-J. Lee, Role of yttrium in activation of $\langle c + a \rangle$ slip in magnesium: An atomistic approach, *Scripta Materialia* 108 (2015) 104-108.
- [5] C. Bettles, M. Barnett, *Advances in wrought magnesium alloys: Fundamentals of processing, properties and applications*, Woodhead Publishing, 2012, p. 480.
- [6] N. Kumar, D. Choudhuri, R. Banerjee, R.S. Mishra, Strength and ductility optimization of Mg–Y–Nd–Zr alloy by microstructural design, *International Journal of Plasticity* 68(0) (2015) 77-97.
- [7] Z. Wu, W.A. Curtin, The origins of high hardening and low ductility in magnesium, *Nature* 526 (2015) 62-7.
- [8] J. Wu, S. Si, K. Takagi, T. Li, Y. Mine, K. Takashima, Y.L. Chiu, Study of basal $\langle a \rangle$ and pyramidal $\langle c + a \rangle$ slips in Mg-Y alloys using micro-pillar compression, *Philosophical Magazine* 100(11) (2020) 1454-1475.
- [9] H. Fan, J.A. El-Awady, Molecular Dynamics Simulations of Orientation Effects during Tension, Compression, and Bending Deformations of Magnesium Nanocrystals, *Journal of Applied Mechanics, Transactions ASME* 82(10) (2015).
- [10] B. Li, Q.W. Zhang, S.N. Mathaudhu, Basal-pyramidal dislocation lock in deformed magnesium, *Scripta Materialia* 134 (2017) 37-41.
- [11] K.Y. Xie, Z. Alam, A. Caffee, K.J. Hemker, Pyramidal I slip in c-axis compressed Mg single crystals, *Scripta Materialia* 112 (2016) 75-78.
- [12] Z. Wu, W.A. Curtin, Intrinsic structural transitions of the pyramidal I $\langle c+a \rangle$ dislocation in magnesium, *Scripta Materialia* 116 (2016) 104-107.
- [13] H. Fan, J.A. El-Awady, Towards resolving the anonymity of pyramidal slip in magnesium, *Materials Science and Engineering: A* 644 (2015) 318-324.
- [14] Z. Wu, R. Ahmad, B. Yin, S. Sandlöbes, W.A. Curtin, Mechanistic origin and prediction of enhanced ductility in magnesium alloys, *Science* 359 (2018) 447-452.
- [15] A. Maldar, L. Wang, B. Liu, W. Liu, Z. Jin, B. Zhou, X. Zeng, Activation of $\langle c \rangle$ dislocations in Mg with solute Y, *Journal of Magnesium and Alloys* (2021).

- [16] I. Basu, M. Chen, J. Wheeler, R.E. Schäublin, J.F. Löffler, Segregation-driven exceptional twin-boundary strengthening in lean Mg–Zn–Ca alloys, *Acta Materialia* 229 (2022) 117746.
- [17] J.W. Christian, S. Mahajan., deformation twinning, *Progress in Materials Science* 39 (1995) 1-157.
- [18] R. Ahmad, Z. Wu, W.A. Curtin, Analysis of double cross-slip of pyramidal I $\langle c+a \rangle$ screw dislocations and implications for ductility in Mg alloys, *Acta Materialia* 183 (2020) 228-241.
- [19] A. Kumar, B.M. Morrow, R.J. McCabe, I.J. Beyerlein, An atomic-scale modeling and experimental study of $\langle c+a \rangle$ dislocations in Mg, *Materials Science and Engineering: A* 695 (2017) 270-278.
- [20] W.W. Hu, Z.Q. Yang, H.Q. Ye, $\langle c+a \rangle$ dislocations and their interactions with other crystal defects in a Mg alloy, *Acta Materialia* 124 (2017) 372-382.
- [21] D.Y. Sun, M.I. Mendeleev, C.A. Becker, K. Kudin, T. Haxhimali, M. Asta, J.J. Hoyt, A. Karma, D.J. Srolovitz, Crystal-melt interfacial free energies in hcp metals: A molecular dynamics study of Mg, *Physical Review B* 73(2) (2006).
- [22] J.A. Yasi, T. Nogaret, D.R. Trinkle, Y. Qi, L.G. Hector, W.A. Curtin, Basal and prism dislocation cores in magnesium: comparison of first-principles and embedded-atom-potential methods predictions, *Modelling and Simulation in Materials Science and Engineering* 17(5) (2009) 055012.
- [23] X.-Y. Liu, J.B. Adams, F. Ercolessi, J.A. Moriarty, EAM potential for magnesium from quantum mechanical forces, *Modelling and Simulation in Materials Science and Engineering* 4 (1996) 293-303.
- [24] S. Groh, E.B. Marin, M.F. Horstemeyer, D.J. Bammann, Dislocation motion in magnesium: a study by molecular statics and molecular dynamics, *Modelling and Simulation in Materials Science and Engineering* 17(7) (2009) 075009.
- [25] C.M. Byer, B. Li, B. Cao, K.T. Ramesh, Microcompression of single-crystal magnesium, *Scripta Materialia* 62 (2010) 536-539.
- [26] B. Yin, Z. Wu, W.A. Curtin, First-principles calculations of stacking fault energies in Mg–Y, Mg–Al and Mg–Zn alloys and implications for $\langle c + a \rangle$ activity, *Acta Materialia* 136 (2017) 249-261.
- [27] T. Nogaret, W.A. Curtin, J.A. Yasi, L.G. Hector Jr, D.R. Trinkle, Atomistic study of edge and screw $\langle c + a \rangle$ dislocations in magnesium, *Acta Materialia* 58(13) (2010) 4332-4343.

- [28] A. Luque, M. Ghazisaeidi, W.A. Curtin, A new mechanism for twin growth in Mg alloys, *Acta Materialia* 81 (2014) 442-456.
- [29] Y. Liu, N. Li, M. Arul Kumar, S. Pathak, J. Wang, R.J. McCabe, N.A. Mara, C.N. Tomé, Experimentally quantifying critical stresses associated with basal slip and twinning in magnesium using micropillars, *Acta Materialia* 135 (2017) 411-421.
- [30] F. Ning, Q. Le, J. Yan, Y. Jia, Crimp feasibility of AZ31 magnesium alloy wide plate at warm temperatures responding to asymmetry, *Journal of Magnesium and Alloys* 10(3) (2022) 797-810.
- [31] M. Yuasa, Y. Chino, M. Mabuchi, Mechanical and chemical effects of solute elements on generalized stacking fault energy of Mg, *Journal of Materials Research* 29(21) (2014) 2576-2586.
- [32] S.L. Shang, W.Y. Wang, B.C. Zhou, Y. Wang, K.A. Darling, L.J. Kecskes, S.N. Mathaudhu, Z.K. Liu, Generalized stacking fault energy, ideal strength and twinnability of dilute Mg-based alloys: A first-principles study of shear deformation, *Acta Materialia* 67 (2014) 168-180.
- [33] M. Muzyk, Z. Pakiel, K.J. Kurzydowski, Generalized stacking fault energy in magnesium alloys: Density functional theory calculations, *Scripta Materialia* 66(5) (2012) 219-222.
- [34] P. Andric, B. Yin, W.A. Curtin, Stress-dependence of generalized stacking fault energies, *Journal of the Mechanics and Physics of Solids* 122 (2019) 262-279.
- [35] S.H. Zhang, I.J. Beyerlein, D. Legut, Z.H. Fu, Z. Zhang, S.L. Shang, Z.K. Liu, T.C. Germann, R.F. Zhang, First-principles investigation of strain effects on the stacking fault energies, dislocation core structure, and Peierls stress of magnesium and its alloys, *Physical Review B* 95(22) (2017).
- [36] B. Yin, Z. Wu, W.A. Curtin, Comprehensive first-principles study of stable stacking faults in hcp metals, *Acta Materialia* 123 (2017) 223-234.
- [37] S.L. Shang, C.L. Zacherl, H.Z. Fang, Y. Wang, Y. Du, Z.K. Liu, Effects of alloying element and temperature on the stacking fault energies of dilute Ni-base superalloys, *Journal of Physics: Condensed Matter* 24(50) (2012) 505403.
- [38] S.L. Shang, W.Y. Wang, Y. Wang, Y. Du, J.X. Zhang, A.D. Patel, Z.K. Liu, Temperature-dependent ideal strength and stacking fault energy of fcc Ni: a first-principles study of shear deformation, *Journal of Physics: Condensed Matter* 24(15) (2012) 155402.

- [39] E. Tadmor, A first-principles measure for the twinnability of FCC metals, *Journal of the Mechanics and Physics of Solids* 52(11) (2004) 2507-2519.
- [40] N. Bernstein, E. Tadmor, Tight-binding calculations of stacking energies and twinnability in fcc metals, *Physical Review B* 69(9) (2004).
- [41] Z. Wu, M.F. Francis, W.A. Curtin, Magnesium interatomic potential for simulating plasticity and fracture phenomena, *Modelling and Simulation in Materials Science and Engineering* 23(1) (2014) 015004.
- [42] A. Ostapovets, A. Serra, Review of Non-Classical Features of Deformation Twinning in hcp Metals and Their Description by Disconnection Mechanisms, *Metals* 10(9) (2020).
- [43] A. Bilby Bruce, A.G. Crocker, H. Cottrell Alan, The theory of the crystallography of deformation twinning, *Proceedings of the Royal Society of London. Series A. Mathematical and Physical Sciences* 288(1413) (1965) 240-255.
- [44] Z.C. Ma, X.Z. Tang, Y. Mao, Y.F. Guo, The Plastic Deformation Mechanisms of hcp Single Crystals with Different Orientations: Molecular Dynamics Simulations, *Materials (Basel)* 14(4) (2021).
- [45] J. Wang, J.P. Hirth, C.N. Tomé, (-1012) Twinning nucleation mechanisms in hexagonal-close-packed crystals, *Acta Materialia* 57 (2009) 5521-5530.
- [46] N. Stanford, R.K.W. Marceau, M.R. Barnett, The effect of high yttrium solute concentration on the twinning behaviour of magnesium alloys, *Acta Materialia* 82(0) (2015) 447-456.
- [47] Z.Z. Shi, Y. Zhang, F. Wagner, T. Richeton, P.A. Juan, J.S. Lecomte, L. Capolungo, S. Berbenni, Sequential double extension twinning in a magnesium alloy: Combined statistical and micromechanical analyses, *Acta Materialia* 96 (2015) 333-343.
- [48] M.R. Barnett, Twinning and the ductility of magnesium alloys Part II. "Contraction" twins, *Materials Science and Engineering a-Structural Materials Properties Microstructure and Processing* 464 (2007) 8-16.
- [49] M.R. Barnett, Twinning and the ductility of magnesium alloys Part I: "Tension" twins, *Materials Science and Engineering a-Structural Materials Properties Microstructure and Processing* 464 (2007) 1-7.
- [50] L. Zhao, Y. Xin, F. Guo, H. Yu, Q. Liu, A new annealing hardening mechanism in pre-twinned Mg-3Al-1Zn alloy, *Materials Science and Engineering A* 654 (2016) 344-351.

- [51] S. Pan, Y. Xin, G. Huang, Q. Li, F. Guo, Q. Liu, Tailoring the texture and mechanical anisotropy of a Mg-2Zn-2Gd plate by varying the rolling path, *Materials Science and Engineering A-Structural Materials Properties Microstructure and Processing* 653 (2016) 93-98.
- [52] W. He, Q. Zeng, H. Yu, Y. Xin, B. Luan, Q. Liu, Improving the room temperature stretch formability of a Mg alloy thin sheet by pre-twinning, *Materials Science and Engineering A* 655 (2016) 1-8.
- [53] Y. Xin, H. Zhou, H. Yu, R. Hong, H. Zhang, Q. Liu, Controlling the recrystallization behavior of a Mg-3Al-1Zn alloy containing extension twins, *Materials Science and Engineering A* 622 (2015) 178-183.
- [54] Y. Xin, H. Zhou, H. Yu, R. Hong, H. Zhang, Q. Liu, Controlling the recrystallization behavior of a Mg-3Al-1Zn alloy containing extension twins, *Materials Science and Engineering: A* 622(0) (2015) 178-183.
- [55] B. Song, R. Xin, X. Zheng, G. Chen, Q. Liu, Activation of multiple twins by pre-tension and compression to enhance the strength of Mg-3Al-1Zn alloy plates, *Materials Science and Engineering A* 621 (2015) 100-104.
- [56] Y.M. Kim, C. Mendis, T. Sasaki, D. Letzig, F. Pyczak, K. Hono, S. Yi, Static recrystallization behaviour of cold rolled Mg-Zn-Y alloy and role of solute segregation in microstructure evolution, *Scripta Materialia* 136 (2017) 41-45.
- [57] J.K. Kim, S. Sandlöbes, D. Raabe, On the room temperature deformation mechanisms of a Mg-Y-Zn alloy with long-period-stacking-ordered structures, *Acta Materialia* 82 (2015) 414-423.
- [58] H. Zhang, Y. Li, Y. Liu, Q. Zhu, X. Qi, G. Zhu, J. Wang, P. Jin, X. Zeng, The effect of basal $\langle a \rangle$ dislocation on $\{11\text{-}21\}$ twin boundary evolution in a Mg-Gd-Y-Zr alloy, *Journal of Materials Science & Technology* 81 (2021) 212-218.
- [59] D. Raabe, M. Herbig, S. Sandlöbes, Y. Li, D. Tytko, M. Kuzmina, D. Ponge, P.P. Choi, Grain boundary segregation engineering in metallic alloys: A pathway to the design of interfaces, *Current Opinion in Solid State and Materials Science* 18(4) (2014) 253-261.
- [60] J. Kacher, B.P. Eftink, B. Cui, I.M. Robertson, Dislocation interactions with grain boundaries, *Current Opinion in Solid State and Materials Science* 18(4) (2014) 227-243.

- [61] F.P.E. Dunne, Fatigue crack nucleation: Mechanistic modelling across the length scales, *Current Opinion in Solid State and Materials Science* 18(4) (2014) 170-179.
- [62] G.M. Castelluccio, W.D. Musinski, D.L. McDowell, Recent developments in assessing microstructure-sensitive early stage fatigue of polycrystals, *Current Opinion in Solid State and Materials Science* 18(4) (2014) 180-187.
- [63] T.R. Bieler, P. Eisenlohr, C. Zhang, H.J. Phukan, M.A. Crimp, Grain boundaries and interfaces in slip transfer, *Current Opinion in Solid State and Materials Science* 18(4) (2014) 212-226.
- [64] V. Randle, Grain boundary engineering: an overview after 25 years, *Materials Science and Technology* 26(3) (2013) 253-261.
- [65] D. Raabe, S. Sandlöbes, J. Millán, D. Ponge, H. Assadi, M. Herbig, P.P. Choi, Segregation engineering enables nanoscale martensite to austenite phase transformation at grain boundaries: A pathway to ductile martensite, *Acta Materialia* 61(16) (2013) 6132-6152.
- [66] C.Q. Liu, H.W. Chen, H. Liu, X.J. Zhao, J.F. Nie, Metastable precipitate phases in Mg–9.8wt.%Sn alloy, *Acta Materialia* (2017).
- [67] J.F. Nie, Y.M. Zhu, J.Z. Liu, X.Y. Fang, Periodic segregation of solute atoms in fully coherent twin boundaries, *Science* 340(6135) (2013) 957-60.
- [68] Z.R. Zeng, Y.M. Zhu, M.Z. Bian, S.W. Xu, C.H.J. Davies, N. Birbilis, J.F. Nie, Annealing strengthening in a dilute Mg–Zn–Ca sheet alloy, *Scripta Materialia* 107 (2015) 127-130.
- [69] Y.M. Zhu, M.Z. Bian, J.F. Nie, Tilt boundaries and associated solute segregation in a Mg–Gd alloy, *Acta Materialia* 127 (2017) 505-518.
- [70] Y.M. Zhu, S.W. Xu, J.F. Nie, {10-11} Twin boundary structures in a Mg–Gd alloy, *Acta Materialia* 143 (2018) 1-12.
- [71] J.F. Nie, K. Oh-ishi, X. Gao, K. Hono, Solute segregation and precipitation in a creep-resistant Mg–Gd–Zn alloy, *Acta Materialia* 56(20) (2008) 6061-6076.
- [72] X. Zhou, X.-x. Yu, T. Kaub, R.L. Martens, G.B. Thompson, Grain Boundary Specific Segregation in Nanocrystalline Fe(Cr), *Scientific Reports* 6 (2016) 34642.
- [73] S. Taller, V. Pauly, Z. Jiao, R. Hanbury, G.S. Was, Solute segregation and precipitation across damage rates in dual-ion-irradiated T91 steel, *Journal of Nuclear Materials* 563 (2022).
- [74] W. Jia, Y. Liu, T. Yuan, F. Wang, Y. Chen, T. Ma, Grain boundary segregation behavior in Fe-rich Sm-Co-Fe-Cu-Zr magnets, *Materialia* 22 (2022).

- [75] S. Thapliyal, P. Agrawal, P. Agrawal, S.S. Nene, R.S. Mishra, B.A. McWilliams, K.C. Cho, Segregation engineering of grain boundaries of a metastable Fe-Mn-Co-Cr-Si high entropy alloy with laser-powder bed fusion additive manufacturing, *Acta Materialia* 219 (2021).
- [76] L.T. Belkacemi, E. Meslin, J.P. Crocombette, B. Radiguet, F. Leprêtre, B. Décamps, Striking effect of solute elements (Mn, Ni) on radiation-induced segregation/precipitation in iron-based model alloys, *Journal of Nuclear Materials* 548 (2021).
- [77] L. Li, Z. Li, A. Kwiatkowski da Silva, Z. Peng, H. Zhao, B. Gault, D. Raabe, Segregation-driven grain boundary spinodal decomposition as a pathway for phase nucleation in a high-entropy alloy, *Acta Materialia* 178 (2019) 1-9.
- [78] M. Kuzmina, D. Ponge, D. Raabe, Grain boundary segregation engineering and austenite reversion turn embrittlement into toughness: Example of a 9wt.% medium Mn steel, *Acta Materialia* 86 (2015) 182-192.
- [79] M. Herbig, D. Raabe, Y.J. Li, P. Choi, S. Zaeferrer, S. Goto, Atomic-scale quantification of grain boundary segregation in nanocrystalline material, *Phys Rev Lett* 112(12) (2014) 126103.
- [80] M. Herbig, M. Kuzmina, C. Haase, R.K.W. Marceau, I. Gutierrez-Urrutia, D. Haley, D.A. Molodov, P. Choi, D. Raabe, Grain boundary segregation in Fe–Mn–C twinning-induced plasticity steels studied by correlative electron backscatter diffraction and atom probe tomography, *Acta Materialia* 83 (2015) 37-47.
- [81] X. Sauvage, F. Cuvilly, A. Russell, K. Edalati, Understanding the role of Ca segregation on thermal stability, electrical resistivity and mechanical strength of nanostructured aluminum, *Materials Science and Engineering: A* 798 (2020).
- [82] T. Masuda, X. Sauvage, S. Hirosawa, Z. Horita, Achieving highly strengthened Al–Cu–Mg alloy by grain refinement and grain boundary segregation, *Materials Science and Engineering: A* 793 (2020).
- [83] Z. Feng, X. Luo, Y. Chen, N. Chen, G. Wu, Surface severe plastic deformation induced solute and precipitate redistribution in an Al-Cu-Mg alloy, *Journal of Alloys and Compounds* 773 (2019) 585-596.
- [84] A. Devaraj, W. Wang, R. Vemuri, L. Kovarik, X. Jiang, M. Bowden, J.R. Trelewicz, S. Mathaudhu, A. Rohatgi, Grain boundary segregation and intermetallic precipitation in coarsening resistant nanocrystalline aluminum alloys, *Acta Materialia* 165 (2019) 698-708.

- [85] N. Zhang, K.K. Wen, T.T. Yang, P. Jia, X.C. Cai, C.C. Du, J.K. Yu, B.R. Sun, T.D. Shen, Grain boundary status dependent mechanical property of annealed nanocrystalline Ni(Fe) alloy, *Journal of Materials Research and Technology* (2022).
- [86] M. Liu, W. Liu, X. He, Y. Gao, R. Liu, X. Zhou, Defects evolution and element segregation of Ni-Mo-Cr alloy irradiated by 30 keV Ar ions, *Nuclear Engineering and Technology* 52(8) (2020) 1749-1755.
- [87] D.H. Ping, Y.F. Gu, C.Y. Cui, H. Harada, Grain boundary segregation in a Ni–Fe-based (Alloy 718) superalloy, *Materials Science and Engineering: A* 456(1-2) (2007) 99-102.
- [88] D. Tytko, P.-P. Choi, J. Klöwer, A. Kostka, G. Inden, D. Raabe, Microstructural evolution of a Ni-based superalloy (617B) at 700°C studied by electron microscopy and atom probe tomography, *Acta Materialia* 60(4) (2012) 1731-1740.
- [89] C. He, Z. Li, H. Chen, N. Wilson, J.F. Nie, Unusual solute segregation phenomenon in coherent twin boundaries, *Nature communications* 12(1) (2021) 722.
- [90] X.-F. Gu, T. Furuhashi, L. Chen, P. Yang, Study on the planar segregation of solute atoms in Mg-Al-Gd alloy, *Scripta Materialia* 150 (2018) 45-49.
- [91] H. Somekawa, H. Watanabe, D.A. Basha, A. Singh, T. Inoue, Effect of twin boundary segregation on damping properties in magnesium alloy, *Scripta Materialia* 129 (2017) 35-38.
- [92] Z. Yang, M.F. Chisholm, G. Duscher, X. Ma, S.J. Pennycook, Direct observation of dislocation dissociation and Suzuki segregation in a Mg–Zn–Y alloy by aberration-corrected scanning transmission electron microscopy, *Acta Materialia* 61(1) (2013) 350-359.
- [93] M. Bugnet, A. Kula, M. Niewczas, G.A. Botton, Segregation and clustering of solutes at grain boundaries in Mg–rare earth solid solutions, *Acta Materialia* 79 (2014) 66-73.
- [94] M. Ghazisaeidi, L.G. Hector, W.A. Curtin, Solute strengthening of twinning dislocations in Mg alloys, *Acta Materialia* 80 (2014) 278-287.
- [95] J.P. Hadorn, T.T. Sasaki, T. Nakata, T. Ohkubo, S. Kamado, K. Hono, Solute clustering and grain boundary segregation in extruded dilute Mg–Gd alloys, *Scripta Materialia* 93 (2014) 28-31.
- [96] L. Huber, J. Rottler, M. Militzer, Atomistic simulations of the interaction of alloying elements with grain boundaries in Mg, *Acta Materialia* 80 (2014) 194-204.

- [97] Z.R. Zeng, Y.M. Zhu, S.W. Xu, M.Z. Bian, C.H.J. Davies, N. Birbilis, J.F. Nie, Texture evolution during static recrystallization of cold-rolled magnesium alloys, *Acta Materialia* 105 (2016) 479-494.
- [98] C.D. Barrett, A. Imandoust, H. El Kadiri, The effect of rare earth element segregation on grain boundary energy and mobility in magnesium and ensuing texture weakening, *Scripta Materialia* 146 (2018) 46-50.
- [99] T.T.T. Trang, J.H. Zhang, J.H. Kim, A. Zargaran, J.H. Hwang, B.C. Suh, N.J. Kim, Designing a magnesium alloy with high strength and high formability, *Nature communications* 9(1) (2018).
- [100] Z.R. Zeng, Y.M. Zhu, R.L. Liu, S.W. Xu, C.H.J. Davies, J.F. Nie, N. Birbilis, Achieving exceptionally high strength in Mg₃Al₁₁Zn-0.3Mn extrusions via suppressing intergranular deformation, *Acta Materialia* 160 (2018) 97-108.
- [101] A.A. Kaya, A Review on Developments in Magnesium Alloys, *Frontiers in Materials* 7 (2020).
- [102] M. Bian, X. Huang, Y. Chino, Solute segregation assisted grain boundary precipitation and its impact to ductility of a precipitation-hardenable magnesium alloy, *Materials Science and Engineering: A* 819 (2021).
- [103] J. Messina, R. Luo, K. Xu, G. Lu, H. Deng, M.A. Tschopp, F. Gao, Machine learning to predict aluminum segregation to magnesium grain boundaries, *Scripta Materialia* 204 (2021).
- [104] R. Pei, Y. Zou, D. Wei, T. Al-Samman, Grain boundary co-segregation in magnesium alloys with multiple substitutional elements, *Acta Materialia* 208 (2021).
- [105] Z.-M. Hua, M. Zha, Z.-Y. Meng, S.-B. Jin, G. Sha, T.-S. Wang, C. Wang, H.-L. Jia, Y. Gao, H.-Y. Wang, Rapid dislocation-mediated solute repartitioning towards strain-aging hardening in a fine-grained dilute magnesium alloy, *Materials Research Letters* 10(1) (2022) 21-28.
- [106] Z. Zhang, J. Zhang, J. Xie, S. Liu, Y. He, R. Wang, D. Fang, W. Fu, Y. Jiao, R. Wu, Significantly enhanced grain boundary Zn and Ca co-segregation of dilute Mg alloy via trace Sm addition, *Materials Science and Engineering: A* 831 (2022).
- [107] Z. Wang, M. Saito, K.P. McKenna, L. Gu, S. Tsukimoto, A.L. Shluger, Y. Ikuhara, Atom-resolved imaging of ordered defect superstructures at individual grain boundaries, *Nature* 479(7373) (2011) 380-3.

- [108] J. Zhang, Y. Dou, Y. Zheng, Twin-boundary segregation energies and solute-diffusion activation enthalpies in Mg-based binary systems: A first-principles study, *Scripta Materialia* 80 (2014) 17-20.
- [109] Z. Pei, R. Li, J.-F. Nie, J.R. Morris, First-principles study of the solute segregation in twin boundaries in Mg and possible descriptors for mechanical properties, *Materials & Design* 165 (2019) 107574.
- [110] D. Zhao, Y. Li, Revealing the factors influencing grain boundary segregation of P, As in Si: Insights from first-principles, *Acta Materialia* 168 (2019) 52-62.
- [111] S. Fabris, C. Elsässer, First-principles analysis of cation segregation at grain boundaries in α -Al₂O₃, *Acta Materialia* 51(1) (2003) 71-86.
- [112] D. Zhao, Y. Li, Carbon segregation at $\Sigma 3 \{112\}$ grain boundaries in silicon, *Computational Materials Science* 143 (2018) 80-86.
- [113] L. Huber, R. Hadian, B. Grabowski, J. Neugebauer, A machine learning approach to model solute grain boundary segregation, *npj Computational Materials* 4(1) (2018) 64.
- [114] R. Tran, Z. Xu, N. Zhou, B. Radhakrishnan, J. Luo, S.P. Ong, Computational study of metallic dopant segregation and embrittlement at molybdenum grain boundaries, *Acta Materialia* 117 (2016) 91-99.
- [115] M.A. Gibson, C.A. Schuh, Segregation-induced changes in grain boundary cohesion and embrittlement in binary alloys, *Acta Materialia* 95 (2015) 145-155.
- [116] R. Sandström, C.M. Lousada, The role of binding energies for phosphorus and sulphur at grain boundaries in copper, *Journal of Nuclear Materials* 544 (2021).
- [117] G.H. Huang, D.D. Yin, J.W. Lu, H. Zhou, Y. Zeng, G.F. Quan, Q.D. Wang, Microstructure, texture and mechanical properties evolution of extruded fine-grained Mg-Y sheets during annealing, *Materials Science and Engineering: A* 720 (2018) 24-35.
- [118] L.R. Xiao, X.F. Chen, Y. Cao, H. Zhou, X.L. Ma, D.D. Yin, B. Ye, X.D. Han, Y.T. Zhu, Solute segregation assisted nanocrystallization of a cold-rolled Mg–Ag alloy during annealing, *Scripta Materialia* 177 (2020) 69-73.
- [119] Z. Zhang, J. Zhang, J. Xie, S. Liu, Y. He, K. Guan, R. Wu, Developing a low-alloyed fine-grained Mg alloy with high strength-ductility based on dislocation evolution and grain boundary segregation, *Scripta Materialia* 209 (2022) 114414.

- [120] H. Dieringa, Y. Huang, P. Wittke, M. Klein, F. Walther, M. Dikovits, C. Poletti, Compression-creep response of magnesium alloy DieMag422 containing barium compared with the commercial creep-resistant alloys AE42 and MRI230D, *Materials Science and Engineering: A* 585 (2013) 430-438.
- [121] C. Xu, T. Nakata, G.H. Fan, X.W. Li, G.Z. Tang, S. Kamado, Enhancing strength and creep resistance of Mg–Gd–Y–Zn–Zr alloy by substituting Mn for Zr, *Journal of Magnesium and Alloys* 7(3) (2019) 388-399.
- [122] K. Li, Q. Huo, Y. Zhang, C. Zhang, W. Huang, Y. Ye, A. Hashimoto, X. Yang, Effects of aging on the creep properties of hot-compressed Mg-2.5 wt%Nd binary alloy, *Materials Science and Engineering: A* 771 (2020) 138618.
- [123] J.W. Gibbs, *The Collected Works of J. Willard Gibbs*, Yale University Press, London, 1948, p. 461.
- [124] D. McLean, *Grain boundaries in metals*, Oxford University Press, London, 1957.
- [125] M.A. Gibson, C.A. Schuh, A survey of ab-initio calculations shows that segregation-induced grain boundary embrittlement is predicted by bond-breaking arguments, *Scripta Materialia* 113 (2016) 55-58.
- [126] P. Lejček, M. Šob, V. Paidar, Interfacial segregation and grain boundary embrittlement: An overview and critical assessment of experimental data and calculated results, *Progress in Materials Science* 87 (2017) 83-139.
- [127] B.D. Snow, D.D. Doty, O.K. Johnson, A Simple Approach to Atomic Structure Characterization for Machine Learning of Grain Boundary Structure-Property Models, *Frontiers in Materials* 6 (2019).
- [128] T.A. Sharp, S.L. Thomas, E.D. Cubuk, S.S. Schoenholz, D.J. Srolovitz, A.J. Liu, Machine learning determination of atomic dynamics at grain boundaries, *Proc Natl Acad Sci* (2018).
- [129] Q. Zhu, A. Samanta, B. Li, R.E. Rudd, T. Frolov, Predicting phase behavior of grain boundaries with evolutionary search and machine learning, *Nature communications* 9(1) (2018) 467.
- [130] C.L. White, W.A. Coghlan, The spectrum of binding energies approach to grain boundary segregation, *Metallurgical Transactions A* 8(9) (1977) 1403-1412.
- [131] M. Yamaguchi, M. Shiga, H. Kaburaki, Grain Boundary Decohesion by Impurity Segregation in a Nickel-Sulfur System, *Science* 307 (2005) 393-397.

- [132] A.R. Miedema, Surface Segregation in Alloys of Transition Metals %J International Journal of Materials Research, 69(7) (1978) 455-461.
- [133] E.R. Homer, D.M. Hensley, C.W. Rosenbrock, A.H. Nguyen, G.L.W. Hart, Machine-Learning Informed Representations for Grain Boundary Structures, *Frontiers in Materials* 6 (2019).
- [134] H.-T. Ma, R. Yuan, Y.-P. Xie, H. Gao, L.-J. Hu, X.-D. Li, Y.-C. Qian, Z.-H. Dai, The role of Ag, Ca, Zr and Al in strengthening effects of ZK series alloys by altering G.P. zones stability, *Acta Materialia* 147 (2018) 42-50.
- [135] C. Varvenne, G.P.M. Leyson, M. Ghazisaeidi, W.A. Curtin, Solute strengthening in random alloys, *Acta Materialia* 124 (2017) 660-683.
- [136] S. Sandlöbes, M. Friák, S. Zaefferer, A. Dick, S. Yi, D. Letzig, Z. Pei, L.F. Zhu, J. Neugebauer, D. Raabe, The relation between ductility and stacking fault energies in Mg and Mg–Y alloys, *Acta Materialia* 60(6-7) (2012) 3011-3021.
- [137] S. Sandlöbes, S. Zaefferer, I. Schestakow, S. Yi, R. Gonzalez-Martinez, On the role of non-basal deformation mechanisms for the ductility of Mg and Mg–Y alloys, *Acta Materialia* 59(2) (2011) 429-439.
- [138] S. Sandlöbes, I. Schestakow, S.B. Yi, S. Zaefferer, J.Q. Chen, M. Friák, J. Neugebauer, D. Raabe, The Relation between Shear Banding, Microstructure and Mechanical Properties in Mg and Mg-Y Alloys, *Materials Science Forum* 690 (2011) 202-205.
- [139] N. Stanford, D. Atwell, A. Beer, C. Davies, M.R. Barnett, Effect of microalloying with rare-earth elements on the texture of extruded magnesium-based alloys, *Scripta Materialia* 59(7) (2008) 772-775.
- [140] K. Wei, L. Xiao, B. Gao, L. Li, Y. Liu, Z. Ding, W. Liu, H. Zhou, Y. Zhao, Enhancing the strain hardening and ductility of Mg-Y alloy by introducing stacking faults, *Journal of Magnesium and Alloys* 8(4) (2020) 1221-1227.
- [141] S. Sandlöbes, M. Friák, J. Neugebauer, D. Raabe, Basal and non-basal dislocation slip in Mg–Y, *Materials Science and Engineering: A* 576 (2013) 61-68.
- [142] S. Sandlöbes, Z. Pei, M. Friák, L.F. Zhu, F. Wang, S. Zaefferer, D. Raabe, J. Neugebauer, Ductility improvement of Mg alloys by solid solution: Ab initio modeling, synthesis and mechanical properties, *Acta Materialia* 70 (2014) 92-104.

- [143] D. Zhang, L. Jiang, J.M. Schoenung, S. Mahajan, E.J. Lavernia, TEM study on relationship between stacking faults and non-basal dislocations in Mg, *Philosophical Magazine* 95(34) (2015) 3823-3844.
- [144] N. Miyazawa, S. Suzuki, M. Mabuchi, Y. Chino, An atomistic study of Y segregation at a {10-11}–{10-12} double twin in Mg, *AIP Advances* 7(3) (2017) 035308.
- [145] N. Miyazawa, S. Suzuki, M. Mabuchi, Y. Chino, Atomic simulations of the effect of Y and Al segregation on the boundary characteristics of a double twin in Mg, *Journal of Applied Physics* 122(16) (2017) 165103.
- [146] T. Yoshida, M. Yuasa, M. Mabuchi, Y. Chino, Effect of segregated elements on the interactions between twin boundaries and screw dislocations in Mg, *Journal of Applied Physics* 118(3) (2015) 034304.
- [147] M. Yuasa, K. Masunaga, M. Mabuchi, Y. Chino, Interaction mechanisms of screw dislocations with and twin boundaries in Mg, *Philosophical Magazine* 94(3) (2014) 285-305.
- [148] M. Yuasa, K. Masunaga, T. Yoshida, M. Mabuchi, Y. Chino, Interactions of a screw dislocation with a {10-11}–{10-12} double twin in Mg, *Acta Materialia* 61(13) (2013) 4714-4725.

Chapter 3: Methodology

Traditionally the materials science research relies on the two pillars of experimentation and theoretical modeling. With the fast growth of computational power and advancement of simulation techniques, computational simulations emerge as the third pillar indispensable for modern materials research. Many microstructural ingredients and the complexity of possible interaction phenomena among the various lattice defects have to be considered in material research, which often brings redundant work to experimental scientists. Thanks to modern high-performance computers, modelling and simulation can deal with a vast number of similar simulations, providing an efficient pathway for predicting material properties and offering fundamental insights into materials. In addition, one aspect computational simulations often outshine the other two research pillars is the capability to probe phenomena at small scales, i.e., sub-micro, nano or even atomic scales, where the most fundamental physical mechanisms and structure-property relationships reside. Such capability is of particular relevance to this thesis work, as it aims to reveal the fundamental deformation mechanisms in Mg alloys at the dislocation and twin boundary levels.

The set of computational simulations to achieve such small-scale resolution are generally referred to as atomistic simulations. In this work, two atomistic simulation techniques were employed, namely first principles calculations based on DFT and the classical MD simulations, as already briefly mentioned in the Introduction Chapter. Together they offer calculation of solute segregation energy and reveal dynamic mechanism of twinning and dislocation at atomic scale.

Below these two simulation techniques, first-principles DFT and MD, are briefly described. More specific technical details are also available in individual chapters after. In addition, the Voronoi tessellation technique and some dislocation mechanics are also introduced due to the construction of simulation models in current thesis.

3.1 First Principles DFT Calculations

DFT based first principles calculations is presently the most successful and promising approach to compute the electronic structure of matter, providing a “standard tool” for diverse materials modeling problems in physics, chemistry, materials science, and multiple branches of engineering. The following is a brief overview of first principles method, whose details can be found in various literatures [1-6].

Theoretically, the quantum mechanical behavior of particles can be described by the many-body Schrödinger equation—more precisely, the time independent, nonrelativistic Schrödinger equation, by defining their relative wave functions, from which the total energy can be determined. The equation (in atomic units) is shown as,

$$\hat{H}\Psi = E\Psi \quad (3.1)$$

where, Ψ is the wave function, E the total energy of the system and \hat{H} the Hamiltonian operator of a system consisting of M nuclei and N electrons given by,

$$\hat{H} = -\frac{1}{2} \sum_{i=1}^N \nabla_i^2 - \frac{1}{2} \sum_{A=1}^M \frac{1}{M_A} \nabla_A^2 - \sum_{i=1}^N \sum_{A=1}^M \frac{Z_A}{r_{iA}} + \sum_{i=1}^N \sum_{j>i}^N \frac{1}{r_{ij}} + \sum_{A=1}^M \sum_{B>A}^M \frac{Z_A Z_B}{R_{AB}} \quad (3.2)$$

The first two terms represent the kinetic energy of the electrons and nuclei. The other three terms describe the attractive electrostatic interaction between the nuclei and the electrons and repulsive potential due to the electron-electron and nucleus-nucleus interactions.

Based on Born-Oppenheimer approximation [7], the nuclei move much slower than the electrons because of their large mass difference, so the electrons can be considered as moving around the fixed nuclei. Therefore, the nuclear kinetic energy is zero and their potential energy is approximate a constant and the electronic Hamiltonian reduces to,

$$\hat{H}_{\text{elec}} = -\frac{1}{2} \sum_{i=1}^N \nabla_i^2 - \sum_{i=1}^N \sum_{A=1}^M \frac{Z_A}{r_{iA}} + \sum_{i=1}^N \sum_{j>i}^N \frac{1}{r_{ij}} = \hat{T} + \hat{V}_{\text{Ne}} + \hat{V}_{\text{ee}} \quad (3.3)$$

Then, the solution of the Schrödinger equation with \hat{H}_{elec} is the electronic wave function Ψ_{elec} and the electronic energy E_{elec} . The total energy E_{tot} is then the sum of E_{elec} and the constant nuclear repulsion term E_{nuc} ,

$$\hat{H}_{\text{elec}} \Psi_{\text{elec}} = E_{\text{elec}} \Psi_{\text{elec}} \quad (3.4)$$

$$E_{\text{tot}} = E_{\text{elec}} + E_{\text{nuc}} \quad (3.5)$$

where,

$$E_{\text{nuc}} = \sum_{A=1}^M \sum_{B>A}^M \frac{Z_A Z_B}{R_{AB}} \quad (3.6)$$

Following the Hohenberg-Kohn-Sham theorem [1], \hat{H} is a unique functional of the electron density $\rho(\mathbf{r})$ and thus the total energy, $E[\rho(\mathbf{r})]$ is determined by the electron density alone. The functional is proposed by Kohn and Sham [4] shown as,

$$E[\rho(\vec{r})] = T[\rho(\vec{r})] + E_{\text{ext}}[\rho(\vec{r})] + E_{\text{Hartree}}[\rho(\vec{r})] + E_{\text{xc}}[\rho(\vec{r})] \quad (3.7)$$

where $T[\rho(\vec{r})]$ is the kinetic energy of a non-interacting electron gas, $E_{\text{ext}}[\rho(\vec{r})]$ the energy arising from ion-electron interaction and $E_{\text{Hartree}}[\rho(\vec{r})]$ the interaction energy of electrons. $E_{\text{xc}}[\rho(\vec{r})]$ is the exchange and correlation energy and it can be solved by using the Local Density Approximation (LDA) or Generalized Gradient Approximation (GGA). The DFT based Kohn-Sham equation becomes a useful and reliable technique to solve many-body electron problems in chemistry, physics and materials science [3, 5, 6].

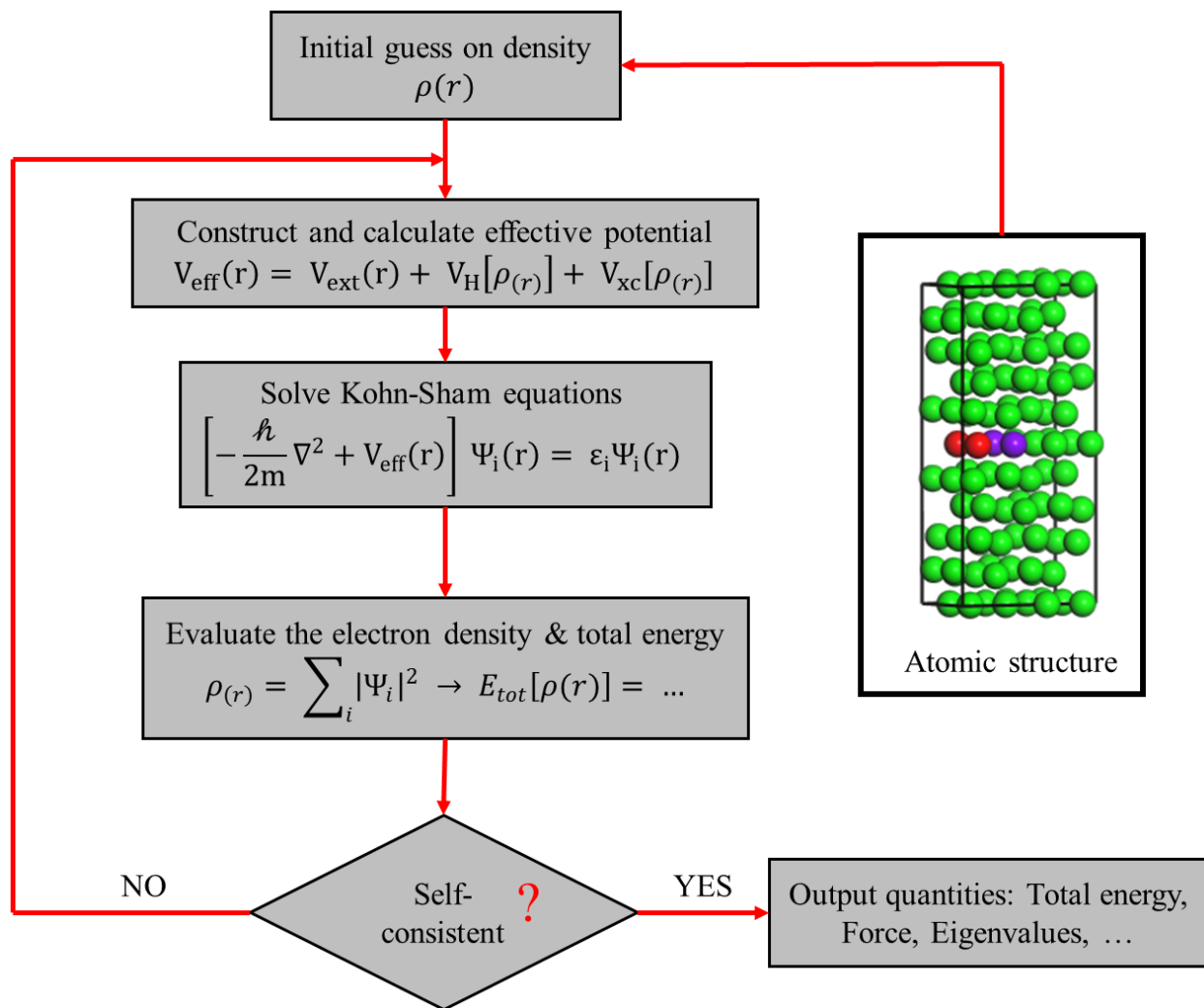


Figure 3.1. A flow chart illustrating the iteration scheme of electronic structure calculations based on DFT.

Figure 3.1 shows a flow diagram of a typical DFT calculation. At first, an initial guess for the electron density is assumed, which is required for the calculation of $V_{\text{eff}}(r)$, the diagonalization of the Kohn-Sham equations, and the subsequent evaluation of $\rho(r)$ along with E_{tot} . If the convergence criterion is not fulfilled, the numerical procedure will be continued with the last $\rho(r)$ instead of the initial guess. When the criterion is satisfied, various output quantities such as total energy, force, atomic position etc. are computed and output.

In this thesis, DFT calculations were performed based on a commercial code, Vienna Ab-initio Simulation Package (VASP) [4, 5]. The generalized gradient approximation (GGA) of Perdew-Burke-Ernzerhof (PBE) based on plane-wave basis sets was employed to describe the exchange-correlation interaction. The projector-augmented wave (PAW) method was used to describe the electron-ion interactions. The first principles calculations can accurately calculate the interaction energy between Mg and different solutes at grain boundaries, providing a clear energetic map at the atomic scale for identifying promising solutes for the design of novel Mg alloys.

3.2 Molecular Dynamics Simulation

Unlike quantum mechanics (QM) that aims to solve many-body interactions upon electron wave function, classical mechanics (CM) abstracts away the variance of electronic band structure and depicts an atom to be an independent object of fixed mass. In MD simulation, the atom is treated as a collection of interacting classical particles. This reduces the computational cost associated with the motion of individual electrons and interactions between electrons which should be considered in the first-principles calculations. As a result, a larger system including tens of millions of atoms can be studied by MD.

The motions of atoms in MD can be described by Newton's equation of motion,

$$\mathbf{f}_i = m_i \mathbf{a}_i \quad (3.8)$$

Here, \mathbf{f}_i is the force acting on the atom, m_i is the atom mass and \mathbf{a}_i is its acceleration. In addition, according to the classical Hamiltonian equation of motion [8], the Hamiltonian \mathbf{H} is defined as a function of the momentum \mathbf{p}_i and position coordinates \mathbf{r}_i ,

$$\mathbf{H}(\mathbf{p}_i, \mathbf{r}_i) = \sum_{i=1}^N \frac{\mathbf{p}_i^2}{2m_i} + V(\mathbf{r}_i) \quad (3.9)$$

The first and second terms on the right represent the kinetic and potential energy, respectively. Due to the conservation of force field acting on the system, \mathbf{f}_i can be calculated as the derivative of the potential energy with respect to the position of the particle, \mathbf{r}_i ,

$$\mathbf{f}_i = m_i \mathbf{a}_i = -\nabla V_i = -\frac{dE}{d\mathbf{r}_i} \quad (3.10)$$

To calculate the potential energy E, many functional forms of the potentials have been developed. The embedded atom method (EAM) based potential is the most widely used potential for simulating metallic materials due to the accurate description of the atomic interactions. The functional form of the EAM potential is expressed as [9],

$$U = \sum_i F(\rho_i) + \sum_{i \neq j} \varphi(r_{ij}) \quad (3.11)$$

Here, F is the embedding function that can be calculated by the electron density ρ_i ($\rho_i = \sum_{j, i \neq j} \rho_{ij}(r_{ij})$) and $\varphi(r_{ij})$ is a pair potential accounting for the nuclei interactions. $\varphi(r_{ij})$ can be obtained via fitting experimental data and has a functional form of [10],

$$\varphi(r_{ij}) = \frac{1}{4\pi\epsilon_0} \frac{Z_{i,eff} Z_{j,eff}}{r_{ij}} \quad (3.12)$$

ρ_i can be obtained ab initio calculations.

Once forces are calculated from atom positions and empirical potentials, we can integrate Newton's equation of motion on atoms, and the most common integration method is the so-called Verlet algorithm [11]. The algorithm begins with a Taylor expansion of the coordinate of an atom around time t,

$$\mathbf{r}_i(t + \Delta t) = \mathbf{r}_i(t) + \mathbf{v}_i(t)\Delta t + \frac{\mathbf{f}_i}{2m} \Delta t^2 + \frac{\Delta t^3}{3!} \frac{\delta^3 \mathbf{r}_i(t)}{\delta t^3} + O(\delta t^3) \quad (3.13)$$

similarly,

$$\mathbf{r}_i(t - \Delta t) = \mathbf{r}_i(t) + \mathbf{v}_i(t)\Delta t + \frac{\mathbf{f}_i}{2m}\Delta t^2 + \frac{\Delta t^3}{3!} \frac{\delta^3 \mathbf{r}_i(t)}{\delta t^3} + O(\delta t^3) \quad (3.14)$$

Summing these two equations, we obtain atom position in next time step,

$$\mathbf{r}_i(t + \Delta t) \approx 2\mathbf{r}_i(t) - \mathbf{r}_i(t - \Delta t) + \frac{\mathbf{f}_i}{m}\Delta t^2 \quad (3.15)$$

and the velocity,

$$\mathbf{v}_i(t) = \frac{\mathbf{r}_i(t + \Delta t) - \mathbf{r}_i(t - \Delta t)}{2\Delta t} + O(\Delta t^2) \quad (3.16)$$

After each step, the current temperature, potential energy and the total energy can be calculated.

Figure 3.2 shows the general workflow of MD with the Verlet algorithm. The forces are calculated by setting the initial atomic position, velocities and the provided interatomic potential. Positions are advanced to the lower energy state via a small-time interval, generating the new position and velocities. The above steps are repeated with these new data until an equilibrium is reached.

For an atomistic simulation, it is very important to select an appropriate statistical ensemble for regulating a confined system of atoms. An ensemble depends on macroscopically observable variables such as volume (V), pressure (P), temperature (T) and energy (E) etc. There are three important thermodynamic ensembles [12]:

- 1) A microcanonical ensemble (NVE ensemble) keeps micro-states quantities constant, i.e., the number of particles in the system (N), the volume of the system (V), and the total energy of the system (E) so that no particles and energy exchange with the environment of an isolated system.
- 2) A canonical ensemble (NVT ensemble) where the number of particles (N) in the system, the volume of the system (V), and the temperature of the system (T) are constant, describes a closed system in thermal equilibrium with a constant-temperature heat bath.

3) A grand canonical ensemble (μVT ensemble) describes an open system in thermal and chemical equilibrium with a reservoir. μVT refer to the constant values of the chemical potential of particles in the system (μ), the volume of the system (V), and the temperature of the system (T).

In this thesis, all MD simulations were performed using an open source software LAMMPS [13] and several reliable EAM potentials were selected for the simulations. LAMMPS is a versatile and widely adopted tool for running simulations for large complicate systems. It provides a range of material properties and helps us to understand the atomic mechanism of different dynamic processes. Specifically, large-scale MD simulations were carried out to deform Mg polycrystals and thus twin related events such as twin variant selection, nucleation and growth, twinning interface disconnections as well as solute effect on activity of dislocations were carefully investigated.

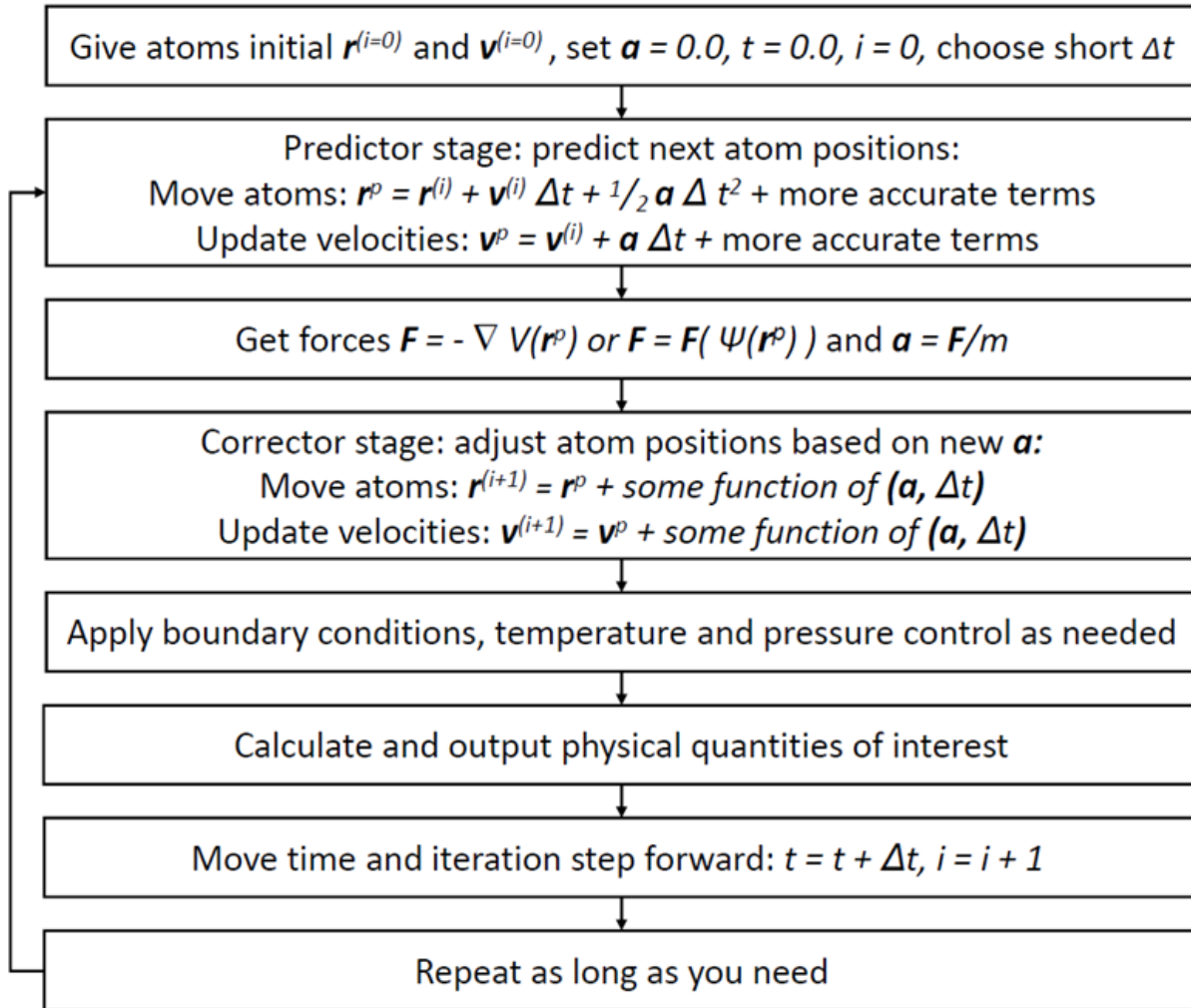


Figure 3.2. A schematic of the molecular dynamics simulation algorithm.

3.3 Voronoi Tessellation Technique

In current thesis, polycrystalline Mg microstructures have to be constructed for a large-scale classic MD simulation. The well-known Voronoi tessellation technique is regularly used for constructing such polycrystals [14-16]. Here, a brief introduction of this technique is presented.

As shown in **Figure 3.3(a)** and (b), a discrete set of particles are given in two- and three-dimensional systems. The collection of all Voronoi cells of these particles is therefore termed as the Voronoi tessellation. Generally, the Voronoi cell of a particle s_i is defined as the set,

$$V(s_i) = \{x \in M | d(x, s_i) \leq d(x, s_j), i \neq j\} \quad (3.17)$$

where M is a two- or three-dimensional space and the metric d is the standard Euclidean one, the set of particle positions $\{s_i\} \subset M$. The Voronoi cells are convex polygons in two dimensions as shown in **Figure 3.3(a)** while in three dimensions, they are convex polyhedral as shown in **Figure 3.3(b)**. As shown in **Figure 3.3**, the Voronoi cells have different numbers of edges and faces, as well as different areas and volumes. The construction of polycrystals can be performed by filling crystal atoms into the partitions and the resulting polycrystals will consist of grains with different size and shapes.

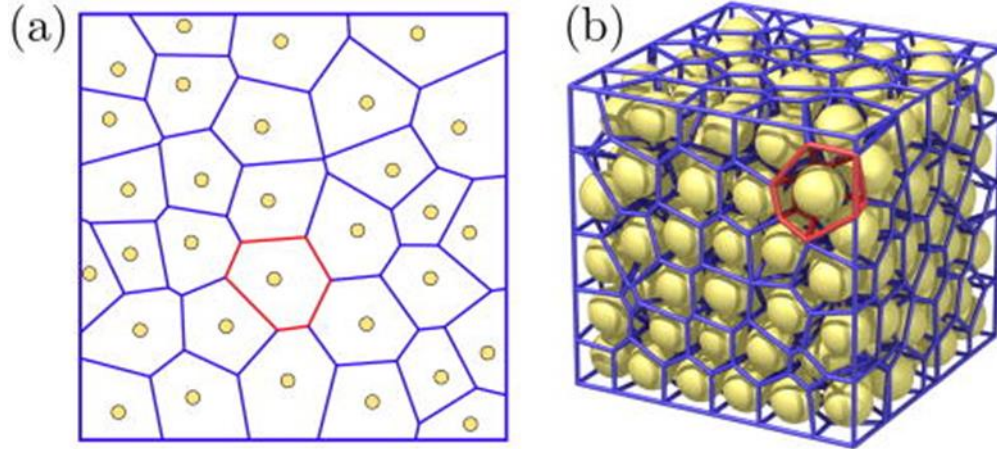


Figure 3.3. a) Voronoi tessellation in two dimensions. (b) Three-dimensional Voronoi tessellation for a set of particles shown as yellow spheres. The blue lines show the entire Voronoi tessellation, while the red lines highlight a single Voronoi cell as a convex polyhedron [14]. [Figure adapted with permissions]

Figure 3.4 shows a general procedure to construct polycrystals by using a Voronoi tessellation and details are listed as following:

- (a) Choose the size of simulation box and introduce nodes (black dots) given positions.
- (b) Link the nodes with their neighbors (red lines) and periodic boundary conditions are employed.
- (c) Obtain the normal (blue lines) to the linking lines. These blue lines define the future GBs.
- (d) Replace the nodes with unit cells which have been set different crystal orientations.

(e) Expand each unit cell in the three directions of space and remove atoms that are outside of the grains.

(f) After all cells have been expanded and cut inside their respective grains, one obtains the final polycrystal.

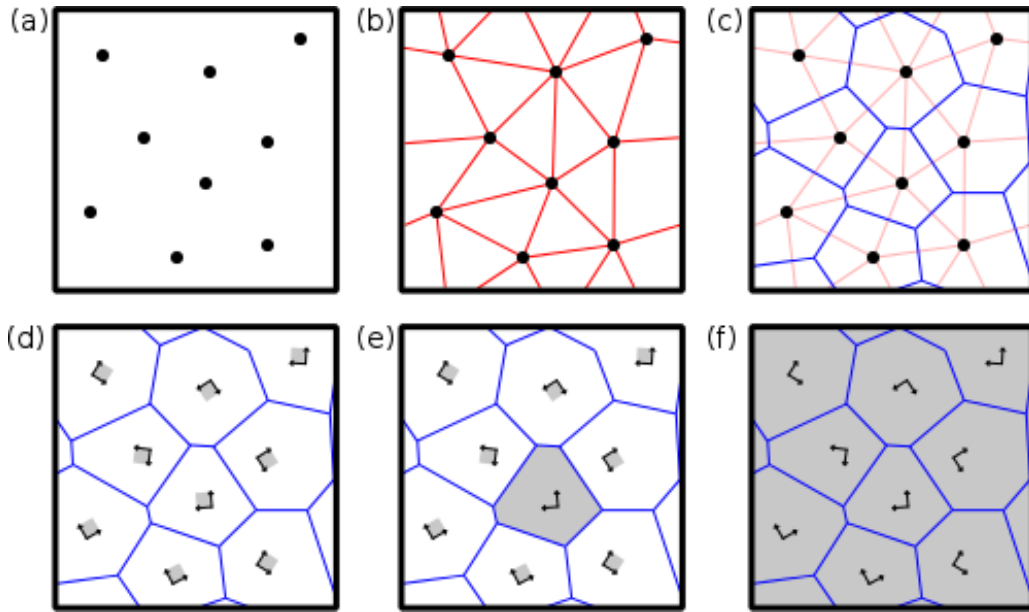


Figure 3.4. Illustration of using a Voronoi tessellation to construct polycrystals [16]. [Figure adapted with permissions]

In this thesis, the polycrystalline Mg, Mg-Al and Mg-Y alloy systems were built using Voronoi tessellation technique for the investigation of twinning mechanism in Mg polycrystal and solute effect on modification of deformation modes in Mg-RE alloys using atomistic simulations implemented by LAMMPS.

3.4 Dislocation Mechanics

The solute defect on critical shear stress of dislocations was examined in detail using atomistic simulations implemented by LAMMPS in the current thesis. Therefore, the displacement field of edge dislocations were used to generate the initial dislocation structures by displacing two half

crystals. In Cartesian coordinates, the displacement field corresponding to edge dislocations can be written in the following forms [17],

$$u_x = \frac{b}{2\pi} \left[\tan^{-1} \frac{y}{x} + \frac{xy}{2(1+\nu)(x^2+y^2)} \right] \quad (3.18)$$

$$u_y = -\frac{b}{2\pi} \left[\frac{1-2\nu}{4(1-\nu)} \ln(x^2+y^2) + \frac{x^2-y^2}{4(1-\nu)(x^2+y^2)} \right] \quad (3.19)$$

or expressed in the polar coordinates,

$$u_\theta = \frac{b}{2\pi} \left[-\frac{1-2\nu}{2(1-\nu)} \sin\theta \ln r + \frac{\sin\theta}{4(1-\nu)} + \theta \cos\theta \right] \quad (3.20)$$

$$u_r = \frac{b}{2\pi} \left[-\frac{1-2\nu}{2(1-\nu)} \cos(\theta) \ln r - \frac{\cos\theta}{4(1-\nu)} + \theta \sin\theta \right] \quad (3.21)$$

where b and ν represent the Burger's vector and Poisson's ratio, respectively.

In this thesis, three common edge dislocations on basal, prismatic and pyramidal planes, respectively, were considered in the calculation of critical shear stress by performing MD simulations on LAMMPS.

3.5 References

- [1] P. Hohenberg, W. Kohn, Inhomogeneous Electron Gas, *Physical Review* 136(3B) (1964) B864-B871.
- [2] R.O. Jones, O. Gunnarsson, The density functional formalism, its applications and prospects, *Reviews of Modern Physics* 61(3) (1989) 689-746.
- [3] W. Koch, M.C. Holthausen, *A Chemist's Guide to Density Functional Theory*, 2001.
- [4] W. Kohn, L.J. Sham, Self-Consistent Equations Including Exchange and Correlation Effects, *Physical Review* 140(4A) (1965) A1133-A1138.
- [5] D.S. SHOLL, J.A. STECKEL, *Density functional theory: a practical introduction*, 2009.
- [6] W. Kohn, Overview of Density Functional Theory, in: E.K.U. Gross, R.M. Dreizler (Eds.), *Density Functional Theory*, Springer US, Boston, MA, 1995, pp. 3-10.
- [7] R. Car, M. Parrinello, Unified approach for molecular dynamics and density-functional theory, *Physical Review Letters* 55(22) (1985) 2471-2474.

- [8] K. Zhou, B. Liu, Chapter 1 - Fundamentals of classical molecular dynamics simulation, in: K. Zhou, B. Liu (Eds.), *Molecular Dynamics Simulation*, Elsevier 2022, pp. 1-40.
- [9] M.S. Daw, M.I. Baskes, Embedded-atom method: Derivation and application to impurities, surfaces, and other defects in metals, *Physical Review B* 29(12) (1984) 6443-6453.
- [10] M.S. Daw, S.M. Foiles, M.I. Baskes, The embedded-atom method: a review of theory and applications, *Materials Science Reports* 9(7) (1993) 251-310.
- [11] D. Frenkel, B. Smit, Chapter 4 - Molecular Dynamics Simulations, in: D. Frenkel, B. Smit (Eds.), *Understanding Molecular Simulation (Second Edition)*, Academic Press, San Diego, 2002, pp. 63-107.
- [12] R.K. Pathria, *Statistical mechanics*, Elsevier 2016.
- [13] A.P. Thompson, H.M. Aktulga, R. Berger, D.S. Bolintineanu, W.M. Brown, P.S. Crozier, P.J. in 't Veld, A. Kohlmeyer, S.G. Moore, T.D. Nguyen, R. Shan, M.J. Stevens, J. Tranchida, C. Trott, S.J. Plimpton, LAMMPS - a flexible simulation tool for particle-based materials modeling at the atomic, meso, and continuum scales, *Computer Physics Communications* 271 (2022).
- [14] E.A. Lazar, J. Lu, C.H. Rycroft, Voronoi cell analysis: The shapes of particle systems, *American Journal of Physics* 90(6) (2022) 469-480.
- [15] V. Lucarini, Three-Dimensional Random Voronoi Tessellations: From Cubic Crystal Lattices to Poisson Point Processes, *Journal of Statistical Physics* 134(1) (2009) 185-206.
- [16] P. Hirel, AtomsK: A tool for manipulating and converting atomic data files, *Computer Physics Communications* 197 (2015) 212-219.
- [17] D. Hull, D.J. Bacon, Chapter 4 - Elastic Properties of Dislocations, in: D. Hull, D.J. Bacon (Eds.), *Introduction to Dislocations (Fifth Edition)*, Butterworth-Heinemann, Oxford, 2011, pp. 63-83.

Chapter 4: Deformation Twinning Behavior in Polycrystalline

Magnesium: An Atomistic Study

4.1 Preface

Pervasive deformation twinning in magnesium greatly affects its strength and formability. A three-dimensional evolution for twinning at atomic scale is extremely difficult to characterize experimentally. Therefore, this paper presents twinning response in deformation of polycrystalline Mg by means of large-scale classic molecular dynamics simulations. An algorithm was firstly proposed to identify active twin variants in simulation of Mg polycrystal. Then, several twin-related events, including formation of stacking faults in nucleation and growth of twinning and disconnection assisted migration of twinning interface, are presented carefully. The discovery of different types of disconnections in this paper is expected to extend the understanding of twinning in Mg as well as other hcp structures.

- This chapter presents an article to be submitted as:

Deformation Twinning Behavior in Polycrystalline Magnesium: An Atomistic Study

Huicong Chen, Cheng Chen, Jun Song

4.2 Abstract

The current work presents systematic investigation of twinning behaviors in Mg polycrystal under different stress loading. An algorithm is firstly proposed to identify the active twin variants in deformation simulation of Mg polycrystal. Then, the effect of loading directions on the selection of twin variants has been quantitatively described by introducing Schmid factors. The three-dimensional illustration of twinning shows that the nucleation and growth of $\{10\bar{1}1\}$ and $\{10\bar{1}2\}$ twins is accompanied by the formation and migration of stacking faults inside these twins while no stacking fault is observed in $\{11\bar{2}1\}$ twins. In addition, profuse disconnections are observed on twinning boundary (TB) interfaces. For $\{10\bar{1}1\}$ twin, we determine four kinds of disconnections with step height of h_0 , $2h_0$, $3h_0$ and $4h_0$, where steps of h_0 and $3h_0$ are immobile along twinning direction because their formation is due to the interaction between stacking faults and TB interface, while the other two disconnections forming away from the interaction sites can move freely along twinning direction. In case of $\{11\bar{2}1\}$ twin, only one type of disconnection with step height of $(\mathbf{b}_{1/2}, h_{1/2})$ is characterized. These disconnections are found to play an important role in assisting growth of deformation twins in Mg polycrystal.

4.3 Introduction

Magnesium (Mg) and its alloys have been of great interests to researchers and industries because of their potential in light-weighting structural components [1]. However, the engineering applications of Mg and its alloys (hereafter referred to as Mg alloys for simplicity) have been greatly limited by their poor ductility and formability at the room temperature. Such limitation is fundamentally attributed to their hexagonal close-packed (HCP) crystal structure which renders insufficient operative slip systems available to acquire homogenous deformation [2-6]. Besides

dislocation slips, twinning is another main deformation mode in Mg alloys for strain accommodation. Furthermore, the crystal reorientation resulted from twinning can tailor the basal texture [7, 8] and introduce slip planes favorably oriented for activation [8]. As such, twinning has been considered as a potential remedy to aid Mg alloys in enhancing their room temperature ductility and formability, with numerous studies performed along this line.

There have been extensive research efforts devoted to developing desirable Mg alloys by controlling deformation twinning. Mg alloys have profuse twinning modes which lead to various misorientation angles between twin and matrix and thus, texture can be tailored by activation of twin types. Accordingly, pre-deformation method [8-11] has been widely used to engineer texture by introducing different pre-twinning structures. Furthermore, criteria of variant selection in terms of Schmid factor and strain accommodation is therefore proposed to quantitatively predict the activation of twins in deformation of polycrystalline Mg alloys under different loading conditions [12-14]. In addition, periodical segregation of solute atoms to fully coherent twinning boundaries (CTBs) was recently observed in Mg alloys [15], which provides insights of developing new alloys with high strength and ductility. For example, co-segregation of Zn and Ca in grain boundaries (GBs) leads to the formation of the finer microstructure during the heat treatment in the Mg-0.3Zn-0.1Ca alloy and hence significant improvement of both ductility and strength was obtained [16]. Despite the increasing consideration of twinning in design of Mg alloys, the underlying mechanism have not been well understood. For example, mechanism of nucleation and growth of twins in Mg is not clear. Besides, TBs are found not fully coherent and many disconnections and steps form along twinning interfaces, which potentially influence the current understanding of many twinning related events such as microstructure evolution and solute segregation.

Therefore, many theoretical studies have been conducted, attempting to overcome this gap. In terms of twinning mechanism, it can be divided into three stages, i.e., nucleation, propagation and growth. Generally, twin commences with the formation of a nucleus when a suitable defect configuration is present, such as at a grain boundary [17, 18] where a higher stress level is always provided. In hcp metals, according to the pole model proposed by Thompson and Millard [19], a pole source of twinning is formed by the reaction of dislocation with Burger's vector $[0001]$ and then a sessile dislocation with Burger's vector $[10\bar{1}0]$ forms in the twin lattice, leaving a double step in the interface. In addition, Startsev et al. [20] proposed that twinning dislocations (TDs) can also be produced by a mutual reaction among basal dislocations of $[\bar{2}110]$. Both mechanisms [19, 20] require the activity of both basal and pyramidal slip systems and result in the motion of similar dislocations. Later, topological analysis [21, 22] of a twinning dislocation suggested that a twinning dislocation can simply be thought of as a line defect having both a dislocation and step character and the height of the step is dependent on the type of dislocation and consists of n crystallographic planes. According to this character, a new twinning mechanism was suggested by Wang et al. [18, 23] who proposed multiple TDs and one partial dislocation are required to simultaneously created to form the minimum stable nucleus, corresponding to a thickness of 17 crystallographic $(10\bar{1}2)$ planes in Mg. Their results showed that a twinning mechanism starting with a single TD such as the simple pole mechanism [20, 21] is impossible. Capolungo and Beyerlein [24] illustrated that the activation and piling up of either prismatic or basal $\langle a \rangle$ slip dislocations, or partial basal dislocations result in the non-coplanar dissociation that produces one or two TDs. Then, these TDs serve as twinning nucleus. These recent theories imply that deformation twins have imperfect structures in the twinned region and twinning boundary (TB) interface such as the stacking faults and disconnections/steps [25, 26]. Recent molecular dynamics

(MD) studies [27-30] have shown that interfacial disconnections are formed during and after twinning nucleation, and transformation between basal-prismatic (BP) interfaces and $\{10\bar{1}2\}$ twinning boundary (TB) occurs via the migration of these disconnections throughout the twinning growth process.. A very recent MD simulation on polycrystalline Mg [26] revealed that the symmetric steps along TB interface are formed due to the interaction between basal stacking faults (BSFs) and TB interface, favoring the growth of $\{10\bar{1}1\}$ twin [26]. However, this study did not consider other important twinning modes in Mg such as $\{11\bar{2}1\}$ twin and description of different disconnections is not included which is very important to understand how twinning proceed with these interface defects. Similar simulations [31] were also performed on nano-twinned polycrystalline Mg and the authors investigated effect of twinning lamella size and temperature on the migration of TBs, but they ignore the importance of twinning mechanism of a twin-free polycrystal.

Due to grain size, orientation, shape as well as grain boundary (GB) defects, results such as microstructures and mechanical response may vary in a Mg polycrystal model. So far, most computational studies of twinning are limited to Mg single crystal or bicrystal models and simulations on polycrystals are imperative to provide an accurate understanding of twinning. Therefore, the current work firstly constructed a polycrystalline Mg and then performed MD simulation to deform the polycrystal and initiate twins for further analysis. 3D twinning structures were characterized and examined, illustrating the characteristic of microstructure evolution of three twin modes i.e., $\{10\bar{1}2\}$ $\{10\bar{1}1\}$ and $\{11\bar{2}1\}$. Then, Schmid factors were calculated to quantitatively predict the activation of twin variants. Finally, mechanism of twinning growth of $\{10\bar{1}1\}$ and $\{11\bar{2}1\}$ twins assisted by disconnections along TB interface are discussed and compared in detail.

4.4 Computational Methodology

To simulate a polycrystalline Mg microstructure, a full periodic simulation box with dimensions of $100 \text{ nm} \times 100 \text{ nm} \times 100 \text{ nm}$ were constructed. The simulation box consists of multiple grains of different orientations, with the individual grain volume partition constructed using the Voronoi tessellation method [32]. The grains are randomly oriented, created by rotating the lattice within each grain around the reference axes of $X = [0001]$, $Y = [\bar{1}010]$ and $Z = [1\bar{2}10]$ by random angles, as illustrated in **Figure 4.1(b)**. In the representative polycrystalline model used in our simulations, there are a total of 15 randomly oriented grains, numbered as G1-G15 as shown in **Figure 4.1(a)** and the corresponding geometrical orientation distribution is shown in **Figure 4.1(c)**. The angles between the c -axis of each grain and the reference axes X , Y and Z are listed in **Table 4.1**.

Following the model construction, MD simulations were then performed using Large-scale Atomic/Molecular Massively Parallel Simulator (LAMMPS) [33]. The interatomic interactions are prescribed by the embedded-atom method (EAM) [34] potential developed by Wilson and Mendeleev [35]. This EAM potential is chosen for our study because it is widely used in atomistic investigations on the deformation behavior of pure Mg [26]. The model was first relaxed using conjugate gradient minimization method [36]. Afterwards the model was equilibrated at 300K for 100ps using the isothermal–isobaric (NPT) ensemble [37] to ensure zero pressures along all three periodic directions. Following the equilibration, six samples were individually deformed under uniaxial tensile or compression stress loading along X , Y and Z axes to a total strain of 20% at a constant strain rate of $1 \times 10^9 \text{ s}^{-1}$. The integration time-step is fixed at 2 fs. Ovito [38] is used to visualize the results. The common-neighbor analysis (CNA) method [39] is used to identify the local defects and orientation mapping method [40] is used to color each atom. The dislocation extraction algorithm (DXA) [41] is performed to extract dislocations in deformed sample.

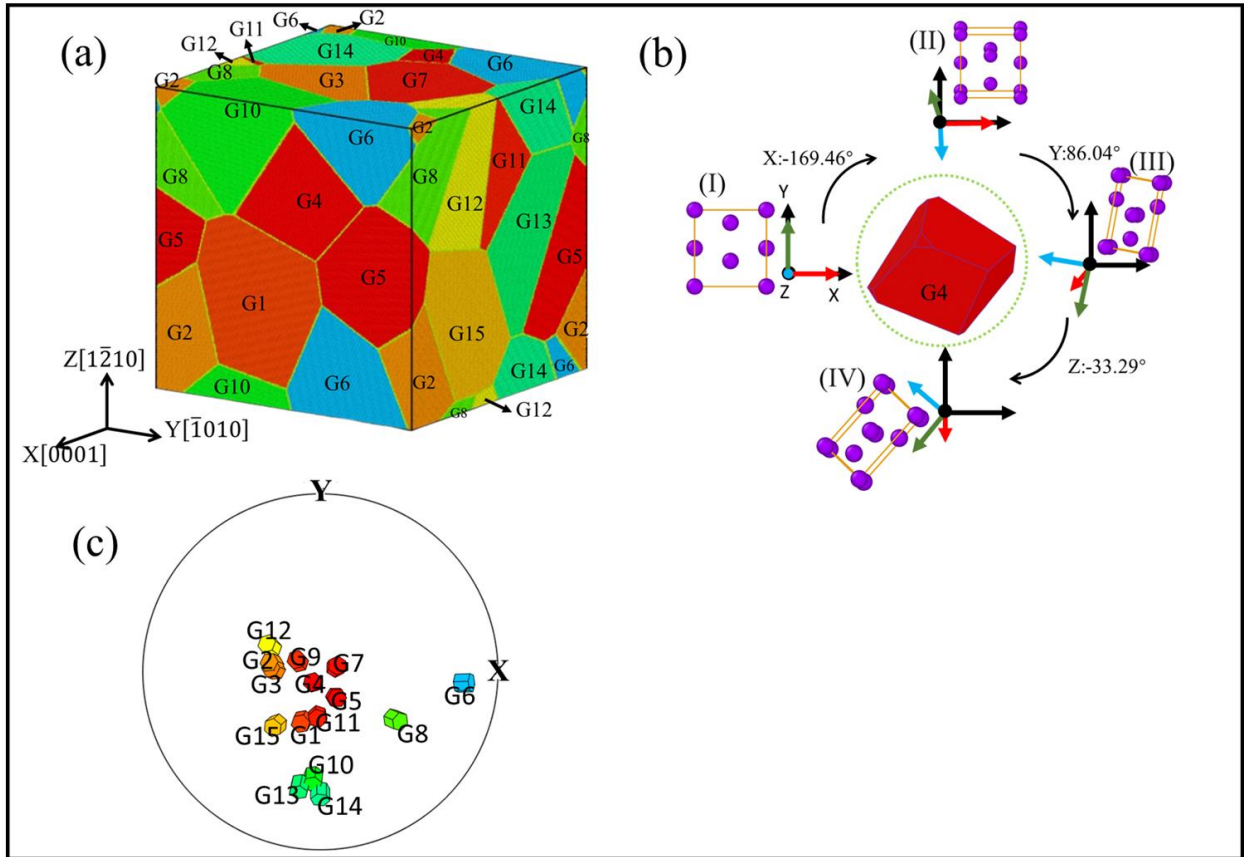

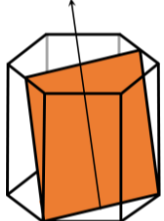



Figure 4.1. (a) the polycrystal Mg microstructure; (b) Example of forming a grain (G4) with specific orientation after three rotation operations; (c) the geometrical orientation distribution of each grain illustrated in pole figure. Atoms are colored by their local orientation in figure (a) and the same coloring method is adopted to reveal the microstructure in this work.

Table 4.1. Angles between the c-axis of each grain and the reference (also loading) directions, i.e., X, Y and Z directions as shown in **Figure 4.1**.

| Grains | Angles (°) | | |
|---------------|--------------------|--------------------|--------------------|
| | X-direction | Y-direction | Z-direction |
| G1 | 81.58 | 74.34 | 17.88 |
| G2 | 67.91 | 79.56 | 24.67 |
| G3 | 68.65 | 82.01 | 22.93 |
| G4 | 86.67 | 87.82 | 3.98 |
| G5 | 82.87 | 85.36 | 8.52 |
| G6 | 20.22 | 88.45 | 69.84 |
| G7 | 82.76 | 80.72 | 11.81 |
| G8 | 55.48 | 75.81 | 38.13 |
| G9 | 79.75 | 78.26 | 15.69 |
| G10 | 86.83 | 47.38 | 42.79 |
| G12 | 88.75 | 76.54 | 13.52 |
| G13 | 67.09 | 71.67 | 30.03 |
| G14 | 81.30 | 43.68 | 47.64 |
| G15 | 69.65 | 72.84 | 27.13 |

Table 4.2. Illustration of three twin modes and six twin variants of each twin mode represented by boundary misorientation axis and angles in Mg. The extension twin $\{10\bar{1}2\}$ and $\{11\bar{2}1\}$, and the contraction twin $\{10\bar{1}1\}$ are defined as ET1012, ET1121 and CT1011, respectively. V_i ($i=1\sim 6$) represent the six twin variants for each twin type.

| Twin modes | Illustration | Twin variant | Plane | Direction | Rotation axis | Rotation angle |
|--------------------------------|---|--------------|----------------------|----------------------|----------------------|----------------|
| $\{10\text{-}12\}$ (ET1012) |  | V1 | $(10\bar{1}2)$ | $[\bar{1}011]$ | $[1\bar{2}10]$ | 86.3° |
| | | V2 | $(01\bar{1}2)$ | $[0\bar{1}11]$ | $[2\bar{1}\bar{1}0]$ | |
| | | V3 | $(\bar{1}102)$ | $[1\bar{1}01]$ | $[11\bar{2}0]$ | |
| | | V4 | $(\bar{1}012)$ | $[10\bar{1}1]$ | $[\bar{1}2\bar{1}0]$ | |
| | | V5 | $(0\bar{1}12)$ | $[01\bar{1}1]$ | $[\bar{2}110]$ | |
| | | V6 | $(1\bar{1}02)$ | $[\bar{1}101]$ | $[\bar{1}\bar{1}20]$ | |
| $\{11\text{-}21\}$ (ET1121) |  | V1 | $(11\bar{2}1)$ | $[\bar{1}\bar{1}26]$ | $[\bar{1}100]$ | 34.2° |
| | | V2 | $(\bar{1}2\bar{1}1)$ | $[1\bar{2}16]$ | $[\bar{1}010]$ | |
| | | V3 | $(\bar{2}111)$ | $[2\bar{1}\bar{1}6]$ | $[0\bar{1}10]$ | |
| | | V4 | $(\bar{1}\bar{1}21)$ | $[11\bar{2}6]$ | $[1\bar{1}00]$ | |
| | | V5 | $(1\bar{2}11)$ | $[\bar{1}2\bar{1}6]$ | $[10\bar{1}0]$ | |
| | | V6 | $(2\bar{1}\bar{1}1)$ | $[\bar{2}116]$ | $[01\bar{1}0]$ | |
| $\{10\text{-}11\}$ (CT1011) |  | V1 | $(10\bar{1}1)$ | $[\bar{1}012]$ | $[1\bar{2}10]$ | 56.2° |
| | | V2 | $(01\bar{1}1)$ | $[0\bar{1}12]$ | $[2\bar{1}\bar{1}0]$ | |
| | | V3 | $(\bar{1}101)$ | $[1\bar{1}02]$ | $[11\bar{2}0]$ | |
| | | V4 | $(\bar{1}011)$ | $[10\bar{1}2]$ | $[\bar{1}2\bar{1}0]$ | |
| | | V5 | $(0\bar{1}11)$ | $[01\bar{1}2]$ | $[\bar{2}110]$ | |
| | | V6 | $(1\bar{1}01)$ | $[\bar{1}102]$ | $[\bar{1}\bar{1}20]$ | |

4.5 Results and Discussion

4.5.1 Loading Dependence of Twinning Modes

Figure 4.2 shows that at a strain of 8%, size of twin lamellas in compression samples (Figure 4.2(a)-(c)) is much larger than those in tension samples (Figure 4.2 (d)-(f)) and the activated twinning

types are various in tensile and compression stress load. As shown in **Figure 4.3** and **Figure 4.4**, samples deformed under tension and compression stress loading along X-direction are selected as representatives to compare the microstructural differences because of changing loading modes. Twin will rotate the c-axis of the matrix by a specific rotation degree about a particular rotation axis to form a mirror symmetry relationship with its matrix. Therefore, a particular twinning mode can be characterized as a pair of misorientation axis and angle (see **Table 4.2**). According to these axis distributions, the misorientation at 86.3° and 56.2° both share the $\langle 1\bar{2}10 \rangle$ axis and corresponds to $\{10\bar{1}2\}$ and $\{10\bar{1}1\}$ twins, respectively while $\{11\bar{2}1\}$ has the misorientation of 34.2° about $\langle 10\bar{1}0 \rangle$ axis.

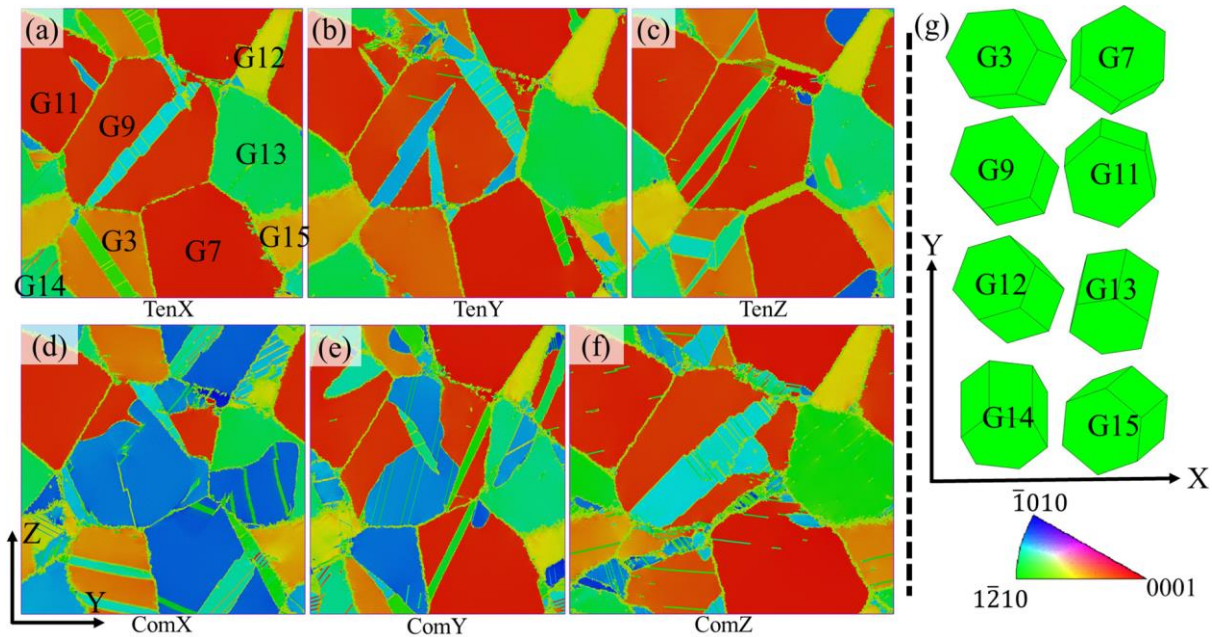


Figure 4.2. Snapshots of microstructures viewed along X-direction for each sample deformed to a strain of 8% under uniaxial tensile stress loading (a-b) and (d-f) uniaxial compression stress loading, respectively; (g) geometrical orientation of each grain in the sample coordinate.

In the current simulation, all three twinning types in **Table 4.2** are observed in the sample deformed under tensile loading stress along X-direction and more contraction $\{10\bar{1}1\}$ twins are activated. For example, **Figure 4.3(a)** shows primarily activated twin T1 in grain G5 and twin T2 in grain G1

are corresponding to contraction twinning mode $\{10\bar{1}1\}$. Another two twin lamellas T3 and T4 in G5 (**Figure 4.3**figure 4(b)) and T8 in grain G2 (**Figure 4.3**(f)) are also identified as $\{10\bar{1}1\}$ twin. Besides, twin T6 and twin T7, identified as extension twinning mode $\{10\bar{1}2\}$ and $\{11\bar{2}1\}$ respectively, are characterized in G5 and G6 at a strain of 6.2% (**Figure 4.3**(c)). T6 is activated due to high local stress produced by the twin-twin interaction [42] of T1, T3 and T4 in G5. Different from the case of tensile stress loading, as shown in **Figure 4.4**, extension twinning modes $\{10\bar{1}2\}$ and $\{11\bar{2}1\}$ are dominated in the compression stress loading. **Figure 4.4**(b) shows T1 in G5 is identified as $\{11\bar{2}1\}$ twin and T2 in G4 is determined as $\{10\bar{1}2\}$ twin. In addition, T5 in G10 and T6 in G1 belong to extension twin $\{10\bar{1}2\}$. Contraction twinning modes such as $\{10\bar{1}1\}$ (T3 in G8) are also observed in some grains.

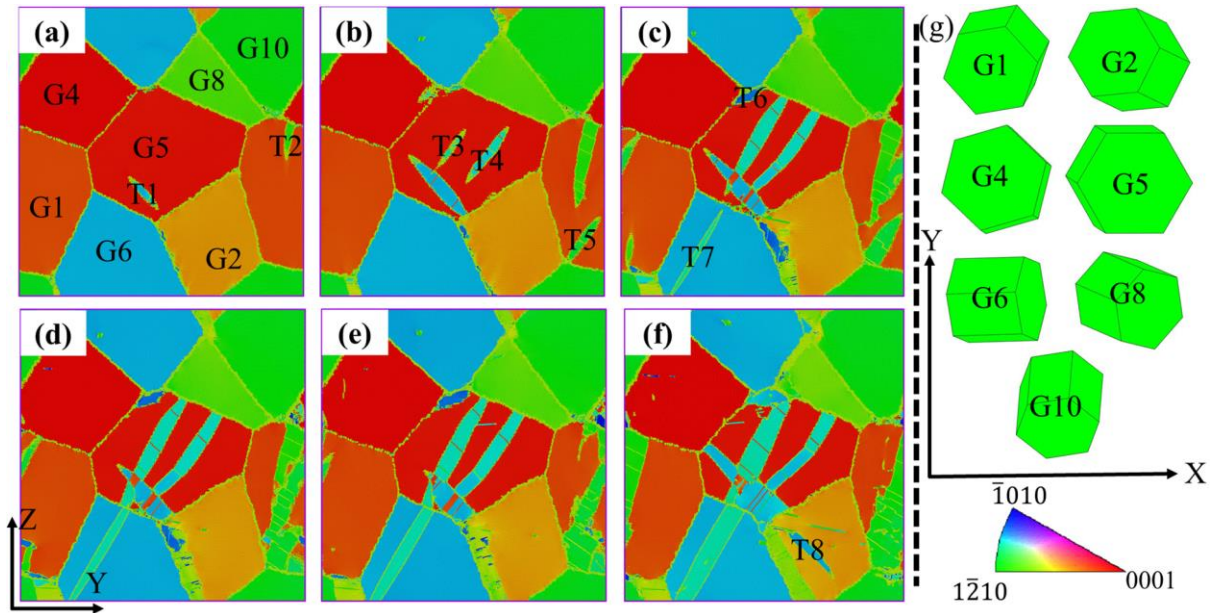


Figure 4.3. Representative overview of twinning evolution during uniaxial tensile stress loading along X-direction at a strain of (a) 4.6%, (b) 5.2%, (c) 6.2%, (d) 6.8%, (e) 7.6%, (f) 12%; (g) geometrical orientation of each grain in the sample coordinate, where G_i ($i=1\sim 15$) represent each grain in the current polycrystal.

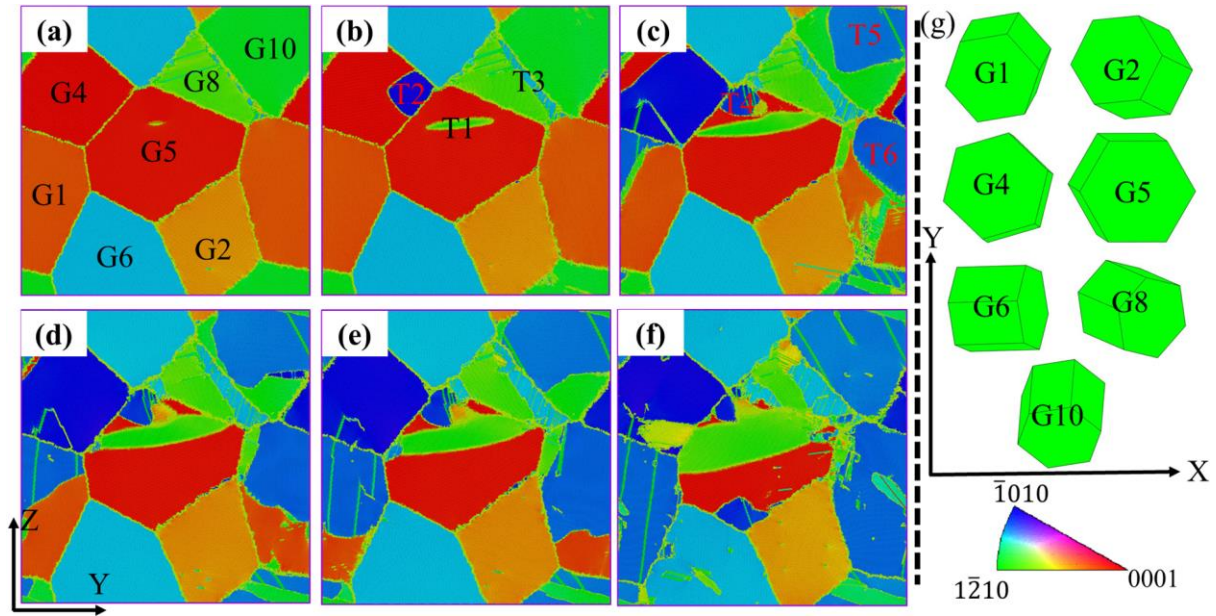


Figure 4.4. Representative overview of twinning evolution during uniaxial compression stress loading along X-direction at a strain of (a) 4.6%, (b) 5.2%, (c) 6.2%, (d) 6.8%, (e) 7.6%, (f) 12%; (g) geometrical orientation of each grain in the sample coordinate.

Unlike dislocation slip, twinning is a polar mechanism (unidirectional) [43], leading to the difference of the activation of twinning modes for compressive and tensile loading. Therefore, the variations of grain orientation in polycrystal are likely to affect the observed deformation modes. As shown in **Table 4.1**, c-axis of most grains form a larger angle ($>65^\circ$) with loading directions along both X- direction, consequently favoring the activation of contraction twinning types when the tensile loading stress is applied along X-direction as observed in **Figure 4.3**. Similarly, extension twinning modes are dominated in the sample deformed by a compression loading stress as shown in **Figure 4.4**. Because of a small angle forming between G6 and X-direction as shown in **Table 4.1**, extension twinning mode $\{11\bar{2}1\}$ is also observed in **Figure 4.4(c)**.

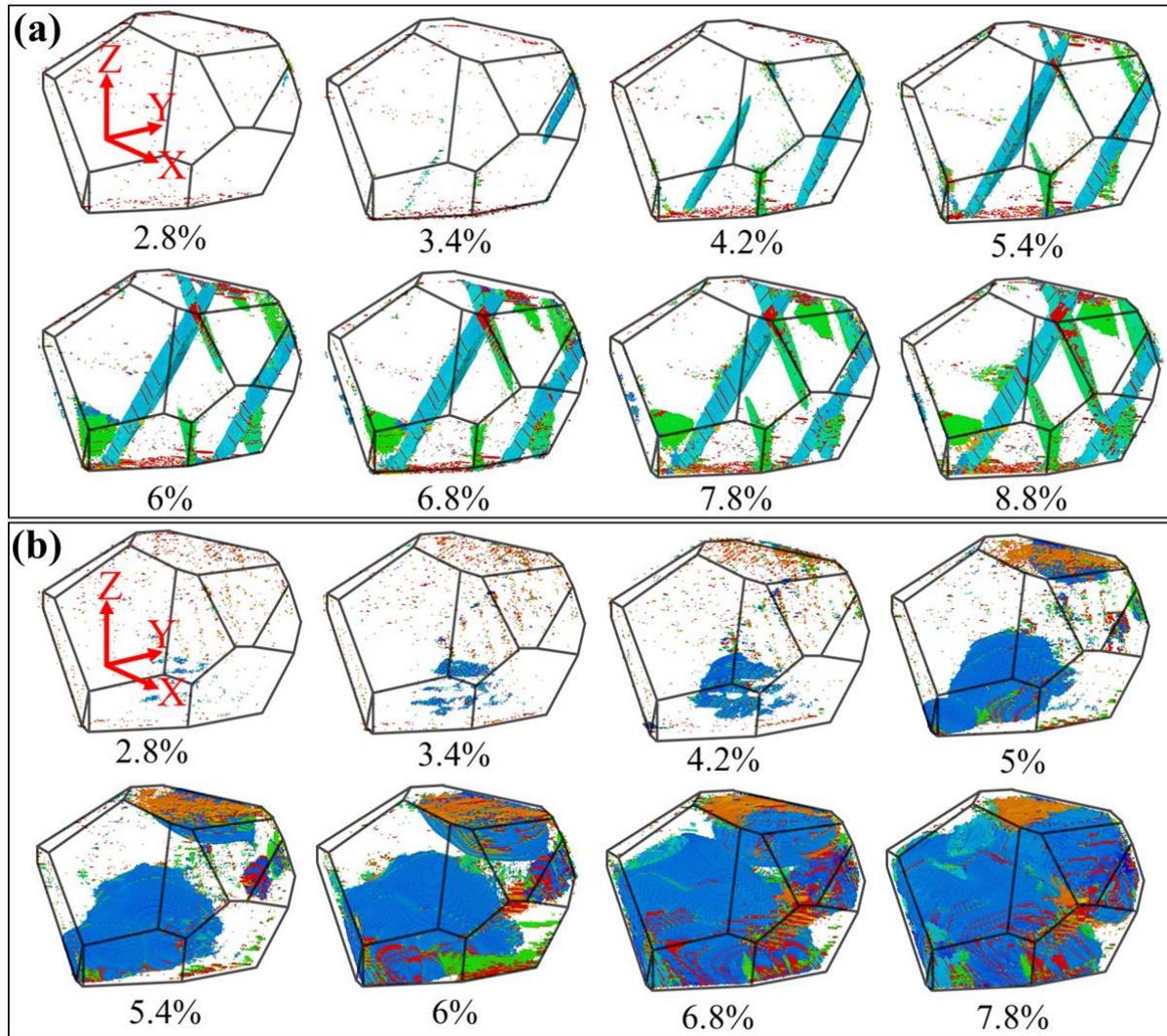


Figure 4.5. 3D view of microstructural evolution of grain 9 (G9) under (a) tensile stress loading along X-direction and (b) compression stress loading along X-direction.

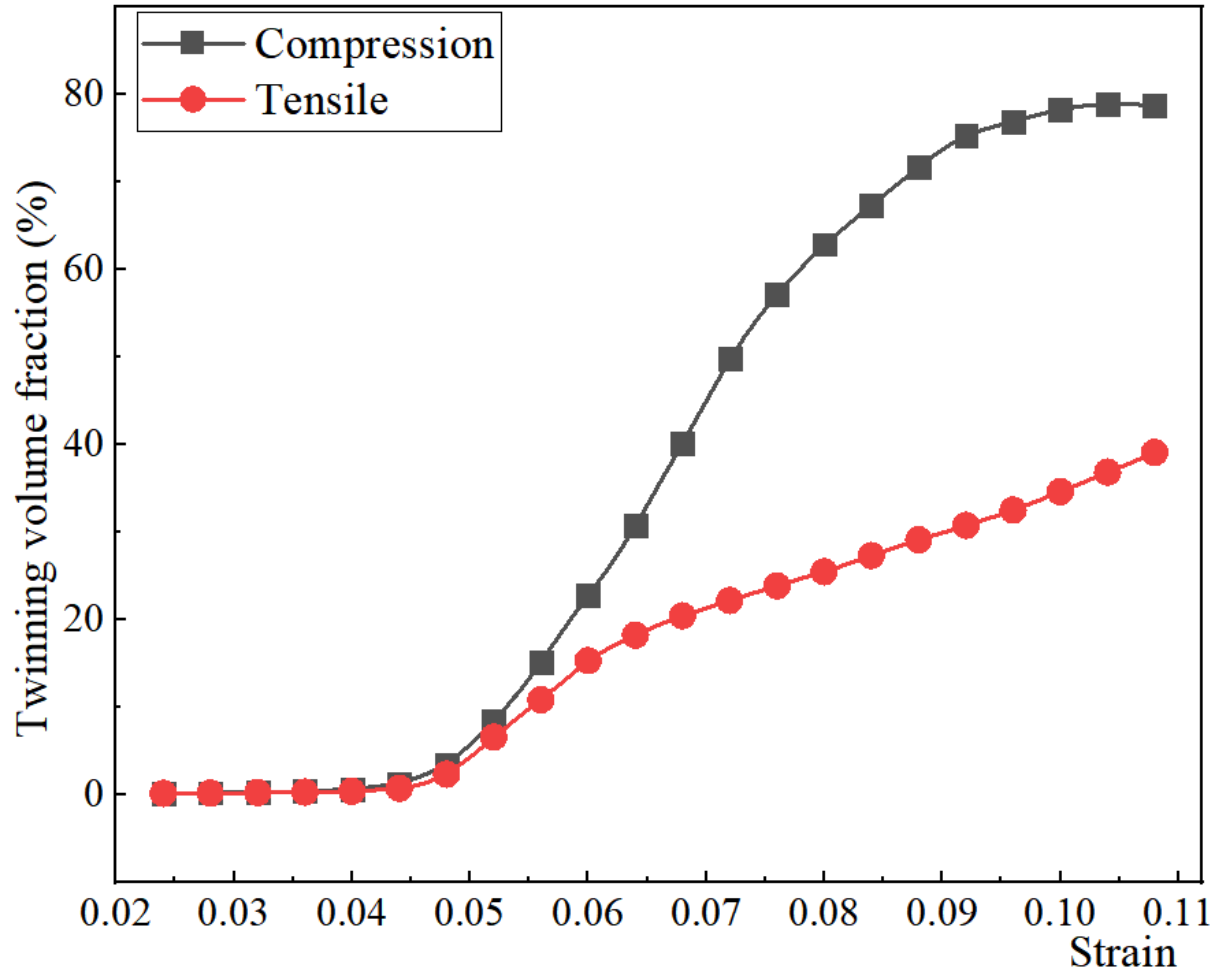


Figure 4.6. Variation of twinning volume in G9 as a function of strain during uniaxial tensile and compression stress loading along X-direction.

In addition to the difference in activation of twinning modes, the growth rate of twins also shows strong dependence on applied loading. **Figure 4.5(a)** and (b) shows three-dimensional observation of microstructural evolution in grain G9 by a series of snapshots at different strains. As shown in **Figure 4.5(a)**, in case of tensile stress loading, twins start to nucleate at a strain of 3.4% and are profusely activated at a strain ranging from 4.2% to 6%. Then the initial twins propagate and grow as the strain proceeds. Finally, their growing rate slows down due to the twin-twin interaction produced by the activation of multiple twinning modes or twin variants. As shown in **Figure 4.6**, the growing rate of the twin volume fraction decreases after the twin-twin interaction appears at a

strain of 6%. However, twins grow faster once they finish nucleation and propagation at a strain of 5% in a compression stress loading as shown in **Figure 4.5(b)**. Only one twin variant of $\{10\bar{1}2\}$ is observed in G9, which avoids the barrier for twinning boundary migration because of the twin-twin interaction. As a result, twins almost swallow the matrix grain (G9) at a strain of 7.8%. As show in **Figure 4.6**, twin grows almost at a constant rate after a strain of 5% and its volume fraction takes up around 80% of the matrix at a strain of 10%. Therefore, the twinning behavior is clearly orientation dependent, which may lead to difference in twin variant selection.

4.5.2 Selection of Twin Variants

It is expected that the activation and probability of twin are closely related to Schmid factor (SF). Using the method listed in **Supplementary Information**, SFs of all possible twin variants from three twin modes (see **Table 4.2**) can be computed. The results are shown in **Figure 4.7**, **Figure 4.8** and **Figure 4.9**, where positive signs “+” represent the active twin variants in tensile stress loading and negative signs “-” stand by the selected variants in compression loading. Note that the values of SFs for a particular twin variant in tension and compression along the same loading direction share equal magnitude but opposite signs.

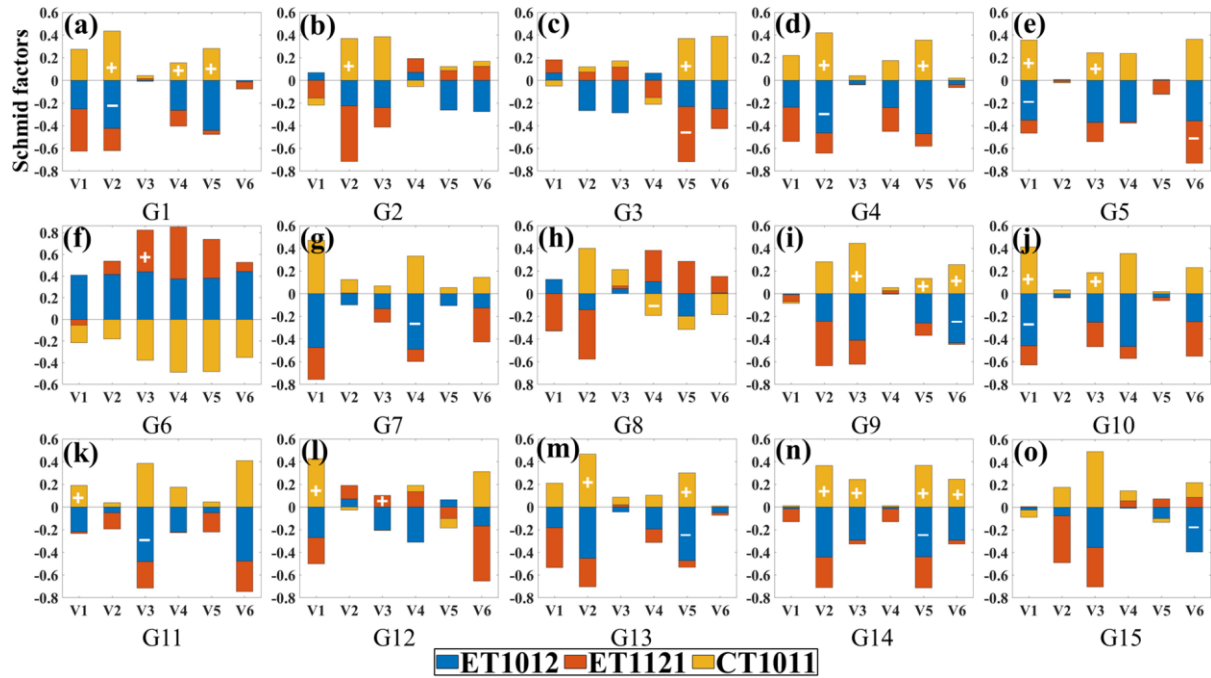


Figure 4.7. Schmid factors of possible twin variants, and the selected variants when the sample is deformed under tensile stress loading along X-direction. Note, Schmid factors in compression stress loading simulation have the same absolute value but in opposite sign with case of tensile stress loading simulation. The embedded symbol “+” means the activated twin variants in simulation of tensile stress loading and “-” stands by the active twin variants in simulation of compression stress loading. Similar marking scheme is used in **Figure 4.9** and **Figure 4.10**.

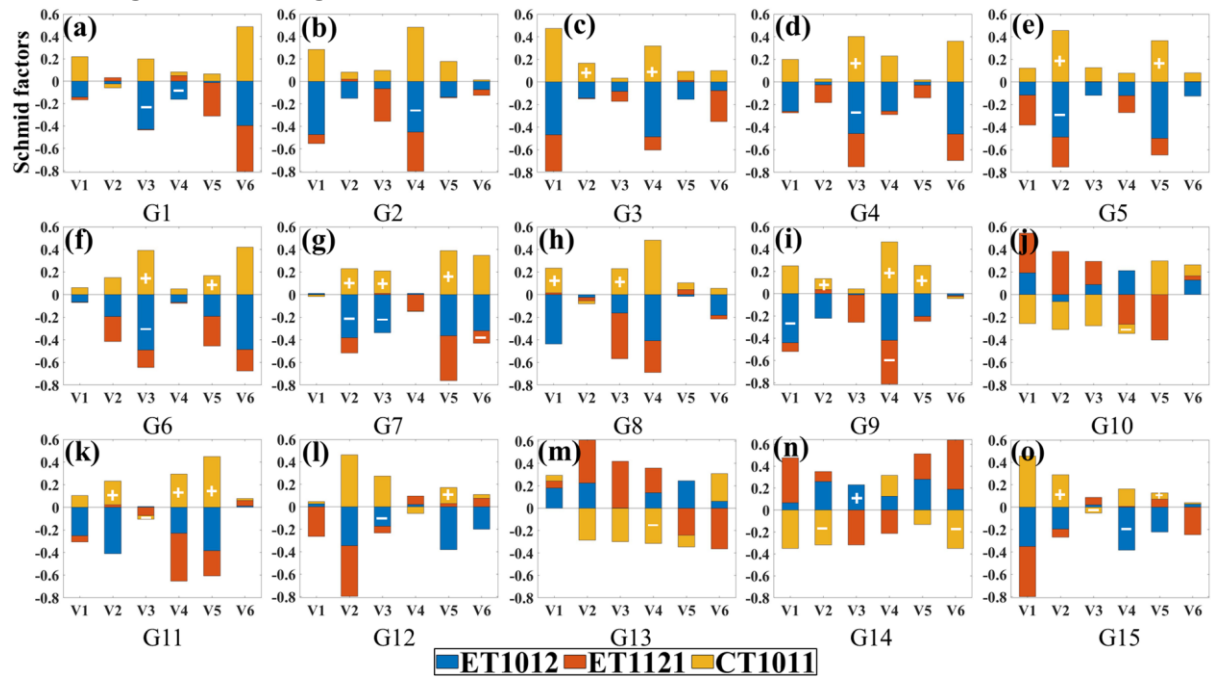


Figure 4.8. Schmid factors of possible twin variants and the selected variants when the sample is deformed under tensile (“+”) and compression (“-”) stress loading along Y-direction.

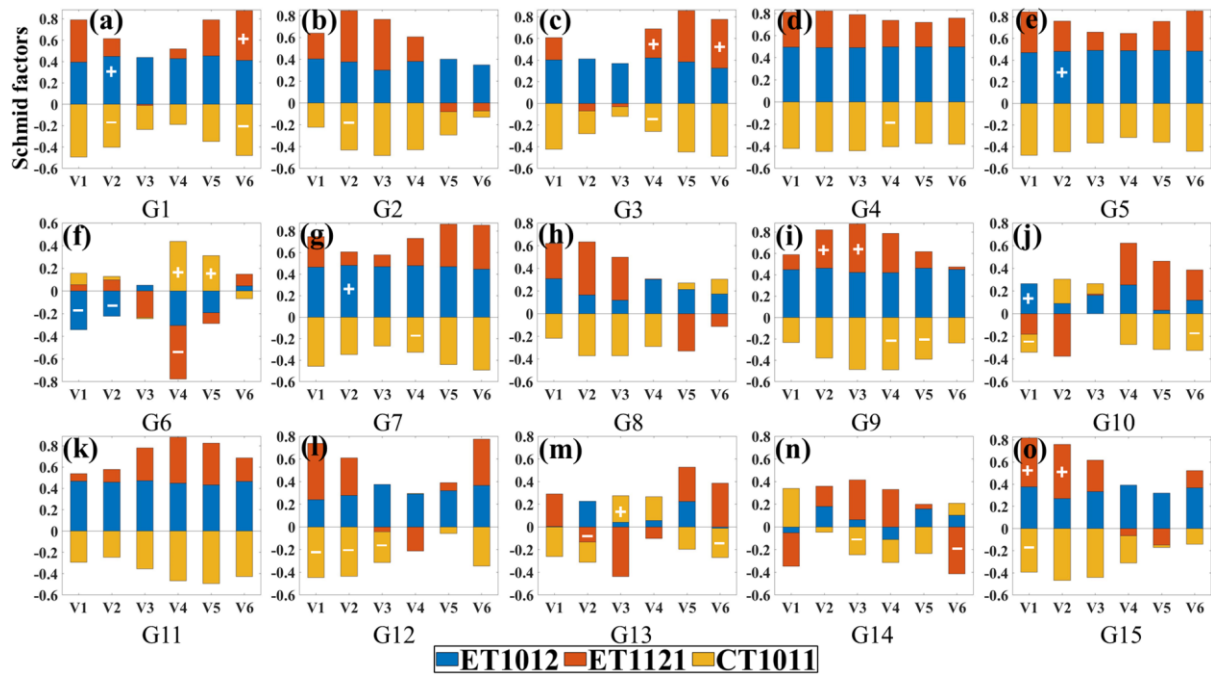


Figure 4.9. Schmid factors of possible twin variants and the selected variants when the sample is deformed under tensile (“+”) and compression (“-”) stress loading along Z-direction.

Figure 4.7 illustrates the SFs of all twin variants and the distribution of SFs on the observed twins in each grain when the stress loading is applied along X-direction. Except for grain G6, variants of most contraction twinning modes have positive SFs in tensile sample along X-direction and consequently, as shown in **Figure 4.3(c)**, only G6 deformed by extension twin $(\bar{2}111)[2\bar{1}\bar{1}6]$, which corresponds to variant V3 (see **Table 4.2**) and has a SF of 0.387. For contraction twin variants in **Figure 4.3(a, b)**, T1, T3 and T4 are characterized as $\{10\bar{1}1\}[10\bar{1}2]$ twins, where T1 belongs to variant V1 which has a SF of 0.357 and T3 and T4 corresponds to variant V3 with a SF of 0.243. Besides, Twins T2 in G1 and T8 in G2 in **Figure 4.3(f)** are determined as variant V2 $(01\bar{1}1)[0\bar{1}12]$ and have SFs of 0.436 and 0.369, respectively. Another two contraction variants marked in **Figure 4.7(a)** are also determined as V4 (SF = 0.154) and V5 (SF = 0.282) in grain G1 which are not revealed in **Figure 4.3**. For the compression stress loading case, tension twin variants are profusely

activated due to their favorable stress state and high SFs as shown in **Figure 4.4**, where T1 and T4 in G5 are determined as V6 ($2\bar{1}\bar{1}1$)[$\bar{2}116$] and V1 ($10\bar{1}2$)[$\bar{1}011$] which have SFs of 0.35 and 0.37, respectively. T2, T5 and T6 in **Figure 4.4**(b, c) all belong to $\{10\bar{1}2\}$ twin but correspond to V2, V1 and V2 in their respective matrix and they all have high rank of SFs, i.e., 0.46, 0.46 and 0.42. Besides, the contraction twin variant T3 (V4 ($\bar{1}011$)[$10\bar{1}2$]) in **Figure 4.4**(b) is also observed due to its favorable stress state where this variant has a positive SF of 0.191. For the stress loading along Y-direction, selection of twinning modes is similar with those in stress loading along X-direction because of their similar initial crystallographic orientation distribution as shown in **Table 4.1** while the selected twin variants may vary due to respective SFs. On the contrary, as shown in **Figure 4.9**, tensile stress loading along Z-direction benefits activation of extension twins and compression stress loading along Z-direction is favorable to activate contraction twins. **Figure 4.7**, **Figure 4.8** and **Figure 4.9** and **Table 4.2** present details of twin variants selection of all active twins and their SFs in the current simulation.

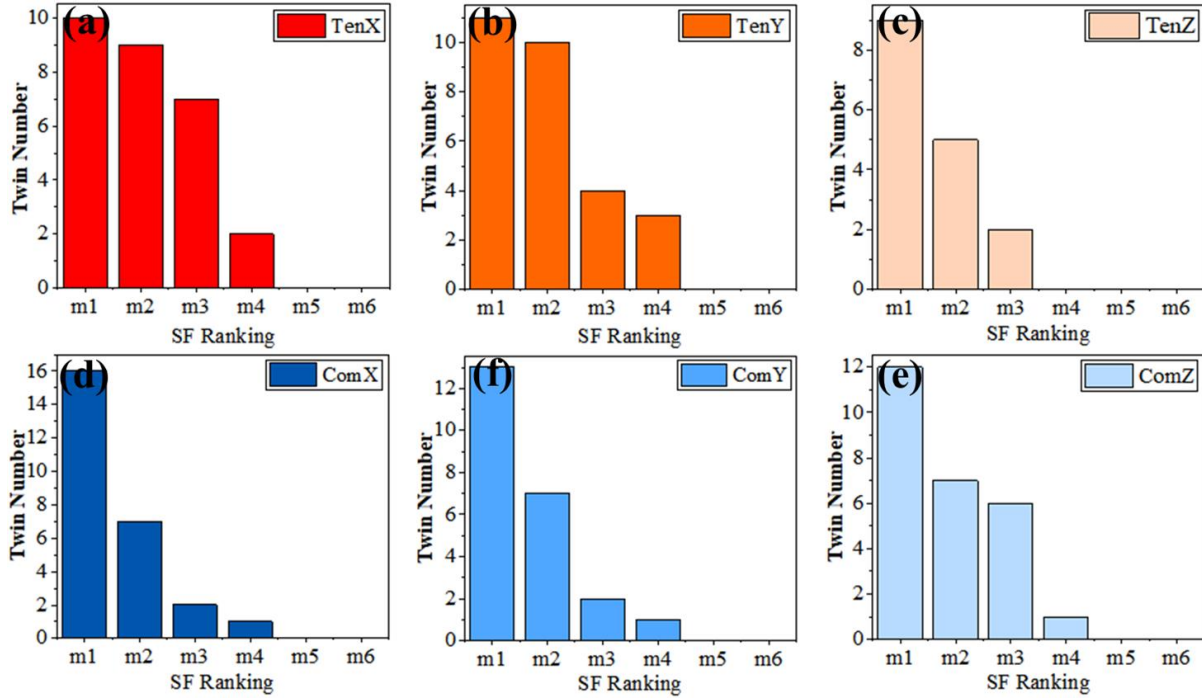


Figure 4.10. The total number of active twins in the sample deformed under different lading directions plotted versus their ranking of Schmid factor.

According to the magnitude of SF, six SFs of each twinning type are classified into six levels as m_i , $i = 1, \dots, 6$, where m_1 and m_6 corresponds to the highest and the lowest values, respectively.

Figure 4.10 plot the distribution of number of observed twins on SFs under different loading conditions. It is obvious that twin variants with the first ranking SF have the highest activation probability regardless of stress loading modes. The statistical analysis indicate that twin variants with high SFs are expected to be activated to accommodate the plastic in deformation of polycrystal. This indication is in agreement with the statistical analyses from the experimental work [17].

4.5.3 Evolution of Twin Structures

4.5.3.1 $\{10\bar{1}2\}$ Extension Twin and $\{10\bar{1}1\}$ Contraction Twin

To analyse the twinning process of $\{10\bar{1}2\}$ and $\{10\bar{1}1\}$ twins, grain G9 is selected and a series of snapshots at different strains are characterized. **Figure 4.11** and **Figure 4.12** illustrate the microstructural evolution for uniaxial compression and tensile loading along X-direction, respectively.

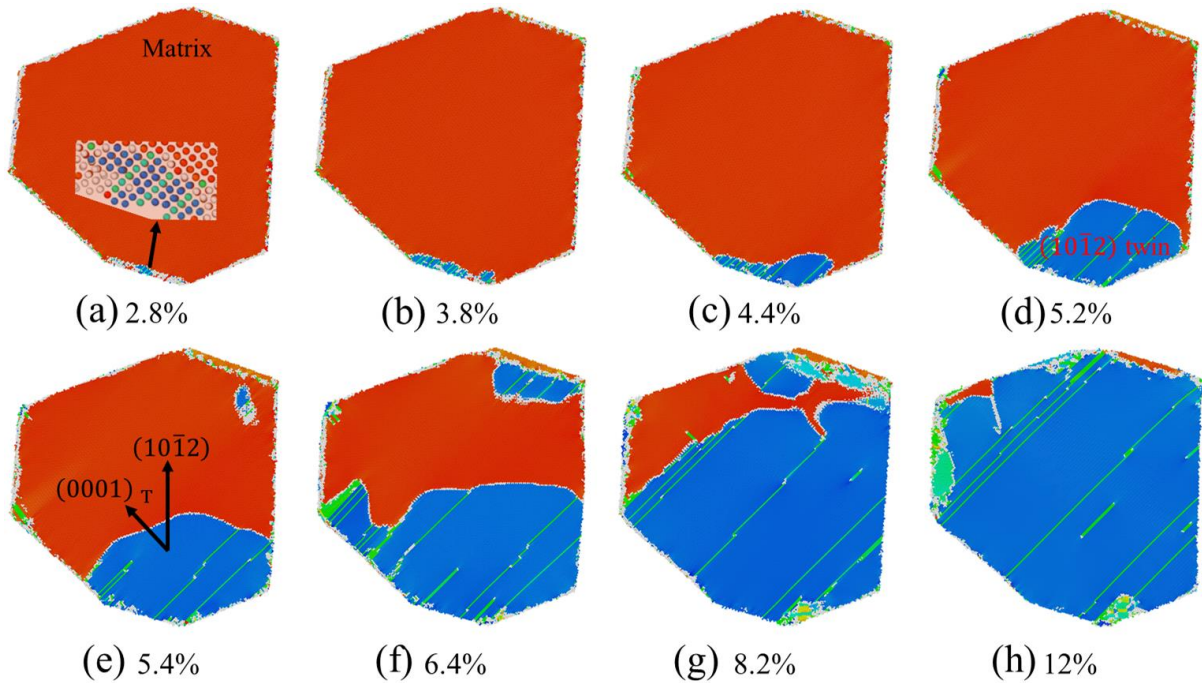


Figure 4.11. Microstructural evolution of the $\{10\bar{1}2\}$ extension twin in G9 during uniaxial compression stress loading along X-direction at different strain levels.

As shown in **Figure 4.11(a)**, the $\{10\bar{1}2\}$ extension twin is observed to nucleate at the grain boundary accompanied by the formation of basal stacking faults (BSFs) inside the twin embryo. Once the embryo grows into an initial lenticular shape as shown in **Figure 4.11(c)**, the $\{10\bar{1}2\}$ twin propagate at high growing rate until it meets the grain boundary at the other end of the grain (**Figure 4.12(d-g)**) and swallow the matrix at a strain of 12% (**Figure 4.12(h)**). It is obvious that TB migration

during twinning growth is not a simple shearing process because of profuse non-TB interfaces such as prismatic/basal (PB) interfaces accompanying the process. Besides, the interaction between the inside BSFs and twinning interface is observed and may provide the source for twinning growth. **Figure 4.14(a)** depicts the BSFs formed in twinned region and PB interfaces which is parallel to either both prismatic plane of the matrix and basal plane of the twin ($\text{prismatic}_M/\text{basal}_T$) or to both prismatic plane of the twin and basal plane of the matrix ($\text{prismatic}_T/\text{basal}_M$).

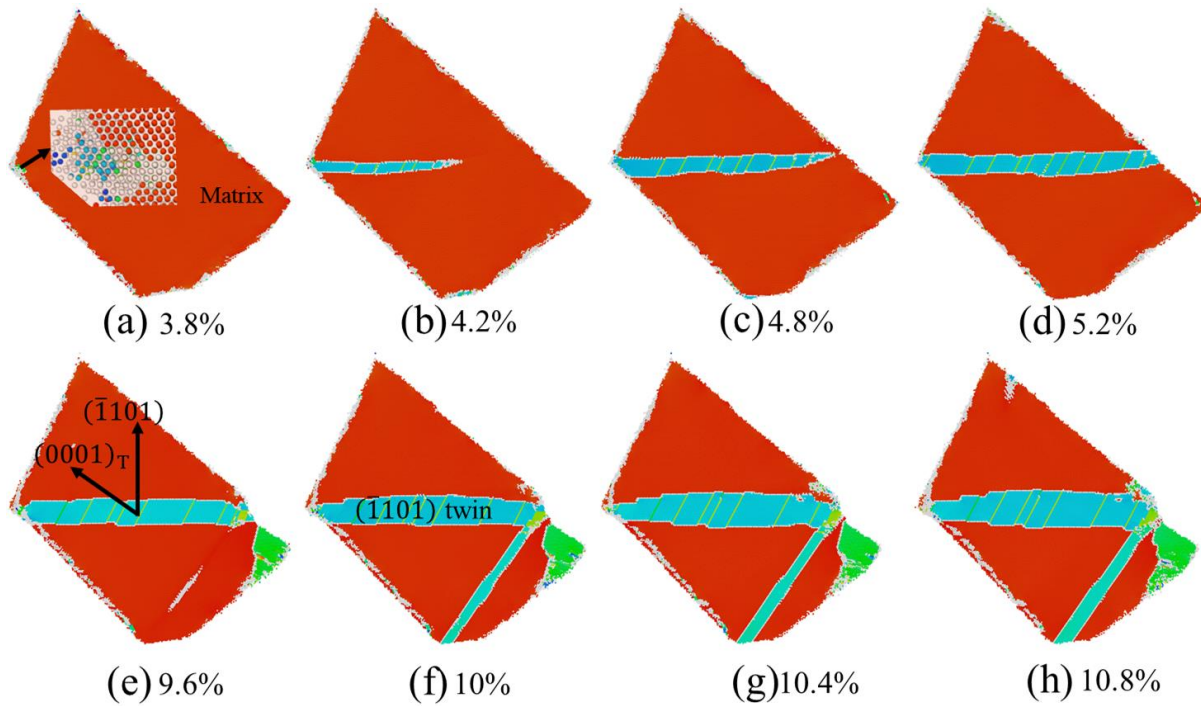


Figure 4.12. Microstructural evolution of the $\{10\bar{1}1\}$ contraction twin in G9 during uniaxial tensile stress loading along X-direction at different strain levels.

Similarly, the $\{10\bar{1}1\}$ twin nucleates as an initial embryo with the formation of BSFs as shown in **Figure 4.12(a)**. However, the $\{10\bar{1}1\}$ twin grows into a plate shape (see **Figure 4.12(b)**) which is surrounded by a pair of planar faults and the tip of the twin propagates until it reaches the grain boundary at the other end of the grain as shown in **Figure 4.12(c)**. Then, further straining widens

the width of the twin fault, leading to growth of twin in the normal direction (see **Figure 4.12(d-e)**). Besides, another $\{10\bar{1}1\}$ twin is already formed at a strain of 10% and interacts with the first twin variant as shown in **Figure 4.12(f)**, which provides a barrier for the migration of the twin fault and restricts the growth of the initial twin variant as shown in **Figure 4.12(g-h)**. Obviously, as shown in **Figure 4.12(d)**, the twin fault is disconnected by profuse steps at twin-matrix interfaces among which the mobile disconnections may migrate with the growth of twin fault. **Figure 4.14(b)** illustrates the BSFs in twinned region and immobile steps/disconnections at twin-matrix interfaces and the BSFs are observed to interact with twin faults. Characteristic of these mobile and immobile steps will be discussed in chapter 4.4.4.2.

Thus, although the difference of twin shapes and growth rate between the $\{10\bar{1}2\}$ extension twin and $\{10\bar{1}1\}$ contraction twin, the growth of both twin modes is accompanied by the formation of BSFs inside twin lamella. In addition, the disconnections and steps at twinning interface play an important role in the growth of twin and these defects have been profusely reported in study of grain boundary motion [25, 27, 44-47].

4.5.3.2 $\{11\bar{2}1\}$ Extension Twin

As shown in **Figure 4.13**, a series of snapshots of grain G3 during uniaxial compression loading along X-direction are captured to analyse the microstructural evolution of the $\{11\bar{2}1\}$ extension twin. Unlike the $\{10\bar{1}2\}$ and $\{10\bar{1}1\}$ twins, as shown in **Figure 4.13(b)**, the $\{11\bar{2}1\}$ twin nucleates at grain boundary without the formation of BSFs inside the twin embryo. Once needle-shaped twin with a pair of planar faults forming from one end of the grain boundary in grain G3 (see **Figure 4.13(b)**), the $\{11\bar{2}1\}$ twin tip propagates in the lateral direction by the planar faults shearing towards the other end of the grain (see **Figure 4.13(b-d)**) until the twin tip meets the other side grain boundary of G3 at a strain of 6.8% as shown in **Figure 4.13(e)**. With further straining, the twin only

grows in vertical direction by the simple atomic shuffle [48], leading to the increase of the width of the twin lamella (see **Figure 4.13(f-h)**). Although we can still observe the interface mismatch (disconnections) at the TB interface as shown in **Figure 4.14(c)**, different from the $\{10\bar{1}2\}$ and $\{10\bar{1}1\}$ twins, the formation of these disconnections is not relevant to the interaction between the BSFs and TB interface because no BSF is characterized inside the $\{11\bar{2}1\}$ twinned region. The disconnection (or interfacial step) is associated with a twinning dislocation as shown in **Figure 4.14(c)**.

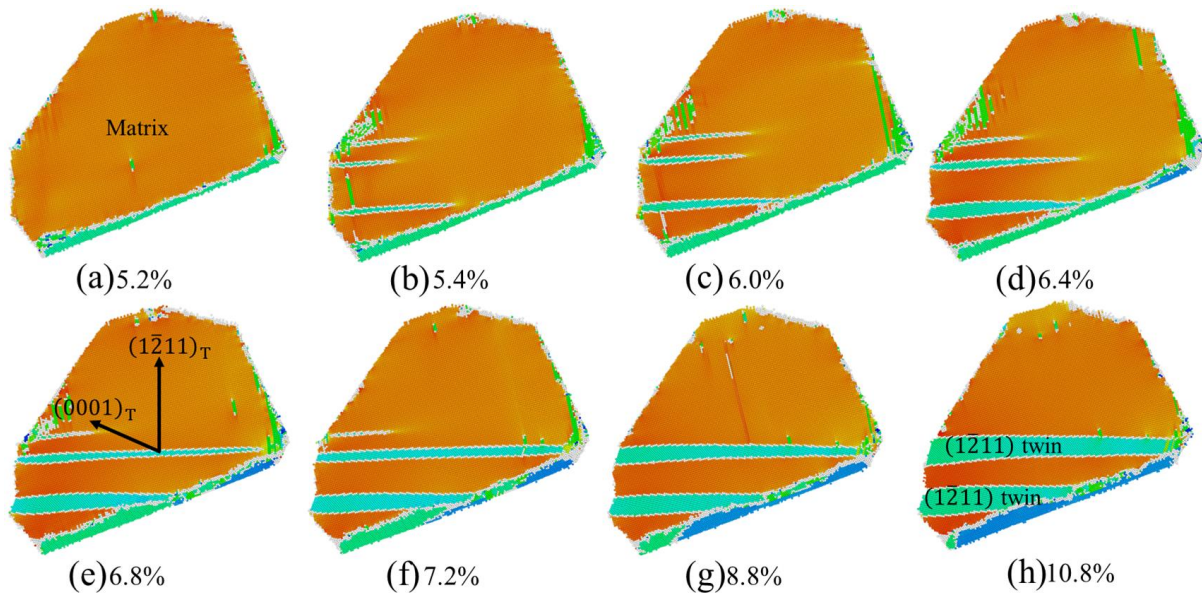


Figure 4.13. Microstructural evolution of the $\{11\bar{2}1\}$ extension twin in G3 during uniaxial compression stress loading along X-direction at different strain levels.

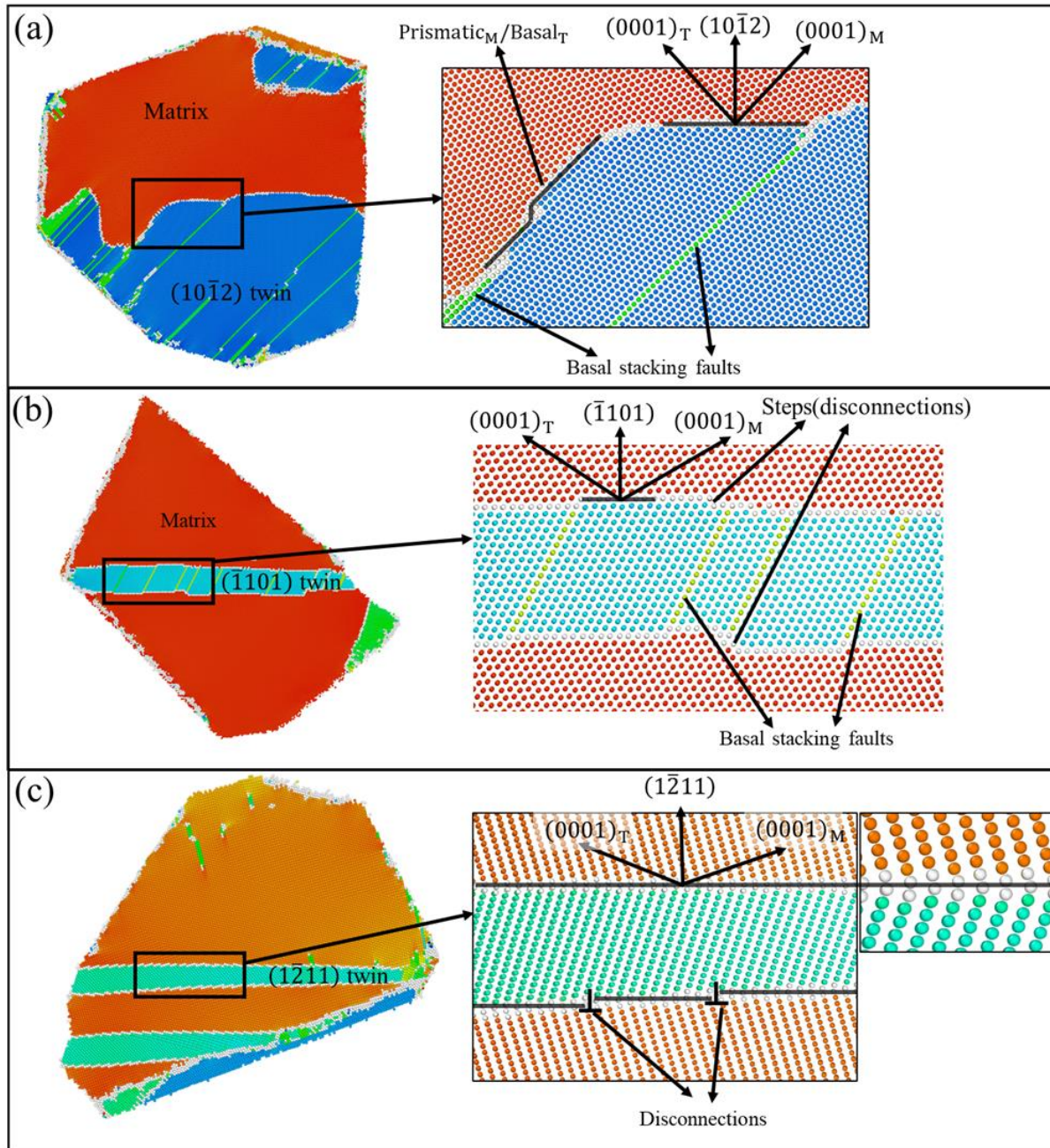


Figure 4.14. Illustration of twinning boundary interface structures for (a) the $\{10\bar{1}2\}$ twin, (b) the $\{10\bar{1}1\}$ twin and (c) the $\{12\bar{1}1\}$ twin, respectively.

4.5.4 Disconnections at Twin-Matrix Interface

4.5.4.1 $\{11\bar{2}1\}$ Extension Twin

Following Serra et al [22], **Figure 4.15(a)** shows the relaxed structure of a ‘perfect’, i.e., undislocated $\{11\bar{2}1\}$ interface which is characterized by the twinning plane $K_1 = \{11\bar{2}1\}$, twinning direction $\eta_1 = \frac{1}{6}[\bar{1}2\bar{1}6]$, conjugate plane $K_2 = \{0001\}$ and conjugate direction $\eta_2 = \frac{1}{3}[1\bar{2}10]$. The images are viewed from a $[10\bar{1}0]$ zone axis and the filled circles represent atoms and different colors, i.e., green, red, black and yellow denote the different positions of atoms at the four successive layers along the $[10\bar{1}0]$ direction in the idea hcp lattice. In particular, the green and red circles correspond to atoms in the position A of the ...ABAB... stacking sequence formed by (0001) planes while the black and yellow circles correspond to atoms in the position B of (0001) planes. Fernández et al [49] have shown that two possible initial configurations (structures R and D) of $(11\bar{2}1)$ TB exist and R structure would reach the same configuration with D structure after relaxation, where the matrix half-crystal and twinned half-crystal have the same stacking sequence of ...ABAB... respect to the reflection in the interfacial plane. Besides, the recent ab initio calculations and atomistic simulations [45] suggest that Type I (D) twin has much lower energy compared to the type II structure (R) although both structures can stably exist. Therefore, in the current EAM potential-based calculation, the more stable (D) one is observed as shown in **Figure 4.15(a, b)**.

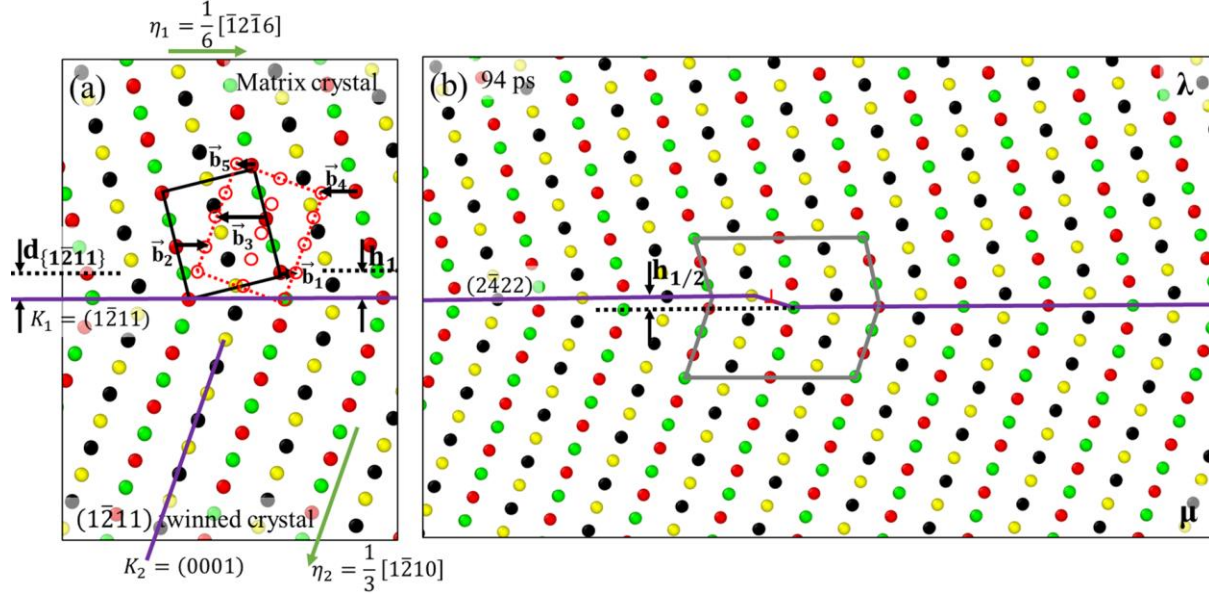


Figure 4.15. The $[10\bar{1}0]$ projection of (a) the undislocated $\{11\bar{2}1\}$ TB interface showing the twinning elements and the displacement by which matrix atoms move to the lattice sites in the twin; (b) the distorted $\{11\bar{2}1\}$ TB showing the interfacial step associated with a twinning dislocation at a time of 94 ps. In the matrix crystal of Figure (a), filled symbols represent lattice sites of the matrix and open symbols (red) are lattice sites of the twin.

In crystallography, twins can lead to a multiplicity of defects, called disconnections with finite h and \mathbf{b} values parallel to the interface. Therefore, these defects can be expressed by a pair of Burgers vector \mathbf{b} and step height h , i.e., (\mathbf{b}_i, h_i) and for each disconnection, there is a complementary one with opposite sign of Burgers vector and negative step sense written as $(-\mathbf{b}_i, -h_i)$. The Burgers vectors are obtained by combining two displacements by translation vectors, one belonging to the matrix crystal, $\mathbf{t}(\lambda)$, and the other to the twin, $\mathbf{t}(\mu)$. Then, the Burgers can be written as $\mathbf{b} = \mathbf{t}(\lambda) - \mathbf{t}(\mu)$ and the step height is equal to $\mathbf{n} \cdot \mathbf{t}(\lambda) = \mathbf{n} \cdot \mathbf{t}(\mu)$ where \mathbf{n} is the unit normal to the K_1 plane. Detailed description can be found in [50, 51]. Burgers vectors in the transformation from the matrix atoms to the twin atoms are shown in **Figure 4.15(a)**, where five Burgers vectors are presented. The most frequently discussed disconnection in $(11\bar{2}1)$ are $\pm(\mathbf{b}_1, h_1)$, where $\mathbf{t}(\lambda) = \frac{1}{3}[1\bar{2}10]$, $\mathbf{t}(\mu) = \frac{1}{3}[\bar{1}2\bar{1}0]$, $\mathbf{b}_1 = 0.0197[\bar{1}2\bar{1}6]$, $|\mathbf{b}_1| = 0.491$, $h = d_{\{11\bar{2}1\}}$ and the magnitude of shear s is given

by $s = |\mathbf{b}|/h = 0.614$. The calculation details can be referred in [22]. The lattice parameters calculated by the EAM potential [35] are $a = 3.185$ and $\kappa = c/a = 1.628$. However, as shown in **Figure 4.15(b)**, this disconnection is not observed at the interface while the disconnections $(\mathbf{b}_{1/2}, h_{1/2})$ are characterized. The height of this step is equal to the atomic plane spacing, $d_{\{2\bar{4}22\}}$, and its Burgers vector is $|\mathbf{b}_{1/2}| = |\mathbf{b}_1|/2$. Accordingly, the disconnections (b_1, h_1) in $\{11\bar{2}1\}$ twins are unstable and their dissociations into $(\mathbf{b}_{1/2}, h_{1/2})$ ones are hence energetically degenerate. Details of shear and shuffle components of the displacements produced by passage of a disconnection in growth of $\{11\bar{2}1\}$ can be found in the simulation study by Khater et al [52]. Here, we will focus on the characteristic of $\{10\bar{1}1\}$ TB interface as follows.

4.5.4.2 $\{10\bar{1}1\}$ Contraction Twin

To investigate the migration of steps and disconnections at $\{10\bar{1}1\}$ TB interface, a series of snapshots of grain G9 deformed under the uniaxial tensile stress loading are captured at different timesteps as shown in **Figure 4.16**, where the matrix atoms have been deleted and atoms in GB, TB interface and twinned region are kept. There are two types of steps, i.e., step A and step B (see **Figure 4.16(a)**). Steps A, consisting of two or four layers of $\{10\bar{1}1\}$ atoms exist at the front of the migration line and move continuously along the interface (see **Figure 4.16(b)**) until they merge into GB when reaching the other side of GB. Steps B are left after steps A interact with BSFs. Steps B are formed due to the interaction between BSFs and twinning interface as shown in **Figure 4.16(a)**. Unlike steps A, steps B propagate conservatively and shift vertically as the twin lamella is thickening as shown in **Figure 4.16(d)**. Interestingly, as shown in **Figure 4.16(c)**, the front of migration line which consists of steps A is also disconnected due to the formation of BSFs in twinned region and divided into several segments. Each segment is observed to migrate at different

velocity, and the center segment moves at the highest velocity, which could be the reason why the twin lamella is usually characterized as a lenticular shape. Besides, the newly nucleated steps A at GB often consist of two layers of $\{10\bar{1}1\}$ atoms (see **Figure 4.16(a)**) because this type of step has the lowest formation energy among four possible ones [45, 53]. These steps can also catch up with the previous ones, then merging into new steps with four layers of atoms. Therefore, basal/prismatic interfaces may form at the disconnection sites as shown in **Figure 4.16(c)**, where the interfaces are parallel to either both the basal plane of the matrix and prismatic plane of the twin (i.e., basal_M/prismatic_T interface) or to both the basal plane from the twin and the prismatic plane from the matrix (i.e., basal_T/prismatic_M interface). The transformation and subsequent twinning growth are accompanied by nucleation and migration of disconnections (steps) and growth of stacking faults. The BSFs only grow along stacking fault planar direction and do not migrate along twinning direction i.e., the distance between different BSFs keeps constant.

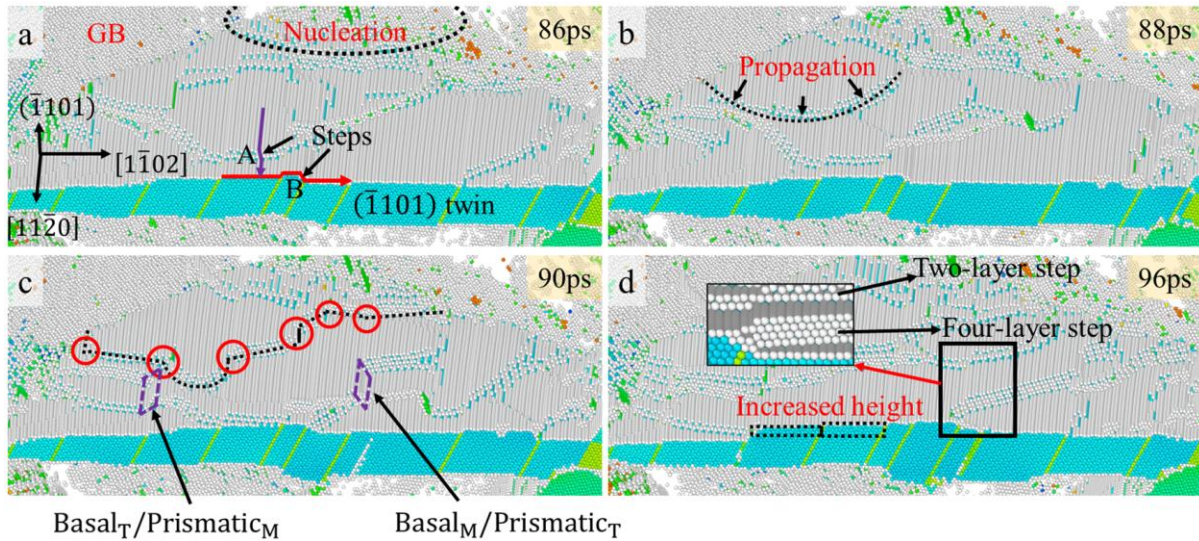


Figure 4.16. Illustration of the growth of the $\{10\bar{1}1\}$ twin by movement of steps along the twin boundary interface in G9 during uniaxial tensile stress loading along X-direction at different timesteps.

The crystallographic structure of a perfect $(1\bar{1}01)$ TB in Mg are shown **Figure 4.17(a)**, where black and yellow colors represent the A-type and B-type sites, respectively. The matrix is twinned by the transformation from matrix sites to twin sites and translation of atoms in the first four layers are as shown in **Figure 4.17(a)** where the red circles represent atoms in twinned crystal. Accordingly, there are four kinds of disconnections (\mathbf{b}_i, h_i) ($i=1, 2, 3, 4$), where $h_i = ih_0$ and $h_0 = d_{(10\bar{1}1)}$. As shown in **Figure 4.16(d)**, two steps are observed in the translation from matrix sites to twin sites and magnitudes of their height are h_2 ($2h_0$) and h_4 ($4h_0$). This observation agrees with topological analysis in a bicystal model [53, 54] which reveals that the two steps have minimal shuffles. Besides steps with h_2 and h_4 , another two steps which have height of h_1 and h_3 are also observed as shown in **Figure 4.17(b)**. They exist near the interaction site between BSFs and TB interface, which are not the same case with h_2 - and h_4 - steps. For example, h_2 -step in **Figure 4.17(b)** exists in between two BSFs and it is mobile along twinning direction. After h_2 -step passes by the interface, twin grow vertically by a height of h_2 (see **Figure 4.16**). For h_1 - and h_3 - steps, they can not move along twinning direction (immobile), and they only migrate along $[11\bar{2}0]$ direction, leading to propagation of BSFs. Considering h_1 - and h_3 - steps having much higher formation energy and lower mobility along twinning direction than steps with height of h_2 and h_4 , their formation is related to dislocation interaction between BSFs and h_2 -step. Twinning dislocation of the step (\mathbf{b}_2, h_2) is mixed and can have a screw component as [55],

$$b_2^{(1\bar{1}01)} = \frac{1}{2} \left(\frac{4\kappa^2 - 9}{3 + 4\kappa^2} \right) [1\bar{1}0\bar{2}] \pm \frac{1}{6} [11\bar{2}0]$$

where, the screw component can either be $\frac{1}{6} [11\bar{2}0]$ or $-\frac{1}{6} [11\bar{2}0]$, corresponding to one-half the lattice vector, $a/2$. In addition, the stacking fault partials $\frac{1}{3} [10\bar{1}0]$ can be expressed as [56],

$$\frac{1}{3}[10\bar{1}0] = \frac{1}{6}[11\bar{2}0] + \frac{1}{6}[2\bar{1}\bar{1}0]$$

Hence, the combination of h_2 -step and h_1 -step may generate a new step with height of h_3 if they have the same sense or a new step with height of h_1 if they have opposite signs. Similarly, when h_2 -step meets with h_3 step, a new step with height of h_1 forms. Interestingly, h_1 - and h_3 - steps are symmetrically distributed along each twinning planar and each pair of steps have a total height of h_2 or h_4 . As shown in **Figure 4.17(b)**, the total height of step h_1^1 and h_1^2 is equal to h_2 and the combination of h_3^1 and h_3^2 is corresponding to h_4 . This characteristic may result from the interaction between BSFs and h_2 or h_4 step, leaving to two possible immobile disconnections at TB interface.

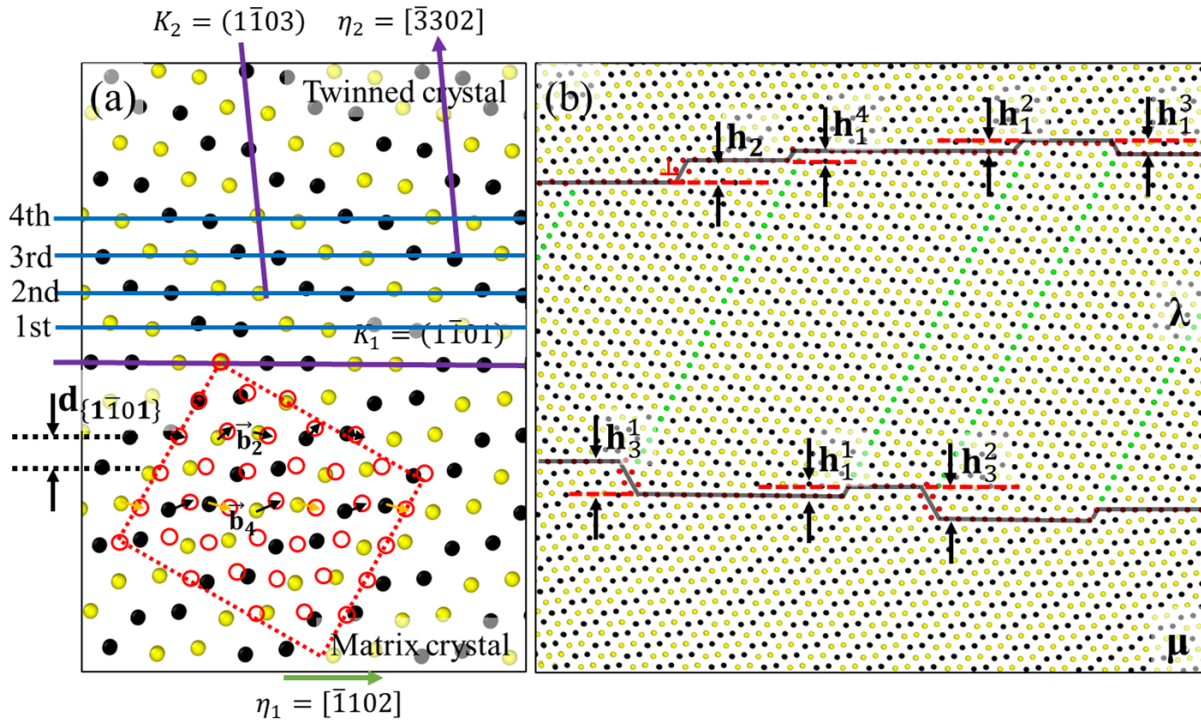


Figure 4.17. The $[11\bar{2}0]$ projection of (a) the undislocated $\{1\bar{1}01\}$ TB interface showing the twinning elements and the displacement by which matrix atoms move to the lattice sites in the twin; (b) the disconnected $\{1\bar{1}01\}$ TBs showing the interfacial steps with different height in G9 deformed at a time of 122 ps under a uniaxial tensile stress loading along X-direction. In figure (a), filled symbols represent lattice sites (type A in black and type B in yellow) of the matrix and open symbols (red) are lattice sites of the twin. In figure (b) Stacking faults consist of atoms in green color.

In the bicrystal simulation, a perfect $\{10\bar{1}1\}$ TB structure was often introduced at its minimum energy state and its growth starts from nucleation of a step with two layers of $\{10\bar{1}1\}$ atoms at TB interface because this initial nucleation state requires the lowest formation energy [45, 53]. However, in the polycrystal, GBs provide source sites for the nucleation of these two-layer-atom steps and since the BSFs inside twinned region interrupt the continuity of the TB interface, the steps will move as a unit in between two BSFs, which may reduce the energy barrier for TB interface migration for twinning in a polycrystal.

4.6 Conclusions

In this work, MD simulations are performed to investigate twin variant selection of three twin modes as well as mechanisms of growth of tension and compression twins in polycrystalline Mg at the atomic scale. The following conclusions can be reached:

- (1) Twin activation is orientation dependent and twin variants with high Schmid factor are preferentially selected to be activated with high probability.
- (2) The nucleation and growth of $\{10\bar{1}1\}$ and $\{10\bar{1}2\}$ twins are accompanied by the formation and propagation of basal stacking faults while no stacking fault is observed in $\{11\bar{2}1\}$ twin.
- (3) The disconnections $(\mathbf{b}_{1/2}, h_{1/2})$ are characterized in $\{11\bar{2}1\}$ twin. Two types of disconnections are observed in $\{10\bar{1}1\}$ twin. The first type of steps with height of $2h_0$ and $4h_0$ are mobile while the other type of steps with h_0 and $3h_0$ are immobile. The formation of h_0 - and $3h_0$ -steps may be due to the interaction between BSF and $2h_0$ - or $4h_0$ - step.
- (4) Due to the formation of BSFs inside twinned region, the front line of mobile steps in $\{10\bar{1}1\}$ twin is divided into different segments and each segment will move as a unit at different velocity.

When the mobile interfacial steps are consumed during twin growth, new steps are nucleated and glide on the TB interface, leading to twin growth in the lateral and vertical directions.

(5) The immobile steps in $\{10\bar{1}1\}$ twin, i.e., h_0 and $3h_0$ exist in the interaction site between BSFs and TB interface and they moves up conservatively accompanying the propagation of stacking fault plane as twin grows in the normal direction.

4.7 Acknowledgement

The authors acknowledge financial support from Natural Sciences and Engineering Research Council of Canada (RGPIN-2017-05187), McGill Engineering Doctoral Award (MEDA), China Scholarship Council (201706050149), and thank Compute Canada for providing computing resources.

4.8 Supplementary Information

4.8.1 Identification of Twin Variant

In HCP Mg alloys, six twin variants for each twinning modes exist and may evolve during deformation. **Table 4.2** lists four twinning modes, i.e., $\{10\bar{1}2\}$ (ET1012), $\{11\bar{2}1\}$ (ET1121) and $\{10\bar{1}1\}$ (CT1011) in Mg and their respective variants V_i ($i = 1-6$) which are represented by the rotation axis and rotation angle. In current polycrystalline model, as shown in **Figure 4.1**, the sample coordinate (reference coordinate) is set as $X \parallel [0001]_s$, $Y \parallel [\bar{1}010]_s$ and $Z \parallel [1\bar{2}10]_s$ and then the crystal basis vectors (crystal coordinate) $[0001]_c$, $[\bar{1}010]_c$ and $[1\bar{2}10]_c$ (**Figure S4.1(b)**) can be expressed in sample coordinate by three Euler angles, respectively, as shown in **Figure S4.1(a)**. As shown in **Figure 4.1**, the polycrystal is constructed by specifying the positions of nodes (grains) and each grain is rotated about X, Y and Z by an angle of α , β and γ , respectively corresponding to the following three rotation matrices,

$$\begin{aligned}
R_X(\alpha) &= \begin{bmatrix} 1 & 0 & 0 \\ 0 & \cos\alpha & -\sin\alpha \\ 0 & \sin\alpha & \cos\alpha \end{bmatrix} \\
R_Y(\beta) &= \begin{bmatrix} \cos\beta & 0 & \sin\beta \\ 0 & 1 & 0 \\ -\sin\beta & 0 & \cos\beta \end{bmatrix} \\
R_Z(\gamma) &= \begin{bmatrix} \cos\gamma & -\sin\gamma & 0 \\ \sin\gamma & \cos\gamma & 0 \\ 0 & 0 & 1 \end{bmatrix}
\end{aligned} \tag{S4.1}$$

which are referred as basic rotation matrices. Thus, we obtain the rotation matrix of parent grain as,

$$\mathbf{R}_p = \begin{bmatrix} R_{11} & R_{12} & R_{13} \\ R_{21} & R_{22} & R_{23} \\ R_{31} & R_{32} & R_{33} \end{bmatrix} = R_Z(\gamma) \cdot R_Y(\beta) \cdot R_X(\alpha) \tag{S4.2}$$

The mostly common used Euler angles $(\varphi_1, \varnothing, \varphi_2)$ are formulated in Bunge convention [57] and the rotation matrix from the sample frame to the crystal orthogonal frame is given by,

$$\mathbf{R} = \begin{bmatrix} R_{11} & R_{12} & R_{13} \\ R_{21} & R_{22} & R_{23} \\ R_{31} & R_{32} & R_{33} \end{bmatrix} = \begin{bmatrix} \cos\varphi_1 \cos\varphi_2 - \sin\varphi_1 \sin\varphi_2 \cos\varnothing & \sin\varphi_1 \cos\varphi_2 + \cos\varphi_1 \sin\varphi_2 \cos\varnothing & \sin\varphi_2 \sin\varnothing \\ -\cos\varphi_1 \sin\varphi_2 - \sin\varphi_1 \cos\varphi_2 \cos\varnothing & -\sin\varphi_1 \sin\varphi_2 + \cos\varphi_1 \cos\varphi_2 \cos\varnothing & \cos\varphi_2 \sin\varnothing \\ \sin\varphi_1 \sin\varnothing & -\cos\varphi_1 \sin\varnothing & \cos\varnothing \end{bmatrix} \tag{S4.3}$$

Once the rotation matrices are computed by Eq. (S4.2), Euler angles can be obtained from equation (S4.3) (let $\mathbf{R} = \mathbf{R}_p$) as,

$$\begin{aligned}
\varphi_1 &= \sin^{-1} \left(\frac{\cos\alpha_3}{\sqrt{\cos\gamma_1^2 + \cos\gamma_2^2}} \right), \in [0, 2\pi] \\
\varnothing &= \cos^{-1}(\cos\gamma_3), \in [0, \pi] \\
\varphi_2 &= \cos^{-1} \left(\frac{\cos\gamma_2}{\sqrt{\cos\gamma_1^2 + \cos\gamma_2^2}} \right), \in [0, 2\pi]
\end{aligned} \tag{S4.4}$$

Since we have obtained the orientation matrix of each parent grain, next we can calculate the theoretical orientation matrices of possible twin variants.

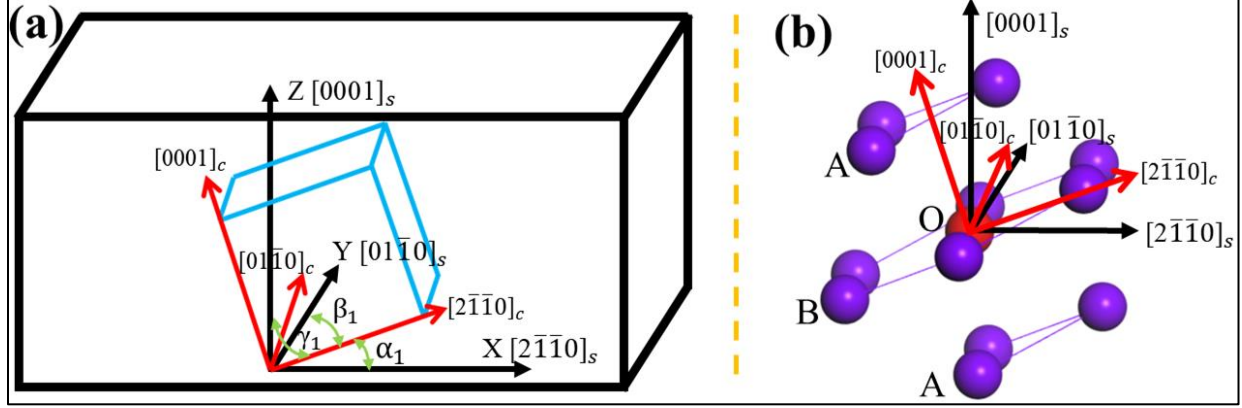


Figure S4.1. (a) Definition of crystal (c) and sample (s) coordinate systems for cubic box, which are highlighted by red and black color, respectively. α , β and γ are defined as the direction angles between a crystal axis and X, Y and Z, respectively. (b) Schematics of HCP configurations, showing a central atom (red) and its nearest neighbors (purple).

To express the twin variants by rotation matrix, another representation of the rotation matrix is introduced via specifying the rotation axis \mathbf{d} and the rotation angle ω . \mathbf{d} is a unit vector, which can be represented by its components d_1, d_2, d_3 (direction cosines) and we can thus write the rotation as $\mathbf{R} = \{\mathbf{d}, \omega\}$ [58]. To obtain a specific rotation, one first carries out a rotation which transforms the Z(X/Y)-axis into the direction \mathbf{d} ; then rotates about the Z-axis through the angle ω ; finally, performs the inverse of the first rotation. The process is expressed as,

$$\mathbf{R}(\mathbf{d}, \omega) = \mathbf{R}_{\mathbf{Z} \rightarrow \mathbf{d}}^{-1} \cdot \mathbf{R}_{\omega}^{\mathbf{Z}} = \mathbf{R}_{\mathbf{Z} \rightarrow \mathbf{d}} = \begin{bmatrix} (1 - d_1^2)\cos\omega + d_1^2 & d_1d_2(1 - \cos\omega) + d_3\sin\omega & d_1d_3(1 - \cos\omega) - d_2\sin\omega \\ d_1d_2(1 - \cos\omega) - d_3\sin\omega & (1 - d_2^2)\cos\omega + d_2^2 & d_2d_3(1 - \cos\omega) + d_1\sin\omega \\ d_1d_3(1 - \cos\omega) + d_2\sin\omega & d_2d_3(1 - \cos\omega) - d_1\sin\omega & (1 - d_3^2)\cos\omega + d_3^2 \end{bmatrix} \quad (\text{S4.5})$$

Using rotation axis and rotation angle of each twin variant in **Table 4.2**, we can thus calculate rotation matrix \mathbf{R}_t^c of all twin variants in crystallographic coordinate system and obtain the rotation matrix from the sample coordinate to the twin variant system by the following inner product of matrices,

$$\mathbf{R}_t^s = \mathbf{R}_p \cdot \mathbf{R}_t^c \quad (\text{S4.6})$$

We can also calculate the Euler angles of specific twin variant using Eq. (S4.3) and letting $\mathbf{R} = \mathbf{R}_t^c$.

4.8.2 Calculation of Schmid Factor

As listed in **Table 4.2**, In HCP Mg alloys, each twinning mode has six twin variants that can be activated during deformation. The probability of the activation of a particular twinning system depends strongly on the mutual orientation of the loading direction and twinning elements (twinning plane and twinning direction) and the critical resolved shear stress (CRSS), τ . This orientation dependence is characterized by the Schmid factor (SF), m , which is defined as,

$$m = \cos \varphi \cdot \cos \lambda \quad (S4.7)$$

where φ is the angle between loading axis and normal to twinning plane, and λ is the angle between loading axis and twinning direction.

Due to the asymmetry of c/a ratio in hcp structures, Miller-Bravais notation with 4 axes is usually adopted to characterize crystal planes and directions. With respect to this four-vector basis, a twinning system with a twinning direction \mathbf{r} and a twinning plane \mathbf{p} can be introduced as $[uvtw]$ and (hkl) , respectively. \mathbf{r} and \mathbf{p} have the relationship,

$$[uvtw] = [hkil]^* = [hkil\lambda^{-2}] \quad (S4.8)$$

where, $\lambda^{-2} = \frac{2}{3}(c/a)^2$, * represents the reciprocal lattice.

According to Eq. (S4.7), it is necessary to calculate the inner product of loading axis and slip direction as well as the loading axis and slip plane. The cosine value of two vectors, $\mathbf{r}_1 = [u_1v_1t_1w_1]$ and $\mathbf{r}_2 = [u_2v_2t_2w_2]$, is given by,

$$\cos(\mathbf{r}_1 \cdot \mathbf{r}_2) = \frac{\mathbf{r}_1 \cdot \mathbf{r}_2}{|\mathbf{r}_1| |\mathbf{r}_2|} = \frac{u_1u_2 + v_1v_2 + t_1t_2 + \lambda^2w_1w_2}{(u_1^2 + v_1^2 + t_1^2 + \lambda^2w_1^2)^{1/2}(u_2^2 + v_2^2 + t_2^2 + \lambda^2w_2^2)^{1/2}} \quad (S4.9)$$

where $\mathbf{r}_1 \cdot \mathbf{r}_2 = \frac{3a^2}{2}(u_1u_2 + v_1v_2 + t_1t_2 + \lambda^2w_1w_2)$.

By combining Eq. (S4.8) and Eq. (S4.9), the cosine value between the line direction $\mathbf{r}_1 = [u_1v_1w_1t_1]$ and plane $\mathbf{p}_1 = [h_1k_1i_1l_1]$ is given by,

$$\cos(\mathbf{r}_1 \cdot \mathbf{p}_1) = \frac{\mathbf{r}_1}{|\mathbf{r}_1|} \cdot \frac{\mathbf{p}_1}{|\mathbf{p}_1|} = \frac{u_1 h_1 + v_1 k_1 + t_1 i_1 + w_1 l_1}{(u_1^2 + v_1^2 + t_1^2 + \lambda^2 w_1^2)^{1/2} (h_1^2 + k_1^2 + l_1^2 + \lambda^{-2} l_1^2)^{1/2}} \quad (S4.10)$$

As a result, when the load is applied with the direction of direction $\mathbf{r}_1 = [u_1 v_1 w_1 t_1]$, the twinning plane $\mathbf{p}_1 = [h_1 k_1 i_1 l_1]$ and the twinning direction $\mathbf{r}_2 = [u_2 v_2 t_2 w_2]$, Schmid factor can be derived by multiplying of Eqs. (S4.9) and (S4.10) as given,

$$\left(\frac{\mathbf{r}_1}{|\mathbf{r}_1|} \cdot \frac{\mathbf{r}_2}{|\mathbf{r}_2|}\right) \times \left(\frac{\mathbf{r}_1}{|\mathbf{r}_1|} \cdot \frac{\mathbf{p}_1}{|\mathbf{p}_1|}\right) = \frac{\cos(\mathbf{r}_1 \cdot \mathbf{r}_2) \times \cos(\mathbf{r}_1 \cdot \mathbf{p}_1)}{(u_1^2 + v_1^2 + t_1^2 + \lambda^2 w_1^2)^{1/2} (u_2^2 + v_2^2 + t_2^2 + \lambda^2 w_2^2)^{1/2}} \times \frac{u_1 h_1 + v_1 k_1 + t_1 i_1 + w_1 l_1}{(u_1^2 + v_1^2 + t_1^2 + \lambda^2 w_1^2)^{1/2} (h_1^2 + k_1^2 + l_1^2 + \lambda^{-2} l_1^2)^{1/2}} \quad (S4.11)$$

4.9 References

- [1] T.M. Pollock, Weight loss with magnesium alloys, *Science* 328 (2010) 986-987.
- [2] S.K. Sahoo, S. Biswas, L.S. Toth, P.C. Gautam, B. Beausir, Strain hardening, twinning and texture evolution in magnesium alloy using the all twin variant polycrystal modelling approach, *International Journal of Plasticity* 128 (2020).
- [3] Q. Peng, Y. Sun, J. Wang, Q. Zu, M. Yang, H. Fu, Structural characteristics of $\{101^{-1}\}$ contraction twin-twin interaction in magnesium, *Acta Materialia* 192 (2020) 60-66.
- [4] S. Kweon, D.S. Raja, Investigation of the mechanical response of single crystal magnesium considering slip and twin, *International Journal of Plasticity* 112 (2019) 1-17.
- [5] Z. Huang, J.-F. Nie, Interaction between hydrogen and solute atoms in $\{101^{-2}\}$ twin boundary and its impact on boundary cohesion in magnesium, *Acta Materialia* 214 (2021).
- [6] H. Fallahi, C. Davies, Evolution of twinning during cyclic loading of magnesium alloy examined by quasi-in-situ EBSD, *Materials Science and Engineering: A* 820 (2021).
- [7] S.H. Park, J.H. Lee, Y.-H. Huh, S.-G. Hong, Enhancing the effect of texture control using $\{10-12\}$ twins by retarding detwinning activity in rolled Mg-3Al-1Zn alloy, *Scripta Materialia* 69(11-12) (2013) 797-800.
- [8] Y. Xin, M. Wang, Z. Zeng, G. Huang, Q. Liu, Tailoring the texture of magnesium alloy by twinning deformation to improve the rolling capability, *Scripta Materialia* 64 (2011) 986-989.
- [9] D. Hou, TianmoLiu, L. Luo, L. Lu, H. Chen, D. Shi, Twinning behaviors of a rolled AZ31 magnesium alloy under multidirectional loading, *Materials Characterization* 124 (2017) 122-128.

- [10] B. Song, R. Xin, X. Zheng, G. Chen, Q. Liu, Activation of multiple twins by pre-tension and compression to enhance the strength of Mg-3Al-1Zn alloy plates, *Materials Science and Engineering A* 621 (2015) 100-104.
- [11] K.B. Nie, K.K. Deng, X.J. Wang, F.J. Xu, K. Wu, M.Y. Zheng, Multidirectional forging of AZ91 magnesium alloy and its effects on microstructures and mechanical properties, *Materials Science and Engineering: A* 624 (2015) 157-168.
- [12] S. Mu, J.J. Jonas, G. Gottstein, Variant selection of primary, secondary and tertiary twins in a deformed Mg alloy, *Acta Materialia* 60(5) (2012) 2043-2053.
- [13] É. Martin, L. Capolungo, L. Jiang, J.J. Jonas, Variant selection during secondary twinning in Mg-3%Al, *Acta Materialia* 58 (2010) 3970-3983.
- [14] S. Godet, L. Jiang, A. Luo, J. Jonas, Use of Schmid factors to select extension twin variants in extruded magnesium alloy tubes, *Scripta Materialia* 55 (2006) 1055-1058.
- [15] J.F. Nie, Y.M. Zhu, J.Z. Liu, X.Y. Fang, Periodic segregation of solute atoms in fully coherent twin boundaries, *Science* 340(6135) (2013) 957-60.
- [16] Z.R. Zeng, Y.M. Zhu, S.W. Xu, M.Z. Bian, C.H.J. Davies, N. Birbilis, J.F. Nie, Texture evolution during static recrystallization of cold-rolled magnesium alloys, *Acta Materialia* 105 (2016) 479-494.
- [17] I.J. Beyerlein, L. Capolungo, P.E. Marshall, R.J. McCabe, C.N. Tomé, Statistical analyses of deformation twinning in magnesium, *Philosophical Magazine* 90(16) (2010) 2161-2190.
- [18] J. Wang, I.J. Beyerlein, C.N. Tomé, An atomic and probabilistic perspective on twin nucleation in Mg, *Scripta Materialia* 63 (2010) 741-746.
- [19] N. Thompson, D.J. Millard, XXXVIII. Twin formation, in cadmium, *The London, Edinburgh, and Dublin Philosophical Magazine and Journal of Science* 43(339) (1952) 422-440.
- [20] V.I. Startsev, V.P. Soldatov, M.M. Brodsky, The rate of twin layer growth in bismuth single crystals, 18(2) (1966) 863-871.
- [21] R.C. Pond, J.P. Hirth, Defects at Surfaces and Interfaces, in: H. Ehrenreich, D. Turnbull (Eds.), *Solid State Physics*, Academic Press 1994, pp. 287-365.
- [22] A. Serra, D.J. Bacon, R.C. Pond, The crystallography and core structure of twinning dislocations in H.C.P. metals, *Acta Metallurgica* 36(12) (1988) 3183-3203.
- [23] J. Wang, J.P. Hirth, C.N. Tomé, (-1012) Twinning nucleation mechanisms in hexagonal-close-packed crystals, *Acta Materialia* 57 (2009) 5521-5530.

- [24] L. Capolungo, I. Beyerlein, Nucleation and stability of twins in hcp metals, *Physical Review B* 78(2) (2008).
- [25] A. Ostapovets, A. Serra, Review of Non-Classical Features of Deformation Twinning in hcp Metals and Their Description by Disconnection Mechanisms, *Metals* 10(9) (2020).
- [26] G. Agarwal, A.M. Dongare, Deformation Twinning in Polycrystalline Mg Microstructures at High Strain Rates at the Atomic Scales, *Scientific Reports* 9(1) (2019) 3550.
- [27] D.E. Spearot, L. Capolungo, C.N. Tomé, Shear-driven motion of Mg {10-12} twin boundaries via disconnection terrace nucleation, growth, and coalescence, *Physical Review Materials* 3(5) (2019) 053606.
- [28] A. Ostapovets, R. Gröger, Twinning disconnections and basal–prismatic twin boundary in magnesium, *Modelling and Simulation in Materials Science and Engineering* 22(2) (2014) 025015.
- [29] Q. Zu, X.-Z. Tang, S. Xu, Y.-F. Guo, Atomistic study of nucleation and migration of the basal/prismatic interfaces in Mg single crystals, *Acta Materialia* 130 (2017) 310-318.
- [30] Y. Liu, N. Li, S. Shao, M. Gong, J. Wang, R.J. McCabe, Y. Jiang, C.N. Tome, Characterizing the boundary lateral to the shear direction of deformation twins in magnesium, *Nature communications* 7 (2016) 11577.
- [31] C. Xu, L. Yuan, D. Shan, B. Guo, The influence of lamellar twins on deformation mechanism in nanocrystalline magnesium under uniaxial compression, *Journal of Materials Science* 54(19) (2019) 12623-12642.
- [32] P.M. Derlet, H. Van Swygenhoven, Atomic positional disorder in fcc metal nanocrystalline grain boundaries, *Physical Review B* 67(1) (2003).
- [33] S. Plimpton, Fast Parallel Algorithms for Short-Range Molecular Dynamics, *Journal of Computational Physics* 117 (1995) 1-19.
- [34] M.S. Daw, S.M. Foiles, M.I. Baskes, The embedded-atom method: a review of theory and applications, *Materials Science Reports* 9(7) (1993) 251-310.
- [35] S.R. Wilson, M.I. Mendeleev, A unified relation for the solid-liquid interface free energy of pure FCC, BCC, and HCP metals, *The Journal of Chemical Physics* 144(14) (2016) 144707.
- [36] A.V. Ivanov, V.M. Uzdin, H. Jónsson, Fast and robust algorithm for energy minimization of spin systems applied in an analysis of high temperature spin configurations in terms of skyrmion density, *Computer Physics Communications* 260 (2021).

- [37] M.E. Tuckerman, J. Alejandre, R. López-Rendón, A.L. Jochim, G.J. Martyna, A Liouville-operator derived measure-preserving integrator for molecular dynamics simulations in the isothermal–isobaric ensemble, *Journal of Physics A: Mathematical and General* 39(19) (2006) 5629-5651.
- [38] A. Stukowski, Visualization and analysis of atomistic simulation data with OVITO—the Open Visualization Tool, *Modelling and Simulation in Materials Science and Engineering* 18(1) (2009) 015012.
- [39] H. Tsuzuki, P.S. Branicio, J.P. Rino, Structural characterization of deformed crystals by analysis of common atomic neighborhood, *Computer Physics Communications* 177(6) (2007) 518-523.
- [40] J.C. E, M.X. Tang, D. Fan, L. Wang, S.N. Luo, Deformation of metals under dynamic loading: Characterization via atomic-scale orientation mapping, *Computational Materials Science* 153 (2018) 338-347.
- [41] A. Stukowski, K. Albe, Extracting dislocations and non-dislocation crystal defects from atomistic simulation data, *Modelling and Simulation in Materials Science and Engineering* 18(8) (2010) 085001.
- [42] Q. Yu, J. Wang, Y. Jiang, R.J. McCabe, N. Li, C.N. Tomé, Twin–twin interactions in magnesium, *Acta Materialia* 77 (2014) 28-42.
- [43] J.W. Christian, S. Mahajan., deformation twinning, *Progress in Materials Science* 39 (1995) 1-157.
- [44] J.P. Hirth, G. Hirth, J. Wang, Disclinations and disconnections in minerals and metals, 117(1) (2020) 196-204.
- [45] O. MacKain, M. Cottura, D. Rodney, E. Clouet, Atomic-scale modeling of twinning disconnections in zirconium, *Physical Review B* 95(13) (2017) 134102.
- [46] O. MacKain, Atomistic modeling of twinning in hexagonal close-packed metals- disconnection nucleation and migration in zirconium, titanium and magnesium, 2017.
- [47] Y. Deng, C. Deng, Size and rate dependent grain boundary motion mediated by disconnection nucleation, *Acta Materialia* 131 (2017) 400-409.
- [48] N. Stanford, R.K.W. Marceau, M.R. Barnett, The effect of high yttrium solute concentration on the twinning behaviour of magnesium alloys, *Acta Materialia* 82(0) (2015) 447-456.

- [49] J.R. Fernández, A.M. Monti, R.C. Pasianott, V. Vitek, An atomistic study of formation and migration of vacancies in (1121) twin boundaries in Ti and Zr, *Philosophical Magazine A* 80(6) (2000) 1349-1364.
- [50] J.P. Hirth, J. Wang, C.N. Tomé, Disconnections and other defects associated with twin interfaces, *Progress in Materials Science* 83 (2016) 417-471.
- [51] J.M. Howe, R.C. Pond, J.P. Hirth, The role of disconnections in phase transformations, *Progress in Materials Science* 54(6) (2009) 792-838.
- [52] H.A. Khater, A. Serra, R.C. Pond, Atomic shearing and shuffling accompanying the motion of twinning disconnections in Zirconium, *Philosophical Magazine* 93 (2013) 1279-1298.
- [53] J. Wang, I.J. Beyerlein, J.P. Hirth, Nucleation of elementary $\{10\text{-}11\}$ and $\{-1013\}$ twinning dislocations at a twin boundary in hexagonal close-packed crystals, *Modelling and Simulation in Materials Science and Engineering* 20(2) (2012) 024001.
- [54] A. Serra, R.C. Pond, D.J. Bacon, Computer simulation of the structure and mobility of twinning dislocations in H.C.P. Metals, *Acta Metallurgica et Materialia* 39(7) (1991) 1469-1480.
- [55] J. Wang, I.J. Beyerlein, J.P. Hirth, C.N. Tomé, Twinning dislocations on $\{1\text{-}011\}$ and $\{1\text{-}013\}$ planes in hexagonal close-packed crystals, *Acta Materialia* 59(10) (2011) 3990-4001.
- [56] B. Li, E. Ma, Zonal dislocations mediating $\{10\text{-}11\}\langle 10\text{-}12\rangle$ twinning in magnesium, *Acta Materialia* 57 (2009) 1734-1743.
- [57] K.U. F., T.C. N., W.H. R., *TEXTURE AND ANISOTROPY*, Cambridge University Press, Cambridge, 1998.
- [58] H.J. Bunge, *Texture Analysis in Materials Science*, Butterworth & Co, German Democratic Republic, 1982.

Chapter 5: Atomic-scale Investigation of Deformation Behavior in Polycrystalline Mg, Mg-Al and Mg–Y alloys

5.1 Preface

It is well known that rare earth (RE) elements are the most promising alloying elements to substantially enhance the mechanical and physical properties of Mg alloys. However, alloying with RE elements are cost prohibitive and not widely available. Therefore, there is a need to focus beyond RE elements in design of high-performance Mg alloys. The important step is to understand the difference of deformation response for between Mg-RE alloys and no RE contained Mg alloys. Therefore, this chapter systematically characterized and compared the activation of deformation modes in Mg and Mg-Al/Y systems by performing the tension and compression stress loading on three Mg alloy systems via molecular dynamics simulations. Different deformation modes were observed in the selected systems and the results were discussed in an attempt to provide deeper insight into the special role of RE solute in affecting the material behavior of the studied alloys.

- This chapter presents a short communication to be submitted as:

Atomic-scale Investigation of Deformation Behavior in Polycrystalline Mg, Mg-Al and Mg–Y alloys

Huicong Chen, Jingli Li, Jun Song and Xin Yi

5.2 Abstract

Large-scale molecular dynamics (MD) simulations have been used to investigate the effect of rare earth elements on the activation of deformation modes under tension and compression loading. The results show the deformation response of polycrystalline Mg and Mg-Al systems is observed to be dominated by the nucleation and growth of compression and tension twins in a compression loading while dislocations are more profuse under a tensile loading. In addition, twinning volume increase faster in compression stress loading than that in tensile stress loading. In case of Mg-Y alloy system, twinning occurs only in the compressed sample and pyramidal slips are activated in tensile sample to accommodate plastic strain along c-axis. This particular observation is found to be ascribed to addition of Y.

5.3 Introduction

Magnesium (Mg) has the highest strength to weight ratio among structural materials, providing great potential for energy savings in the automotive and aerospace industries [1]. Despite its desirable specific strength, low room temperature ductility and formability has severely limited its wide application as a wrought material [2]. This inadequacy is directly associated with a limited number of independent deformation systems which are required for a homogenous deformation at low temperature [1, 2]. In some recent studies [2-13], it has been demonstrated that the addition of certain alloying elements can enhance the performance of Mg alloys, i.e., ductility and formability in wrought processing. Various alloying pathways and choices of alloy elements [2, 3, 8-10, 13-18] have been explored experimentally. For example, alloying with solutes like Y, Zr, Nd and Ca etc. can enhance the activity of non-basal slip systems, therefore, improving ductility [3, 5, 7, 8, 19]. Besides, the modified textures and refined grain sizes due to the microalloying have been

found in Mg-Zn based alloys [3, 14, 17, 18] where the resulting alloy systems exhibit high strength as well as favorable ductility.

To date, though there remain vast possibilities in the periodic table to be explored for the design of Mg alloys, the experimental data so far seem to indicate that the addition of rare earth elements (RE) is more effective in improving the mechanical properties including ductility and formability [2, 6, 10, 13]. For example, it was found that addition of the RE elements such as Nd and Y would significantly increase the CRSS of basal slip and twinning so that the $CRSS_{basal}/CRSS_{twinning}$ ratio increases while the $CRSS_{prismatic}/CRSS_{twinning}$ and the $CRSS_{pyramidal}/CRSS_{twinning}$ ratios decrease [8, 20, 21]. A recent work reported that the poor formability or ductility of pure magnesium is ascribed to pyramidal dislocation transformations to an immobile structure [22]. A subsequent computational study [23] showed that adding appropriate alloying elements can enhance cross-slip of $\langle c+a \rangle$ screw dislocations. Specifically, very dilute addition of RE elements such as Ce, Nd, Y and Gd can lead to obvious such enhancement and therefore, efficiently improve ductility and formability. Moreover, a small addition of RE elements can notably weaken the recrystallization texture and reduce the tension-compression asymmetry (TCA), leading to a significant improvement in the formability [15, 19, 24, 25]. Despite the widespread experimental evidence showing the effectiveness of RE elements in improving the mechanical properties of Mg alloys, the exact mechanisms underlying such improvement are still elusive in many aspects. Thus, proper selection of alloy elements for Mg alloys stays much of a puzzle and often ends up in an *ad-hoc* approach. Therefore, there is a need to focus beyond RE elements in design of high-performance Mg alloys. An immediate and imperative step is to better understand the mechanism of RE effect on deformation response in Mg-RE alloys.

Challenges exist in direct observation of deformation evolution using experimental techniques, especially for obtaining the three-dimensional characterization. Classical molecular dynamics (MD) simulations enable the investigation of the fundamental mechanisms of experimentally observed macroscopic phenomena at the atomic scales and complement the gap. Here, Y was chosen as a representative RE element because it has been experimentally shown to effectively improve mechanical properties of Mg [2, 5, 12, 13, 17, 23, 26]. Therefore, polycrystals for three Mg alloy systems, i.e., pure Mg, Mg-Al and Mg-Y were constructed and then deformed under tensile and compression stress loadings using MD simulations. Microstructure investigations at atomic scale were carried out in order to visualize the difference of deformation response to a tensile/compression loading in the selected alloy systems.

5.4 Simulation Method

As shown in **Figure 5.1(a)**, the simulated Mg polycrystal sample consisting of 12 randomly oriented grains is built with dimensions of $60 \text{ nm} \times 60 \text{ nm} \times 60 \text{ nm}$ using the “Voronoi tessellation method”. The grain orientation distribution is shown in the (0001) pole figure of **Figure 5.1(b)**. MD simulations are performed using Large-scale Atomic/Molecular Massively Parallel Simulator (LAMMPS) [27] and the interatomic forces for pure magnesium is computed by the embedded-atom method (EAM) potential [28]. To construct Mg-Al and Mg-Y alloy models, 1 at% Mg atoms are randomly substituted by Al and Y, respectively and EAM potentials for Mg-Al [29] and for Mg-Y [26] are used to calculate the interatomic forces. Each sample is first relaxed using conjugate gradient minimization method [30] and then equilibrated for 100 ps at 300 K using an isothermal–isobaric (NPT) ensemble [31] to ensure zero pressures along all three periodic directions. Afterwards the model is deformed by a uniaxial tensile/compression loading along the X axis to a total strain of 20% at a constant strain rate of $1 \times 10^9 \text{ s}^{-1}$. The integration time-step is fixed at 2

fs and periodic boundary conditions are applied in all three directions. The Open Visualization Tool (Ovito) [16] is used to visualize the results. The common-neighbor analysis is used to identify the local defects. The dislocation extraction algorithm (DXA) [32] is performed to extract dislocations in deformed sample.

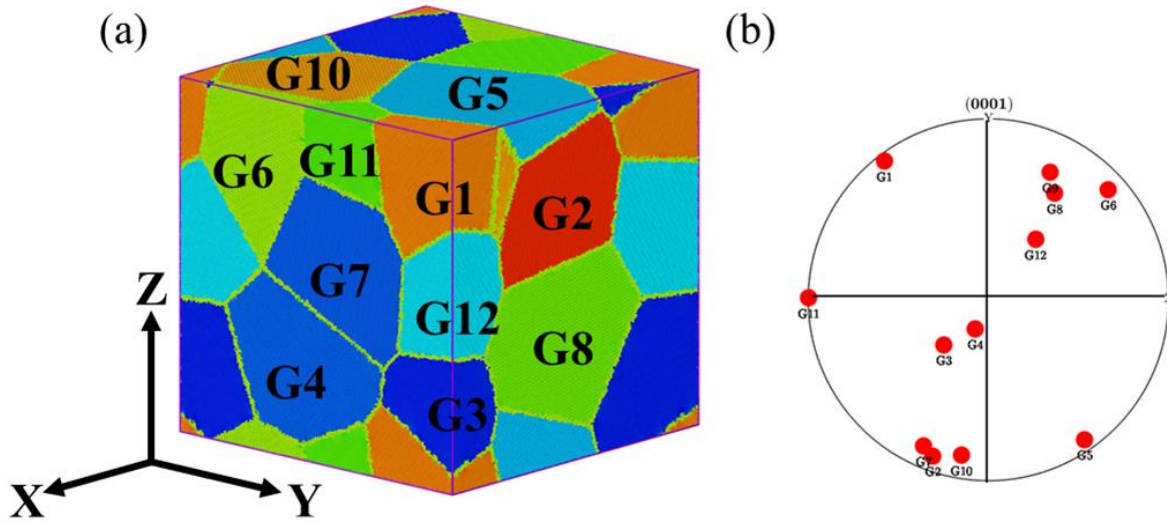


Figure 5.1. (a) Initial polycrystal structures (atoms are colored according to its local lattice orientation) and (b) orientation distribution in pole (0001) figure.

5.5 Results and Discussions

5.5.1 Microstructures in Compression and Tensile Simulation

Figure 5.2(b, c and d) shows snapshots of a section of the polycrystalline microstructure for three alloy systems deformed at a strain of 7.4% under a compression loading along X-direction. Two twinning modes $\{10\bar{1}2\}$ and $\{10\bar{1}1\}$ are determined by using the method in Chapter 4. Twins are observed in all three samples although their volume fraction differs since the solute atoms may influence twinning boundary migration and retard its further growth [33, 34]. Therefore, the matrix grain 9 (G9), as marked in **Figure 5.2**(a), almost twinned in pure Mg (**Figure 5.2**(b)) and partially

twinned in Mg-Al system (**Figure 5.2(c)**). However, only a limited fraction of twinning structure is observed in Mg-Y system as shown in **Figure 5.2(d)**.

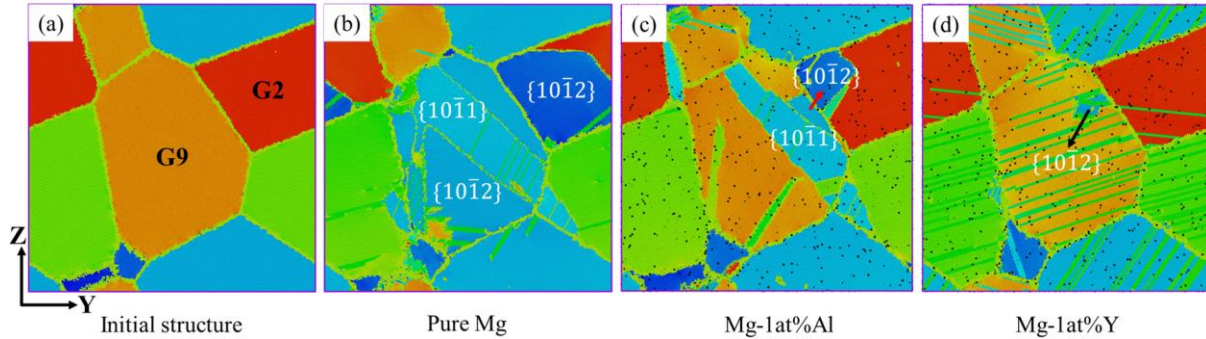


Figure 5.2. Microstructural snapshots perpendicular to X-direction of (a) the initial sample and samples deformed at a strain of 7.4% under uniaxial compression stress loading along X-direction: (b) Pure Mg, (c) Mg-1at%Al and (d) Mg-1at%Y, where atoms Al and Y are colored in black in Figure (c) and (d).

Figure 5.3(b, c and d) shows snapshots of a section of the polycrystalline microstructure for three alloy systems deformed at a strain of 7.4% under a tensile loading along X-direction. Twins are only observed in pure Mg and Mg-Al system and no twin is activated in Mg-Y sample deformed under a tensile loading. Instead of twinning, we can observe many stacking faults formed due to the dislocation nucleation and slip in the deformed Mg-Y system for both compression and tensile stress, which means dislocation slip is dominated in Mg-Y alloy and experimental TEM studies [10, 33, 35] has verified RE elements can promote dislocation, especially non-basal slip systems, and restrict twinning

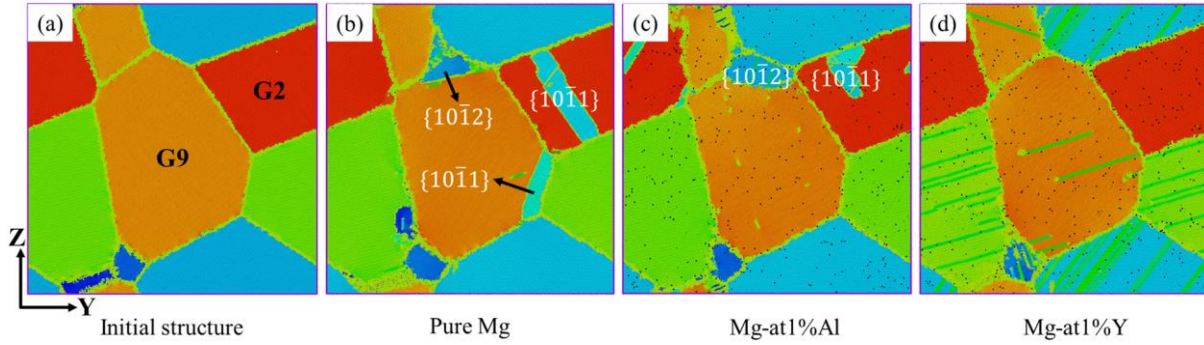


Figure 5.3. Microstructural snapshots perpendicular to X-direction of (a) the initial sample and samples deformed at a strain of 7.4% under uniaxial tensile stress loading along X-direction: (b) Pure Mg, (c) Mg-1at%Al and (d) Mg-1at%Y, where atoms Al and Y are colored in black in Figure (c) and (d).

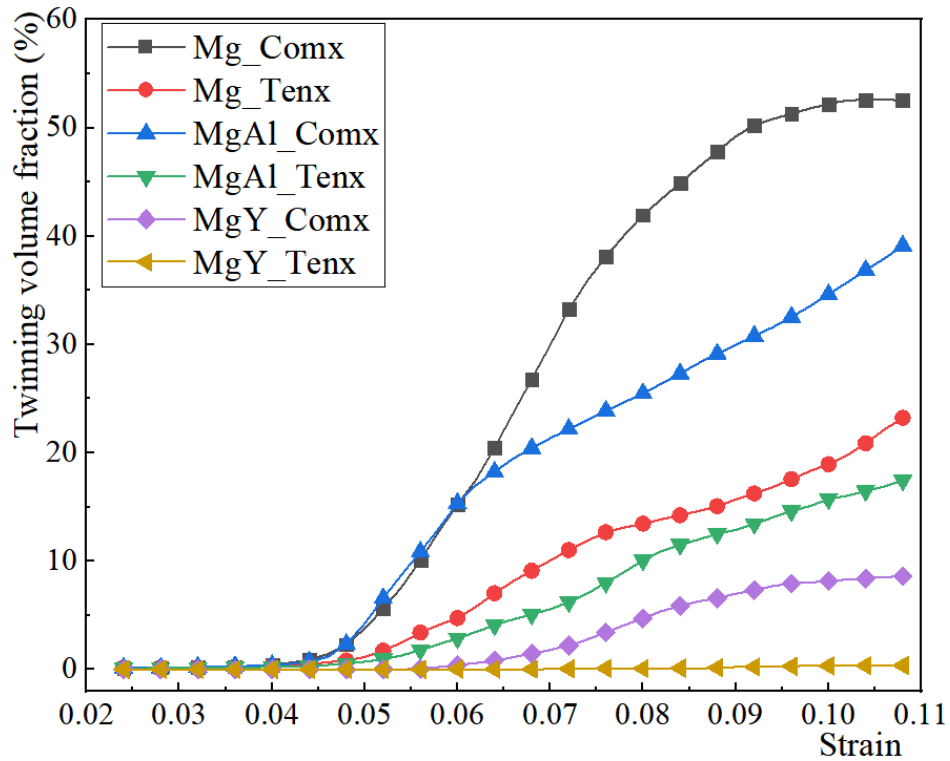


Figure 5.4. Twin volume fraction evolution with straining for three alloy systems of Mg, Mg-Al and Mg-Y under tensile and compression loading.

Figure 5.4 shows the volume fraction of the material undergoing twinning and we find that almost no twin is formed in Mg-Y alloy throughout the tensile loading process and even compression

loading can not largely activate twinning for Mg-Y system. The effect of Y on deformation modes is provided below.

5.5.2 Effect of RE on Deformation Behavior of Magnesium

Figure 5.5 illustrates deformation modes in grain G9 of each sample compressed/tensile to a strain of 7.4%. As shown in **Figure 5.5(a, c)**, no dislocation is observed in matrix of Mg and Mg-Al under compression stress except those geometrically necessary dislocations which forms matrix-twin interfaces and do not provide plastic deformation. However, when Mg and Mg-Al deformed at a tensile loading, small fraction of the matrix twinned, and basal dislocations were also activated. Basal partial dislocations $\frac{1}{3}[01\bar{1}0]$ are dominant in pure Mg and perfect basal dislocations $\frac{1}{3}[11\bar{2}0]$ are profusely formed in Mg-Al system. This is because the leading partial is strongly blocked by Al atoms and is thus compelled to merge with the trailing partial. Once merged, the narrow core structure of the resultant perfect dislocation will restrict its mobility [36]. For Mg-Y alloy system, twin as well as some basal partials, are activated in compression loading simulation. $\frac{1}{18}[2\bar{6}4\bar{3}]$ dislocation is also observed in the matrix, but this type of dislocation is rarely reported in HCP structures and maybe come from grain boundary and twinning boundaries, which is not our focus here. Under tensile loading, Mg-Y deformed by only gliding of slips as shown in **Figure 5.5(f)** where pyramidal dislocation $\frac{1}{9}[10\bar{1}3]$ was also activated to accommodate deformation. More pyramidal slips (**Figure 5.6(e)**) were activated in grain G7 under a tensile loading and this slip also appeared in compression sample (**Figure 5.6(f)**) where there is no competition from twinning to accommodate plasticity. Interestingly, twinning occurred in G7 when Mg-Al system was deformed under both loading states as shown in **Figure 5.6(c)** and (d). Twin growth proceeds by the thermally activated nucleation and expansion of twinning dislocation loops on a pre-existing

twin boundary. The energy barrier for this process can be reduced due to the local concentration of random solutes [33], so twins were observed in Mg-Al samples.

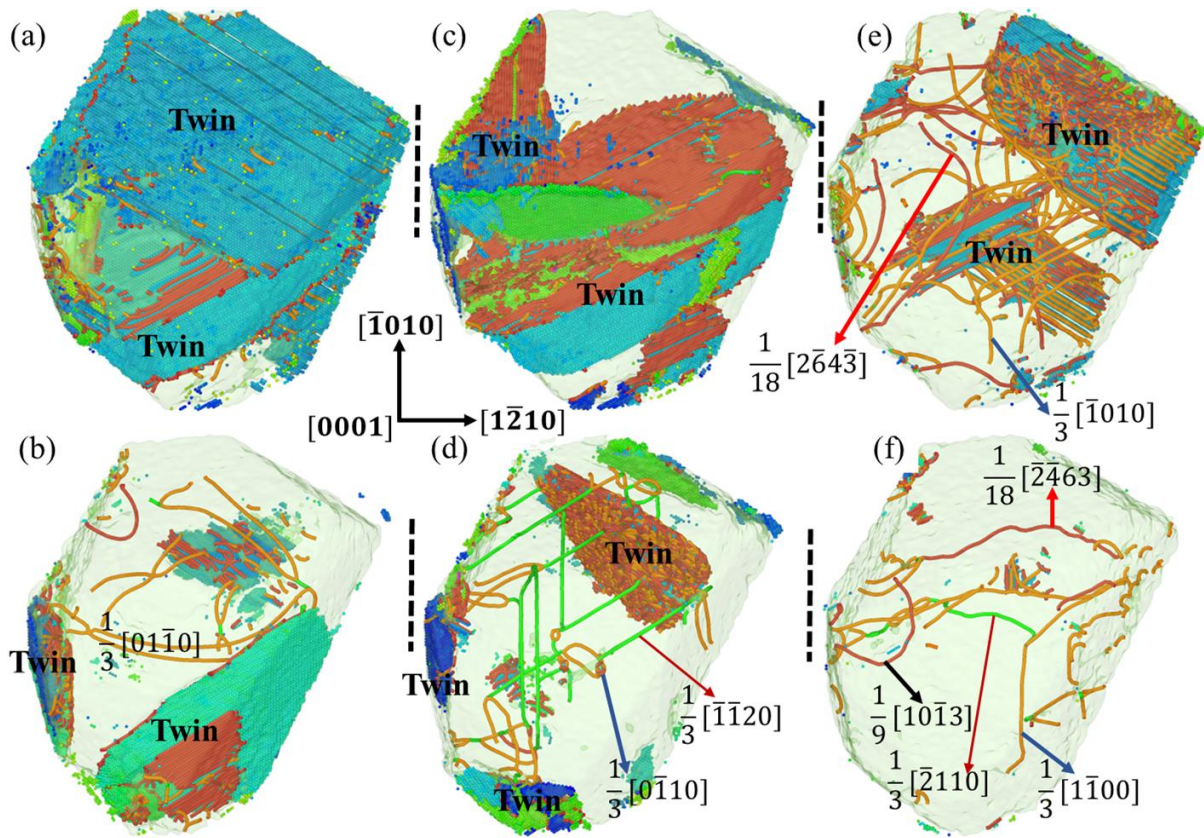


Figure 5.5. Illustration of active deformation modes for grain 9 deformed to a total strain of 7.4% under compression stress (a) pure Mg, (c) Mg-Al and (e) Mg-Y, and under tensile stress (b) pure Mg, (d) Mg-Al and (f) Mg-Y. Atoms of the matrix are deleted and only twinned atoms are revealed in all Figures.

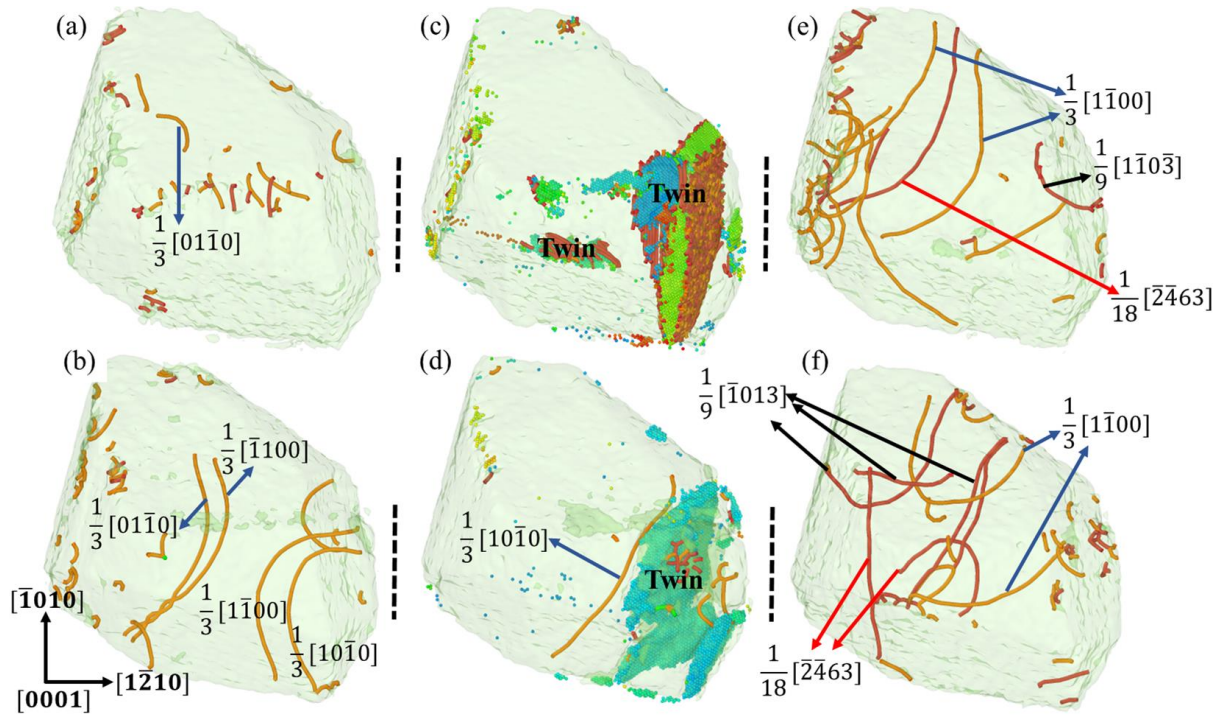


Figure 5.6. Illustration of active deformation modes for grain 7 deformed to a total strain of 7.4% under compression stress (a) pure Mg, (c) Mg-Al and (e) Mg-Y, and under tensile stress (b) pure Mg, (d) Mg-Al and (f) Mg-Y. Atoms of the matrix are deleted and only twinned atoms are revealed in all Figures.

5.6 Conclusion

The deformation response of polycrystalline Mg and Mg-Al systems is observed to be dominated by the nucleation and growth of compression and tension twins in a compression loading while in case of tensile loading, dislocations are more active because of the inactive twinning behavior. Twin is hardly activated in Mg-Y alloy deformed under a tensile loading and thus pyramidal slips would be dominant in accommodating plasticity due to the retardation of twinning.

5.7 Acknowledgements

The authors acknowledge financial support from Natural Sciences and Engineering Research Council of Canada (NSERC), McGill Engineering Doctoral Award (MEDA), China Scholarship Council (201706050149), and thank Compute Canada for providing computing resources.

5.8 References

- [1] T.M. Pollock, Weight loss with magnesium alloys, *Science* 328 (2010) 986-987.
- [2] M.A. Bhatia, S.N. Mathaudhu, K.N. Solanki, Atomic-scale investigation of creep behavior in nanocrystalline Mg and Mg–Y alloys, *Acta Materialia* 99 (2015) 382-391.
- [3] B. Langelier, A.M. Nasiri, S.Y. Lee, M.A. Gharghouri, S. Esmaeili, Improving microstructure and ductility in the Mg-Zn alloy system by combinational Ce-Ca microalloying, *Materials Science and Engineering a-Structural Materials Properties Microstructure and Processing* 620 (2015) 76-84.
- [4] Y.Z. Du, X.G. Qiao, M.Y. Zheng, K. Wu, S.W. Xu, Development of high-strength, low-cost wrought Mg–2.5mass% Zn alloy through micro-alloying with Ca and La, *Materials & Design* 85 (2015) 549-557.
- [5] A. Maldar, L. Wang, B. Liu, W. Liu, Z. Jin, B. Zhou, X. Zeng, Activation of $\langle c \rangle$ dislocations in Mg with solute Y, *Journal of Magnesium and Alloys* (2021).
- [6] B. Lei, B. Jiang, H. Yang, Z. Dong, Q. Wang, M. Yuan, G. Huang, J. Song, D. Zhang, F. Pan, Effect of Nd addition on the microstructure and mechanical properties of extruded Mg-Gd-Zr alloy, *Materials Science and Engineering: A* 816 (2021).
- [7] H.-S. Jang, J.-K. Lee, A.J.S.F. Tapia, N.J. Kim, B.-J. Lee, Activation of non-basal $\langle c + a \rangle$ slip in multicomponent Mg alloys, *Journal of Magnesium and Alloys* (2021).
- [8] J. Wu, S. Si, K. Takagi, T. Li, Y. Mine, K. Takashima, Y.L. Chiu, Study of basal $\langle a \rangle$ and pyramidal $\langle c + a \rangle$ slips in Mg-Y alloys using micro-pillar compression, *Philosophical Magazine* 100(11) (2020) 1454-1475.
- [9] R.K. Mishra, A. Brahme, R.K. Sabat, L. Jin, K. Inal, Twinning and texture randomization in Mg and Mg-Ce alloys, *International Journal of Plasticity* 117 (2019) 157-172.
- [10] Z. Wu, R. Ahmad, B. Yin, S. Sandlöbes, W.A. Curtin, Mechanistic origin and prediction of enhanced ductility in magnesium alloys, *Science* 359 (2018) 447-452.
- [11] S. Sandlöbes, M. Friák, J. Neugebauer, D. Raabe, Basal and non-basal dislocation slip in Mg–Y, *Materials Science and Engineering: A* 576 (2013) 61-68.
- [12] S. Sandlöbes, S. Zaeferrer, I. Schestakow, S. Yi, R. Gonzalez-Martinez, On the role of non-basal deformation mechanisms for the ductility of Mg and Mg–Y alloys, *Acta Materialia* 59(2) (2011) 429-439.

- [13] S. R. AGNEW, M. H. YOO, C.N. TOME'. Application of texture simulation to understanding mechanical behavior of Mg and solid solution alloys containing Li or Y.pdf, *Acta Material* (2001) 4277-4289.
- [14] B.L. Wu, Y.H. Zhao, X.H. Du, Y.D. Zhang, F. Wagner, C. Esling, Ductility enhancement of extruded magnesium via yttrium addition, *Materials Science and Engineering: A* 527(16) (2010) 4334-4340.
- [15] B.Q. Shi, R.S. Chen, W. Ke, Effects of yttrium and zinc on the texture, microstructure and tensile properties of hot-rolled magnesium plates, *Materials Science and Engineering: A* 560 (2013) 62-70.
- [16] A. Stukowski, Visualization and analysis of atomistic simulation data with OVITO—the Open Visualization Tool, *Modelling and Simulation in Materials Science and Engineering* 18(1) (2009) 015012.
- [17] N. Kumar, D. Choudhuri, R. Banerjee, R.S. Mishra, Strength and ductility optimization of Mg–Y–Nd–Zr alloy by microstructural design, *International Journal of Plasticity* 68(0) (2015) 77-97.
- [18] T.T.T. Trang, J.H. Zhang, J.H. Kim, A. Zargarani, J.H. Hwang, B.C. Suh, N.J. Kim, Designing a magnesium alloy with high strength and high formability, *Nature communications* 9(1) (2018).
- [19] Z. Yu, X. Xu, K. Shi, B. Du, X. Han, T. Xiao, S. Li, K. Liu, W. Du, Development and characteristics of a low rare-earth containing magnesium alloy with high strength-ductility synergy, *Journal of Magnesium and Alloys* (2022).
- [20] V. Herrera-Solaz, P. Hidalgo-Manrique, M.T. Pérez-Prado, D. Letzig, J. Llorca, J. Segurado, Effect of rare earth additions on the critical resolved shear stresses of magnesium alloys, *Materials Letters* 128 (2014) 199-203.
- [21] K.-H. Kim, J.B. Jeon, N.J. Kim, B.-J. Lee, Role of yttrium in activation of $\langle c + a \rangle$ slip in magnesium: An atomistic approach, *Scripta Materialia* 108 (2015) 104-108.
- [22] Z. Wu, W.A. Curtin, The origins of high hardening and low ductility in magnesium, *Nature* 526 (2015) 62-7.
- [23] S. Sandlöbes, M. Friák, S. Zaeferrer, A. Dick, S. Yi, D. Letzig, Z. Pei, L.F. Zhu, J. Neugebauer, D. Raabe, The relation between ductility and stacking fault energies in Mg and Mg–Y alloys, *Acta Materialia* 60(6-7) (2012) 3011-3021.

- [24] N. Stanford, D. Atwell, A. Beer, C. Davies, M.R. Barnett, Effect of microalloying with rare-earth elements on the texture of extruded magnesium-based alloys, *Scripta Materialia* 59(7) (2008) 772-775.
- [25] N. Stanford, M.R. Barnett, The origin of “rare earth” texture development in extruded Mg-based alloys and its effect on tensile ductility, *Materials Science and Engineering: A* 496(1) (2008) 399-408.
- [26] Z. Pei, L.F. Zhu, M. Friák, S. Sandlöbes, J. von Pezold, H.W. Sheng, C.P. Race, S. Zaeferrer, B. Svendsen, D. Raabe, J. Neugebauer, Ab initio and atomistic study of generalized stacking fault energies in Mg and Mg–Y alloys, *New Journal of Physics* 15(4) (2013) 043020.
- [27] S. Plimpton, Fast Parallel Algorithms for Short-Range Molecular Dynamics, *Journal of Computational Physics* 117 (1995) 1-19.
- [28] S.R. Wilson, M.I. Mendeleev, A unified relation for the solid-liquid interface free energy of pure FCC, BCC, and HCP metals, *The Journal of Chemical Physics* 144(14) (2016) 144707.
- [29] X.Y. Liu, J.B. Adams, GRAIN-BOUNDARY SEGREGATION IN Al-10%Mg ALLOYS AT HOT WORKING TEMPERATURES, *Acta mater.* 46 (1998).
- [30] A.V. Ivanov, V.M. Uzdin, H. Jónsson, Fast and robust algorithm for energy minimization of spin systems applied in an analysis of high temperature spin configurations in terms of skyrmion density, *Computer Physics Communications* 260 (2021).
- [31] M.E. Tuckerman, J. Alejandre, R. López-Rendón, A.L. Jochim, G.J. Martyna, A Liouville-operator derived measure-preserving integrator for molecular dynamics simulations in the isothermal–isobaric ensemble, *Journal of Physics A: Mathematical and General* 39(19) (2006) 5629-5651.
- [32] A. Stukowski, K. Albe, Extracting dislocations and non-dislocation crystal defects from atomistic simulation data, *Modelling and Simulation in Materials Science and Engineering* 18(8) (2010) 085001.
- [33] A. Luque, M. Ghazisaeidi, W.A. Curtin, A new mechanism for twin growth in Mg alloys, *Acta Materialia* 81 (2014) 442-456.
- [34] J.F. Nie, Y.M. Zhu, J.Z. Liu, X.Y. Fang, Periodic segregation of solute atoms in fully coherent twin boundaries, *Science* 340(6135) (2013) 957-60.

- [35] D. Zhang, L. Jiang, J.M. Schoenung, S. Mahajan, E.J. Lavernia, TEM study on relationship between stacking faults and non-basal dislocations in Mg, *Philosophical Magazine* 95(34) (2015) 3823-3844.
- [36] S.G. Srinivasan, X.Z. Liao, M.I. Baskes, R.J. McCabe, Y.H. Zhao, Y.T. Zhu, Compact and dissociated dislocations in aluminum: implications for deformation, *Phys Rev Lett* 94(12) (2005) 125502.

Chapter 6: Computational Assessment of Solute Segregation at Twin Boundaries in Magnesium: A Two-Factor Model and Solute Effect on Strengthening

6.1 Preface

The study in Chapter 5 illustrated activation of deformation modes were modified due to addition of yttrium in polycrystalline Mg-Y system. However, the simulation in chapter 5 can not quantitatively evaluate the solute contribution to each deformation modes. Therefore, the following two chapters will perform careful studies on solute effect on twinning boundary segregation and motion of dislocations. Specifically, this chapter quantified the degree of solute segregation at two twinning boundaries via employing ab initio calculations. A two-factor model was proposed to predict the solute segregation energy. It also further identified the strengthening or embrittling potency for a range of solute atoms, providing a basis for selecting promising solutes in the development of new high-performance Mg alloys.

- This chapter has published in Journal of Applied Physics, appeared as:

Computational Assessment of Solute Segregation at Twin Boundaries in Magnesium: A Two-Factor Model and Solute Effect on Strengthening

Huicong Chen, Jun Song, Computational assessment of solute segregation at twin boundaries in magnesium: A two-factor model and solute effect on strengthening, Journal of Applied Physics 132(22) (2022) 225102.

6.2 Abstract

This work presents a comprehensive first-principles density functional theory (DFT) study of solute segregation at the $\{10\bar{1}1\}$ and $\{10\bar{1}2\}$ twin boundaries (TBs) in Mg. A total of 56 solute elements were investigated. For each solute element, the preferential segregation sites at the two TBs were identified and the associated segregation energies were computed. A two-factor model that considers both lattice strain and electronegativity, representing the mechanical and chemical effects respectively, has been proposed to predict the solute segregation energy. The model prediction shows good agreement with the DFT calculation. It was found that the mechanical effect dominates the solute segregation energy. However, depending on the site of segregation, the chemical effect can become sizable to warrant consideration. The degree of solute segregation at TBs at different temperatures was then quantified by calculating the solute concentration at TBs at different temperatures. The effect of solutes in either strengthening or weakening the TB was also evaluated. The results provide a basis for selecting promising solutes in the development of new high-performance Mg alloys.

6.3 Introduction

Magnesium (Mg) and its alloys have received great interest in various industrial sectors, including automotive, aerospace, transportation and portable electronics, for promising considerable weight reduction and energy efficiency improvement owing to their low density and high specific strength [1, 2]. However, one major limitation bottlenecking application of Mg and its alloys is their poor deformability at ambient temperature, exhibiting much less plastic deformation compared to most common ductile structural metals, such as aluminum alloys and steels [3-5]. As such, there have been numerous studies attempting to identify ways to overcome this limitation to make Mg and its alloys suitable for more industrial applications.

To date it has been demonstrated that formability of Mg alloys can be enhanced when certain types of alloy elements are included in the composition. For instance, rare-earth (RE) elements such as Y, Gd, Dy, Tb, Er, Ho, Ce and Nd has been experimentally observed to significantly improve the room temperature ductility of Mg alloys [6-9]. Moreover, Mg alloys containing other elements, e.g., Ca, Zn, Mn, Li and Zr also display enhanced room temperature ductility [1, 10-15]. It has been found that adding solutes such as Li [16] or Y [7] can change the SFE in the formation of two $\frac{1}{2}\langle c + a \rangle$ partial dislocations and thus facilitate the activation of $\langle c + a \rangle$ slip. Similarly, Y additions can also result in higher activation of $\langle c \rangle$ slip by reducing the SFE along $\langle c \rangle$ direction on prismatic plane [9]. In addition, solutes additions can significantly decrease the difference of critical resolved shear stress (CRSS) between basal slip and non-basal slip [17, 18]. Consequently, improved ductility is observed in alloyed Mg due to the enhanced activity of non-basal slip. Recently, Wu et al. [19, 20] proposed that adding dilute solutes can stabilize the $\langle c + a \rangle$ cross-slip by inhibiting deleterious $\langle c + a \rangle$ transformation, thereby enabling the hexagonal-close-packed (hcp) Mg to deform plastically along the crystallographic $\langle c \rangle$ direction. Besides dislocations, solute addition is also expected to interact with other defects. In polycrystalline Mg alloys, it has been demonstrated that, via solute decoration and segregation, the behaviors of grain boundaries (GBs) can be modified to result in enhancement in material properties such as strength, toughness, corrosion and fatigue resistance [21-25]. Within the GB family are twin boundaries (TBs), which are of direct relevance to twinning, an important deformation mechanism in Mg alloys [26, 27]. It has been observed that TBs provide preferential locations for solute segregation [28, 29]. As reported by Nie et al., there was periodical solute segregation along deformation TBs in Mg–Zn and Mg–Zn–Gd alloys [28], where the preferential segregation sites at TBs for Gd and Zn were controlled by minimization of elastic strain associated with individual solute atoms. This ordered

distribution of solute atoms would lead to a strengthening effect by restricting further migration of the twin [28] and the other boundaries of submicron grains during plastic deformation [11]. Simultaneously, the solute co-segregation would decrease the grain boundary mobility and inhibit grain growth into preferable orientation (i.e., basal texture orientation) during annealing, improving formability in the following deformation [12]. These findings provide strong experimental evidence indicating it as an effective route to design Mg alloys of desirable properties via control of solute decoration and segregation at TBs. However, a brute-force screening of solute elements to identify the desired candidates for such design route is a difficult and costly task, if at all possible. In this regard, studies have been performed trying to gain mechanistic understanding of solute-TB interaction in order to criteria for solute selection. Zhang et al. calculated the segregation energies at $\{10\bar{1}2\}\langle 10\bar{1}\bar{1}\rangle$ tension twin and diffusion activation enthalpies for a few solute elements, based on which they proposed a design map [30]. However, the set of solutes considered were rather limited with only a tension twin considered. Later Pei et al. [31] conducted first-principles calculations of solute segregation energies in both tension and compression twins for 23 solute elements, and proposed an one-factor model to predict the trend of segregation energies with solute induced mismatch. Yet their model only considered the mechanical contribution, i.e., strain energy, but did not account for the chemical aspect.

In the present study, we aim to obtain a more accurate prediction of solute segregation and better understanding of the origin underlying solute segregation at TBs in Mg. Focusing on two most frequent TBs $\{10\bar{1}2\}$ and $\{10\bar{1}\bar{1}\}$ in Mg, first-principles density functional theory (DFT) calculations were performed to investigate a comprehensive series of solutes at these TBs. A general two-factor parameters model, motivated by the approach by Huber et al. [32], has been developed to predict solute segregation with improved accuracy. The model accounts for both

mechanical contribution and chemical contribution, and further elucidates the origin of solute segregation in TBs. In the end, a design map including segregation and strengthening or embrittling effects was then established to provide insights for solute selection in Mg alloy design.

6.4 Computational Methodology

6.4.1 TB Structural Models

In the present work, two representative TB structures, i.e. $\{10\bar{1}2\}$ and $\{10\bar{1}1\}$ TBs in Mg were selected and constructed. The $\{10\bar{1}2\}$ TB (**Figure 6.1(a)**) had dimensions $12.8 \text{ \AA} \times 7.7 \text{ \AA} \times 26.1 \text{ \AA}$ with 112 atoms, and the $\{10\bar{1}1\}$ TB (**Figure 6.1(b)**) had dimensions $6.3 \text{ \AA} \times 11.8 \text{ \AA} \times 24.6 \text{ \AA}$ with 80 atoms. The corresponding free surface (FS) cells were built with the same cell sizes as the TB models, but with approximately half the numbers of atoms.

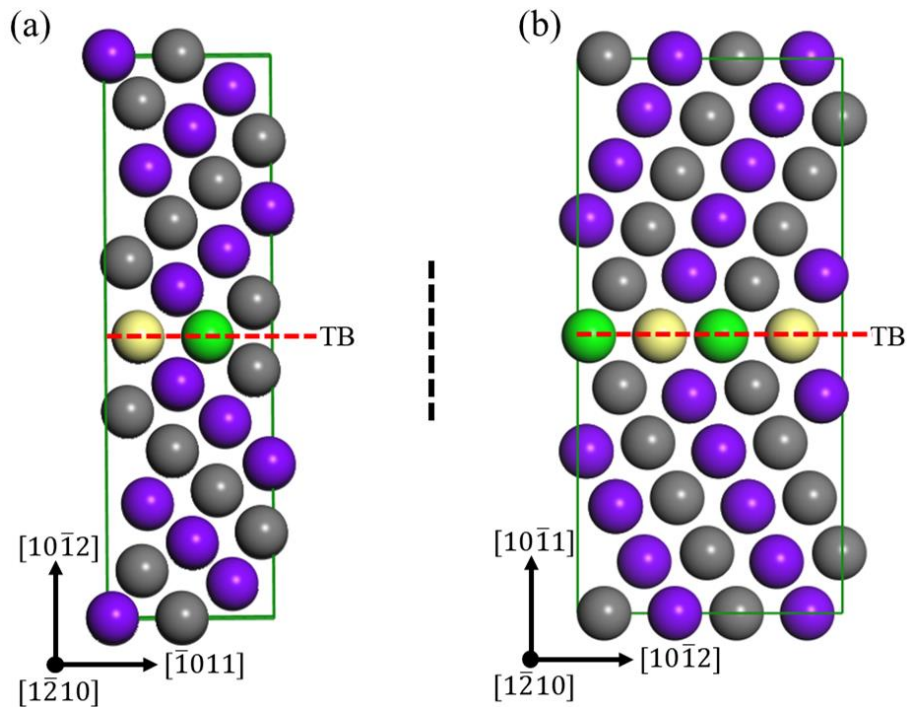


Figure 6.1. Schematic illustration of the TB model used in the current study. (a) $\{10\bar{1}2\}$ TB, (b) $\{10\bar{1}1\}$ TB. The yellow (compression site) and green (extension site) color represent the two different sites at TB, which have different volumetric size for their corresponding sites in bulk, marked purple and grey respectively.

6.4.2 First-principles Density Functional Theory Calculations

The DFT calculations [33, 34] in the present work were carried out using the Vienna Ab-initio simulation package (VASP) [34, 35] within the projector-augmented wave (PAW) method. The generalized gradient approximation (GGA) of Perdew-Burke-Ernzerhof (PBE) based on plane-wave basis sets was employed to describe the exchange-correlation interaction. A plane wave cut-off energy of 400 eV and a Gamma-centered k -point mesh was used for all calculations. Our convergence criteria for total energy and force were selected as $0.01 \text{ eV}\text{\AA}^{-1}$ and 10^{-5} eV/cell respectively. Γ -centered k -point meshes of $5 \times 5 \times 10$ and $7 \times 4 \times 8$ were chosen for the $\{10\bar{1}2\}$ and $\{10\bar{1}1\}$ TBs, respectively. Additionally, the same number of atoms and k -point setting as the TBs were used for bulk calculations.

The solute elements were introduced into the Mg lattice by substituting host Mg atoms. A total of 56 solute elements were considered in the present study. These solute elements were divided into five groups with different marker shapes, i.e., RE rare earth elements (pentagon), 3d transition elements (circle), 4d transition elements (triangle), 5d transition elements (inverted triangle) and other s/p elements (square). Different marker colors are assigned within each group of dopants. As illustrated in **Figure 6.1**, two different-sized sites A (colored in green) and B (colored in yellow) at TBs can be chosen as solute segregation candidates and previous periodic observation [28] has indicated that atoms with larger atomic radii tend to substitute the extension site (A) while smaller atoms prefer to stay at the compression site (B). In this study, we performed calculations for both sites and selected the lower-energy one for further analysis.

6.4.3 Key Parameters for Segregation Analysis

The solution energy of an isolated solute atom, E_{sol} , is defined as:

$$E_{sol}^i = E_{tot}^i[\text{Mg}_{n-1}\text{X}] - E_{tot}^0[\text{Mg}_n] - E_X^0 + E_{\text{Mg}}^0 \quad (6.1)$$

where $E_{tot}^i[\text{Mg}_{n-1}\text{X}]$ is the total energy of the corresponding bulk or TB/FS Mg system where one Mg atom at site i ($i = \text{A/B}$ for TB/FS) is replaced by a solute atom, $E_{tot}^0[\text{Mg}_n]$ is the total energy of solute-free bulk or TB/FS Mg system, E_X^0 and E_{Mg}^0 are cohesive energy of solute atom and Mg in their stable crystalline state respectively. The difference between the solution energies of a solute in the bulk and at TB/FS is characterized as the segregation energy, $E_{\text{seg}}^{\text{TB/FS},i}$, computed using the following equation:

$$E_{\text{seg}}^{\text{TB/FS},i} = E_{\text{sol}}^{\text{TB/FS},i} - E_{\text{sol}}^{\text{Bulk}} \quad (6.2)$$

where $E_{\text{sol}}^{\text{TB/FS},i}$ and $E_{\text{sol}}^{\text{Bulk}}$ are the solution energies of the alloying element doped at site i (A/B) of TB/FS and in the bulk, respectively. The minimum energy was chosen as the segregation energy $E_{\text{seg}}^{\text{TB/FS}}$ where a negative value indicates solute segregation into TB/FS is energetically favorable, in line with the convention used in literatures [28, 30].

The strengthening energy E_{se} which is defined as the change in grain boundary (GB) cohesion per segregated solute is computed by using the following equation [36, 37]:

$$E_{\text{se}} = E_{\text{seg}}^{\text{TB}} - E_{\text{seg}}^{\text{FS}} \quad (6.3)$$

Here, we focus only on the dominant TB/FS segregation site, i.e., the site with the strongest segregation tendency. A negative E_{se} value indicates that the TB is strengthened by the solute while a positive E_{se} value suggests weakening of the TB by the solute, referred to as embrittlement in content below.

6.5 Results and Discussion

6.5.1 Site Preference and Energetics of Solutes at TBs

For both the $\{10\bar{1}1\}$ and $\{10\bar{1}2\}$ TBs, there are two distinct atomic sites that may be occupied by

solute atoms. **Figure 6.2** plots the segregation energy for site A versus that for site B of the $\{10\bar{1}1\}$ TB (**Figure 6.2(a)**) and $\{10\bar{1}2\}$ TB (**Figure 6.2(b)**). Four regions are marked according to segregation energy to reveal segregation preference of dopants at each site as shown in **Figure 6.2(a)** and (b). We find that larger solute atoms, such as atom Ca, Gd and Ce generally prefer the extension site A where bigger Voronoi volume is available while the compression site B with smaller Voronoi volume is favored by smaller solute atoms like Ag, Al and Zn. Interestingly, certain solute atoms prefer neither site, thus expected to resist TB segregation. For example, V and Mo exhibit positive segregation energies at both sites A and B of $\{10\bar{1}1\}$ TB, and the same observation can be noted for Ti, Zr and Nb with respect to $\{10\bar{1}2\}$ TB. which shows that the two solutes will not immediately segregate to $\{10\bar{1}1\}$ TB. The same result can be found in terms of the segregation tendency for Ti, Zr and Nb to $\{10\bar{1}2\}$ TB. Additionally, the segregation energies for Nb and Ta to $\{10\bar{1}1\}$ TB and for V to $\{10\bar{1}2\}$ TB are close to zero, indicative of their little or no tendency towards TB segregation.

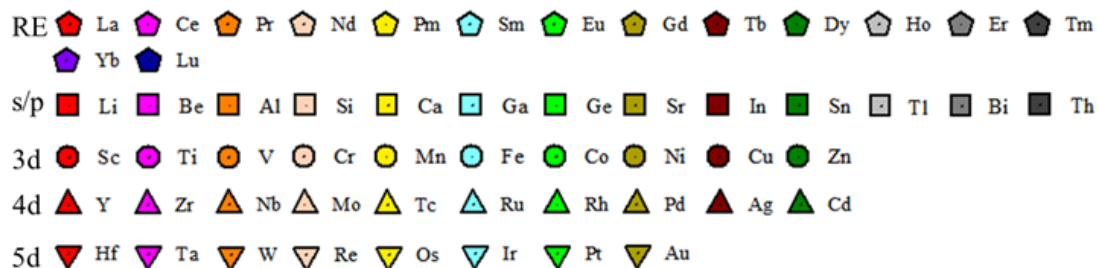
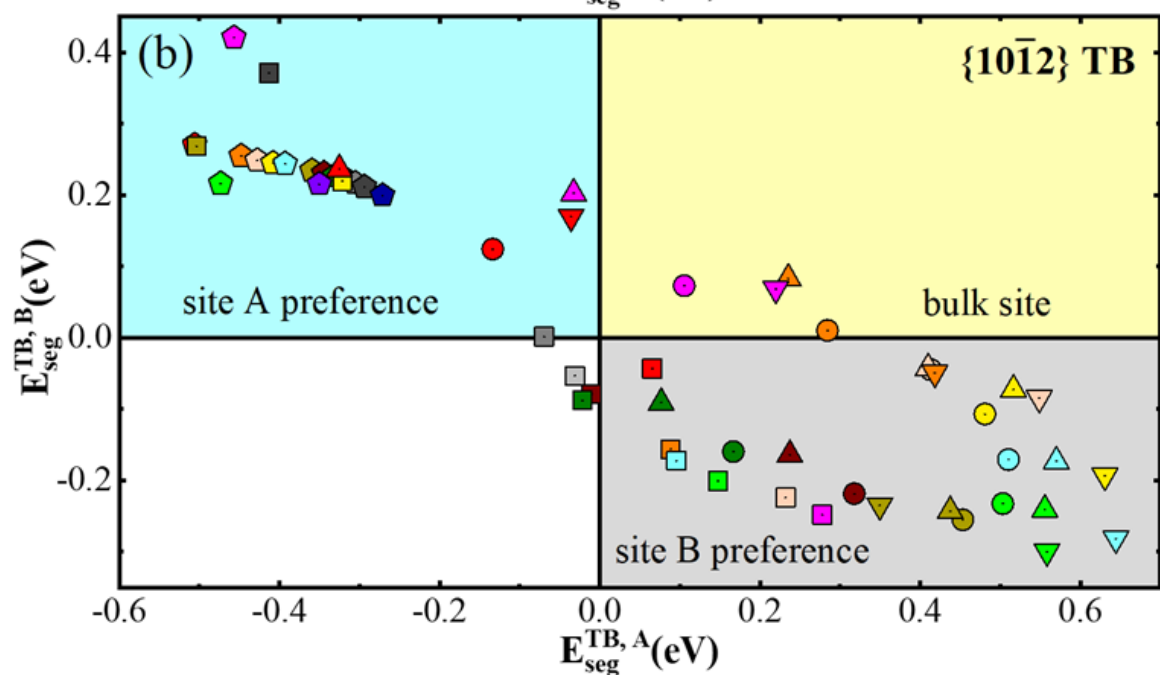
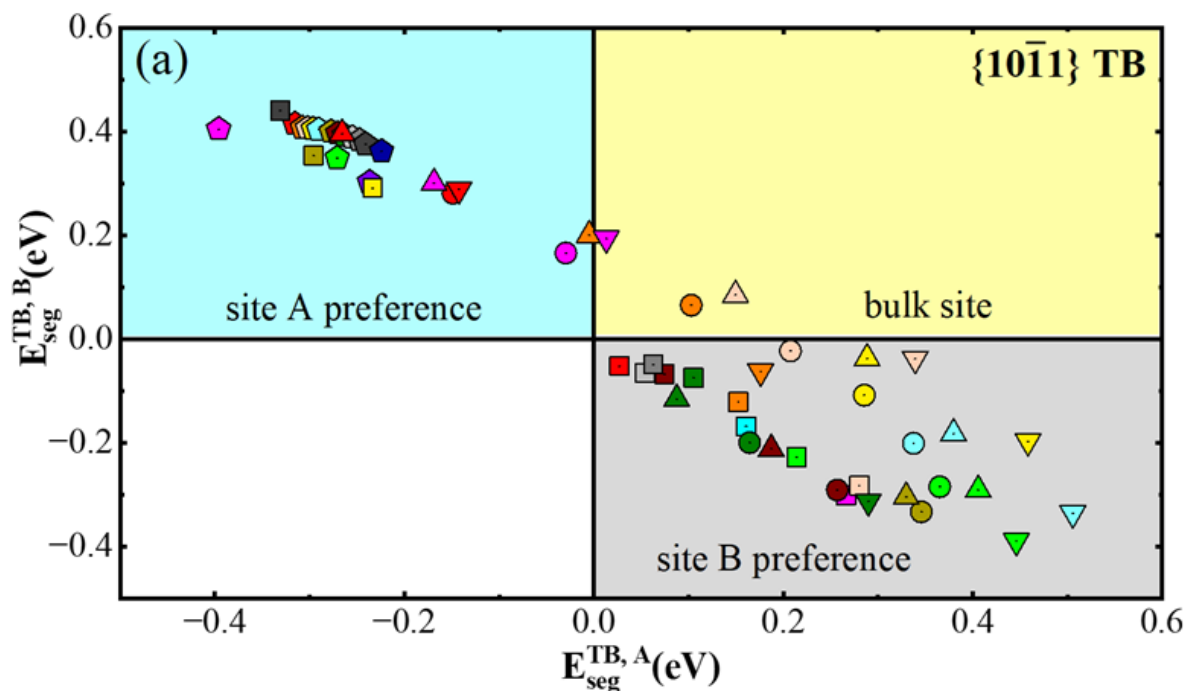


Figure 6.2. The segregation energies of different solute atoms at site A ($E_{seg}^{TB,A}$) versus those ($E_{seg}^{TB,B}$) at site B in (a) $\{10\bar{1}1\}$ and (b) $\{10\bar{1}2\}$ TBs.

Besides the site preference, we can also observe from **Figure 6.2** that the segregation tendency of a solute to the two TBs may differ. In this regard, the segregation energies of solutes at $\{10\bar{1}1\}$ and $\{10\bar{1}2\}$ TBs are compared, with the results shown in **Figure 6.3**. In the figure, $E_{seg}^{1011, X}$ and $E_{seg}^{1012, X}$ denote the lowest segregation energies of a solute X at the $\{10\bar{1}1\}$ and $\{10\bar{1}2\}$ TBs. Among the 56 solute elements investigated here, we find that $E_{seg}^{1011, X}$ and $E_{seg}^{1012, X}$, though may differ, are rather close, mostly within ± 0.15 eV to each other in value, except for the two RE elements Eu and Ce, and the s/p element Sr as shown in **Figure 6.3**.

Anti-segregating tendency is observed for V (3d metal) and Ta (5d metal) in both TBs, which exhibits only positive segregation energies and therefore prefers to stay in bulk environment. Additionally, the segregation energies are positive when atom Cr (3d metal) segregates to $\{10\bar{1}1\}$ TB and atoms Ti (3d metal) and Nb (4d metal) segregate to $\{10\bar{1}2\}$ TB. All other solutes are predicted to have negative segregation energy for both types of TBs and a more negative value indicates a higher potency to segregation. Interestingly, we find that all RE atoms show a segregation preference to $\{10\bar{1}1\}$ TB compared with $\{10\bar{1}2\}$ TB as shown in **Figure 6.3** and most transition metals from 4d and 5d show a stronger segregation tendency to $\{10\bar{1}2\}$ TB. The remaining elements present an approximately equivalent segregation trend at both TBs.

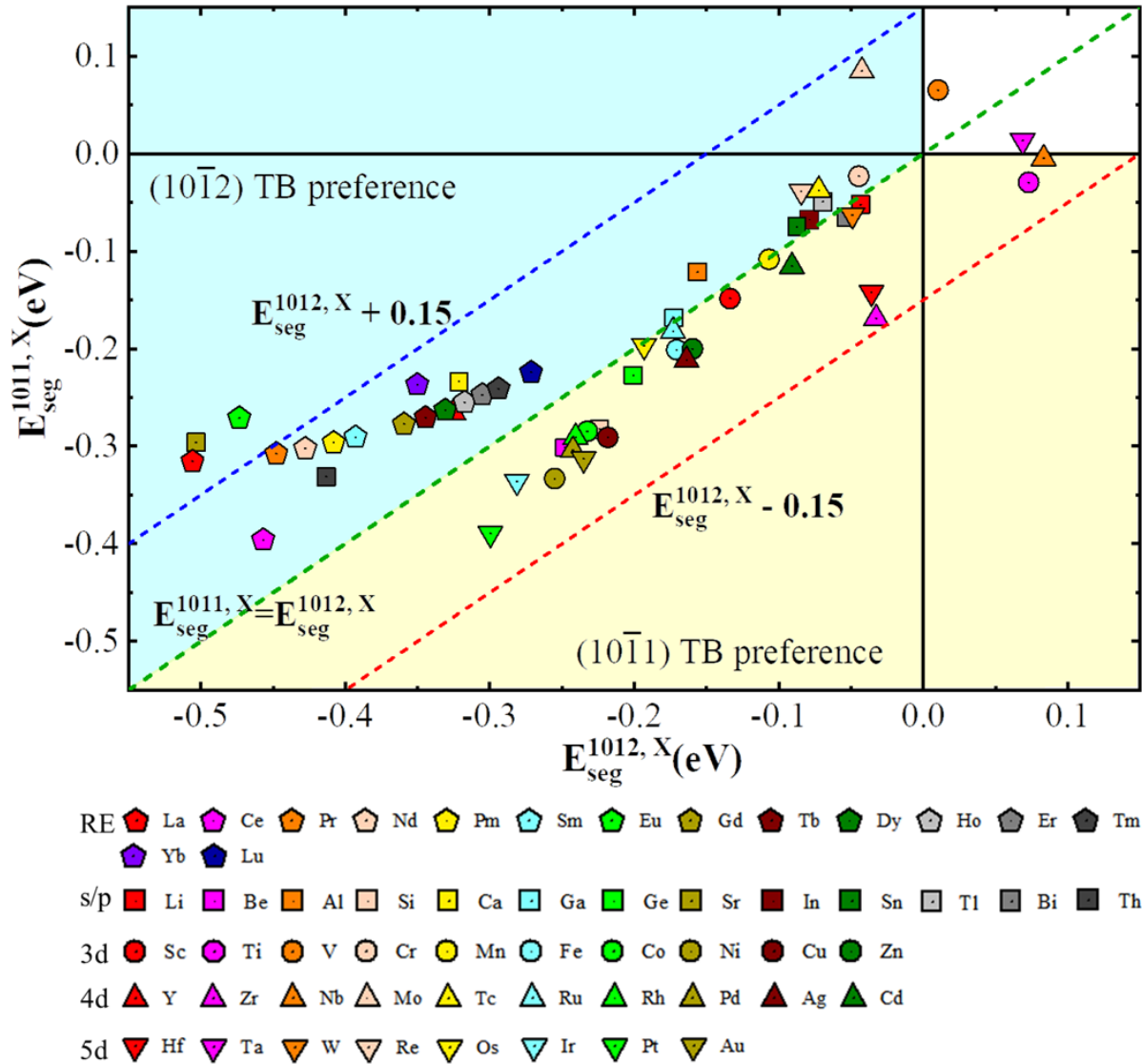


Figure 6.3. The comparison of segregation energy at preferential sites in $\{10\bar{1}1\}$ and $\{10\bar{1}2\}$ TBs.

6.5.2 Factors Affecting Segregation and Predictive Model

The well-known Hume-Rothery size factor rule indicates that extensive substitutional solid solution can be effective only if the relative difference between the atomic size (radii) of the solvent and solute is less than 15% [38] due to lattice distortion produced by solute doping. This rule provides a qualitative description of the tendency of a solute to dissolve in a solvent or interfaces based on mismatch of crystal structures [39]. Many previous studies [28, 37, 40-44] adopted

atomic radius difference as mismatch to predict the segregation trend of solutes to different interfaces. Herein, we take the actually measured volume for each atom by using the definition of Voronoi diagram [45], i.e. one lattice site occupies all space closer to it than to any other sites, to quantitatively describe solute effect on local lattice distortion and predict segregation propensity. This Voronoi volume can directly reflect geometric environment in bulk/TB and has been widely employed in related studies [31, 46-48]. All source data used to calculate the Voronoi volume in this paper is extracted from fully relaxed supercell structures.

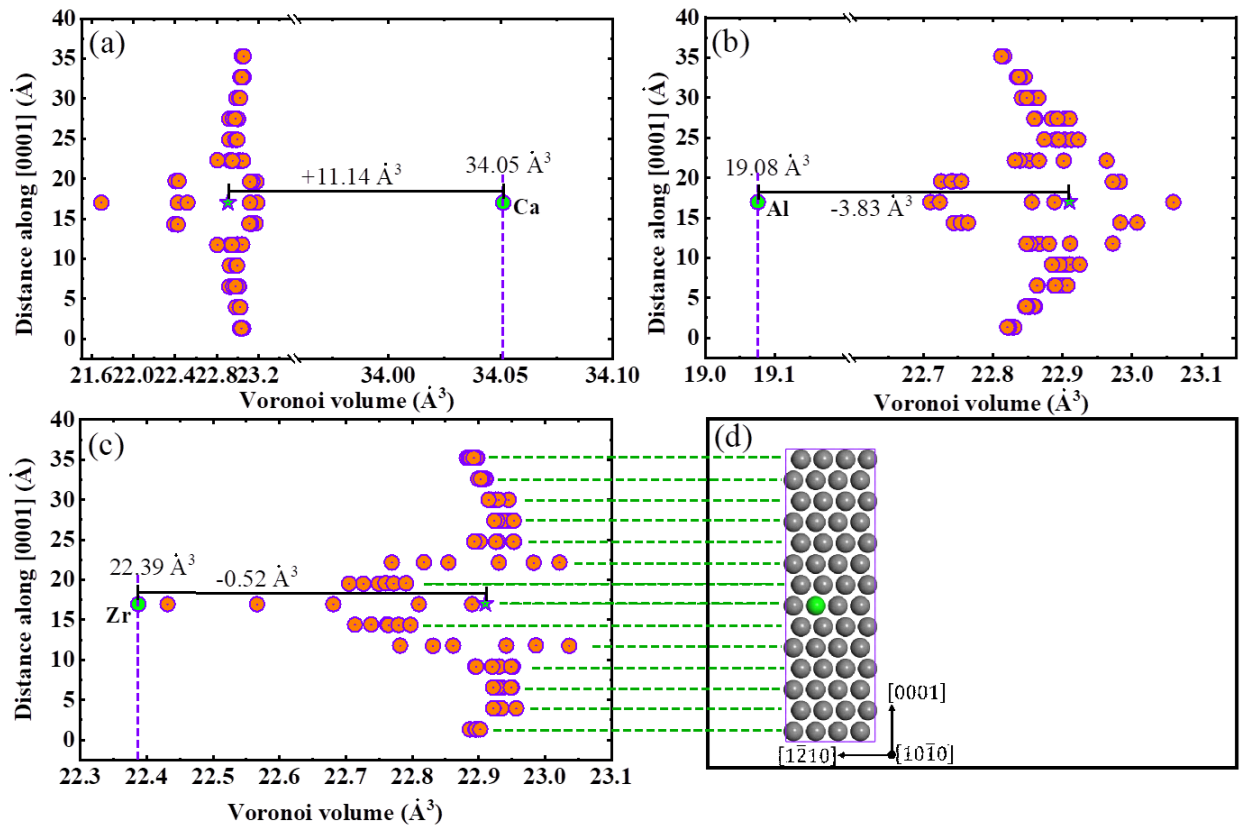


Figure 6.4. The local mismatch around doping site (highlight with green circle) in bulk for three atoms with representative atomic size: (a) Ca; (b) Al; (c) Zr; and the atomic structure used for bulk Mg is shown in (d). The star shape stands by the Voronoi volume in dopant-free bulk and the green circle represents the solute atoms. The negative values in (a-c) indicate the Voronoi volume is reduced due to solute doping.

Figure 6.4(a-c) presents three Voronoi volume distribution corresponding to situations when a bulk (see **Figure 6.4(d)**) site is substituted by Ca, Al and Zr respectively. For a pure bulk site, the

computed Voronoi volume (V_0) is 22.91 \AA^3 marked with a star shape in **Figure 6.4(a-c)** as a reference value site. A volume expansion of 11.14 \AA^3 is produced when Ca is substituted into a bulk site and all the other sites have Voronoi volumes between 21.6 \AA^3 and 23.2 \AA^3 as shown in **Figure 6.4(a)**. However, for a small-diameter atom Al, the volume of substitutional site is reduced to 19.08 \AA^3 and volumes of surrounding atoms vary from 22.7 \AA^3 to 23.1 \AA^3 . From **Figure 6.4(a)** and (b), it is clearly observed that sites with obvious volume change mainly distribute around Ca or Al, which indicates local lattice distortion is produced due to solute doping. Additionally, because atom Zr has a comparatively similar size as Mg, its Voronoi volume, 22.39 \AA^3 , is almost the same with the original bulk-site volume and thus makes little contribution to mismatch (-0.52 \AA^3).

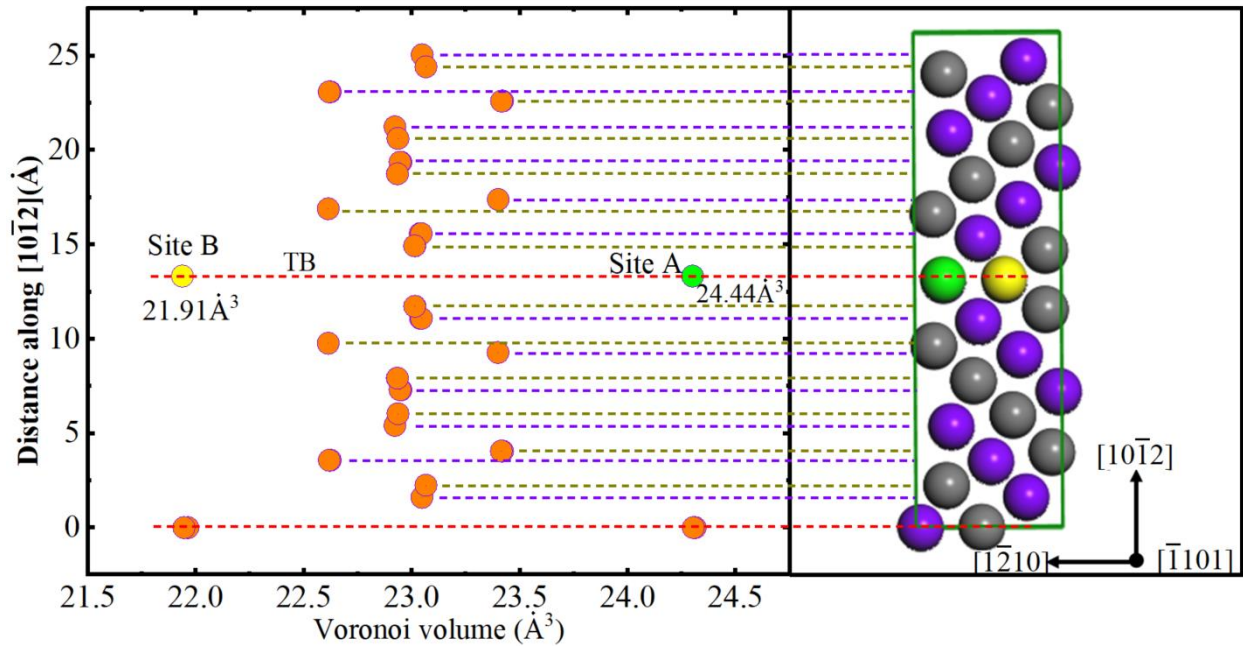


Figure 6.5. Distribution of Voronoi volume in a fully relaxed $\{10\bar{1}2\}$ TB.

Given that core structures of $\{10\bar{1}2\}$ and $\{10\bar{1}1\}$ are relatively similar, we henceforth mainly present Voronoi volume of $\{10\bar{1}2\}$ TB part. As shown in **Figure 6.5**, the computed Voronoi

volumes for site A (V_{TB}^A) and B (V_{TB}^B) at solute-free $\{10\bar{1}2\}$ TB are 24.44 \AA^3 and 21.91 \AA^3 , respectively, which is in agreement with the recent report [31]. We performed the calculation at both sites for each solute and also select Ca, Al and Zr as representatives to analyse the local mismatch at TB. As shown in **Figure 6.6(a)** and (b), the Voronoi volume is increased for both substitutional sites while Ca being doped at extensive site A exhibits smaller volume change than that at compression site B. Al also shows a smaller volume change when it substitutes the compression site B as shown in **Figure 6.6(c)** and (d) In case of Zr substitution (see **Figure 6.6(e)** and (f)), volume change is very small for both sites due to the similar atomic size between Zr and Mg.

To quantitatively describe the size mismatch, here we introduce the size factor (\emptyset) [48]:

$$\emptyset = \frac{V_X^i - V_0^i}{V_0^i} \quad (6.4)$$

V_X^i is the Voronoi volume of solute X doped at site i (i = A/B) and V_0^i is the original Voronoi volume of site A/B and for mismatch in bulk, V_X^i and V_0^i represent the Voronoi volumes of X and host Mg respectively. By this definition, we obtained the size factor of Ca and Al when they segregate into A/B site, i.e. $\emptyset_{Ca}^A = 0.437$, $\emptyset_{Ca}^B = 0.515$, $\emptyset_{Al}^A = 0.196$, $\emptyset_{Al}^B = 0.170$. From these results, it is clearly concluded that Ca-like atoms produce less elastic strain when it substitutes the extended site and Al-like atoms prefer the compressed site in a similar way. Therefore, a negative segregation energy (-0.32 eV) is observed when atom Ca substitutes site A, and site B is the preference site for Al segregating at $\{10\bar{1}2\}$ TB as shown in **Figure 6.2**. Finally, Zr-like atoms impose little effect on local mismatch but the mismatch at compressed site is smaller than that at extended site, so they potentially take the compressed site when segregating to TB.

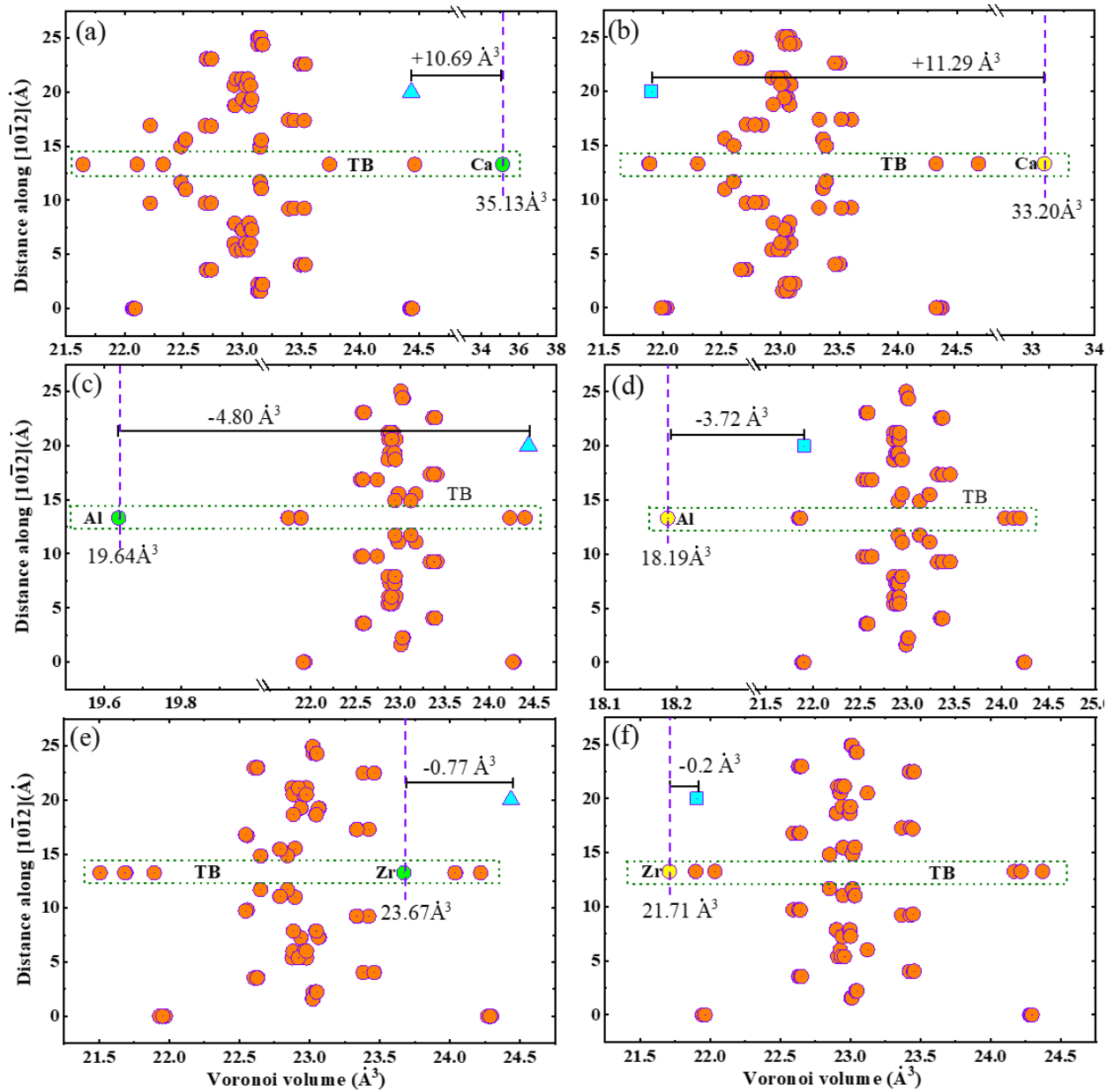


Figure 6.6. The local mismatch around doping site of $\{10\bar{1}2\}$ TB for three atoms with representative atomic size: (a, b) Ca; (c, d) Al; (e, f) Zr.

As described above, volumetric effects induced by solute atoms can precisely predict the selection of segregation sites in TBs. Considering this effect, Pei et al. [31] proposed a model to connect the solute volumes and their segregation energies. Although their predicted trend is in well agreement with values calculated by DFT method, they ignored analysis of chemical effect which may

account for about 35% of the segregation energy. Recently, an unusual solute segregation phenomenon was reported in a Mg–0.4Bi alloy where atoms Bi segregated to the compression sites of the $\{10\bar{1}1\}$ TB although atoms Bi have larger atomic size than Mg and are expected to segregate to the extension sites to minimize elastic strain. In addition, no apparent Bi segregation to either compression or extension sites is found at the $\{10\bar{1}2\}$ TB [49]. The local chemical bonding plays a critical role in explaining such an abnormal observation. Therefore, both chemical and mechanical effects have been considered in the prediction of dopant segregation in molybdenum [37] and applied in a simple lineal model in machine learning analysis of segregation energy [32, 50]. In this study, instead of considering only mechanical contribution to the segregation energies, we investigated the following two-factor linear model to predict the segregation trend

$$E_{\text{seg}}^X = k_\chi (\chi_{\text{Mg}} - \chi_X)^2 + k_m \frac{V_{\text{TB},X} - V_{\text{Mg}}}{V_{\text{Mg}}} \quad (6.5)$$

where $(\chi_{\text{Mg}} - \chi_X)$ is the relative difference in electronegativity (a measure of the chemical effect), and $\frac{V_{\text{TB},X} - V_{\text{Mg}}}{V_{\text{Mg}}}$ is the relative volume change (misfit, a measure of strain). k_χ and k_m are constant coefficients fitted using least squares regression.

Table 6.1. Fitting parameters for the two-factor linear model and their Pearson’s r coefficients.

| TB | Site | k_χ | k_m | R^2 |
|------------------|------|----------|--------|-------|
| $\{10\bar{1}1\}$ | A | 0.232 | -0.752 | 0.83 |
| | B | -0.043 | 0.696 | 0.71 |
| $\{10\bar{1}2\}$ | A | 0.243 | -1.165 | 0.89 |
| | B | -0.092 | 0.523 | 0.71 |

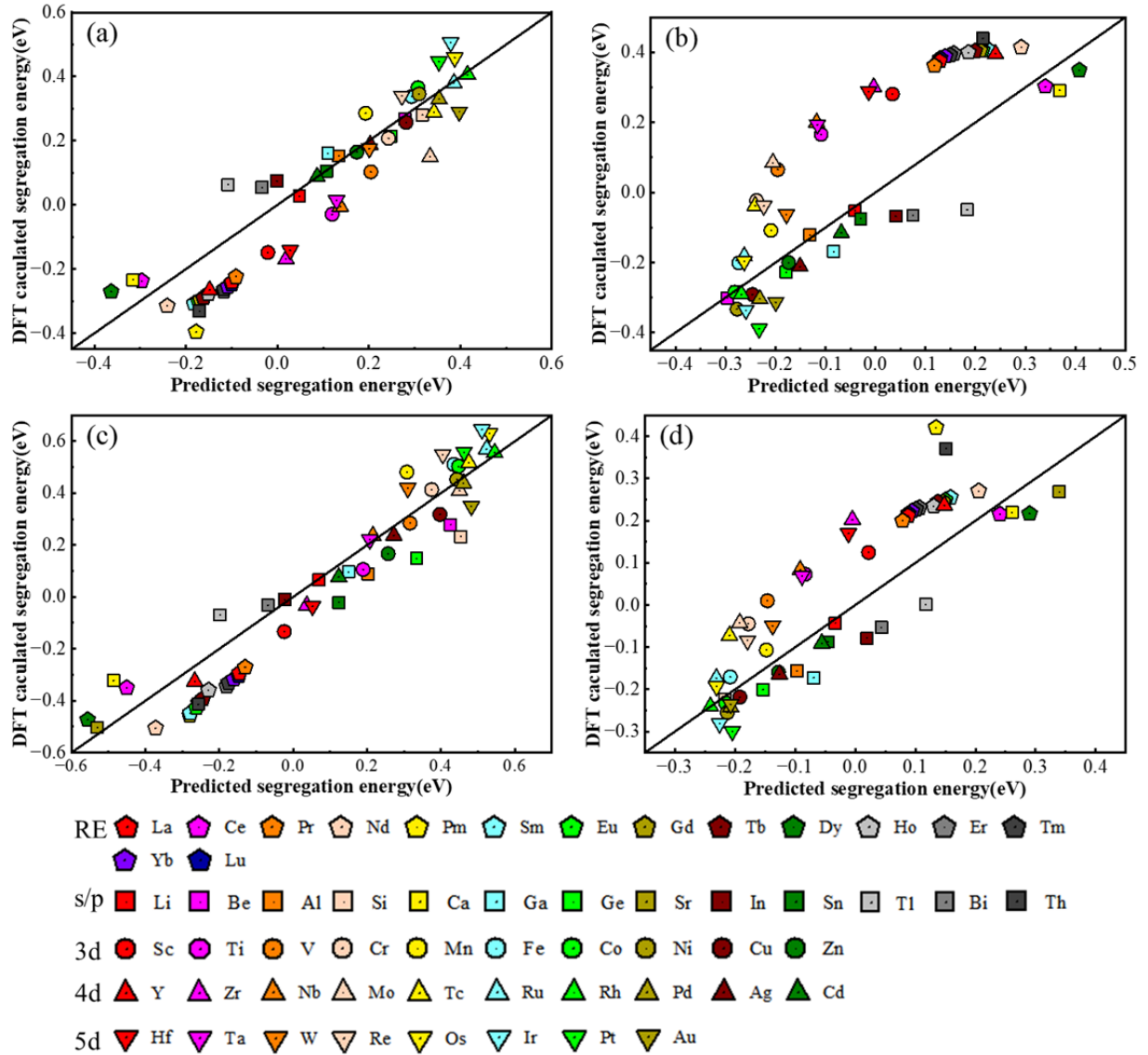


Figure 6.7. Plot of predicted and DFT-computed segregation energies of solutes in the (a) extension site of $\{10\bar{1}1\}$ TB, (b) compression site of $\{10\bar{1}1\}$ TB, (c) extension site of $\{10\bar{1}2\}$ TB and (d) compression site of $\{10\bar{1}2\}$ TB.

The fitting results are listed in **Table 6.1** and comparison of predicted values with the DFT results are illustrated in **Figure 6.7**. We find that this two-factor model is able to account for the variation in the segregation energies ($R^2 > 0.71$) for most solutes. We also find that the mechanical coefficient is generally larger than the chemical coefficient, meaning the mismatch dominates in contribution to segregation energy, which is in agreement with Pei et al.'s proposition [31]. However, the

chemical effect can be sizable and cannot be ignored when the solute substitution occurs at A site.

6.5.3 Segregation Coverage of Solutes at TBs

The level of solute enrichment at TBs can be roughly estimated based on the Langmuir–McLean theory for segregation [31, 50] as the following equation:

$$\frac{C_{TB}^i}{C_{TB}^{i,0} - C_{TB}^i} = \frac{C_b}{1 - C_b} \exp(E_i/k_B T) \quad (6.6)$$

where C_{TB}^i is the maximum fraction of favorable sites for segregated solutes at monolayer TB at 0 K ($C_{TB}^A = C_{TB}^B = 0.5$), C_{TB}^i is actual solute concentration at site i , depending on the solute concentration in the bulk lattice C_b and temperature T . k_B is Boltzmann constant and E_i is a decrease in potential energy for a solute atom as it segregates to the grain boundary region i.e. the segregation energy. A low bulk concentrations 0.8 at.% is taken as proposed in reference [31] to design a single-phase Mg alloys.

Herein, we simply assume that solute atoms only substitute their favorite sites (A or B) because segregation energy for each solute is either positive or negative as shown in **Figure 6.2** and the positive segregation energy almost make no contribution to solute converges at TBs according to Eq. (6.6). Therefore, the maximum concentration for each solute at both TBs will be less than 50%. It is also worth to note that the mutual interaction and competition between different solute elements is not considered in the above calculation for a rough estimation. **Figure 6.8** illustrates the estimated atomic concentrations of two representative solute atoms from each category as function of temperature using the segregation energies in **Figure 6.3**. As the temperature rises, the estimated concentration for all solutes decreases but the decreasing rates are smaller for solutes with more negative E_{seg} values as illustrated in **Figure 6.8**. For examples, the solutes Ti and Nd

have the least and most negative E_{seg} at compression TB and thus possess the largest and smallest decreasing rates within monotonically decreasing region in **Figure 6.8(a)**. We note that the behavior of these solutes in the tensile TB exhibits essentially the same trend as that of the compression TB, albeit some difference in values. The concentration of Zr and Hf is almost zero at tensile TB due to its nearly positive E_{seg} while they have moderate concentration at compression TB. Therefore, these solutes can be selected to tailor a specific type of TB. In addition, solute Ti shows very limited concentration at both TBs than other solutes when T increase to over 300K, which means solutes such as Ti contribute little to modification of TB properties at high temperatures. As observed in Mg-Zn-Gd alloy [28], Zn and/or Gd tend to segregate to TBs in deformed Mg alloy during annealing process, so in this study, the annealing temperature of 200°C (473K) was taken to calculate all solute concentration at TBs and the results are listed in **Table S6.1** (see supplementary material) as one of references for Mg alloy design.

Our results indicate that the preferential segregation will certainly lead to enrichment of solute atoms at TBs, which provides the prerequisite to the manipulation of GBs via solute decoration.

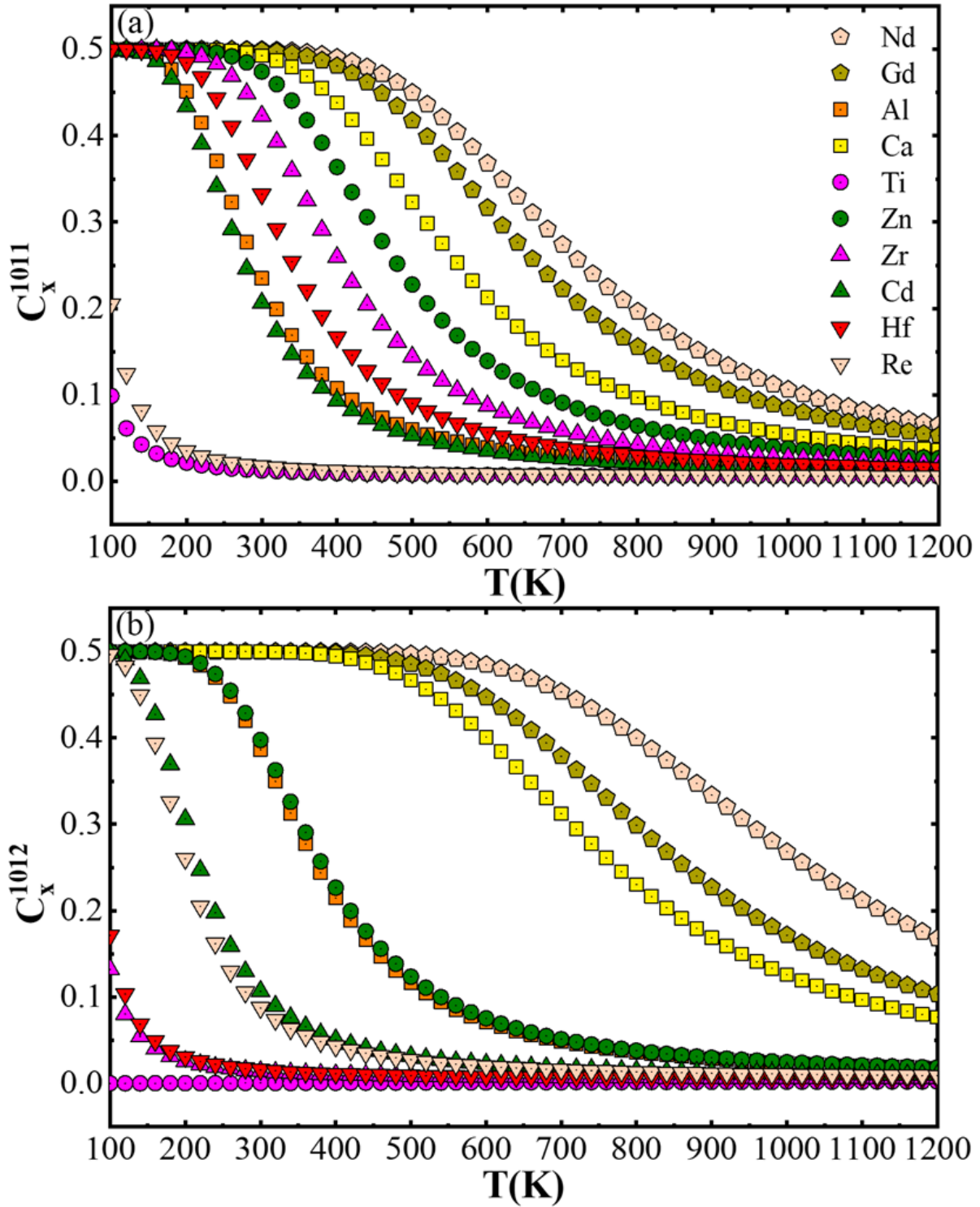


Figure 6.8. Solute concentrations at preferential segregation sites for (a) the compression TB and (b) the tensile TB as a function of temperature using Eq. (6.6) with a nominal bulk concentration of $C_b = 0.8$ at.%.

6.5.4 Mapping of Solute Strengthening and Embrittlement

Fracture in Mg has been closely associated with deformation twinning in previous studies [51-54], particularly $\{10\bar{1}1\}$ compression twinning and $\{10\bar{1}2\} - \{10\bar{1}1\}$ double twinning because these twinning modes can intensify the shear stresses resolved on the basal slip systems, resulting in early shear localization and trans-granular void/crack initiation. The solute segregation at TBs would necessarily affect the deformation twinning. As described above, the strengthening energy E_{se} defined in Eq. (6.3) provides an indication of whether a solute can strengthen or weaken a TB, consequently leading to strengthening and embrittling of TBs respectively. The strengthening energy E_{se} is plotted against the segregation energy E_{seg} , for $\{10\bar{1}1\}$ and $\{10\bar{1}2\}$ TBs in **Figure 6.9(a)** and **(b)** respectively, where three regions are highlighted with different colors according to the segregation and strengthening potency: solutes that have positive E_{seg} (grey region) would prefer to stay in the bulk sites and thus would have no effect on TB strength. For solutes that segregate, those with negative E_{se} (red region) tend to strengthen the TB while those with positive E_{se} (light green region) tend to embrittle it.

For the $\{10\bar{1}1\}$ TB, negative E_{se} representing strengthening, is observed for the elements in the centre of the d band (hereafter referred as d -band centre solutes), i.e., Cr, Mn, Fe for 3d solutes, Zr, Nb, Tc, Ru for 4d solutes, and Re and Os for 5d solutes while all other d -band elements would lead to embrittling effect. Similar trends can be found for the $\{10\bar{1}2\}$ TB. In addition, solutes like Nb and Ti have a strong strengthening effect on $\{10\bar{1}2\}$ TB, but show no tendency for TB segregation with a positive E_{seg} (also see **Figure 6.8**). As shown in **Figure 6.9(a)** and **(b)**, all solutes from the s/p band group are embrittling for both TBs, while most RE elements tend to strengthen TBs, however with lower strengthening effect than that from the d -band centre solutes. In addition, E_{se} values are more negative for RE solutes segregating at $\{10\bar{1}2\}$ TB as shown in **Figure 6.9(a)**

and (b), indicating that the strengthening effect from RE solutes would be stronger on the tension TB than on the compression TB. The results suggest the possibility of modulating deformation twinning induced fracture in Mg alloys through proper TB-solute engineering.

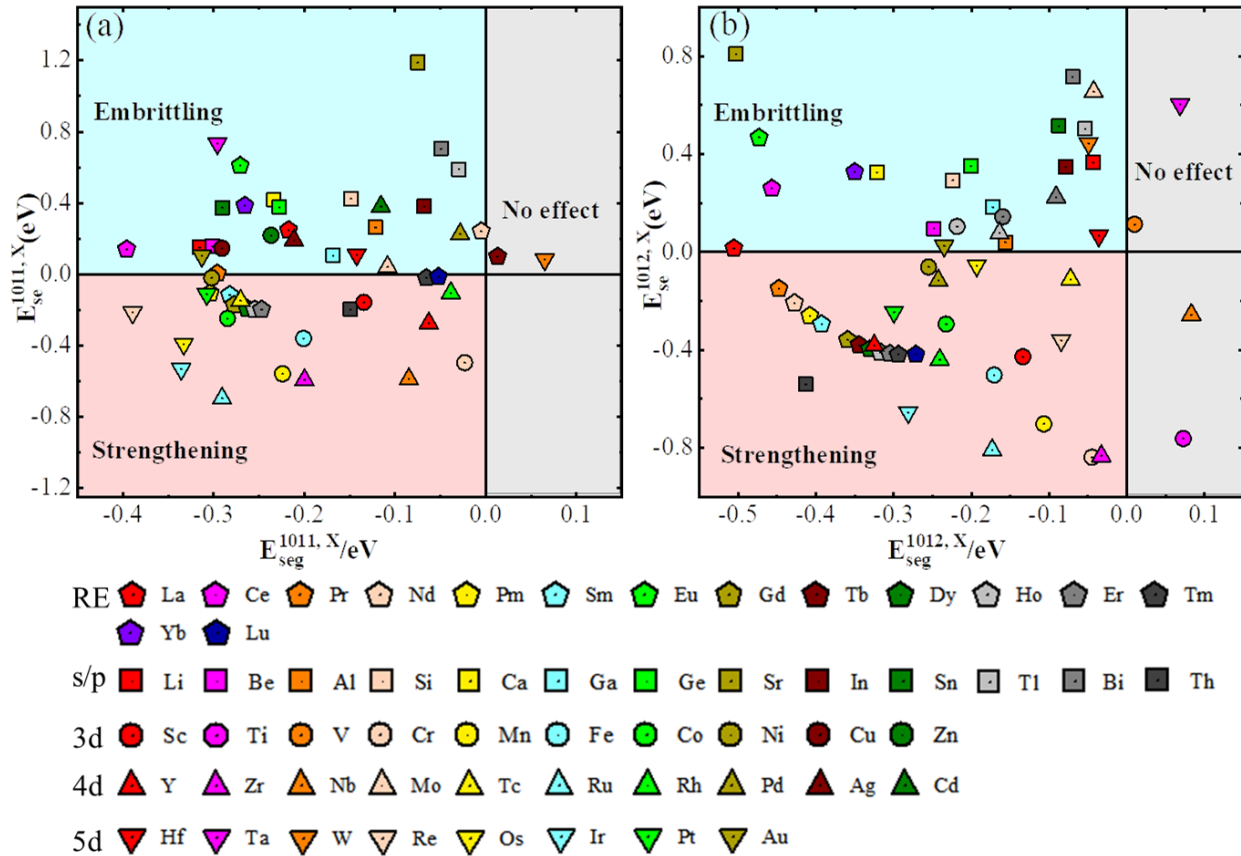


Figure 6.9. Plots of the strengthening energy E_{se} versus segregation energy E_{seg} for all solutes in the (a) $\{10\bar{1}1\}$ TB and (b) $\{10\bar{1}2\}$ TB. Positive and negative E_{seg} values indicate solutes would stay in bulk or segregate at TB, respectively, while positive and negative E_{se} indicate solute would lead to TB embrittlement or strengthening, respectively.

6.6 Conclusion

In conclusion, we have studied the segregation of a total of 56 solute elements on the $\{10\bar{1}1\}$ compression and $\{10\bar{1}2\}$ tensile TBs in Mg using first principles DFT calculations. The preferential locations for these solutes at the TBs were identified, and the associated segregation

energies were obtained. A two-factor model was then developed to predict the solute segregation energy. The model considers both lattice strain induced by solute substitution and the electronegativity difference, representing mechanical and chemical effects due to the solute introduction respectively. The model prediction was found to be in good agreement with the DFT-calculated solute segregation energy. Though the mechanical effect was found to be the dominant one, depending on the site of solute substitution, the chemical effect can become sizable and not be ignored. Based on the solute segregation energetics, the expected solute concentrations at the two TBs at different temperatures were then calculated using the Langmuir-McLean equation. Notable segregation of certain solutes was demonstrated, confirming the possibility of using alloying to modulate TB behaviors. Meanwhile the effect of solutes in either strengthening or weakening the TB was also evaluated. The central *d*-band elements were found to strengthen the TBs, while the solute elements from *s/p* band groups were found to tend to weaken the TBs. On the other hand, the rare earth (RE) elements also tend to strengthen the TBs, but with the strengthening effect being weaker than that from the *d*-band centre solutes. In addition, RE solutes generally show a weaker strengthening effect on the compression TB than on the tension TB. Combining these with the segregation results, a mapping of the potency of different solutes in strengthening and embrittling TBs was established to provide a useful basis for selecting promising solutes in the development of new Mg alloys.

6.7 Acknowledgements

The authors acknowledge financial support from Natural Sciences and Engineering Research Council of Canada (NSERC), McGill Engineering Doctoral Award (MEDA), China Scholarship Council (201706050149), and thank Compute Canada for providing computing resources.

6.8 Supplementary Information

Table S6.1. DFT-computed segregation energies (unit in eV) at site A and B, and strengthening energy (unit in eV) and solubility at 473K provided that solutes segregate at preferential sites.

| Solutes | {10 $\bar{1}$ 1} TB | | | | {10 $\bar{1}$ 2} TB | | | | |
|------------|---------------------------------|---------------------------------|-----------------|--------------------------|---------------------------------|---------------------------------|-----------------|----------------------|-------|
| | E _{seg} ^{X,A} | E _{seg} ^{X,B} | E _{se} | Solubility (T = 473K) | E _{seg} ^{X,A} | E _{seg} ^{X,B} | E _{se} | Solubility (473K) | |
| Re | La | -0.316 | 0.414 | 0.248 | 0.474 | -0.506 | 0.271 | 0.015 | 0.500 |
| | Ce | -0.396 | 0.404 | 0.141 | 0.496 | -0.457 | 0.421 | 0.260 | 0.499 |
| | Pr | -0.308 | 0.407 | 0.004 | 0.469 | -0.448 | 0.255 | -0.150 | 0.499 |
| | Nd | -0.302 | 0.406 | 0.241 | 0.465 | -0.428 | 0.249 | -0.208 | 0.498 |
| | Pm | -0.296 | 0.405 | -0.106 | 0.460 | -0.408 | 0.245 | -0.260 | 0.497 |
| | Sm | -0.291 | 0.404 | -0.116 | 0.455 | -0.393 | 0.244 | -0.295 | 0.496 |
| | Eu | -0.271 | 0.349 | 0.609 | 0.431 | -0.473 | 0.216 | 0.467 | 0.499 |
| | Gd | -0.277 | 0.400 | -0.171 | 0.440 | -0.359 | 0.234 | -0.359 | 0.491 |
| | Tb | -0.271 | 0.397 | 0.100 | 0.430 | -0.344 | 0.231 | -0.380 | 0.487 |
| | Dy | -0.263 | 0.392 | -0.193 | 0.419 | -0.331 | 0.227 | -0.397 | 0.482 |
| | Ho | -0.255 | 0.388 | -0.198 | 0.404 | -0.317 | 0.222 | -0.409 | 0.476 |
| | Er | -0.247 | 0.383 | -0.198 | 0.388 | -0.305 | 0.217 | -0.415 | 0.467 |
| | Tm | -0.241 | 0.376 | -0.021 | 0.375 | -0.294 | 0.211 | -0.419 | 0.458 |
| | Yb | -0.237 | 0.302 | 0.385 | 0.365 | -0.350 | 0.216 | 0.327 | 0.489 |
| Lu | -0.224 | 0.362 | -0.014 | 0.332 | -0.271 | 0.200 | -0.418 | 0.431 | |
| s/p | Li | 0.027 | -0.052 | 0.150 | 0.014 | 0.065 | -0.043 | 0.366 | 0.011 |
| | Be | 0.267 | -0.301 | 0.158 | 0.465 | 0.278 | -0.248 | 0.095 | 0.390 |
| | Al | 0.153 | -0.122 | 0.263 | 0.069 | 0.088 | -0.156 | 0.040 | 0.136 |
| | Si | 0.280 | -0.283 | 0.425 | 0.446 | 0.232 | -0.224 | 0.293 | 0.331 |
| | Ca | -0.234 | 0.291 | 0.417 | 0.357 | -0.321 | 0.220 | 0.325 | 0.478 |
| | Ga | 0.161 | -0.168 | 0.106 | 0.167 | 0.096 | -0.173 | 0.184 | 0.179 |
| | Ge | 0.214 | -0.227 | 0.376 | 0.341 | 0.148 | -0.201 | 0.351 | 0.263 |
| | Sr | -0.296 | 0.353 | 1.189 | 0.460 | -0.503 | 0.269 | 0.808 | 0.500 |
| | In | 0.075 | -0.068 | 0.382 | 0.020 | -0.010 | -0.079 | 0.348 | 0.026 |
| | Sn | 0.105 | -0.075 | 0.374 | 0.024 | -0.022 | -0.087 | 0.514 | 0.032 |
| | Tl | 0.054 | -0.065 | 0.589 | 0.019 | -0.031 | -0.053 | 0.503 | 0.015 |
| | Bi | 0.063 | -0.049 | 0.706 | 0.013 | -0.070 | 0.001 | 0.715 | 0.021 |
| Th | -0.331 | 0.440 | -0.197 | 0.482 | -0.413 | 0.371 | -0.540 | 0.498 | |
| 3d | Sc | -0.149 | 0.281 | -0.158 | 0.118 | -0.134 | 0.124 | -0.428 | 0.088 |
| | Ti | -0.029 | 0.166 | -0.865 | 0.008 | 0.105 | 0.073 | -0.762 | 0.001 |
| | V | 0.103 | 0.065 | 0.202 | 0.001 | 0.284 | 0.010 | 0.113 | 0.003 |
| | Cr | 0.208 | -0.023 | -0.497 | 0.007 | 0.413 | -0.045 | -0.838 | 0.012 |
| | Mn | 0.286 | -0.108 | -0.559 | 0.052 | 0.481 | -0.107 | -0.702 | 0.050 |
| | Fe | 0.338 | -0.201 | -0.361 | 0.264 | 0.510 | -0.171 | -0.502 | 0.173 |
| | Co | 0.365 | -0.285 | -0.248 | 0.449 | 0.503 | -0.233 | -0.294 | 0.354 |

| | | | | | | | | | |
|-----------|----|--------|--------|--------|-------|--------|--------|--------|-------|
| | Ni | 0.346 | -0.333 | -0.021 | 0.483 | 0.453 | -0.255 | -0.062 | 0.404 |
| | Cu | 0.257 | -0.291 | 0.147 | 0.455 | 0.318 | -0.218 | 0.104 | 0.316 |
| | Zn | 0.164 | -0.200 | 0.219 | 0.261 | 0.167 | -0.160 | 0.144 | 0.144 |
| 4d | Y | -0.266 | 0.396 | -0.275 | 0.423 | -0.325 | 0.237 | -0.382 | 0.480 |
| | Zr | -0.169 | 0.301 | -0.593 | 0.168 | -0.033 | 0.202 | -0.833 | 0.009 |
| | Nb | -0.005 | 0.200 | -0.588 | 0.005 | 0.235 | 0.083 | -0.256 | 0.001 |
| | Mo | 0.150 | 0.085 | 0.041 | 0.001 | 0.410 | -0.043 | 0.654 | 0.011 |
| | Tc | 0.289 | -0.037 | -0.149 | 0.010 | 0.517 | -0.072 | -0.111 | 0.023 |
| | Ru | 0.380 | -0.182 | -0.697 | 0.206 | 0.570 | -0.173 | -0.809 | 0.180 |
| | Rh | 0.406 | -0.291 | -0.104 | 0.455 | 0.556 | -0.241 | -0.440 | 0.374 |
| | Pd | 0.330 | -0.304 | 0.225 | 0.467 | 0.438 | -0.243 | -0.117 | 0.378 |
| | Ag | 0.187 | -0.212 | 0.192 | 0.296 | 0.237 | -0.164 | 0.076 | 0.155 |
| | Cd | 0.088 | -0.116 | 0.381 | 0.060 | 0.077 | -0.091 | 0.224 | 0.035 |
| 5d | Hf | -0.142 | 0.288 | 0.111 | 0.105 | -0.036 | 0.170 | 0.066 | 0.010 |
| | Ta | 0.013 | 0.194 | 0.735 | 0.003 | 0.220 | 0.069 | 0.602 | 0.001 |
| | W | 0.176 | -0.063 | 0.083 | 0.018 | 0.418 | -0.049 | 0.444 | 0.013 |
| | Re | 0.339 | -0.038 | -0.216 | 0.010 | 0.549 | -0.084 | -0.360 | 0.030 |
| | Os | 0.458 | -0.197 | -0.391 | 0.251 | 0.631 | -0.193 | -0.055 | 0.240 |
| | Ir | 0.506 | -0.336 | -0.532 | 0.484 | 0.644 | -0.281 | -0.654 | 0.445 |
| | Pt | 0.446 | -0.390 | -0.112 | 0.496 | 0.558 | -0.300 | -0.244 | 0.463 |
| | Au | 0.290 | -0.313 | 0.102 | 0.473 | 0.350 | -0.235 | 0.025 | 0.360 |

6.9 References

- [1] Z. Zeng, N. Stanford, C.H.J. Davies, J.-F. Nie, N. Birbilis, Magnesium extrusion alloys: a review of developments and prospects, *International Materials Reviews* 64(1) (2019) 27-62.
- [2] T.M. Pollock, Weight loss with magnesium alloys, *Science* 328 (2010) 986-987.
- [3] W.S. Miller, L. Zhuang, J. Bottema, A.J. Wittebrood, P.D. Smet, A. Haszler, A. Vieregge, Recent development in aluminium alloys for the automotive industry, *Materials Science and Engineering A* 280 (2000) 37-49.
- [4] H. Somekawa, A. Singh, R. Sahara, T. Inoue, Excellent room temperature deformability in high strain rate regimes of magnesium alloy, *Scientific Reports* 8(1) (2018) 656.
- [5] A. Chen, J. Liu, H. Wang, J. Lu, Y.M. Wang, Gradient twinned 304 stainless steels for high strength and high ductility, *Materials Science and Engineering: A* 667 (2016) 179-188.
- [6] S. Sandlöbes, Z. Pei, M. Friák, L.F. Zhu, F. Wang, S. Zaeferrer, D. Raabe, J. Neugebauer, Ductility improvement of Mg alloys by solid solution: Ab initio modeling, synthesis and mechanical properties, *Acta Materialia* 70 (2014) 92-104.

- [7] S. Sandlöbes, S. Zaeferrer, I. Schestakow, S. Yi, R. Gonzalez-Martinez, On the role of non-basal deformation mechanisms for the ductility of Mg and Mg–Y alloys, *Acta Materialia* 59(2) (2011) 429-439.
- [8] F. Wang, S. Sandlöbes, M. Diehl, L. Sharma, F. Roters, D. Raabe, In situ observation of collective grain-scale mechanics in Mg and Mg–rare earth alloys, *Acta Materialia* 80 (2014) 77-93.
- [9] A. Maldar, L. Wang, B. Liu, W. Liu, Z. Jin, B. Zhou, X. Zeng, Activation of $\langle c \rangle$ dislocations in Mg with solute Y, *Journal of Magnesium and Alloys* (2021).
- [10] W. Gao, H. Liu, A highly ductile magnesium alloy system, *IOP Conference Series: Materials Science and Engineering* 4 (2009).
- [11] Z.R. Zeng, Y.M. Zhu, R.L. Liu, S.W. Xu, C.H.J. Davies, J.F. Nie, N. Birbilis, Achieving exceptionally high strength in Mg₃Al₁Zn-0.3Mn extrusions via suppressing intergranular deformation, *Acta Materialia* 160 (2018) 97-108.
- [12] T.T.T. Trang, J.H. Zhang, J.H. Kim, A. Zargarán, J.H. Hwang, B.C. Suh, N.J. Kim, Designing a magnesium alloy with high strength and high formability, *Nature communications* 9(1) (2018).
- [13] S. Sandlobes, M. Friak, S. Korte-Kerzel, Z. Pei, J. Neugebauer, D. Raabe, A rare-earth free magnesium alloy with improved intrinsic ductility, *Sci Rep* 7(1) (2017) 10458.
- [14] Z.R. Zeng, M.Z. Bian, S.W. Xu, C.H.J. Davies, N. Birbilis, J.F. Nie, Effects of dilute additions of Zn and Ca on ductility of magnesium alloy sheet, *Materials Science and Engineering: A* 674 (2016) 459-471.
- [15] J. Xu, B. Guan, Y. Xin, G. Huang, P. Wu, Q. Liu, Revealing the role of pyramidal $\langle c+a \rangle$ slip in the high ductility of Mg-Li alloy, *Journal of Magnesium and Alloys* (2021).
- [16] S.R. Agnew, J.A. Horton, M.H. Yoo, Transmission electron microscopy investigation of $\langle c+a \rangle$ dislocations in Mg and α -solid solution Mg-Li alloys, *Metallurgical and Materials Transactions A* 33(3) (2002) 851-858.
- [17] K.-H. Kim, J.B. Jeon, N.J. Kim, B.-J. Lee, Role of yttrium in activation of $\langle c+a \rangle$ slip in magnesium: An atomistic approach, *Scripta Materialia* 108 (2015) 104-108.
- [18] G. Nayeri, W.J. Poole, C.W. Sinclair, S. Zaeferrer, Measurement of the critical resolved shear stress for basal slip in magnesium alloys using instrumented indentation, *Scripta Materialia* 156 (2018) 37-41.

- [19] Z. Wu, W.A. Curtin, The origins of high hardening and low ductility in magnesium, *Nature* 526 (2015) 62-7.
- [20] Z. Wu, R. Ahmad, B. Yin, S. Sandlöbes, W.A. Curtin, Mechanistic origin and prediction of enhanced ductility in magnesium alloys, *Science* 359 (2018) 447-452.
- [21] Y.-J. Hu, M.R. Fellingner, B.G. Bulter, Y. Wang, K.A. Darling, L.J. Kecskes, D.R. Trinkle, Z.-K. Liu, Solute-induced solid-solution softening and hardening in bcc tungsten, *Acta Materialia* 141 (2017) 304-316.
- [22] C.A. Stein, A. Cerrone, T. Ozturk, S. Lee, P. Kenesei, H. Tucker, R. Pokharel, J. Lind, C. Hefferan, R.M. Suter, A.R. Ingraffea, A.D. Rollett, Fatigue crack initiation, slip localization and twin boundaries in a nickel-based superalloy, *Current Opinion in Solid State and Materials Science* 18(4) (2014) 244-252.
- [23] D. Raabe, M. Herbig, S. Sandlöbes, Y. Li, D. Tytko, M. Kuzmina, D. Ponge, P.P. Choi, Grain boundary segregation engineering in metallic alloys: A pathway to the design of interfaces, *Current Opinion in Solid State and Materials Science* 18(4) (2014) 253-261.
- [24] J. Kacher, B.P. Eftink, B. Cui, I.M. Robertson, Dislocation interactions with grain boundaries, *Current Opinion in Solid State and Materials Science* 18(4) (2014) 227-243.
- [25] A.T. Lim, M. Haataja, W. Cai, D.J. Srolovitz, Stress-driven migration of simple low-angle mixed grain boundaries, *Acta Materialia* 60(3) (2012) 1395-1407.
- [26] M.R. Barnett, Twinning and the ductility of magnesium alloys Part II. "Contraction" twins, *Materials Science and Engineering a-Structural Materials Properties Microstructure and Processing* 464 (2007) 8-16.
- [27] M.R. Barnett, Twinning and the ductility of magnesium alloys Part I: "Tension" twins, *Materials Science and Engineering a-Structural Materials Properties Microstructure and Processing* 464 (2007) 1-7.
- [28] J.F. Nie, Y.M. Zhu, J.Z. Liu, X.Y. Fang, Periodic segregation of solute atoms in fully coherent twin boundaries, *Science* 340(6135) (2013) 957-60.
- [29] Y.M. Zhu, M.Z. Bian, J.F. Nie, Tilt boundaries and associated solute segregation in a Mg–Gd alloy, *Acta Materialia* 127 (2017) 505-518.
- [30] J. Zhang, Y. Dou, Y. Zheng, Twin-boundary segregation energies and solute-diffusion activation enthalpies in Mg-based binary systems: A first-principles study, *Scripta Materialia* 80 (2014) 17-20.

- [31] Z. Pei, R. Li, J.-F. Nie, J.R. Morris, First-principles study of the solute segregation in twin boundaries in Mg and possible descriptors for mechanical properties, *Materials & Design* 165 (2019) 107574.
- [32] L. Huber, R. Hadian, B. Grabowski, J. Neugebauer, A machine learning approach to model solute grain boundary segregation, *npj Computational Materials* 4(1) (2018) 64.
- [33] W. Kohn, L.J. Sham, Self-Consistent Equations Including Exchange and Correlation Effects, *Physical Review* 140(4A) (1965) A1133-A1138.
- [34] G. Kresse, J. Furthmüller, Efficient iterative schemes for ab initio total-energy calculations using a plane-wave basis set, *Physical Review B* 54(16) (1996) 11169-11186.
- [35] G. Kresse, D. Joubert, From ultrasoft pseudopotentials to the projector augmented-wave method, *Physical Review B* 59(3) (1999) 1758-1775.
- [36] D. Scheiber, R. Pippan, P. Puschnig, A. Ruban, L. Romaner, Ab-initio search for cohesion-enhancing solute elements at grain boundaries in molybdenum and tungsten, *International Journal of Refractory Metals and Hard Materials* 60 (2016) 75-81.
- [37] R. Tran, Z. Xu, N. Zhou, B. Radhakrishnan, J. Luo, S.P. Ong, Computational study of metallic dopant segregation and embrittlement at molybdenum grain boundaries, *Acta Materialia* 117 (2016) 91-99.
- [38] Mihriban O. Pekgülyüz, K.U. Kainer, A.A. Kaya, *Fundamentals of magnesium alloy metallurgy*, Woodhead Publishing, Cambridge, UK, 2013.
- [39] S. Choudhury, J.A. Aguiar, M.J. Fluss, L.L. Hsiung, A. Misra, B.P. Uberuaga, Non-uniform Solute Segregation at Semi-Coherent Metal/Oxide Interfaces, *Scientific Reports* 5 (2015) 13086.
- [40] M.A. Gibson, C.A. Schuh, A survey of ab-initio calculations shows that segregation-induced grain boundary embrittlement is predicted by bond-breaking arguments, *Scripta Materialia* 113 (2016) 55-58.
- [41] P. Lejček, M. Šob, V. Paidar, Interfacial segregation and grain boundary embrittlement: An overview and critical assessment of experimental data and calculated results, *Progress in Materials Science* 87 (2017) 83-139.
- [42] A.Y. Lozovoi, A.T. Paxton, M.W. Finnis, Structural and chemical embrittlement of grain boundaries by impurities: A general theory and first-principles calculations for copper, *Physical Review B* 74(15) (2006).

- [43] H.A. Murdoch, C.A. Schuh, Estimation of grain boundary segregation enthalpy and its role in stable nanocrystalline alloy design, *Journal of Materials Research* 28(16) (2013) 2154-2163.
- [44] M.A. Gibson, C.A. Schuh, Segregation-induced changes in grain boundary cohesion and embrittlement in binary alloys, *Acta Materialia* 95 (2015) 145-155.
- [45] Z. Nilforoushan, A. Mohades, M.M. Rezaii, A. Laleh, 3D hyperbolic Voronoi diagrams, *Computer-Aided Design* 42(9) (2010) 759-767.
- [46] J. von Pezold, L. Lymperakis, J. Neugebauer, Hydrogen-enhanced local plasticity at dilute bulk H concentrations: The role of H–H interactions and the formation of local hydrides, *Acta Materialia* 59(8) (2011) 2969-2980.
- [47] A.J. Cao, Y.Q. Cheng, E. Ma, Structural processes that initiate shear localization in metallic glass, *Acta Materialia* 57(17) (2009) 5146-5155.
- [48] X. Zhou, J. Song, Effects of alloying elements on vacancies and vacancy-hydrogen clusters at coherent twin boundaries in nickel alloys, *Acta Materialia* 148 (2018) 9-17.
- [49] C. He, Z. Li, H. Chen, N. Wilson, J.F. Nie, Unusual solute segregation phenomenon in coherent twin boundaries, *Nature communications* 12(1) (2021) 722.
- [50] L. Huber, J. Rottler, M. Miltzer, Atomistic simulations of the interaction of alloying elements with grain boundaries in Mg, *Acta Materialia* 80 (2014) 194-204.
- [51] D. Ando, J. Koike, Y. Sutou, The role of deformation twinning in the fracture behavior and mechanism of basal textured magnesium alloys, *Materials Science and Engineering: A* 600 (2014) 145-152.
- [52] J. Koike, N. Fujiyama, D. Ando, Y. Sutou, Roles of deformation twinning and dislocation slip in the fatigue failure mechanism of AZ31 Mg alloys, *Scripta Materialia* 63(7) (2010) 747-750.
- [53] B. Li, Q. Ma, Z. McClelland, S.J. Horstemeyer, W.R. Whittington, S. Brauer, P.G. Allison, Twin-like domains and fracture in deformed magnesium, *Scripta Materialia* 69(6) (2013) 493-496.
- [54] S. Niknejad, S. Esmaili, N.Y. Zhou, The role of double twinning on transgranular fracture in magnesium AZ61 in a localized stress field, *Acta Materialia* 102 (2016) 1-16.

Chapter 7: Temperature and Composition Dependent of the Critical Resolved Shear Stresses of Mg-Y Alloys: An Atomistic Study

7.1 Preface

The study in Chapter 5 illustrated modification of twinning and slipping due to addition of yttrium in polycrystalline Mg-Y system. Chapter 6 examined segregation behavior of solutes at twinning boundaries, providing solute effect on strengthening of twinning boundaries. Therefore, to include a fully understanding of solute effect on all defects in Mg, this chapter performed careful atomistic simulations to evaluate evolution of critical shear stress of dislocations with changing Y content and temperature. It also further built the critical shear stress dependence of dislocation on temperature and Y content. The result in this chapter provides support for the design of Mg-Y systems by controlling Y content and temperature.

- This chapter presents an article to be submitted as:

Temperature and Composition Dependent of the Critical Resolved Shear Stresses of Mg-Y Alloys: An Atomistic Study

Huicong Chen, Jun Song

7.2 Abstract

Extensive atomistic simulations are carried out to investigate the critical shear stress of three main edge dislocations in Mg-Y alloy as a function of temperature ranging from 0K to 500K and Y composition from 0.5 at% to 3.0 at%. The results show that at 0 K, basal slip is more sensitive to the Y solute compared to prismatic and pyramidal slip. This stronger hardening effect of Y on basal slip makes the easy activation of non-basal slip systems. Furthermore, Pyramidal slip is observed more sensitive to temperature, and combined with Y addition, more pyramidal slips are potentially activated at finite temperature. The current simulation shows a promising pathway of improvement for ductility of Mg alloys by controlling the content of Y at finite temperature.

7.3 Introduction

Magnesium (Mg) is the lightest structural metal with high specific strength, good corrosion and heat resistance as well as the abundant reserves in the Earth's crust [1-5]. Therefore, widening its applications in the automotive and aerospace industries can help combat the global warming by building an energy-saving transportation system with reduced weight. Mg also has excellent biocompatibility and thus attractive for biomedical applications [6-9]. However, the low toughness and low ductility of Mg result in poor formability, which limits its desirability for many applications.

The lack of formability is connected to the inability of hexagonal-close-packed (hcp) Mg to accommodate plasticity in the crystallographic $\langle c \rangle$ direction. Generally, the plasticity in the $\langle a \rangle$ direction in a hcp polycrystal is achieved by basal and prismatic dislocations, and deformation in the $\langle c \rangle$ direction requires the activation of $\langle c + a \rangle$ pyramidal dislocations. Basal dislocation is the most easily activated slip system due to its lowest resolved critical shear stress (CRSS), about 0.5MPa [10-12]. CRSS of prismatic $\langle a \rangle$ dislocation is around 40 MPa [10-12], making it difficult

competing with basal dislocation for accommodating plasticity in the $\langle a \rangle$ direction. These two slip systems can only provide limited deformation modes, which can not meet the Von Mises criteria to deform the material homogeneously in a polycrystalline Mg [13]. Twinning with CRSS around 12 MPa [14], is also profusely observed in Mg, but this deformation mode can only provide limited plasticity in the $\langle c \rangle$ axis. Therefore, activating more $\langle c + a \rangle$ is imperative for development of new Mg alloys with desirable formability and much work has been devoted recently to study how to enhance non-basal slip dislocations in Mg, especially to improve the activation of the $\langle c + a \rangle$ pyramidal dislocations at all length scales experimentally, computationally, and theoretically [15-23].

One encouraging approach is to enhance the ductility of Mg through introducing solute elements. It is found that the $\langle c + a \rangle$ dislocation is not stable on the easy-glide pyramidal II planes and thus it tends to dissociate into basal-associated immobile structures (called PB transition), leading to the immediate hardening [18]. On the other hand, the cross-slip of the $\langle c + a \rangle$ from pyramidal II plane to pyramidal I plane enable the continuous and stable slipping of $\langle c + a \rangle$ dislocation on pyramidal planes [15]. However, the energy barrier for the PB transition is usually lower than that for the cross-slip. Consequently, $\langle c + a \rangle$ is dominated by the PB transformation in pure Mg. Thanks to the alloying strategy, introducing specific solutes can change the energy barrier for these two competitive mechanisms. For example, the small addition of favorable solutes such as Ca, Zr, Nd, Y, Ce, Er and Gd can significantly decrease the energy barrier for the cross-slip to a lower level than that for PB transition, contributing in a high ductility and formability of these Mg based alloys [15, 22]. Furthermore, alloying is also an effective way to modify the sequence of the activation of different deformation modes by reducing the differences in the CRSS between basal and non-basal slips [12, 14, 21, 24-29]. Accordingly, non-basal slips become more operative to

accommodate more plasticity during deformation at room temperature. The effect of RE elements has received considerable attention in last two decades for this purpose [21, 22, 28, 30-36]. The improved ductility has been observed in Mg-Nd [35, 36], Mg-Y [22, 34] and Mg-Ce [30, 32, 33] alloy systems, which is mainly ascribed to the enhanced pyramidal $\langle c + a \rangle$ slip. Herrera-Solaz et al [28] found that compared to pure Mg, the presence of Nd increases the CRSS of basal slip and twinning and thus the CRSS ratio between pyramidal and basal slip systems is decreased to an extent where the non-basal systems are activated readily. The recent atomistic simulation results [21, 25] also indicate that the larger solute strengthening effect on basal and prismatic slip than pyramidal slip due to addition of Nd/Y can potentially reduce the CRSS difference of three main slip systems.

The above findings give an insight and a guide to design of new Mg alloys with enhanced ductility and formability. However, difficulties of experimental characterization limit the accurate calculation of CRSS, and the previous atomistic simulations were usually performed at 0K, but temperature (T) is also an important factor influencing the dislocation activity [11, 30, 37]. Therefore, it is imperative to provide a detailed description of dependence of CRSS on temperature as well as solute concentration.

Therefore, the aim of this work is to conduct a detailed atomistic study to provide a comprehensive analysis of the critical stress across both temperature and composition in Mg-Y alloy. Three main dislocations on the basal, prismatic and pyramidal planes will be considered.

7.4 Methodology

Molecular statics (MS) and Molecular dynamics (MD) simulations were carried out using the Large-scale Atomic/Molecular Massively Parallel Simulator (LAMMPS) package [38]. The second nearest neighbor modified embedded-atom method (2NN MEAM) interatomic potentials

were employed to describe interatomic interactions for pure Mg [39] and Mg-Y [40] systems. These potentials can accurately describe all the important slip systems and have been used in the realistic atomistic studies of general magnesium deformation and failure problems [15, 16, 18, 39, 40]. Visualization was generated using open source software Ovito [41].

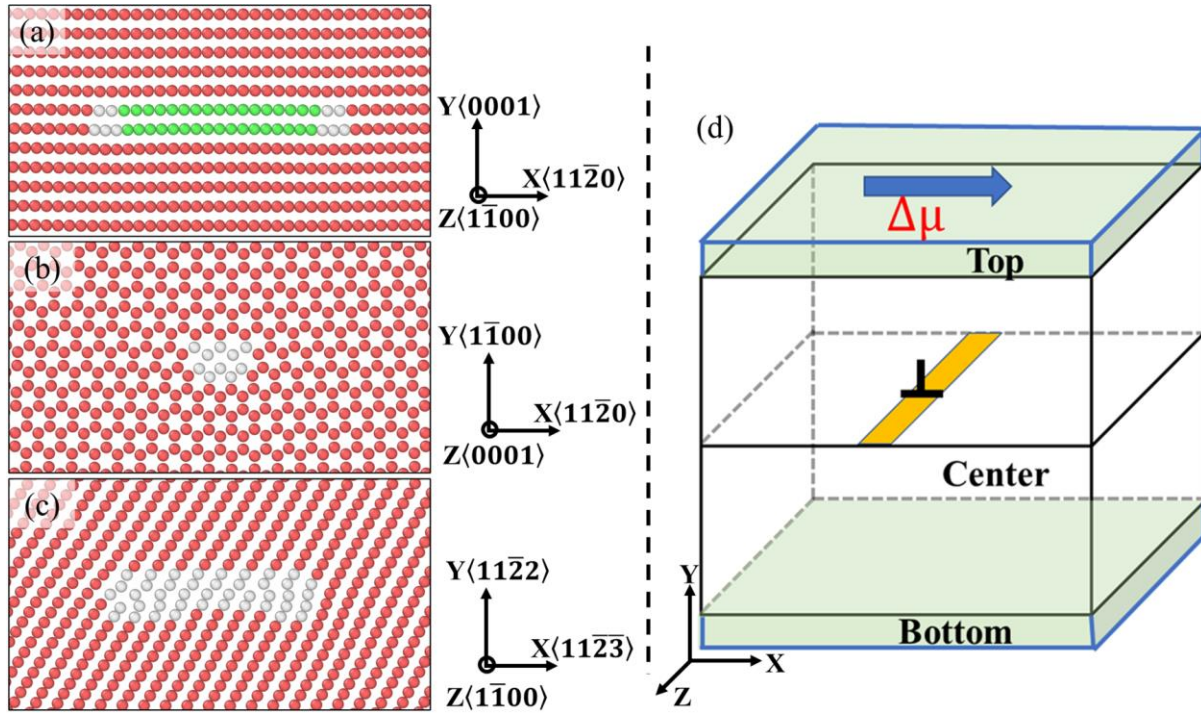


Figure 7.1. Core structures of edge dislocations on (a) basal, (b) prismatic and (c) pyramidal II planes using a MEAM interatomic potential for pure Mg [39]. (d) Schematic view of the simulation cell showing the shearing procedure to move a dislocation.

The basal $\langle a \rangle$ slip, prismatic $\langle a \rangle$ slip and second-order pyramidal II $\langle c+a \rangle$ slip were considered in the current simulation. All dislocations were created at the center of the simulation cell by displacing all atoms according to the Volterra fields [42] with x-axis being along the dislocation line direction and the y-axis being normal to the slip plane. The simulation cells have dimensions ($l_x \times l_y \times l_z$) of 31.6 nm \times 52 nm \times 11 nm, 3.16 nm \times 52 nm \times 16 nm and 30 nm \times 32.9 nm \times 22 nm for supercells enclosing the basal, prismatic and pyramidal II slips respectively. Periodic boundary conditions were only imposed along the x and z directions, while atoms in the top and

bottom regions were constrained to two-dimensional dynamics by fixing their normal direction. Following the initial dislocation creation, each system was relaxed using energy minimization. The core structures after relaxation for pure Mg was illustrated in **Figure 7.1(a-c)**. The alloy systems were created on base of the pure Mg system, and alloying was done by randomly substituting Mg atoms by solute atoms throughout each system, followed by relaxation.

After the relaxation, the simulation box was then deformed to drive dislocation motions. Rigid strain-controlled loading method [43, 44] was used to apply a shear displacement, as schematically illustrated in **Figure 7.1(d)**. The simulation boxes were partitioned into three regions, as noted in **Figure 7.1(d)**, where the center region located free atoms while atoms in the bottom and top regions were held rigid and not allowed to relax. In performing the deformation, the top block was displaced incrementally, each time by a small distance $\Delta\mu$, along x direction, to induce shear deformation and thus drive gliding of the dislocation. Here, $\Delta\mu = \delta\varepsilon \times l_y$, where $\delta\varepsilon (=6 \times 10^{-6})$ is the corresponding strain increment and l_y is dimension of the simulation box along y direction. For MS simulation, i.e., the shearing deformation at $T = 0\text{K}$, conjugate gradient minimization [45] was applied to relax the system after each incremental displacement. Since only one dislocation is considered in the current models, the plasticity is solely accommodated by the dislocation motion. The critical shear stress can be represented by the flow stress on the shear stress–strain curves after yielding of dislocation. The corresponding stress at each strain was computed from the internal force per unit area [10],

$$\sigma^{xy} = \frac{\sum_{i \in Top} F_i^x}{A} = \frac{N^{Top} F^{Top}}{A} \quad (7.1)$$

where N^{Top} and F^{Top} are the number of atoms and the average force for each atom in top layer, respectively. A is the cross section area normal to the y direction. The instant shear strain ε^{xy} was

calculated by the displacement of the center-of-mass position of atoms in the top layer from its reference configuration, i.e., the relaxed structure prior to loading. Thus, we have:

$$\varepsilon^{xy} = \frac{1}{l_y} (u_i^x - u_0^x) \quad (7.2)$$

where u_i^x is the center-of-mass position of atoms from the top layer after the i th strain loading and u_0^x is the initial position.

For MD simulation ($T > 0K$), to generate a shearing stress, a constant force was applied along the Burgers vector direction to each atom on the top surface of the simulation cell. The central atoms were equilibrated at desired temperature for 40ps, followed by the shearing deformation at the strain rate of $1.5 \times 10^{-5} s^{-1}$ for 4ns. NVT ensemble was used to keep the temperature constant, and time was integrated using Verlet algorithm with a time step of 2 fs in all MD simulations. The stress and strain are calculated using the equation (7.1) and (7.2), respectively. The CRSS σ_{CRSS} was taken to be the average of flow stresses after the dislocation starts gliding at a critical stress of σ_j^{xy} , i.e.,

$$\sigma_{CRSS} = \frac{\sum_{i \geq j} \sigma_i^{xy}}{N_{yield}} \quad (7.3)$$

where σ_i^{xy} is the stress after yielding and N_{yield} is the number of peak stresses around the yielding point.

Six compositions ($C_Y = 0.5, 1.0, 1.5, 2.0, 2.5$ and 3.0 at%) and six temperatures ($T = 0, 10, 200, 300, 400, 500K$) were chosen in this study. Calculation for each composition was repeated for three times using different solute configuration.

7.5 Results and Discussion

7.5.1 Solute Effect on CRSS at 0K

7.5.1.1 Stress-Strain Curves

Figure 7.2 shows stress-strain responses from the MS simulations for dislocations in pure Mg and the σ_{CRSS} values were calculated as 1.5MPa, 11.5MPa and 200Mpa for basal, prismatic and pyramidal slip systems, respectively. The large difference of σ_{CRSS} among these slip systems limits activation of different deformation modes beyond basal slip and such a strong anisotropy result in low ductility and poor formability for pure Mg.

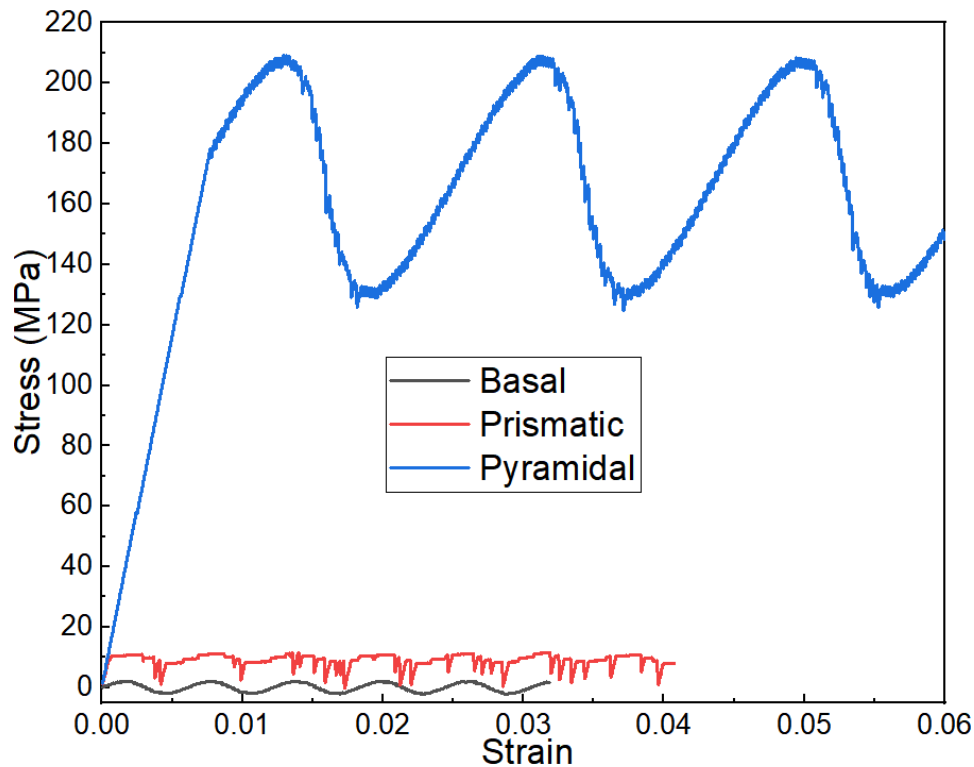


Figure 7.2. Simulated stress–strain curves for pure Mg on the basal, prismatic, and pyramidal II planes, at 0 K.

Figure 7.2 and Figure 7.3 show representative stress-strain curves for three dislocations in pure Mg and Mg - (0.5-3) at.% Y at 0 K, respectively. For pure Mg, the stress reaches the peak value for

each dislocation in pure Mg periodically (see **Figure 7.2**) to overcome Peierls-Nabarro (PN) barriers when they transit between neighbouring Peierls valleys. For Mg-Y alloying systems the flow stress is purely affected by the solute atoms in the absence of kinetic contributions at finite temperature. As shown in **Figure 7.3**, each curve shows an initial linear increase of stress with strain due to elastic deformation. After reaching the yielding point, the stress fluctuates around an average value because of dislocation-phonon interactions. Different from motion of dislocation in pure Mg, solute dragging effect is introduced due to Mg-Y interactions, so pronounced fluctuations are observed for Mg-Y alloys as shown in **Figure 7.3**. Therefore, the increase and decrease of stress around a fluctuation in each curve represent the dislocation approaching and escaping from solutes, respectively. Also, the random distribution of Y atoms in and around the glide plane would lead to the subsequent smaller or larger peaks in stress as shown in **Figure 7.3(a-c)**. The maximum values in each curve indicate the strength resulting from local solutes and this is the reason why we take an average value of flow stress in each curve as the CRSS for statistical analysis.

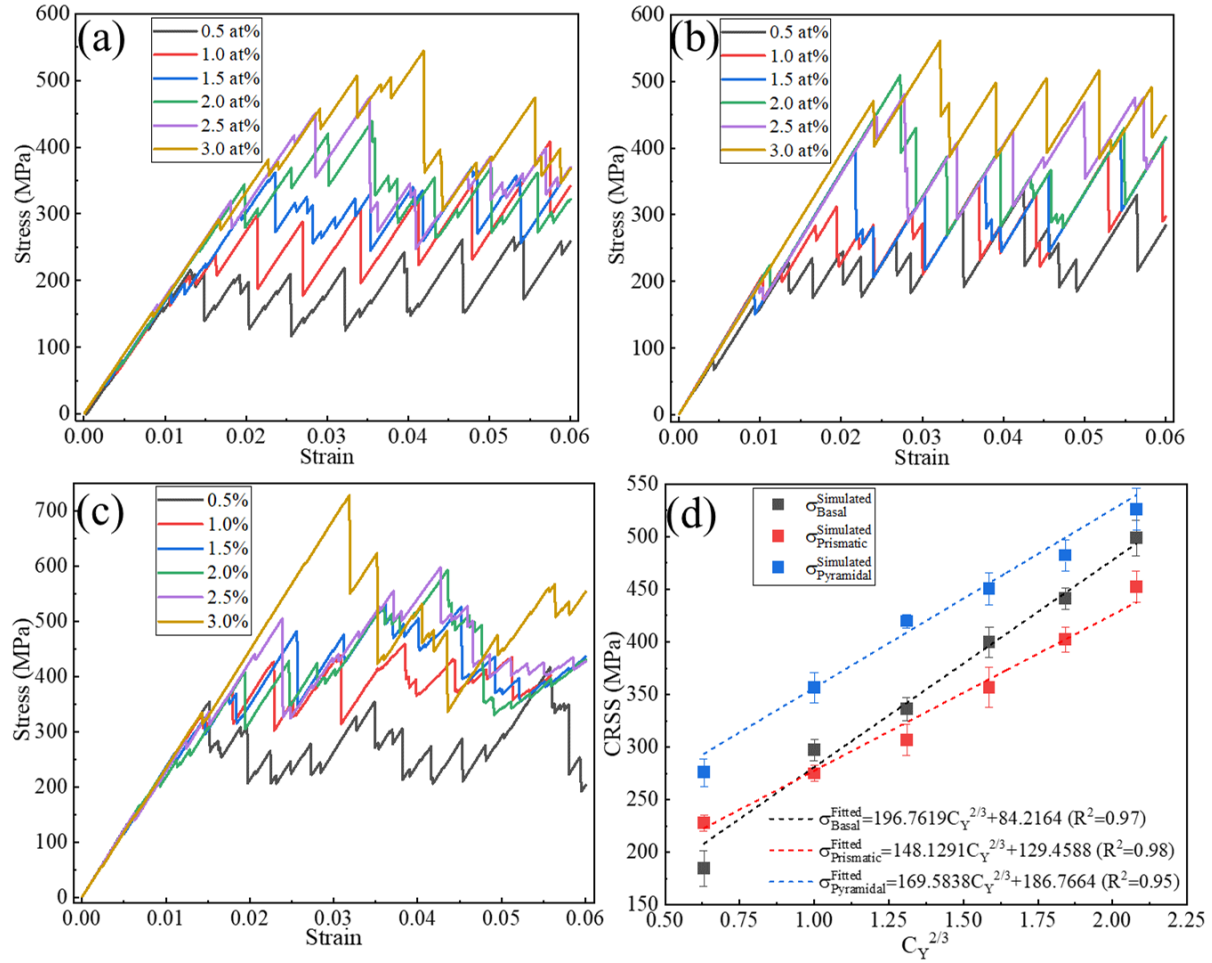


Figure 7.3. The stress-strain responses of (a) basal dislocation, (b) prismatic dislocation and (c) pyramidal II dislocation moving at 0K and (d) the CRSS distribution with different Y content and the fitted results, where solid squares are simulation results, and dashed lines are the linear fitting. Error bars represent standard deviation.

7.5.1.2 Evolution of CRSS with Y Content

According to Labusch's statistics of local obstacles [46, 47], solute effect on CRSS follows the $C^{2/3}$ power law at low temperature, even at $T = 0$ K [48]. Thus, $C_Y^{2/3}$ is used in the plot CRSS versus Y concentration. The σ_{CRSS} was computed by using equation (7.3) and the results were provided in **Figure 7.3(d)**, showing that the increased σ_{CRSS} with increasing Y content, i.e. $\sigma_{CRSS} \propto C_Y^{2/3}$ for all dislocations due to the solution hardening effect [49]. However, the amount of CRSS

increment for each slip system is different. For example, the σ_{CRSS} of basal slip is much smaller than that of prismatic and pyramidal slips in pure Mg and their ratios (i.e. $\sigma_{CRSS}^{Prismatic} / \sigma_{CRSS}^{Basal}$ and $\sigma_{CRSS}^{Pyramidal} / \sigma_{CRSS}^{Basal}$) are 7.6 and 133, respectively. With the addition of 0.5 at% Y, the σ_{CRSS} of basal, prismatic and pyramidal slips is increased to 184 MPa, 227MPa and 270MPa respectively. Obviously, CRSS ratios between basal and non-basal slip systems ($\frac{\sigma_{CRSS}^{Prismatic}}{\sigma_{CRSS}^{Basal}} \cong 1.23$ and $\frac{\sigma_{CRSS}^{Pyramidal}}{\sigma_{CRSS}^{Basal}} \cong 1.47$) are significantly reduced and with more Y atoms added, much smaller difference is observed as shown in **Figure 7.3(d)**. Interestingly, prismatic slip would be dominated beyond basal slip when Y content reaches 1 at% according to the current simulation.

A linear curve fit was then applied to the data in **Figure 7.3(d)** to compare the trend of CRSS varying with Y concentration $C_Y^{2/3}$ for each dislocation and the results were plotted in **Figure 3(d)** noted by the dash lines. Coefficients of $C_Y^{2/3}$ for basal, prismatic and pyramidal slips are fitted as around 196, 148 and 169 (see **Figure 7.3(d)**), indicating that addition of Y results in the largest hardening effect on basal slip, the intermediate hardening effect on pyramidal slip and the smallest hardening effect on prismatic slip. Thanks to the faster increase of CRSS in basal dislocation with increasing Y concentration, the anisotropy in CRSS for the major slip systems is reduced, resulting in the easier activation of non-basal slip. Therefore, the improved ductility and deformability would be present in Mg-Y alloy systems. Such modification is in good agreement with the results from previous experiments in the Y-alloyed Mg [15, 22].

7.5.2 Solute Effect on CRSS at Finite Temperature

7.5.2.1 Stress-strain Curves

Using MD simulation method, the stress–strain curves for Mg - (0.5–3) at.% Y alloys were obtained at temperatures of 100 K, 200 K, 300 K, 400 K and 500K. The results for basal, prismatic

and pyramidal slip systems are presented in **Figure 7.4**, **Figure 7.5** and **Figure 7.6** respectively. In all cases, the stress initially increases nearly linearly with increasing strain representing an elastic regime since the dislocation is immobile near the bottom of a Peierls valley. Once reaching the critical stress where the dislocation overcome the barrier from Peierls valley and solute dragging, the stress then shows a decrease to a local minimum indicating material softening i.e., plastic events.

The influence of temperature on the stress-strain behavior was also captured. Mechanical curves of three dislocations in the current simulation show the similar trend with varying temperature as shown in **Figure 7.4**, **Figure 7.5** and **Figure 7.6**, where the initial yielding is reached at a lower strain as the temperature increases. Therefore, a significant softening of dislocation is observed when the temperature is raised, especially for pyramidal slip as shown in **Figure 7.6**, where the largest stress was reduced to 400 MPa at 500K from 600 MPa at 100 K for Mg – 3 at.% Y and a similar decrease in CRSS is also observed for the other alloy systems as the temperature increases. Also, instead of a smooth curve, fluctuations are noted for stress-strain curves across all compositions due to drag-controlled dynamic behavior. This is expected for the motion of dislocations since the drag coefficient increases with increasing temperature once a dislocation overcomes the initial threshold stress. [50] This fluctuation is more pronounced for basal slip system at a temperature beyond 200 K as shown in **Figure 7.4**.

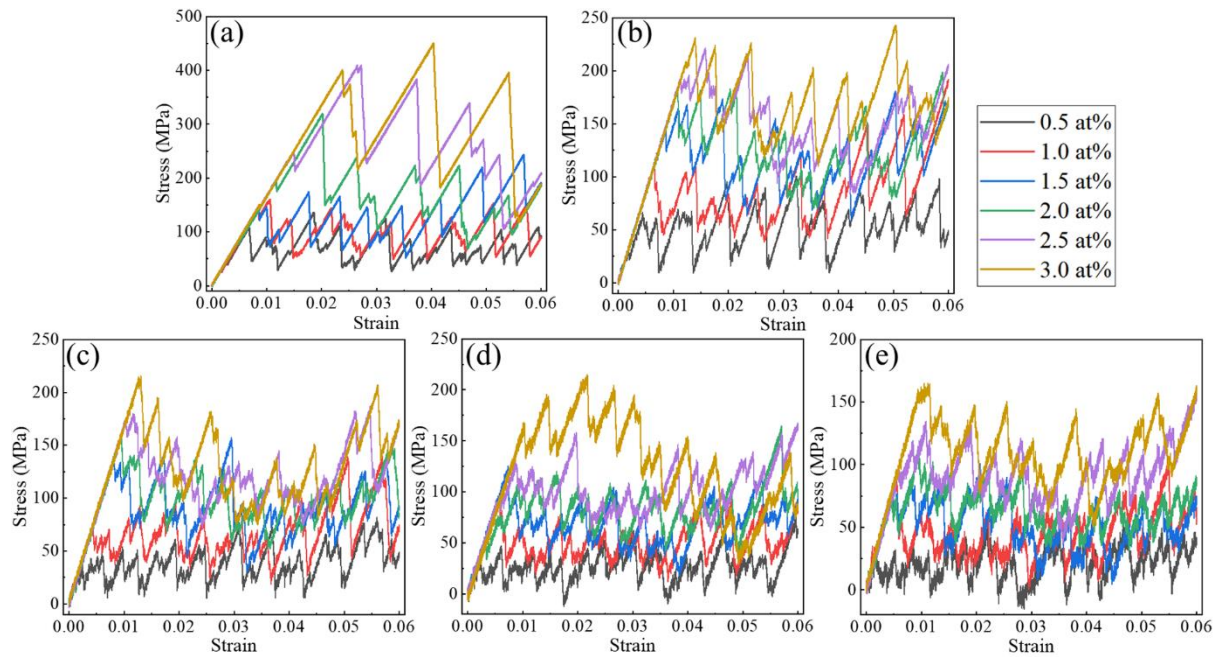


Figure 7.4. The stress-strain responses of the basal dislocation decorated with different Y content moving at temperatures of (a) 100K, (b) 200K, (c) 300K, (d) 400K and (e) 500K.

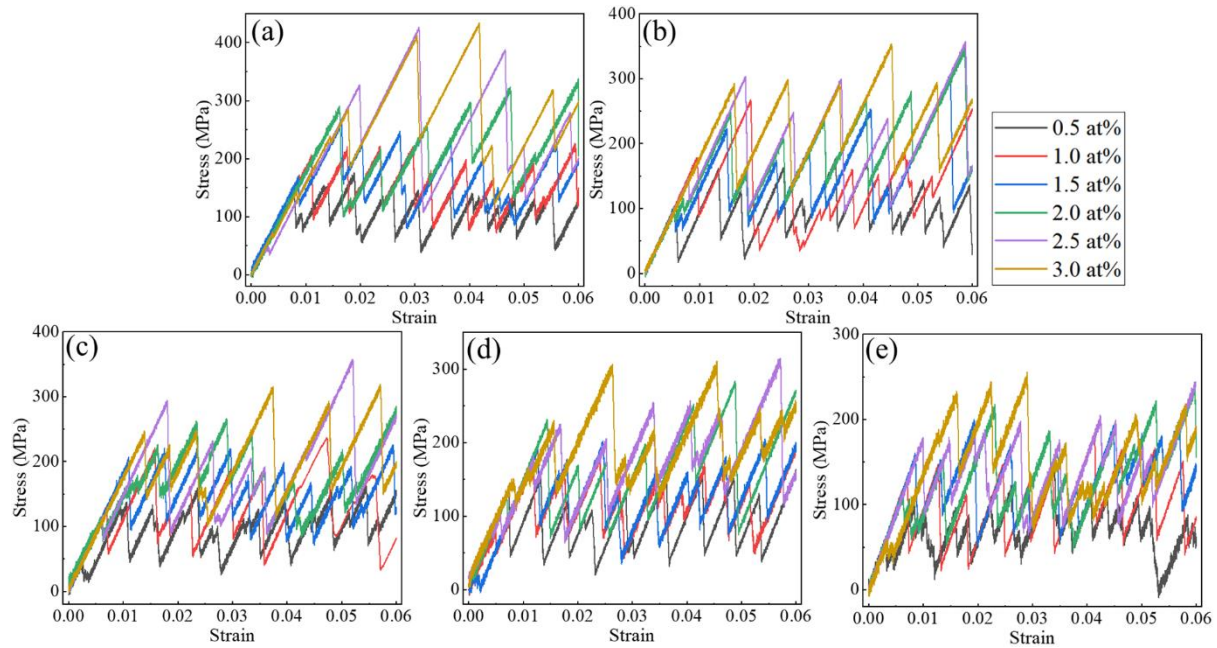


Figure 7.5. The stress-strain responses of the prismatic dislocation decorated with different Y content moving at temperatures of (a) 100K, (b) 200K, (c) 300K, (d) 400K and (e) 500K.

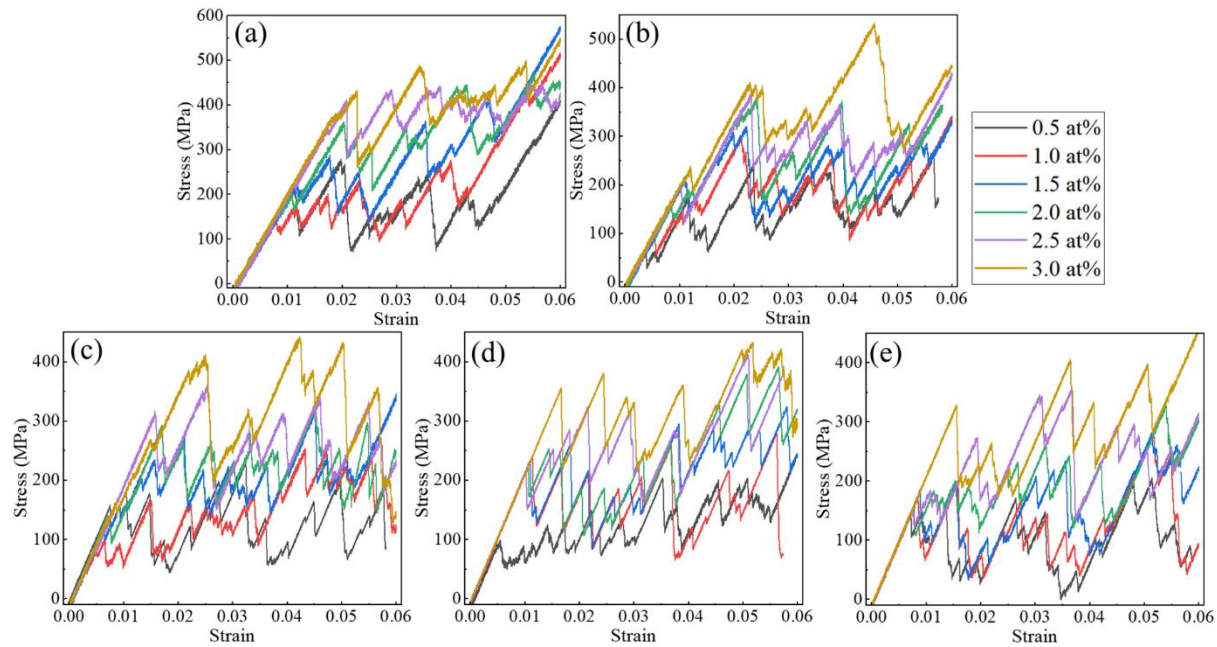


Figure 7.6. The stress-strain responses of the pyramidal dislocation decorated with different Y content moving at temperatures of (a) 100K, (b) 200K, (c) 300K, (d) 400K and (e) 500K.

7.5.2.2 Evolution of CRSS Versus Y Content and Temperature

The CRSS for glide on three dislocations as a function of solute concentration for different temperatures is plotted in **Figure 7.7**. It is evident that the minimum applied resolved shear stress for dislocation glide at $T > 0\text{K}$ is less than Peierls stress (at 0K) due to the presence of kinetic contributions at finite temperature. At low temperature, CRSS firstly increases at a larger rate with increasing Y for all three dislocations. Since motion of a dislocation is thermodynamically related, then raising temperature decrease the barrier for initiating a dislocation. Therefore, a slow increase of CRSS with Y is observed when temperature is raised to above 100 K as shown in **Figure 7.7(a-c)**. Similarly, at a specific temperature, CRSS increases at a different rate for different dislocations and the strongest solution hardening is observed for basal dislocation, leading to a reduction of anisotropy in the CRSSes for the major slip systems. Accordingly, the easy activation of non-basal

slip systems must be helpful for improvement of the formability and ductility in processing of Mg-Y alloys at ambient or high temperature.

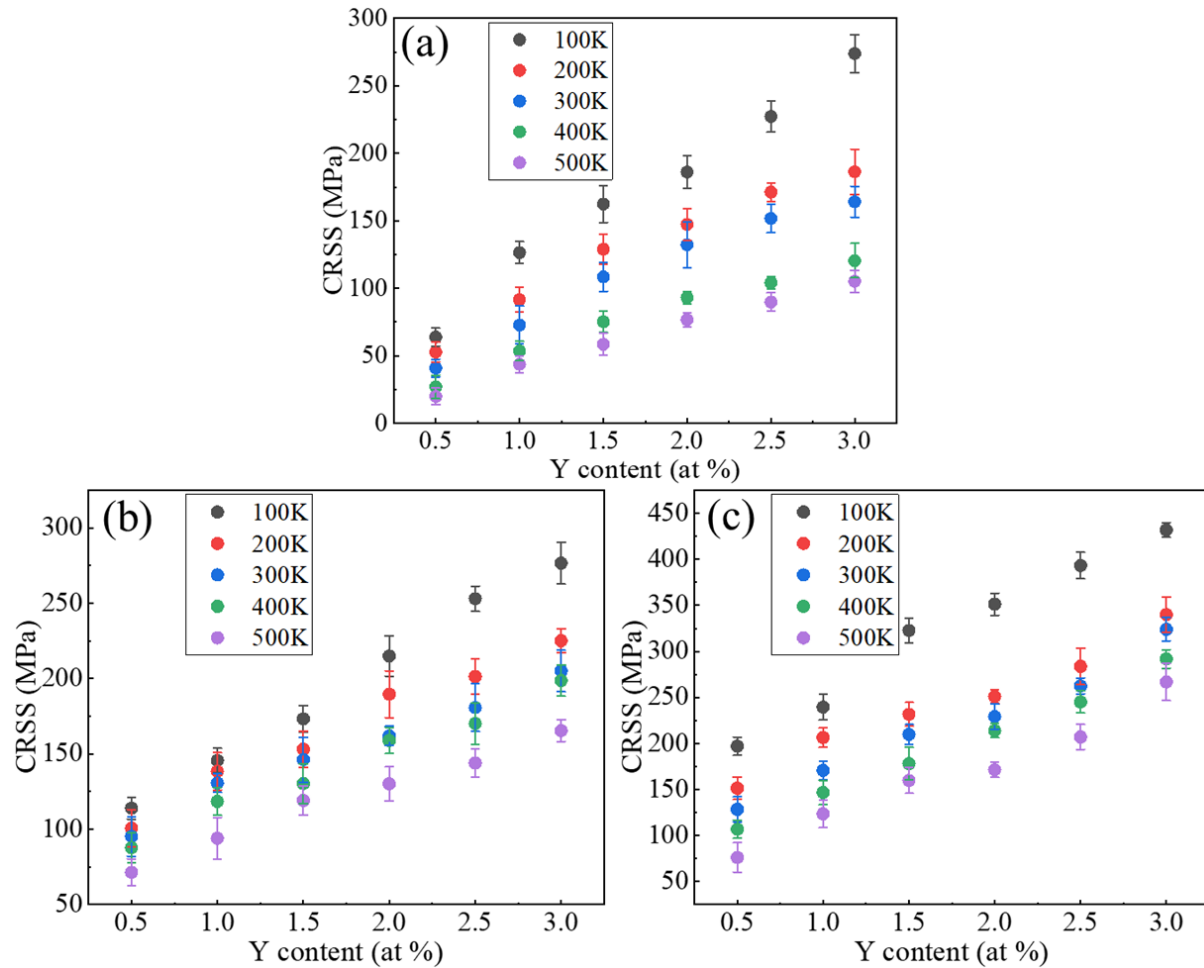


Figure 7.7. Plot of CRSS evolution as a function of Y content for (a) basal, (b) prismatic and (c) pyramidal dislocations moving at various temperatures. Error bars represent standard deviation.

Figure 7.8 provides results of evolution of CRSS for glide on three slip planes as a function of temperature across all alloying compositions. As mentioned above, the CRSS decreases with increasing temperature and as shown in **Figure 7.8**. This indicates that the dislocation glide is controlled by a thermal activation mechanism. CRSS of basal dislocation becomes more sensitive to temperature for simulation cells with more Y atoms as shown in **Figure 7.8** (a), where CRSS presents a faster drop for alloys at higher Y concentration. Unlike basal slip, CRSS tendency of

prismatic slip shows slight difference for evolution of CRSS with temperature at various Y concentration. For a fixed composition, CRSS for glide on pyramidal plane is much more sensitive to temperature than CRSS of basal and prismatic slip systems. For example, in case of Mg-2.5 at%Y, CRSS of pyramidal slip at 100 K is about 400MPa and decreased by 175 MPa when temperature is increased to 500 K as shown in **Figure 7.8 (c)**. In comparison, CRSS of basal and prismatic slip systems is decreased by 100 MPa and 80 MPa when temperature is increased from 100 K to 500 K as shown in **Figure 7.8(a)** and (b). This observation is consistent with a general proposition that pyramidal $\langle c+a \rangle$ is thermally activated deformation mechanism in HCP Mg [23, 24, 29]. However, addition of RE elements, such as Y solute in current simulation, can reduce the anisotropy of CRSS in main slip systems of Mg alloys and thus potentially improve their formability at finite temperature.

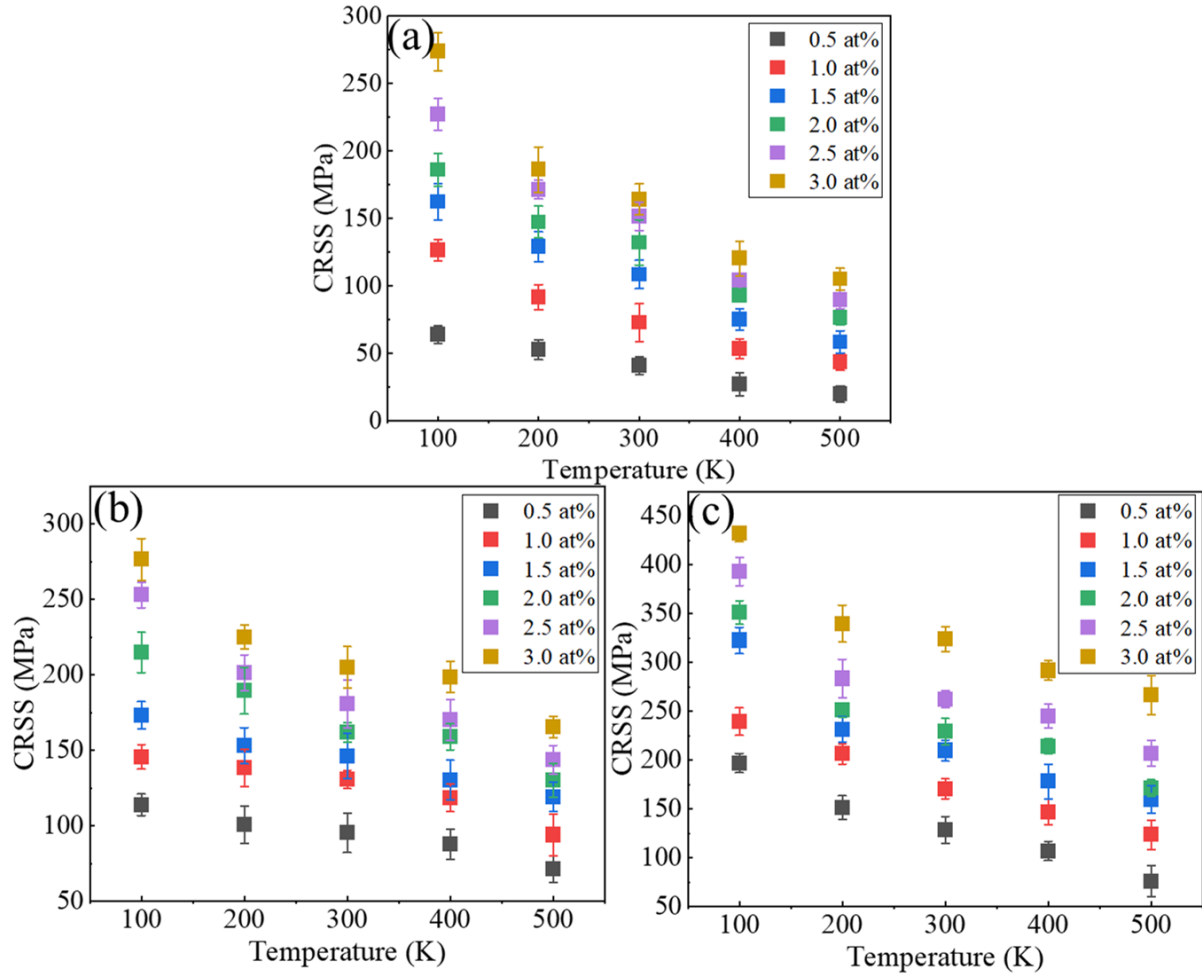


Figure 7.8. Plot of CRSS as a function of temperature for (a) basal, (b) prismatic and (c) pyramidal dislocations decorated with different Y content. Error bars represent standard deviation.

7.5.3 Descriptor Map of CRSS Versus Y Content and Temperature

In this study, we have calculated strengthening effect of Y on three main dislocations in Mg at finite temperature. Evolution of CRSS versus Y content and temperature is shown in **Figure 7.9**.

As a good measure of the solute strengthening effect for dislocations, CRSS is taken as a descriptor for Y effect on ductility in Mg-Y alloys. The map in **Figure 7.9** indicates the modification of CRSS due to addition of Y at different temperature. For example, when Mg-Y is deformed at room temperature, i.e., around 300K, CRSS of three dislocations would increase to the same level due to an addition of 1.5% Y, promoting activation of non-basal slip systems and thus enhancing the

ductility. This is consistent with the recent experimental observations in Mg-Y alloys where profuse pyramidal $\langle c+a \rangle$ were activated [22, 51].

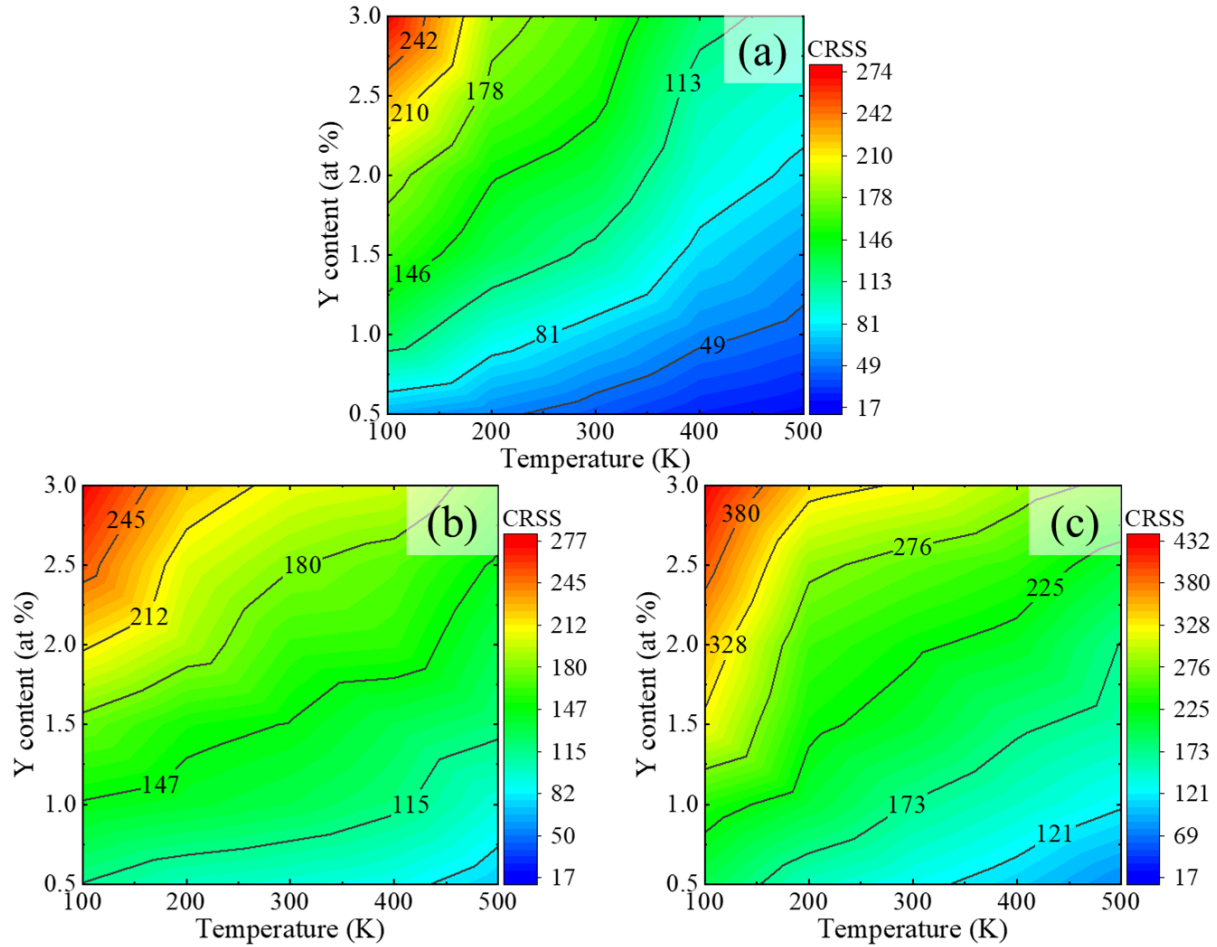


Figure 7.9. The descriptor map for CRSS evolution as a function of temperature and Y concentration.

7.6 Conclusions

Extensive MD simulations were carried out in this work to obtain reliable data for evolution of CRSS with Y content and temperature. The conclusions are as follows:

1. From simulation at 0K, basal slip is more sensitive to the Y solute compared to prismatic and pyramidal slip. This stronger hardening effect of Y on basal slip makes the easy activation of non-basal slip systems.

2. Pyramidal slip is observed more sensitive to temperature, and combined with Y addition, more pyramidal slips are potentially activated at finite temperature.
3. Indicators in the current simulation show a promising pathway of improvement for ductility of Mg alloys by controlling the content of Y at finite temperature.

7.7 Acknowledgements

The authors acknowledge financial support from Natural Sciences and Engineering Research Council of Canada (NSERC), McGill Engineering Doctoral Award (MEDA), China Scholarship Council (201706050149), and thank Compute Canada for providing computing resources.

7.8 References

- [1] Y. Yang, X. Xiong, J. Chen, X. Peng, D. Chen, F. Pan, Research advances in magnesium and magnesium alloys worldwide in 2020, *Journal of Magnesium and Alloys* 9(3) (2021) 705-747.
- [2] R. M, S. P, Review on the effect of different processing techniques on the microstructure and mechanical behaviour of AZ31 Magnesium alloy, *Journal of Magnesium and Alloys* 9(5) (2021) 1692-1714.
- [3] J.F. Nie, K.S. Shin, Z.R. Zeng, Microstructure, Deformation, and Property of Wrought Magnesium Alloys, *Metallurgical and Materials Transactions A* 51(12) (2020) 6045-6109.
- [4] U.M. Chaudry, K. Hamad, J.-G. Kim, On the ductility of magnesium based materials: A mini review, *Journal of Alloys and Compounds* 792 (2019) 652-664.
- [5] Z. Zeng, N. Stanford, C.H.J. Davies, J.-F. Nie, N. Birbilis, Magnesium extrusion alloys: a review of developments and prospects, *International Materials Reviews* 64(1) (2019) 27-62.
- [6] M.D. Costantino, A. Schuster, H. Helmholtz, A. Meyer-Rachner, R. Willumeit-Romer, B.J.C. Luthringer-Feyerabend, Inflammatory response to magnesium-based biodegradable implant materials, *Acta Biomater* 101 (2020) 598-608.
- [7] V. Luque-Agudo, M.C. Fernandez-Calderon, M.A. Pacha-Olivenza, C. Perez-Giraldo, A.M. Gallardo-Moreno, M.L. Gonzalez-Martin, The role of magnesium in biomaterials related infections, *Colloids Surf B Biointerfaces* 191 (2020) 110996.

- [8] R. Unbehau, B.J.C. Luthringer-Feyerabend, R. Willumeit-Romer, The impact of brain cell metabolism and extracellular matrix on magnesium degradation, *Acta Biomater* 116 (2020) 426-437.
- [9] H. Zhou, B. Liang, H. Jiang, Z. Deng, K. Yu, Magnesium-based biomaterials as emerging agents for bone repair and regeneration: from mechanism to application, *Journal of Magnesium and Alloys* 9(3) (2021) 779-804.
- [10] M. Stricker, W.A. Curtin, Prismatic Slip in Magnesium, *The Journal of Physical Chemistry C* 124(49) (2020) 27230-27240.
- [11] H. Tonda, S. Ando, Effect of temperature and shear direction on yield stress by $\{11\text{-}22\} \langle -1\text{-}123 \rangle$ slip in HCP metals, *Metallurgical and Materials Transactions A* 33(3) (2002) 831-836.
- [12] W.B. Hutchinson, M.R. Barnett, Effective values of critical resolved shear stress for slip in polycrystalline magnesium and other hcp metals, *Scripta Materialia* 63(7) (2010) 737-740.
- [13] K. Wei, R. Hu, D. Yin, L. Xiao, S. Pang, Y. Cao, H. Zhou, Y. Zhao, Y. Zhu, Grain size effect on tensile properties and slip systems of pure magnesium, *Acta Materialia* 206 (2021).
- [14] N. Li, L. Yang, C. Wang, M.A. Monclús, D. Shi, J.M. Molina-Aldareguía, Deformation mechanisms of basal slip, twinning and non-basal slips in Mg–Y alloy by micropillar compression, *Materials Science and Engineering: A* 819 (2021).
- [15] Z. Wu, R. Ahmad, B. Yin, S. Sandlöbes, W.A. Curtin, Mechanistic origin and prediction of enhanced ductility in magnesium alloys, *Science* 359 (2018) 447-452.
- [16] R. Ahmad, Z. Wu, S. Groh, W.A. Curtin, Pyramidal II to basal transformation of $\langle c + a \rangle$ edge dislocations in Mg-Y alloys, *Scripta Materialia* 155 (2018) 114-118.
- [17] Z. Wu, W.A. Curtin, Mechanism and energetics of $\langle c + a \rangle$ dislocation cross-slip in hcp metals, *Proceedings of the National Academy of Sciences of the United States of America* 113(40) (2016) 11137-11142.
- [18] Z. Wu, W.A. Curtin, The origins of high hardening and low ductility in magnesium, *Nature* 526 (2015) 62-7.
- [19] T. Nogaret, W.A. Curtin, J.A. Yasi, L.G. Hector Jr, D.R. Trinkle, Atomistic study of edge and screw $\langle c + a \rangle$ dislocations in magnesium, *Acta Materialia* 58(13) (2010) 4332-4343.

- [20] D. Buey, L.G. Hector, M. Ghazisaeidi, Core structure and solute strengthening of second-order pyramidal $\langle c+a \rangle$ dislocations in Mg-Y alloys, *Acta Materialia* 147 (2018) 1-9.
- [21] K.-H. Kim, J.B. Jeon, N.J. Kim, B.-J. Lee, Role of yttrium in activation of $\langle c + a \rangle$ slip in magnesium: An atomistic approach, *Scripta Materialia* 108 (2015) 104-108.
- [22] S. Sandlöbes, M. Friák, J. Neugebauer, D. Raabe, Basal and non-basal dislocation slip in Mg–Y, *Materials Science and Engineering: A* 576 (2013) 61-68.
- [23] D. Zhang, L. Jiang, J.M. Schoenung, S. Mahajan, E.J. Lavernia, TEM study on relationship between stacking faults and non-basal dislocations in Mg, *Philosophical Magazine* 95(34) (2015) 3823-3844.
- [24] G. Zhu, L. Wang, H. Zhou, J. Wang, Y. Shen, P. Tu, H. Zhu, W. Liu, P. Jin, X. Zeng, Improving ductility of a Mg alloy via non-basal $\langle a \rangle$ slip induced by Ca addition, *International Journal of Plasticity* 120 (2019) 164-179.
- [25] K.-H. Kim, J.H. Hwang, H.-S. Jang, J.B. Jeon, N.J. Kim, B.-J. Lee, Dislocation binding as an origin for the improvement of room temperature ductility in Mg alloys, *Materials Science and Engineering: A* 715 (2018) 266-275.
- [26] T. Tsuru, D.C. Chrzan, Effect of solute atoms on dislocation motion in Mg: an electronic structure perspective, *Sci Rep* 5 (2015) 8793.
- [27] G. Nayyeri, W.J. Poole, C.W. Sinclair, S. Zaefferer, Measurement of the critical resolved shear stress for basal slip in magnesium alloys using instrumented indentation, *Scripta Materialia* 156 (2018) 37-41.
- [28] V. Herrera-Solaz, P. Hidalgo-Manrique, M.T. Pérez-Prado, D. Letzig, J. Llorca, J. Segurado, Effect of rare earth additions on the critical resolved shear stresses of magnesium alloys, *Materials Letters* 128 (2014) 199-203.
- [29] H.-S. Jang, J.-K. Lee, A.J.S.F. Tapia, N.J. Kim, B.-J. Lee, Activation of non-basal $\langle c + a \rangle$ slip in multicomponent Mg alloys, *Journal of Magnesium and Alloys* (2021).
- [30] Y. Chino, M. Kado, M. Mabuchi, Compressive deformation behavior at room temperature – 773K in Mg–0.2mass%(0.035at.%)Ce alloy, *Acta Materialia* 56(3) (2008) 387-394.
- [31] G. Liu, J. Zhang, G. Xi, R. Zuo, S. Liu, Designing Mg alloys with high ductility: Reducing the strength discrepancies between soft deformation modes and hard deformation modes, *Acta Materialia* 141 (2017) 1-9.

- [32] R.K. Sabat, A.P. Brahme, R.K. Mishra, K. Inal, S. Suwas, Ductility enhancement in Mg-0.2%Ce alloys, *Acta Materialia* 161 (2018) 246-257.
- [33] R.K. Mishra, A. Brahme, R.K. Sabat, L. Jin, K. Inal, Twinning and texture randomization in Mg and Mg-Ce alloys, *International Journal of Plasticity* 117 (2019) 157-172.
- [34] D. Zhang, H. Wen, M.A. Kumar, F. Chen, L. Zhang, I.J. Beyerlein, J.M. Schoenung, S. Mahajan, E.J. Lavernia, Yield symmetry and reduced strength differential in Mg-2.5Y alloy, *Acta Materialia* 120 (2016) 75-85.
- [35] N. Kumar, D. Choudhuri, R. Banerjee, R.S. Mishra, Strength and ductility optimization of Mg–Y–Nd–Zr alloy by microstructural design, *International Journal of Plasticity* 68(0) (2015) 77-97.
- [36] B. Lei, B. Jiang, H. Yang, Z. Dong, Q. Wang, M. Yuan, G. Huang, J. Song, D. Zhang, F. Pan, Effect of Nd addition on the microstructure and mechanical properties of extruded Mg-Gd-Zr alloy, *Materials Science and Engineering: A* 816 (2021).
- [37] H. Fan, Q. Wang, X. Tian, J.A. El-Awady, Temperature effects on the mobility of pyramidal $\langle c + a \rangle$ dislocations in magnesium, *Scripta Materialia* 127 (2017) 68-71.
- [38] S. Plimpton, Fast Parallel Algorithms for Short-Range Molecular Dynamics, *Journal of Computational Physics* 117 (1995) 1-19.
- [39] Z. Wu, M.F. Francis, W.A. Curtin, Magnesium interatomic potential for simulating plasticity and fracture phenomena, *Modelling and Simulation in Materials Science and Engineering* 23(1) (2014) 015004.
- [40] R. Ahmad, S. Groh, M. Ghazisaeidi, W.A. Curtin, Modified embedded-atom method interatomic potential for Mg–Y alloys, *Modelling and Simulation in Materials Science and Engineering* 26(6) (2018) 065010.
- [41] A. Stukowski, Visualization and analysis of atomistic simulation data with OVITO—the Open Visualization Tool, *Modelling and Simulation in Materials Science and Engineering* 18(1) (2009) 015012.
- [42] D. Hull, D.J. Bacon, Chapter 4 - Elastic Properties of Dislocations, in: D. Hull, D.J. Bacon (Eds.), *Introduction to Dislocations (Fifth Edition)*, Butterworth-Heinemann, Oxford, 2011, pp. 63-83.

- [43] Y.N. Osetsky, D.J. Bacon, An atomic-level model for studying the dynamics of edge dislocation in metals, *Modelling and Simulation in Materials Science and Engineering* 11 (2003).
- [44] D. Rodney, Activation enthalpy for kink-pair nucleation on dislocations: Comparison between static and dynamic atomic-scale simulations, *Physical Review B* 76(14) (2007).
- [45] A.V. Ivanov, V.M. Uzdin, H. Jónsson, Fast and robust algorithm for energy minimization of spin systems applied in an analysis of high temperature spin configurations in terms of skyrmion density, *Computer Physics Communications* 260 (2021).
- [46] G.P.M. Leyson, W.A. Curtin, Friedel vs. Labusch: the strong/weak pinning transition in solute strengthened metals, *Philosophical Magazine* 93(19) (2013) 2428-2444.
- [47] R. LABUSCH, Statistical theories of solid solution hardening, *ACTA METALLURGICA*, 20 (1972).
- [48] P. Yi, R.C. Cammarata, M.L. Falk, Atomistic simulation of solid solution hardening in Mg/Al alloys: Examination of composition scaling and thermo-mechanical relationships, *Acta Materialia* 105 (2016) 378-389.
- [49] S.E. Prameela, P. Yi, Y. Hollenweger, B. Liu, J. Chen, L. Kecskes, D.M. Kochmann, M.L. Falk, T.P. Weihs, Strengthening magnesium by design: Integrating alloying and dynamic processing, *Mechanics of Materials* (2022).
- [50] K. Chu, M.E. Foster, R.B. Sills, X. Zhou, T. Zhu, D.L. McDowell, Temperature and composition dependent screw dislocation mobility in austenitic stainless steels from large-scale molecular dynamics, *npj Computational Materials* 6(1) (2020).
- [51] J. Wu, S. Si, K. Takagi, T. Li, Y. Mine, K. Takashima, Y.L. Chiu, Study of basal $\langle a \rangle$ and pyramidal $\langle c+a \rangle$ slips in Mg-Y alloys using micro-pillar compression, *Philosophical Magazine* 100(11) (2020) 1454-1475.

Chapter 8: Conclusions

8.1 Final Conclusions

In this thesis, we investigated systematically the underlying atomistic mechanisms operative in polycrystalline Mg. By performing the atomistic simulations, selection of twin variants and characteristic of various twinning boundaries (TBs) as well as the deformation response in Mg-Y alloy were studied, aiming to reveal twinning mechanism for the defect engineering of Mg toward desirable strength and ductility. The main results are summarized as follows:

1. Twin activation is orientation dependent and twin variants with high Schmid factor are preferentially selected to be activated with high probability.
2. The nucleation and growth of $\{10\bar{1}1\}$ and $\{10\bar{1}2\}$ twins are accompanied by the formation and propagation of basal stacking faults while no stacking fault is observed in $\{11\bar{2}1\}$ twin.
3. Only one kind of disconnection, i.e., $(\mathbf{b}_{1/2}, h_{1/2})$ is characterized in $\{11\bar{2}1\}$ twin while two types of disconnections are observed in $\{10\bar{1}1\}$ twin. In case of $\{10\bar{1}1\}$ twin, the first type of steps with height of $2h_0$ and $4h_0$ are mobile while the other type of steps with height of h_0 and $3h_0$ are immobile. The formation of h_0 - and $3h_0$ -steps may be due to the interaction between BSF and $2h_0$ - or $4h_0$ - step.
4. Due to the formation of BSFs inside $\{10\bar{1}1\}$ twinned region, the front line of mobile steps is divided different segments and each segment will move as a unit at different velocity. When the mobile interfacial steps are consumed during twin growth, new steps are nucleated and glide on the TB interface, leading to twin growth in the lateral and vertical directions.

5. In $\{10\bar{1}1\}$ twin, the immobile steps i.e., h_0 and $3h_0$ exist in the interaction site between BSFs and TB interface and they move up conservatively accompanying the propagation of stacking fault plane as twin grows in the normal direction.
6. The deformation response of polycrystalline Mg and Mg-Al systems is observed to be dominated by the nucleation and growth of compression and tension twins in a compression loading and dislocations would be more profuse under a tensile loading where growth of twinning is lazy. Twin is hardly activated in Mg-Y alloy deformed under a tensile loading where pyramidal slips would be promoted due to the retardation of twinning.
7. One of the solute effects is from solute segregation at TBs. The ab initio calculation shows that the negative segregation energy increases the solute solubility at TBs and the solute concentration at TBs can be controlled by the combination of bulk concentration and annealing temperature. In addition, a two-factor considers both lattice strain induced by solute substitution and the electronegativity difference, representing mechanical and chemical effects due to the solute introduction respectively. The model prediction was found to be in good agreement with the DFT-calculated solute segregation energy. In terms of the strengthening energy, we find that central d-band elements have stronger strengthening effect on TB cohesion than elements at borders. Additionally, solutes from s/p band groups are embrittling to TB cohesion and rare earth elements present a weaker strengthening effect on compression TB than that of tensile TB.
8. Another solute effect is on the modification of critical stress for dislocations in Mg. From MD simulation at 0K, basal slip is more sensitive to the Y solute compared to prismatic and pyramidal slip. This stronger hardening effect of Y on basal slip makes the easy activation of non-basal slip systems. Furthermore, pyramidal slip is observed more sensitive to temperature, and combined with Y addition, more pyramidal slips are potentially activated at finite temperature.

9. Indicators obtained in the calculations of solute effect on TBs and dislocations provide a useful basis for selecting promising solutes in the development of new Mg alloys.

8.2 Contributions to Original Knowledge

The contributions to original knowledge established in this thesis are summarized as follows:

1. A novel algorithm on the basis of crystallographic misorientation was first developed to effectively identify twin variant in deformed polycrystalline Mg. The method can be extended to be used in other hcp metals such as Zr and Ti.
2. The Schmid factor was first adopted in atomistic simulation of polycrystalline hcp structures to evaluate the activation of twin variants, providing important pathway for future analysis of twinning behavior in hcp polycrystals.
3. Three-dimensional characterization of the nucleation and growth of twins in Mg polycrystal was presented for the first time, providing details of how twins nucleate from grain boundaries and propagate through the matrix at atomistic scale.
4. For the first time, the disconnection assisted twinning growth along horizontal and vertical direction was presented, revealing twinning mechanism in terms of interface defects.
5. Two factor model was first proposed to predict the segregation tendency at twinning boundaries in Mg, providing a rational prediction by considering the contributions from both mechanical and chemical effect.
6. The dependence of critical shear stress of main dislocations in Mg on temperature and Y content was first constructed, confirming that sequence for the activation of dislocations can be modified by adding suitable Y as well as controlling temperature.

8.3 Future Work

This thesis represents an important step towards a comprehensive understanding of the twin variant selection in polycrystalline Mg, characteristic of three twin boundary interfaces, grain boundary segregation and solute strengthening of dislocations. However, many unsolved issues still exist, and a plethora of interesting topics are left. Future works could be directed in the following specific areas:

1. ***Formation mechanism of twinning interface disconnections***: Several types of disconnections have been determined to play the vital role in twinning mechanism, so the formation mechanism of these disconnections in terms of dislocation reactions and the energy barrier calculation requires further investigations.
2. ***Grain boundary mobility in unalloyed Mg and Mg alloys***: Solute segregation were found to potentially strengthening or embrittling grain boundaries in current study, so more work should be focused on solute effect on grain boundary mobility, which would provide theoretical support for microstructural control considering solute segregation.
3. ***Dislocation mobility in Mg alloys***: Tailoring activation of dislocations are of particular interest in design of high ductility Mg alloys. Only critical resolved shear stress was considered in examination of solute effect on motion of dislocations. Therefore, solute effect on mobility of dislocations in Mg alloys needs further studies.
4. ***Solute effect on dislocation-twinning boundary interactions***: As a dislocation approaches a twin, the stress field around them starts to interact strongly, resulting in several scenarios in terms of slip transfer, such as dislocation pileup, perfect transmission, and partial transmission. Therefore, it would be interesting to know how these processes are affected by introducing solute atoms.